

Low-Dimensional Inorganic Nanofunctional Materials: Design, Assembly, and Application for Chemical Engineering (I)

Guest Editors: Lan Xiang, Guo Gao, Yunpeng Yin, Huijun Wu,
Yongcheng Jin, and Wancheng Zhu





**Low-Dimensional Inorganic
Nanofunctional Materials: Design, Assembly,
and Application for Chemical Engineering (I)**

Journal of Nanomaterials

**Low-Dimensional Inorganic
Nanofunctional Materials: Design, Assembly,
and Application for Chemical Engineering (I)**

Guest Editors: Lan Xiang, Guo Gao, Yunpeng Yin,
Huijun Wu, Yongcheng Jin, and Wancheng Zhu



Copyright © 2013 Hindawi Publishing Corporation. All rights reserved.

This is a special issue published in "Journal of Nanomaterials." All articles are open access articles distributed under the Creative Commons Attribution License, which permits unrestricted use, distribution, and reproduction in any medium, provided the original work is properly cited.

Editorial Board

Katerina E. Aifantis, Greece
Nageh K. Allam, USA
Margarida Amaral, Portugal
Xuedong Bai, China
Lavinia Balan, France
Enrico Bergamaschi, Italy
Theodorian Borca-Tasciuc, USA
C. Jeffrey Brinker, USA
Christian Brosseau, France
Xuebo Cao, China
Shafiq Chowdhury, USA
Kwang-Leong Choy, UK
Cui ChunXiang, China
Miguel A. Correa-Duarte, Spain
Shadi A. Dayeh, USA
Claude Estourns, France
Alan Fuchs, USA
Lian Gao, China
Russell E. Gorga, USA
Hongchen Chen Gu, China
Mustafa O. Guler, Turkey
John Zhanhu Guo, USA
Smrati Gupta, Germany
Michael Harris, USA
Zhongkui Hong, China
Michael Hu, USA
David Hui, USA
Y.-K. Jeong, Republic of Korea
Sheng-Rui Jian, Taiwan
Wanqin Jin, China
Rakesh K. Joshi, UK
Zhenhui Kang, China
Fathallah Karimzadeh, Iran
Alireza Khataee, Iran
Do Kyung Kim, Korea

Alan K. T. Lau, Hong Kong
Burtrand Lee, USA
Jun Li, Singapore
Benxia Li, China
Xing-Jie Liang, China
Shijun Liao, China
Gong Ru Lin, Taiwan
J. -Y. Liu, USA
Tianxi Liu, China
Jue Lu, USA
Songwei Lu, USA
Daniel Lu, China
Ed Ma, USA
Gaurav Mago, USA
Santanu K. Maiti, India
Sanjay R. Mathur, Germany
V. Mittal, United Arab Emirates
Weihai Ni, Germany
Sherine Obare, USA
Atsuto Okamoto, Japan
Abdelwahab Omri, Canada
Edward Andrew Payzant, USA
Kui-Qing Peng, China
Anukorn Phuruangrat, Thailand
Mahendra Rai, India
Suprakas Sinha Ray, South Africa
Ugur Serincan, Turkey
Huaiyu Shao, Japan
Donglu Shi, USA
Vladimir Sivakov, Germany
Marinella Striccoli, Italy
Bohua Sun, South Africa
Saikat Talapatra, USA
Nairong Tao, China
Titipun Thongtem, Thailand

Somchai Thongtem, Thailand
Alexander Tolmachev, Ukraine
Valeri P. Tolstoy, Russia
Tsung-Yen Tsai, Taiwan
Takuya Tsuzuki, Australia
Raquel Verdejo, Spain
Mat U. Wahit, Malaysia
Zhenbo Wang, China
Ruiping Wang, Canada
Shiren Wang, USA
Cheng Wang, China
Yong Wang, USA
Jinquan Wei, China
Ching-Ping Wong, Hong Kong
Xingcai Wu, China
Guodong Xia, Hong Kong
Zhi Li Xiao, USA
Ping Xiao, UK
Yangchuan Xing, USA
Shuangxi Xing, China
N. Xu, China
Doron Yadlovker, Israel
Yingkui Yang, China
Khaled Youssef, USA
Kui Yu, Canada
William W. Yu, USA
Haibo Zeng, China
Tianyou Zhai, Japan
Renyun Zhang, Sweden
Bin Zhang, China
Yanbao Zhao, China
Lianxi Zheng, Singapore
Chunyi Zhi, Hong Kong

Contents

Low-Dimensional Inorganic Nanofunctional Materials: Design, Assembly, and Application for Chemical Engineering (I), Lan Xiang, Guo Gao, Yunpeng Yin, Huijun Wu, Yongcheng Jin, and Wancheng Zhu

Volume 2013, Article ID 306834, 2 pages

Synthesis of Flexible Aerogel Composites Reinforced with Electrospun Nanofibers and Microparticles for Thermal Insulation, Huijun Wu, Yantao Chen, Qiliang Chen, Yunfei Ding, Xiaoqing Zhou, and Haitao Gao

Volume 2013, Article ID 375093, 8 pages

Electrochemical Sensor for o-Nitrophenol Based on β -Cyclodextrin Functionalized Graphene Nanosheets, Jinlong Liu, Yihong Chen, Yujing Guo, Fengling Yang, and Fangqin Cheng

Volume 2013, Article ID 632809, 6 pages

Influence of the Process Parameters on the Formation of $\text{CaSO}_4 \cdot 0.5\text{H}_2\text{O}$ Whiskers, Kangbi Luo, Huping Li, Chunmei Li, and Ping Ning

Volume 2013, Article ID 906267, 6 pages

Synthesis of $\text{Al}(\text{OH})_3$ Nanostructures from $\text{Al}(\text{OH})_3$ Microagglomerates via Dissolution-Precipitation Route, Bo Yu, Zhenhao Tian, Jie Xiong, and Lan Xiang

Volume 2013, Article ID 718979, 6 pages

Anti-Icing Property of Superhydrophobic Octadecyltrichlorosilane Film and Its Ice Adhesion Strength, Liang Ge, Guifu Ding, Hong Wang, Jinyuan Yao, Ping Cheng, and Yan Wang

Volume 2013, Article ID 278936, 5 pages

Design and Evaluation of a Three Dimensionally Ordered Macroporous Structure within a Highly Patterned Cylindrical Sn-Ni Electrode for Advanced Lithium Ion Batteries, Yongcheng Jin, Hirokazu Munakata, Naoya Okada, and Kiyoshi Kanamura

Volume 2013, Article ID 937019, 6 pages

Effect of the Flow Channel Structure on the Nanofiltration Separation Performance, Zhi Chen, Ben Zhao, Fanglei Chen, and Jianming Li

Volume 2013, Article ID 132919, 10 pages

Hydrothermal Synthesis of SBA-15 Using Sodium Silicate Derived from Coal Gangue, Jing Wang, Li Fang, Fangqin Cheng, Xiaofang Duan, and Rongming Chen

Volume 2013, Article ID 352157, 6 pages

Influence of Activity of $\text{CaSO}_4 \cdot 2\text{H}_2\text{O}$ on Hydrothermal Formation of $\text{CaSO}_4 \cdot 0.5\text{H}_2\text{O}$ Whiskers, S. C. Hou and L. Xiang

Volume 2013, Article ID 237828, 5 pages

Surfactant-Free Solvothermal Method for Synthesis of Mesoporous Nanocrystalline TiO_2 Microspheres with Tailored Pore Size, Yajing Zhang, Sujuan Zhang, Kangjun Wang, Fu Ding, and Jing Wu

Volume 2013, Article ID 294020, 7 pages



Efficient Removal of Cr(VI) with Fe/Mn Mixed Metal Oxide Nanocomposites Synthesized by a Grinding

Method, Wang Weilong and Fu Xiaobo

Volume 2013, Article ID 514917, 8 pages

Influence of the Mixing Ways of Reactants on ZnO Morphology, Lining Yang and Lan Xiang

Volume 2013, Article ID 289616, 6 pages

Effect of Copper Nanoparticles Dispersion on Catalytic Performance of Cu/SiO₂ Catalyst for Hydrogenation of Dimethyl Oxalate to Ethylene Glycol, Yajing Zhang, Na Zheng, Kangjun Wang,

Sujuan Zhang, and Jing Wu

Volume 2013, Article ID 629375, 6 pages

Editorial

Low-Dimensional Inorganic Nanofunctional Materials: Design, Assembly, and Application for Chemical Engineering (I)

Lan Xiang,¹ Guo Gao,² Yunpeng Yin,³ Huijun Wu,⁴ Yongcheng Jin,⁵ and Wancheng Zhu⁶

¹ Department of Chemical Engineering, Tsinghua University, Beijing 100084, China

² Department of Bio-Nano-Science and Engineering, Shanghai Jiao Tong University, Shanghai 200240, China

³ IBM Albany NanoTech Research and Development Center, Albany, NY 12309, USA

⁴ College of Civil Engineering, Guangzhou University, Guangzhou 510006, China

⁵ Department of Applied Chemistry, Tokyo Metropolitan University, Tokyo 00813, Japan

⁶ Department of Chemical Engineering, Qufu Normal University, Qufu 273165, China

Correspondence should be addressed to Lan Xiang; xianglan@mail.tsinghua.edu.cn

Received 25 August 2013; Accepted 25 August 2013

Copyright © 2013 Lan Xiang et al. This is an open access article distributed under the Creative Commons Attribution License, which permits unrestricted use, distribution, and reproduction in any medium, provided the original work is properly cited.

Synthesis of low-dimensional inorganic nanofunctional materials is an increasingly important subject for chemical engineering researchers owing to their intriguing properties and wide applications in many chemical engineering fields such as ceramics, catalyst, and composite. Great progress was achieved in both theoretical and technical aspects for low-dimensional inorganic nanofunctional materials with desired composition, morphology, structure, and even facets. Thus, fabricating the low-dimensional inorganic nanofunctional materials, revealing the size-, shape-, composition-, and surface-dependent properties, and uncovering the potential applications in chemical engineering fields have turned to be an urgent and booming issue.

This special issue focuses on the development of new theories and technologies for the synthesis, characterization, and application of low-dimensional inorganic nanofunctional materials, especially those with potential applications in chemical engineering fields. A total of 13 research articles reporting on the design and assembly of various shaped low-dimensional nanomaterials including nanoparticles (B. Yu and L. Xiang, Y. Zhang, and N. Zheng et al.), nanosheets (J. Liu et al., B. Yu, and L. Xiang), nanofibers (H. Wu et al.), as well as micro-nano spheres and whiskers (L. Yang and L. Xiang, S. C. Hou and L. Xiang, K. Luo et al., Y. Zhang, and S. Zhang et al.) are presented in the special issue. The articles cover diversified object materials such as Cu (Y. Zhang and

N. Zheng et al.), SiO₂ (H. Wu et al.), TiO₂ (Y. Zhang and S. Zhang et al.), ZnO (L. Yang and L. Xiang), Al(OH)₃ (B. Yu and L. Xiang), CaSO₄ (S. C. Hou and L. Xiang and K. Luo et al.), graphene (J. Liu et al.), Sn/Ni (Y. Jin et al.), and Fe/Mn nanocomposites (W. Weilong and F. Xiaobo). The traditional fabrication processes such as precipitation (B. Yu and L. Xiang and L. Yang and L. Xiang), phase separation (L. Ge et al.), hydrothermal conversion (K. Luo et al. and J. Wang et al.), solvothermal reaction (Y. Zhang and S. Zhang et al.), and sol-gel process (H. Wu et al. and Y. Zhang and N. Zheng et al.) have been extensively presented in the synthesis of the nanomaterials, less common but promising methods such as electrospinning (H. Wu et al.), colloidal crystal templating and electroplating process (Y. Jin et al.), and grinding (W. Weilong and F. Xiaobo), are also introduced.

The application prospects relevant to chemical engineering in these articles range from reinforcing materials (S. C. Hou and L. Xiang and K. Luo et al.) to thermal insulations (H. Wu et al.) and anti-icing (L. Ge et al.), from nanofiltration separation (Z. Chen et al.) to heavy metal removal (W. Weilong and F. Xiaobo), and from electrochemical sensor (J. Liu et al.) to photocatalyst (Y. Zhang and S. Zhang et al.), as well as lithium ion batteries (Y. Jin et al.) and hydrogenation (Y. Zhang and N. Zheng et al.). It is exciting to report these contributions representing both traditional and modern research directions. We hope this issue will promote the

development of the making technologies of low-dimensional inorganic materials and their further scaleup and potential applications in chemical engineering fields.

Acknowledgments

We would like to thank all the authors and coauthors who have made conspicuous contributions and all the reviewers for their valuable time and dedication to this special issue.

*Lan Xiang
Guo Gao
Yunpeng Yin
Huijun Wu
Yongcheng Jin
Wancheng Zhu*

Research Article

Synthesis of Flexible Aerogel Composites Reinforced with Electrospun Nanofibers and Microparticles for Thermal Insulation

Huijun Wu,^{1,2} Yantao Chen,¹ Qiliang Chen,^{1,2} Yunfei Ding,^{1,2}
Xiaoqing Zhou,^{1,2} and Haitao Gao¹

¹ College of Civil Engineering, Guangzhou University, Guangzhou 510006, China

² Guangdong Provincial Key Laboratory of Building Energy Efficiency, Guangzhou University, Guangzhou 510006, China

Correspondence should be addressed to Huijun Wu; wuhuijun@tsinghua.org.cn

Received 28 December 2012; Accepted 11 April 2013

Academic Editor: Yongcheng Jin

Copyright © 2013 Huijun Wu et al. This is an open access article distributed under the Creative Commons Attribution License, which permits unrestricted use, distribution, and reproduction in any medium, provided the original work is properly cited.

Flexible silica aerogel composites in intact monolith of 12 cm were successfully fabricated by reinforcing SiO₂ aerogel with electrospun polyvinylidene fluoride (PVDF) webs via electrospinning and sol-gel processing. Three electrospun PVDF webs with different microstructures (e.g., nanofibers, microparticles, and combined nanofibers and microparticles) were fabricated by regulating electrospinning parameters. The as-electrospun PVDF webs with various microstructures were impregnated into the silica sol to synthesize the PVDF/SiO₂ composites followed by solvent exchange, surface modification, and drying at ambient atmosphere. The morphologies of the PVDF/SiO₂ aerogel composites were characterized and the thermal and mechanical properties were measured. The effects of electrospun PVDF on the thermal and mechanical properties of the aerogel composites were evaluated. The aerogel composites reinforced with electrospun PVDF nanofibers showed intact monolith, improved strength, and perfect flexibility and hydrophobicity. Moreover, the aerogel composites reinforced with the electrospun PVDF nanofibers had the lowest thermal conductivity (0.028 W·m⁻¹·K⁻¹). It indicates that the electrospun PVDF nanofibers could greatly improve the mechanical strength and flexibility of the SiO₂ aerogels while maintaining a lower thermal conductivity, which provides increasing potential for thermal insulation applications.

1. Introduction

Silica aerogel is a highly porous material with pore diameters in the range of 2–50 nm [1, 2]. The nanoporous structure of the silica aerogels having a high porosity above 90% makes the aerogels a highly thermal insulating materials with a super-low thermal conductivity as low as 0.013 W·m⁻¹·K⁻¹. The silica aerogels have well been acknowledged as one of the most attracting thermal insulation materials for wide applications in aircrafts and aerospace, chemical engineering, building constructions, and so forth [3–5]. However, the silica aerogels generally have poor mechanical stability (e.g., low strength and high brittleness) owing to their nanoporous nature and high porosity. The flexural strength of the pure silica aerogel with the density of 0.1 g·cm⁻³ was approximately 0.02 MPa [6] and the collapse strength under compression

of the silica aerogel with the density of 0.21 g·cm⁻³ was approximately 2.5 MPa [7]. The low flexural and collapse strength of the aerogels greatly limited their applications for thermal insulation.

Besides strengthening the aerogel framework by optimizing the sol-gel techniques [8], adding reinforced fibers into the silica aerogels and synthesizing the fiber-reinforced aerogel composites have become one of the most effective methods so as to improve the mechanical properties of the aerogels [2]. Various inorganic fibers [9–11] such as glass fibers, mullite fibers, ceramic fibers, and aluminum fibers were used to reinforce the aerogels. The previous literatures [9, 10] showed that the organic fibers could significantly improve the compressing strength of the aerogels. Moreover, the inorganic fibers could improve the shielding ability of the aerogels to the heat radiation at high temperature. However, owing to

the brittleness of the inorganic fibers, the aerogel composites reinforced by the inorganic fibers were brittle and less flexible. Feng et al. [12] synthesized the carbon aerogel composites reinforced by carbon fibers via the pyrolysis of the resorcinol-formaldehyde (RF) aerogels reinforced with oxidized polyacrylonitrile (PAN). Finlay et al. [13] impregnated the 2-mm-length short-cut natural polymer fibers into clay aerogels and achieved 4-time increase in compressive strength while only 20% increase in density. Compared to the inorganic fibers, the organic fibers have better flexibility so that the organic fibers are advantageous to synthesize flexible aerogel composites.

The previous literatures [9–13] on the aerogel composites focused on the reinforcements of the inorganic and organic fibers with the diameters in dozens of or several microns. The diameters of the reinforced fibers are greatly greater than those of the holes and the particles of the SiO₂ aerogels (namely, in several or dozens of nanometers). The great difference in the sizes of the reinforced fibers and the aerogel matrix leads to a great difference of the strains of the fibers and aerogels during the drying process of the fiber/aerogel composites. It often results in great cracks and weak mechanical stability of the fiber reinforced aerogel composites [14]. Therefore, reducing the diameters of the reinforced fibers and decreasing the difference of the sizes of the reinforced fibers and the aerogel matrix may improve the monolith integrity and the mechanical stability of the fiber/aerogel composites.

Electrospinning is a simple and low-cost method for making polymer and ceramic fibers with superfine diameters [15–17]. In recent years, it has attracted an increasing interest in the electrospinning technique owing to the promising properties of the electrospun nanofibers. Various structured and assembled nanofibers have been developed via electrospinning for specific functions and wide applications [18–20]. Very recently, Li et al. [21] developed a type of SiO₂ aerogel composite reinforced with electrospun poly(ethylene oxide) (PEO)/Elast-Eon TM (E2A) nanofibers via hybrid film casting and nanofiber electrospinning. Since the electrospun PEO/E2A nanofibers had the diameter of approximately 500 nm which was significantly finer than common inorganic and organic fibers and more closer to the size of the SiO₂ aerogels, the aerogel composites reinforced with the electrospun PEO/E2A nanofibers developed by Li et al. [21] showed intact morphology, little cracks, and good flexibility. However, the size of the flexible aerogel composite specimen prepared by Li et al. [21] was small (1.307 cm × 1.264 cm × 0.0857 cm). Moreover, the thermal conductivity of the aerogel composites was significantly increased to 0.0505 W/(m·K) owing to the limitation of the fabrication technique. Therefore, although the electrospun nanofibers have been proposed to strengthen the aerogels, the preparation technique of the electrospun nanofibers reinforced aerogel composites with larger size, and lower thermal conductivity has to be further developed.

In this paper, flexible SiO₂ aerogel composites reinforced with electrospun PVDF web were synthesized via electrospinning and sol-gel processing. Three electrospun PVDF webs with different microstructures are fabricated and then used to reinforce the SiO₂ aerogels. The effects of the electrospun PVDF on the thermal conductivity and the mechanical properties of the SiO₂ aerogels composites are evaluated.

2. Materials and Methods

2.1. Materials. Tetraethylorthosilicate (>98%, TEOS), ethylalcohol (>99%, EtOH), N,N-dimethyl-formamide (>98%, DMF), *n*-hexane (>99%), and trimethylchlorosilane (>95%, TMCS) were purchased from Baishi Co. Ltd. (China) and used as received. Hydrochloric acid (37%, HCl) and ammonia (25%, NH₄OH) were purchased from Guanghua Co. Ltd. (China) and used after diluted 10-fold with deionized water. PVDF was purchased from Baishi Co. Ltd. (China).

2.2. Electrospinning of PVDF Web. PVDF solutions with certain concentrations (namely, 18 wt.%, 23 wt.%, and 28 wt.%) were prepared by dissolving PVDF particles in DMF in a water bath at 65°C under magnetic stirring for 6 h, followed by cooling to room temperature with continuation of stirring for another 6 h. The PVDF solutions were, respectively, inserted into a plastic syringe with a stainless steel nozzle with the diameter of 1.0 mm for electrospinning by using an electrospinning apparatus (Model: NEU) from Kato Tech Co. Ltd., Japan. The apparatus consists of a syringe pump for supplying the PVDF solution, a grounded electrode for collecting the fibres, and a DC power for supplying high voltage. In the electrospinning process, the voltage of 13 kV was applied to the stainless steel connected with the PVDF solution. The distance of the nozzle and the collecting electrodes was 15 cm. The electrospun PVDF webs with a certain thickness were collected via electrospinning for about 5 days. The PVDF webs were dried at 80°C for 12 h before being used to reinforce the SiO₂ aerogels.

2.3. Preparation of Silica Sol. 100 mL silica sol was prepared by a two-step acid/base catalyzed sol-gel process. In the first step, TEOS, EtOH, deionized H₂O, and HCl were mixed in the molar ratio 1 : 7 : 1 : 1 × 10⁻⁵ and magnetically stirred for 30 mins. The solution was then refluxed for 24 h at room temperature. In the second step, DMF, H₂O, and NH₄OH were added into the stock solution and stirred for 30 mins. The final molar ratio of TMOS : EtOH : H₂O : DMF : HCl : NH₄OH is 1 : 7 : 2 : 0.25 : 10⁻⁵ : 3.57 × 10⁻³.

2.4. Synthesis of SiO₂ Aerogel Composites Reinforced with Electrospun PVDF Web. The electrospun PVDF webs were added into the silica sol as framework and the PVDF/SiO₂ composites were obtained. The PVDF/SiO₂ composite gelled to monoliths after 0.5–1 h. The composite gels were kept at room temperature for 2 days for further solidification to form silica monoliths. These monoliths were aged in H₂O/EtOH (1 : 4, vol.) solution for 24 h and then TEOS/EtOH (1 : 4, vol.) solution to strengthen the gel network. The water and ethanol solvents in the pores of the wet gel were exchanged with isopropanol and *n*-hexane, respectively. After being immersed in a solution of 10% vol. TMCS/*n*-hexane at 35°C for about 8 h for surface modification, the monoliths were washed in *n*-hexane for 32 h. The SiO₂ aerogel composites reinforced with electrospun PVDF webs were synthesized by drying the monoliths at 70°C for 12 h followed by further drying at 100°C for 12 h.

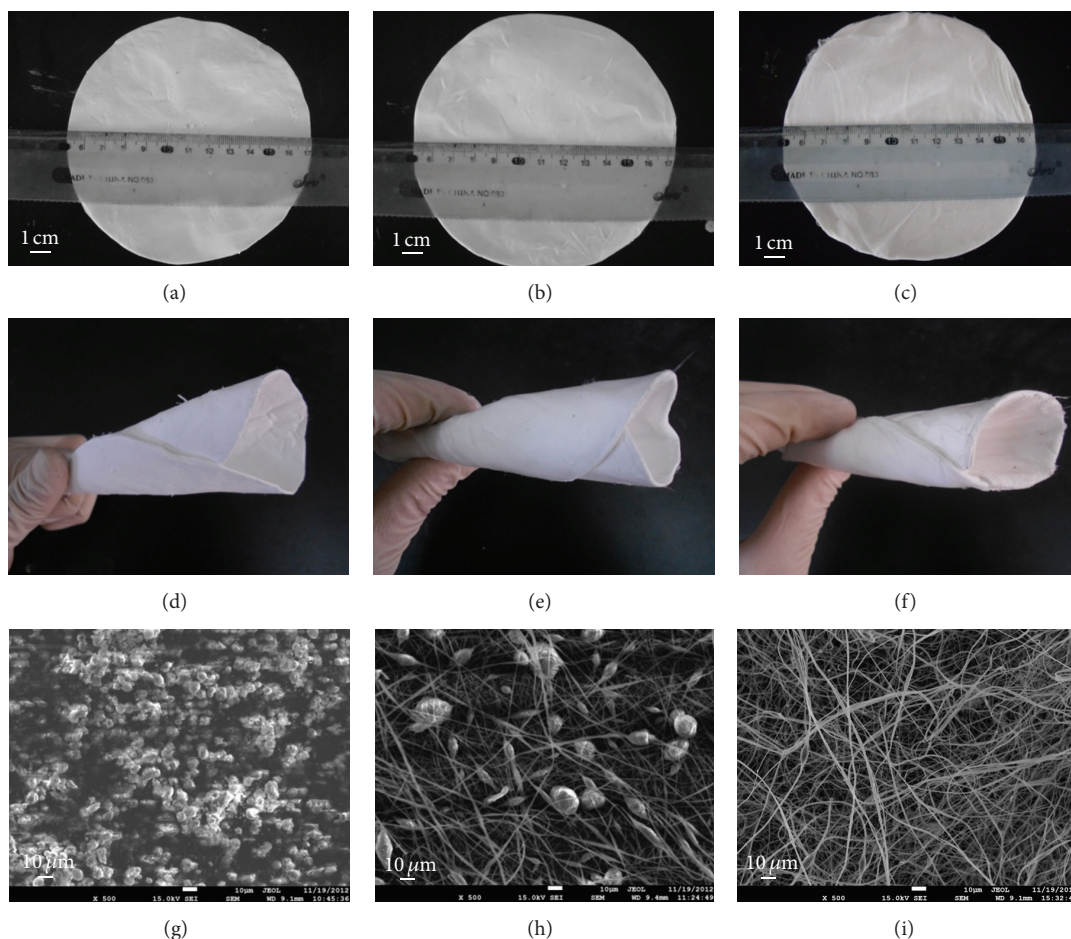


FIGURE 1: Morphology and microstructure of three electrospun PVDF webs (a, d, and g) microparticles electrospun from 18 wt.% PVDF; (b, e, and h) combined microparticles and nanofibers electrospun from 23 wt.% PVDF; (c, f, and i) nanofibers electrospun from 28 wt.% PVDF.

2.5. Instruments and Characterizations. The as-synthesized SiO_2 aerogel composites reinforced with electrospun PVDF webs were coated with gold/palladium to be investigated on their morphology and microstructure by using a 1530VP scanning electron microscopy (SEM, LEO, Germany). The thermal conductivity was measured by a TPS2500 thermal conductivity apparatus (Hot Disk, Germany) in terms of a transient plane heat source method at room temperature. The testing power and period of the thermal conductivity apparatus were 10 mW and 20 s, respectively. The thermostability of the aerogel composites was measured by using a TGA400 thermal gravimetric analyzer (TG, PerkinElmer, USA) at the heating rate of $10^\circ\text{C}/\text{min}$, respectively. The surface hydrophobicity of the aerogel composites was determined using a Kruss DSA100 droplet scanning analysis (DSA, Germany) at a static analysis mode.

The bulk density of the aerogel composite was determined by measuring the weight and volume of the aerogel composites. The compression tests of the aerogel composite were carried out on a WHY-50 automatic pressure testing machine (Hualong, China) at a time-displacement model with a loading speed of 2 mm/min. The bending modulus

of the aerogel composites was investigated with a three-point flexural bending method on a CMT6104 universal testing machine (Sunthink, China) with a loading speed of 5 mm/min at room temperature [9].

3. Results and Discussion

3.1. Microstructures of Three Electrospun PVDF Webs from Different Concentrations. Figure 1 shows the morphologies and microstructures of the three electrospun PVDF webs from the different PVDF/DMF solutions with various concentration (namely, 18 wt.%, 23 wt.%, 28 wt.%). Figures 1(a)–1(f) are the optical images of the three electrospun PVDF webs cut in circles with the diameter about 12 cm. It can be observed that the two PVDF webs electrospun from the 23 wt.% and 28 wt.% PVDF solutions have better integrity and flexibility than that from 18 wt.% PVDF solution. Figures 1(g)–1(i) show the SEM images of the three electrospun PVDF webs. Three different microstructures (namely, microparticles, combined microparticles and nanofibers, and nanofibers) could be observed which were electrospun from the PVDF solutions with the concentrations of 18 wt.%, 23 wt.%, and 28 wt.%,

TABLE 1: Properties of electrospun PVDF webs from different concentrations.

Concentration of PVDF solution (wt.%)	Properties of electrospun PVDF webs		
	Microstructures	Density ($\text{g}\cdot\text{cm}^{-3}$)	Thermal conductivity ($\text{W}\cdot\text{m}^{-1}\cdot\text{K}^{-1}$)
18	Microparticle	0.277	0.048
23	Microparticle/nanofiber	0.235	0.041
29	Nanofiber	0.202	0.037

respectively. The microparticles with the diameter in several micrometers were obtained via electrospinning from the 18 wt.% PVDF solution, while the nanofibers with the diameter in several hundred nanometers were obtained from the 28 wt.% PVDF solution. For the 23 wt.% PVDF solution both the microparticles and the nanofibers could be observed in the electrospun PVDF web.

It has been well acknowledged that the microstructures of the electrospun PVDF web are relevant to the viscosity of the PVDF solution. As the viscosity of PVDF solution was increased from 18 wt.% to 23 wt.%, the proportion of nanofiber in webs was increased due to the increased spinnability. Table 1 lists physical properties of the three electrospun PVDF webs. It can be observed that the PVDF nanofibers electrospun from 28 wt.% solution had the lowest density of $0.202 \text{ g}\cdot\text{cm}^{-3}$ and the lowest thermal conductivity of $0.037 \text{ W}\cdot\text{m}^{-1}\cdot\text{K}^{-1}$, compared to the microparticles and the combined microparticles and nanofibers electrospun from 23 wt.% and 18 wt.%, respectively.

3.2. Morphologies of SiO_2 Aerogel Composites Reinforced Electrospun PVDF Webs. Figure 2 shows optical and SEM image of the SiO_2 aerogel composites reinforced with the three electrospun PVDF webs with different microstructures. The SiO_2 aerogel composites were cut as the specimen in circles with the diameter about 12 cm. It can be observed that the SiO_2 aerogel composite specimens reinforced with the electrospun PVDF nanofibers and with combined PVDF microparticles and nanofibers showed intact integrity with a large size of diameter of 12 cm, which is significantly bigger than that in the previous literature [21]. From Figures 2(e) and 2(f) the SiO_2 aerogel composite specimens reinforced with the electrospun PVDF nanofibers and with combined PVDF microparticles and nanofibers showed good flexibility even if they were bending into a circle. Therefore, the intact and flexible SiO_2 aerogel composite specimens reinforced with the electrospun PVDF nanofibers and with combined PVDF microparticles and nanofibers have been firstly synthesized in this study. As a comparison, the SiO_2 aerogel composite specimen reinforced with electrospun PVDF microparticles (Figure 2(a)) was fragile and readily turned into pieces while being bended. As the external bend force was exerted on the specimens, the specimen reinforced with microparticle was easily broken.

The description of the morphologies of the aerogel composites reinforced with the three microstructured PVDF webs is shown in Table 2. The intact morphology of the aerogel composites reinforced with PVDF nanofibers and the

fragile morphology of that reinforced with PVDF microparticles imply that the electrospun PVDF nanofibers effectively improved the strength and the flexibility of the aerogels. It is because the electrospun PVDF nanofibers absorb the destructive energy and keep the integration of aerogel composite specimens. The second reason is that the diameter of the PVDF nanofibers is around $20 \sim 200 \text{ nm}$ which is much closer to the size of holes and particles of the SiO_2 aerogels. Moreover, as the electrospun PVDF nanofibers were added in the SiO_2 aerogels, the SiO_2 aerogels were separated into large quantity of small areas as shown in Figure 2(i). For the aerogel composites reinforced with electrospun PVDF nanofibers the induced tension difference between the interfaces of the nanofibers and the aerogel was reduced and the defects being bended were correspondingly decreased. As a result, the aerogel composites reinforced with electrospun PVDF nanofibers exhibited more perfect flexibility than the pure SiO_2 aerogel and the SiO_2 aerogel composites reinforced with electrospun PVDF microparticles.

Figure 3 shows the contact angle of the pure aerogel and the aerogel composites reinforced with electrospun PVDF webs. It can be observed that the contact angle of the pure aerogel is 139.0° . The contact angle of the aerogel composites was slightly reduced to $128.5^\circ - 134.1^\circ$ as the electrospun PVDF webs were added. It may be because the added electrospun PVDF microparticles or nanofibers increase the surface roughness of the aerogels. The SiO_2 aerogel composites reinforced with electrospun PVDF microparticles were still perfectly hydrophobic to water so that the aerogel composites could keep perfect thermal insulations even in moist environment.

3.3. Thermal Properties of SiO_2 Aerogel Composites Reinforced with Electrospun PVDF Webs. Table 3 lists the thermal conductivities of the SiO_2 aerogel composites reinforced with the electrospun PVDF webs with three different microstructures at room temperature. From Tables 1 and 3, it can be observed that the thermal conductivity of the electrospun PVDF nanofibrous webs was significantly decreased from $0.037 \text{ W}\cdot\text{m}^{-1}\cdot\text{K}^{-1}$ and $0.027 \text{ W}\cdot\text{m}^{-1}\cdot\text{K}^{-1}$ as the electrospun PVDF nanofibrous webs were filled with SiO_2 aerogels. It is because the pores of the electrospun PVDF nanofibrous webs in the micron scale were filled with and separated by the aerogels to smaller pores in the nanometer scale. The gas thermal conductivity of the electrospun PVDF webs filled with nanoporous aerogels was significantly reduced since the size of the aerogel nanopores was even smaller than that of the molecular free path of the air in the pores. As a result

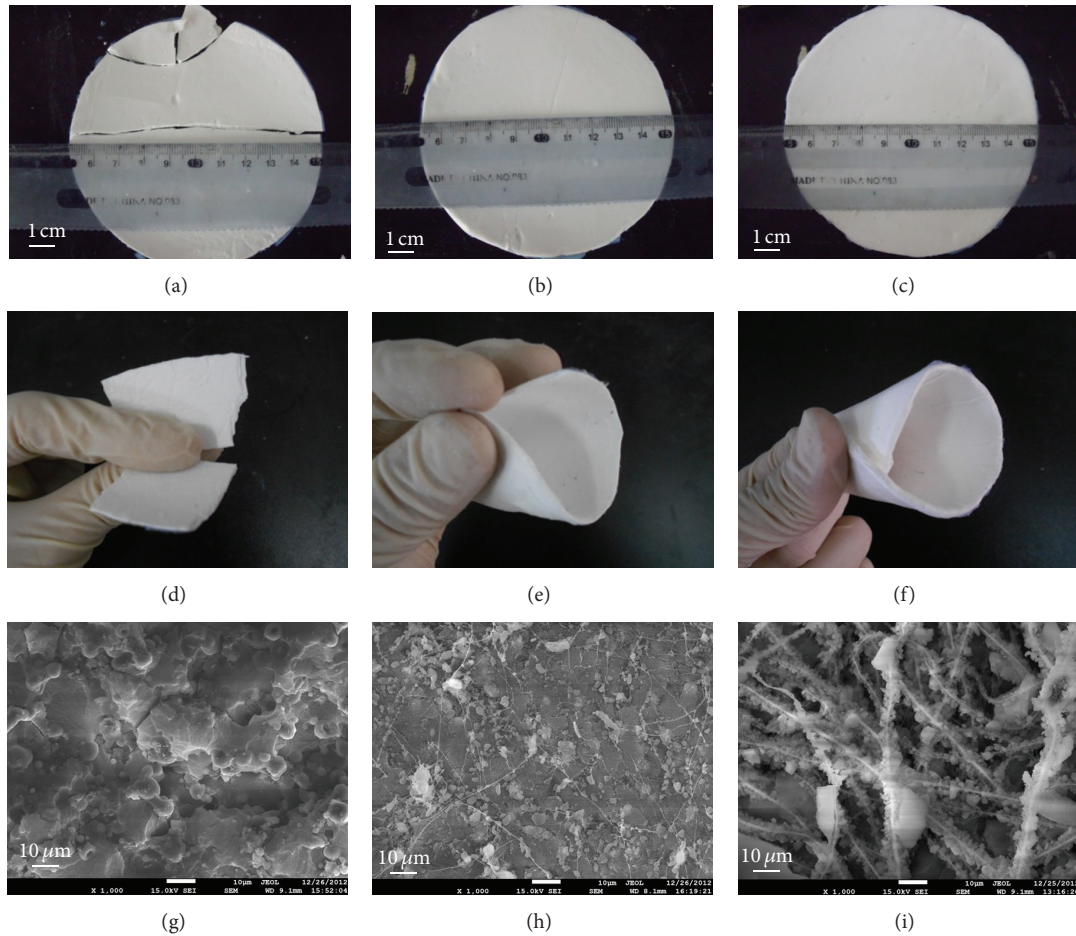


FIGURE 2: Morphology and flexibility of SiO_2 aerogel composites reinforced with electrospun PVDF webs: (a, d, and g) microparticles; (b, e, and h) microparticles/nanofibers; (c, f, and i) nanofibers.

TABLE 2: Properties of SiO_2 aerogel composites reinforced with electrospun PVDF webs.

Concentration of PVDF solution (wt.%)	SiO_2 aerogel composites reinforced with electrospun PVDF web		
	Integrity	Flexibility	Density ($\text{g}\cdot\text{cm}^{-3}$)
18	Crack	Fragile	0.277
23	Intact	Flexible	0.235
29	Intact	Flexible	0.202

the aerogel composites reinforced with the electrospun PVDF webs had lower thermal conductivity than the electrospun PVDF webs.

The aerogel composites reinforced with the electrospun PVDF nanofibers yielded the lowest thermal conductivity of $0.027 \text{ W}\cdot\text{m}^{-1}\cdot\text{K}^{-1}$ in all the three aerogel composites. The composite aerogel reinforced with the PVDF microparticles had the highest thermal conductivity of $0.039 \text{ W}\cdot\text{m}^{-1}\cdot\text{K}^{-1}$, and the composite with combined PVDF microparticles and nanofibers had a moderate thermal conductivity of

$0.032 \text{ W}\cdot\text{m}^{-1}\cdot\text{K}^{-1}$. It is because the electrospun nanofibers had smaller diameters and greater specific surface area which is advantageous to shield the heat radiation and reduce the effective thermal conductivity.

Figure 4 shows the thermal gravimetric analysis of the pure SiO_2 aerogels and the SiO_2 aerogel composites reinforced with the electrospun PVDF webs. It can be observed that the SiO_2 aerogel composites have higher thermal stability below 475°C but lower thermal stability above 475°C than the pure SiO_2 aerogels. The pure aerogel showed approximately around 10% weight loss in the temperature range of $350\sim 475^\circ\text{C}$, which is derived from the degeneration of $\text{Si}-\text{O}-\text{C}_2\text{H}_5$ group. The aerogel composites reinforced with the electrospun PVDF webs showed significant weight loss in the temperature range of $450\sim 510^\circ\text{C}$ owing to the degeneration of PVDF. The weight loss of the three aerogel composites reinforced by nanofibers, combined microparticles/nanofibers, and microparticles was 60%, 44%, and 34% at 510°C , respectively. Therefore, the aerogel composites reinforced by PVDF nanofibers showed better stability than that reinforced by PVDF microparticles. However, it should be noted that the PVDF materials including three electrospun

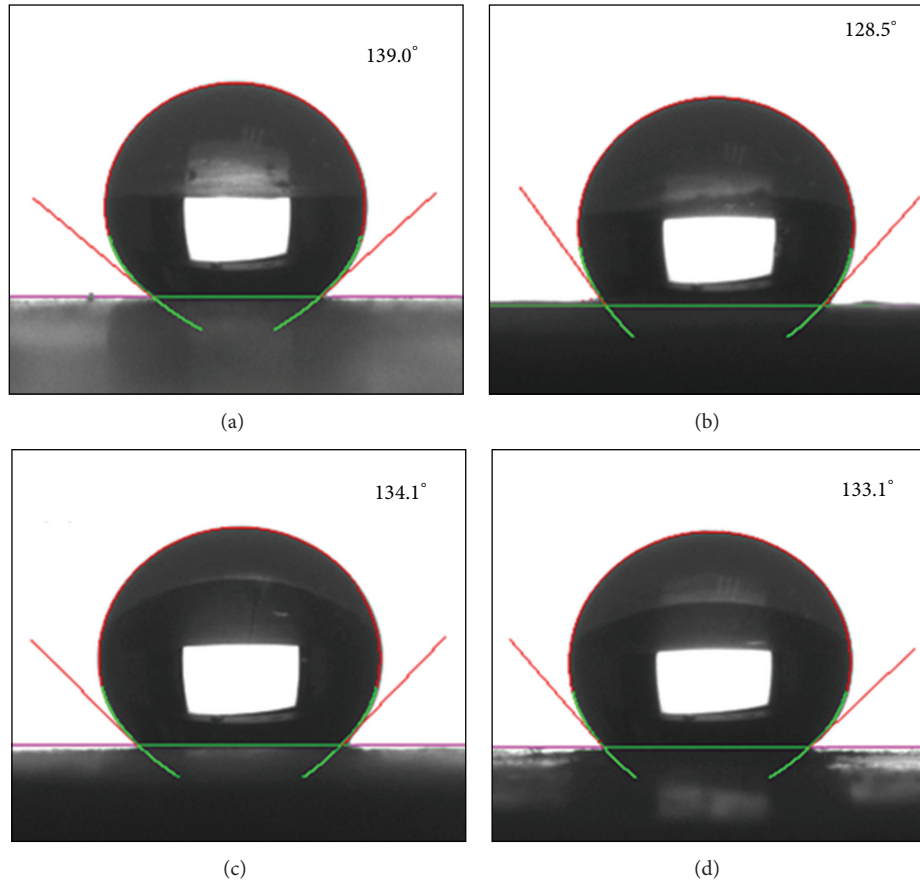


FIGURE 3: Contact angle of aerogel and aerogel composites reinforced with electrospun PVDF webs: (a) pure aerogel; (b) aerogel composites reinforced with electrospun PVDF microparticles; (c) aerogel composites reinforced with electrospun PVDF microparticles nanofibers; (d) aerogel composites reinforced with electrospun PVDF microparticles nanofibers.

PVDF webs may melt at 172°C although no noticeable weight loss exists. Therefore, the SiO_2 aerogel composites reinforced with electrospun PVDF are suitable for the application in thermal insulation below 172°C .

3.4. Mechanical Properties of SiO_2 Aerogel Composites Reinforced with Electrospun PVDF Webs. Table 4 demonstrates the mechanical properties of the aerogel composites reinforced with different electrospun PVDF webs. It can be observed that the composites reinforced with electrospun PVDF nanofibers had the highest tensile strength of 1.03 MPa. The tensile strength of the composites reinforced with combined PVDF microparticles and nanofibers was 0.51 MPa which was significantly less than that of the composites with nanofibers. Figure 5 illustrates the relation of the tensile strength and the deformation for the two aerogel composites. Compared to the combined microparticles/nanofibers reinforced composite, the nanofiber-reinforced composite exhibits higher yield strength. The nanofiber-reinforced composite experienced large deformation with a slight increase of the tensile strength while the combined microparticle/nanofiber-reinforced composite was readily broken at a small deformation. It is because the nanofibers can easily absorb the power

TABLE 3: Thermal conductivity of aerogel composites supported by electrospun PVDF.

Microstructure type of electrospun PVDF	Thermal conductivity of aerogel composites ($\text{W}\cdot\text{m}^{-1}\cdot\text{K}^{-1}$)
Microparticle	0.039
Microparticle/nanofiber	0.032
Nanofiber	0.027
Without PVDF (pure aerogel)	0.024

exerted on the composite which leads an intact morphology of the aerogel composites.

Table 4 also shows that the aerogel composite reinforced with electrospun PVDF nanofiber had the compressive strength of 5.23 MPa, which is significantly higher than that reinforced with PVDF microparticle (2.74 MPa) and noticeably higher than that with the combined PVDF microparticle/nanofiber (4.56 MPa). As a comparison, the compressive strength of the pure SiO_2 aerogels was 4.56 MPa. It can be deduced that the electrospun PVDF nanofibers significantly improved the compressive strength of the aerogels. Moreover, the electrospun PVDF nanofibers significantly

TABLE 4: Mechanical properties of aerogel composite reinforced with electrospun PVDF webs.

Microstructures of electrospun PVDF	Mechanical properties of aerogel composite reinforced with electrospun PVDF webs		
	Tensile strength (MPa)	Compressive strength (MPa)	Bending strength (MPa)
Microparticles	—	2.74	0.12
Microparticles/nanofibers	0.51	4.56	0.79
Nanofibers	1.03	5.23	1.1
Without PVDF (pure aerogel)	—	0.75	—

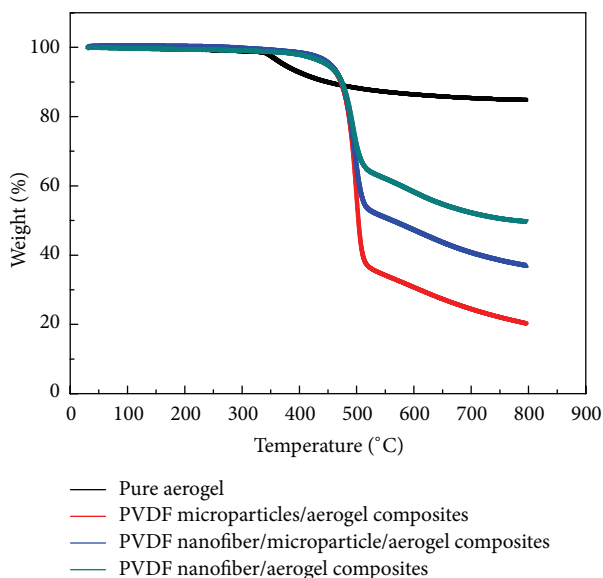


FIGURE 4: Thermal gravimetric analysis of pure aerogel and aerogel composites.

improved the bending strength of the aerogel composites up to 1.10 MPa compared to 0.12 MPa for the aerogel composites reinforced with PVDF microparticles. Therefore, the compressive strength and the flexibility of the SiO_2 aerogels could be significantly improved by using the electrospun PVDF nanofibers as the reinforcements. It opens a promising way to improve the mechanical stability of the aerogels while keeping a low thermal conductivity via reinforcing the SiO_2 aerogels by using electrospun nanofibers.

4. Conclusions

Flexible aerogel composites, with a size of 12 cm diameter and a low thermal conductivity up to $0.027 \text{ W}\cdot\text{m}^{-1}\cdot\text{K}^{-1}$, were successfully synthesized via electrospinning and sol-gel processing. Three SiO_2 aerogel composites reinforced with different electrospun PVDF microstructures (e.g., microparticles, nanofibers, combined microparticles, and nanofibers) were obtained and the effects of the electrospun PVDF microstructures on the thermal and mechanical properties of the aerogel composites were evaluated. The results show that the aerogel composite reinforced with the electrospun PVDF nanofibers had the lowest thermal conductivity and the greatest mechanical strength. The electrospun PVDF nanofiber supported

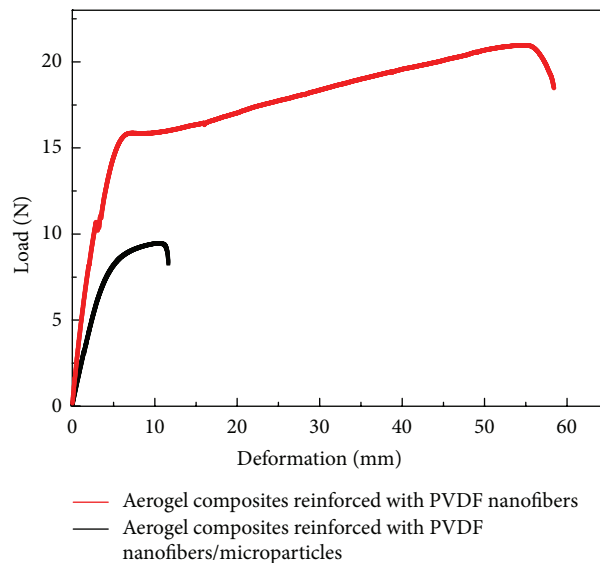


FIGURE 5: Stretching stress-deformation curves of aerogel composite.

SiO_2 aerogel composites that had a low thermal conductivity of $0.027 \text{ W}\cdot\text{m}^{-1}\cdot\text{K}^{-1}$ which was slightly higher than the pure aerogel. However, the compressive strength and the flexibility of the aerogel composites were significantly improved via the reinforcement of the electrospun PVDF fibers. It opens a controllable way to improve and engineer the mechanical properties of the aerogel composites with low thermal conductivity via reinforcing the aerogels by using electrospun nanofibers.

Acknowledgments

This research was supported by Key Project of Ministry of Education of China (211130), Guangdong Natural Science Foundation of China (S2011010003429), Guangdong Undergraduate Innovative Experiment Project of China (1107811020), Guangdong Major Science and Technology Project of China (2012A010800033), and Yangcheng Scholars Research Project of China (10A038G).

References

- [1] J. Fricke and T. Tillotson, "Aerogels: production, characterization, and applications," *Thin Solid Films*, vol. 297, no. 1-2, pp. 212–223, 1997.

- [2] A. C. Pierre, "History of aerogels," in *Aerogels Handbook*, M. A. Aegerter, Ed., pp. 3–20, Springer, London, UK, 2011.
- [3] R. Baetens, B. P. Jelle, and A. Gustavsen, "Aerogel insulation for building applications: a state-of-the-art review," *Energy and Buildings*, vol. 43, no. 4, pp. 761–769, 2011.
- [4] D. M. Smith, A. Maskara, and U. Boes, "Aerogel-based thermal insulation," *Journal of Non-Crystalline Solids*, vol. 225, no. 1–3, pp. 254–259, 1998.
- [5] J. M. Schultz, K. I. Jensen, and F. H. Kristiansen, "Super insulating aerogel glazing," *Solar Energy Materials and Solar Cells*, vol. 89, no. 2–3, pp. 275–285, 2005.
- [6] T. Woignier, J. Reynes, A. Hafidi Alaoui, I. Beurroies, and J. Phalippou, "Different kinds of structure in aerogels: relationships with the mechanical properties," *Journal of Non-Crystalline Solids*, vol. 241, no. 1, pp. 45–52, 1998.
- [7] H. Lu, H. Luo, and N. Leventis, "Mechanical characterization of aerogels," in *Aerogel Handbook*, pp. 499–535, Springer, New York, NY, USA, 2011.
- [8] N. Leventis, C. Sotiriou-Leventis, G. Zhang, and A. M. M. Rawashdeh, "Nanoengineering strong silica aerogels," *Nano Letters*, vol. 2, no. 9, pp. 957–960, 2002.
- [9] Y. Liao, H. Wu, Y. Ding et al., "Engineering thermal and mechanical properties of flexible fiber-reinforced aerogel composites," *Journal of Sol-Gel Science and Technology*, vol. 63, no. 3, pp. 445–456, 2012.
- [10] Z. H. Zhang, J. Shen, X. Y. Ni et al., "Preparation and characterization of hydrophobic silica aerogels doped with fibers," *Rare Metal Materials and Engineering*, vol. 37, no. 2, p. 4, 2008.
- [11] A. Karout, P. Buisson, A. Perrard, and A. C. Pierre, "Shaping and mechanical reinforcement of silica aerogel biocatalysts with ceramic fiber felts," *Journal of Sol-Gel Science and Technology*, vol. 36, no. 2, pp. 163–171, 2005.
- [12] J. Feng, C. Zhang, J. Feng et al., "Carbon aerogel composites prepared by ambient drying and using oxidized polyacrylonitrile fibers as reinforcements," *ACS Applied Materials & Interfaces*, vol. 3, no. 12, pp. 4796–4803, 2011.
- [13] K. Finlay, M. D. Gawryla, and D. A. Schiraldi, "Biologically based fiber-reinforced/clay aerogel composites," *Industrial & Engineering Chemistry Research*, vol. 47, no. 3, pp. 615–619, 2008.
- [14] J. Yang, S. Li, Y. Luo, L. Yan, and F. Wang, "Compressive properties and fracture behavior of ceramic fiber-reinforced carbon aerogel under quasi-static and dynamic loading," *Carbon*, vol. 49, no. 5, pp. 1542–1549, 2011.
- [15] D. H. Reneker and A. L. Yarin, "Electrospinning jets and polymer nanofibers," *Polymer*, vol. 49, no. 10, pp. 2387–2425, 2008.
- [16] D. Li, J. T. McCann, Y. Xia, and M. Marquez, "Electrospinning: a simple and versatile technique for producing ceramic nanofibers and nanotubes," *Journal of the American Ceramic Society*, vol. 89, no. 6, pp. 1861–1869, 2006.
- [17] A. Greiner and J. H. Wendorff, "Electrospinning: a fascinating method for the preparation of ultrathin fibers," *Angewandte Chemie*, vol. 46, no. 30, pp. 5670–5703, 2007.
- [18] D. Zhang and J. Chang, "Patterning of electrospun fibers using electroconductive templates," *Advanced Materials*, vol. 19, no. 21, pp. 3664–3667, 2007.
- [19] D. Li and Y. Xia, "Direct fabrication of composite and ceramic hollow nanofibers by electrospinning," *Nano Letters*, vol. 4, no. 5, pp. 933–938, 2004.
- [20] J. T. McCann, D. Li, and Y. Xia, "Electrospinning of nanofibers with core-sheath, hollow, or porous structures," *Journal of Materials Chemistry*, vol. 15, no. 7, pp. 735–738, 2005.
- [21] L. Li, B. Yalcin, B. N. Nguyen et al., "Flexible nanofiber-reinforced aerogel (xerogel) synthesis, manufacture, and characterization," *ACS Applied Materials & Interfaces*, vol. 1, no. 11, pp. 2491–2501, 2009.

Research Article

Electrochemical Sensor for o-Nitrophenol Based on β -Cyclodextrin Functionalized Graphene Nanosheets

Jinlong Liu,^{1,2} Yihong Chen,¹ Yujing Guo,¹ Fengling Yang,¹ and Fangqin Cheng¹

¹ Research Center for Environmental Science and Engineering, State Environmental Protection Key Laboratory of Efficient Utilization Technology of Coal Waste Resources, Institute of Resources and Environment Engineering, Shanxi University, Taiyuan 030006, China

² Institute of Chemical Ecology, Shanxi Agricultural University, Taigu 030801, China

Correspondence should be addressed to Yujing Guo; guoyj@sxu.edu.cn and Fangqin Cheng; cfangqin@sxu.edu.cn

Received 30 December 2012; Accepted 21 March 2013

Academic Editor: Yongcheng Jin

Copyright © 2013 Jinlong Liu et al. This is an open access article distributed under the Creative Commons Attribution License, which permits unrestricted use, distribution, and reproduction in any medium, provided the original work is properly cited.

An electrochemical sensor for the quantification of o-nitrophenol (o-NP) has been developed based on the β -cyclodextrin functionalized graphene nanosheets modified glassy carbon electrode (CD-GNs/GCE). The results indicated that CD-GNs showed good electrochemical behavior to the redox of o-NP which is attributed to the combination of the excellent properties of graphene and cyclodextrin. The peak currents possess a linear relationship with the concentration of o-NP in the range of 5–400 μ M. The detection limit of o-NP reached to 0.3 μ M on the basis of the signal-to-noise characteristics ($S/N = 3$). The peak potentials for the reversible redox waves are not affected by other nitrophenol isomers (m, p-NP), illustrating good selectivity. Furthermore, the developed electrochemical sensor exhibited good stability and reproducibility for the detection of o-NP and could be used to determine o-NP in real water sample.

1. Introduction

Nitrophenols, an important group of environmental pollutants, are widely distributed in the environment due to their extensive use in the manufacturing of insecticides, pesticides, dyes, plastics, and explosives [1]. o-Nitrophenol (o-NP) is one of the nitrophenols isomers which has exerted significant toxic effects on human beings, animals, and plants. Therefore, the development of a new method capable of rapidly and cost-efficiently detecting o-NP in the low concentration is highly desirable and urgently necessary for the environment and health protection. Several instrumental techniques are routinely utilized for the determination of o-NP including high-performance liquid chromatography [2, 3], UV-vis, fluorescence spectroscopies [4, 5], capillaryzone electrophoresis [6] and electrochemical techniques [7, 8]. Among all these techniques mentioned above, electrochemical methods have received considerable attention for o-NP analysis due to their sensitivity, simplicity, low cost, and easy for on-site determination [9, 10].

Graphene, a one-atom thick and two-dimensional closely packed honeycomb lattice, has received numerous investigations from both the experimental and theoretical scientific

communities since the experimental observation of single layers by Novoselov et al. in 2004 [11]. Due to its large specific surface area, strong mechanical strength, excellent conductivity, and electrocatalytic activity, graphene is an excellent candidate for electrodes material [12–15]. For instance, Li's group reported the basic electrochemical properties of reduced GN film-modified GCE, which exhibited enhanced electrocatalytic activity for some electroactive species [16]. Lin's group reported a GN-chitosan nanocomposite film, which provided a favorable microenvironment for GOD and promoted its direct electron transfer at the electrode surface [17]. Zhou et al. [18] demonstrated an advanced electrochemical sensing and biosensing platform based on GNs, which showed more favorable electron transfer kinetics and much higher electrocatalytic activity towards β -nicotinamide adenine dinucleotide (NADH), free bases of DNA, neurotransmitters, and other biological molecules than those of graphite. All the above studies reveal that graphene can play an important role in accelerating electron transfer and may provide a new opportunity for the development of high-performance electrochemical sensors.

Cyclodextrins (CDs) are cyclic oligosaccharides consisting of (α -1,4)-linked α -D-glucopyranose units, which are

toroidal in shape with a hydrophobic inner cavity and a hydrophilic exterior. CDs have attracted great interest due to their ability to incorporate suitable guest molecules into the hydrophobic cavity [19]. By combining the unique electronic properties of graphene nanosheets with the good water solubility and high supramolecular recognition of β -CD, the β -CD-graphene nanocomposite showed significantly improved electrochemical sensing performance compared to unmodified graphene nanosheets [20].

Herein, β -cyclodextrin functionalized graphene nanosheets modified glassy carbon electrode (CD-GNs/GCE) was fabricated for the determination of o-NP. Due to the unique properties of graphene and CDs, the CD-GNs modified glassy carbon electrode exhibits excellent supramolecular recognition and shows high electrochemical response to o-NP compared with that of the bare GCE and GNs/GCE.

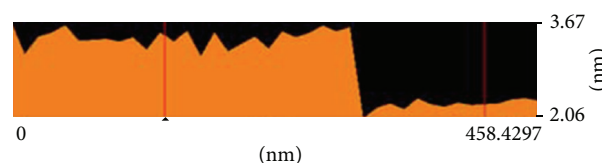
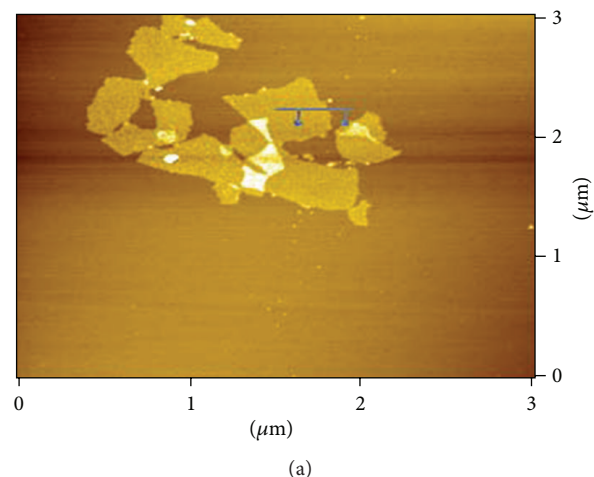
In addition, the electrochemical sensor can recognize o-NP with its isomer and shows good selectivity. Moreover, this method is simple, cost efficient, sensitive, and also can be used for the determination of o-NP in real water sample.

2. Experiment

2.1. Materials. Three nitrophenol isomers were obtained from Aladdin Reagent Inc. and were dissolved by ethanol water solution (1:2). Graphite was purchased from Alfa Aesar. β -Cyclodextrin (β -CD), hydrazine solution (50 wt.%), and ammonia solution (25–28 wt.%) were obtained from Beijing Chemical Reagent factory (Beijing, China). Other chemicals were of analytical grade and used without further purification. Water used throughout all experiments was purified with the Millipore system. All the experiments were carried out at room temperature.

2.2. Apparatus. AFM image was taken by using a SPI3800N microscope (Seiko Instruments Industry Co., Tokyo, Japan) operating in the tapping mode with standard silicon nitride tips. Typically, the surface was scanned at 1 Hz with the resolution of 256 lines/image. Electrochemical measurements were performed with a CHI660C electrochemical workstation (ChenHua Instruments Co., Shanghai, China). A conventional three-electrode system was used, including a saturated calomel electrode (SCE) as reference electrode, a platinum wire as counter electrode, and a bare or modified GCE as working electrode.

2.3. Synthesis of CD-Graphene Hybrid Nanosheets and Pure Graphene. Graphene oxide (GO) was synthesized from natural graphite by Hummers' method with a little modification [21]. CD-GNs were synthesized according to our previous work [20]. Briefly, 20.0 mL of the homogeneous graphene oxide dispersion (0.5 mg/mL) was mixed with 20.0 mL of β -CD aqueous solution (80 mg) and 300.0 μ L of ammonia solution, followed by the addition of 20 μ L of hydrazine solution. After being vigorously shaken or stirred for a few minutes, the vial was put in a water bath (60°C) for 3.5 h. The stable black dispersion was obtained. The dispersion was filtered with a nylon membrane (0.22 μ m) to obtain CD-GNs that can be redispersed readily in water by ultrasonication.



	Z_1 (nm)	Z_2 (nm)	ΔZ (nm)	Distance (nm)	Φ (°)
	3.447118	2.299705	1.147414	277.6326	0.236793

(b)

FIGURE 1: (a) AFM image of CD-GNs. (b) The cross section identified by the line in Figure 1 shows the height of CD-GNs.

Additionally, the preparation of pure graphene was similar to CD-GNs except for the addition of CD.

2.4. Preparation of the CD-GNs/GCE or GNs/GCE and the Electrochemical Measurement. Prior to the modification, the glassy carbon electrode was polished with 1, 0.3, and 0.05 μ m alumina slurry and rinsed thoroughly with doubly distilled water between each polishing step. Then, it was washed successively with 1:1 nitric acid, acetone, and doubly distilled water in an ultrasonic bath and dried in air. Lastly, 5 μ L of 0.25 mg/mL CD-GNs or GNs was carefully cast on the surface of the well-polished GCE and dried in air. The CD-GNs/GCE or GNs/GCE electrode was thus obtained. The electrode was then transferred into 0.1 M pH 7.0 phosphate buffer solution containing o-NP, and the CV or DPV signal was recorded after accumulation for 10 min.

3. Results and Discussion

3.1. The Morphology of the CD-GNs. Atomic force microscopy (AFM) can directly characterize the morphologies and layers of CD-GNs. The AFM samples were prepared by dropping CD-GNs dispersed in water onto clean mica surfaces and dried at room temperature. Figure 1 shows the AFM image of CD-GNs, which illustrates the flake-like shapes of graphene. The average thickness of the graphene nanosheets is about 1–2 nm, a typical characteristic of functional molecule protected single-layer graphene [22].

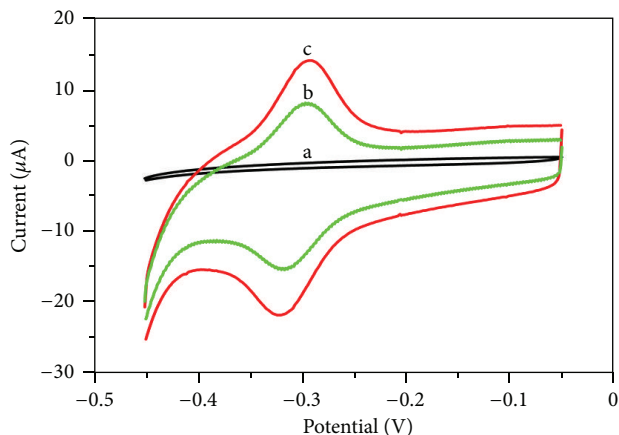
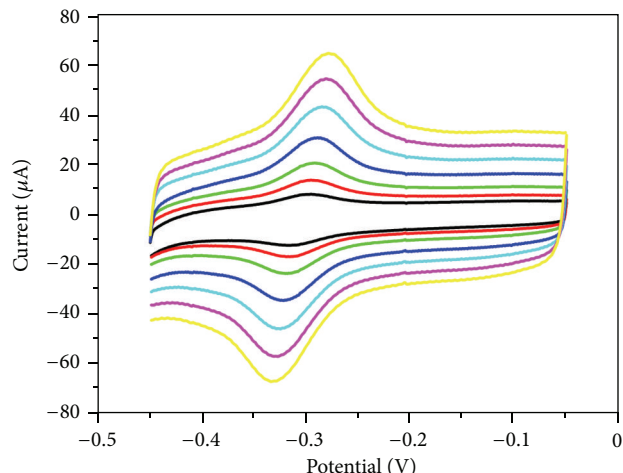


FIGURE 2: Cyclic voltammograms of 50 μM o-NP at GCE (curve a), GNs/GCE (curve b), and CD-GNs/GCE (curve c) in 0.1M phosphate buffer (pH 7.0). Scan rate: 50 mV s^{-1} .

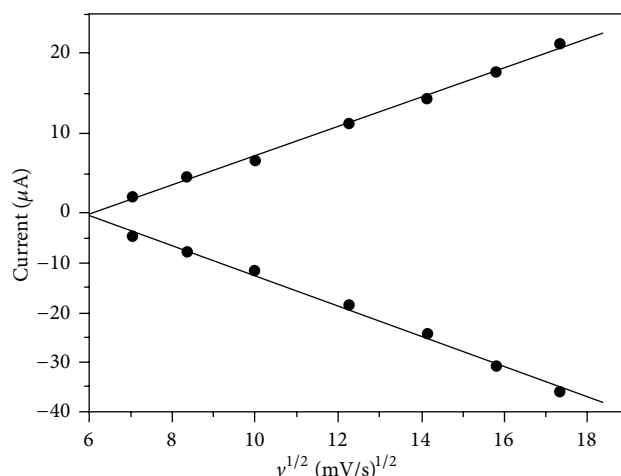
3.2. The Voltammetric Behavior of o-NP. Figure 2 compares the voltammetric behaviors of 50 μM o-NP at the bare GCE (a), the GNs/GCE (b), and the CD-GNs/GCE (c) in 0.1M pH 7.0 phosphate buffer solutions. There are no significant redox peaks at the bare GCE. However, at the GNs/GCE, o-NP shows better electrochemical behavior than the bare GCE, which may be attributed to the excellent conductivity and large surface area of graphene. While at the CD-GNs/GCE, the peak currents show a remarkable increase compared to that at the other two electrodes. This demonstrates that β -CD molecules on the surface of graphene with high supramolecular recognition capability can form host-guest complexes with o-NP. Accordingly, the concentration of o-NP on the electrode has been increased which results in remarkable peak currents enhancement. These phenomena prove that the CD-GNs not only display the excellent properties of graphene, but also exhibit the supramolecular recognition capability of CDs.

The influence of scan rate on the peak current of o-NP at the CD-GNs modified electrode was also investigated. As shown in Figure 3(a), the peak currents of o-NP increased with the increase of the scan rate. At low scan rate (50–300 mVs^{-1}), the peak current (i_p) and the square root of scan rate (ν) exhibited well linear relation. The linear regression equations are i_{pa} (A) = $1.806 \times 10^{-5} - 3.06 \times 10^{-6} \nu^{1/2}$ (V/s) $^{1/2}$ ($r = 0.994$) and i_{pc} (A) = $-1.13 \times 10^{-5} + 1.85 \times 10^{-6} \nu^{1/2}$ (V/s) $^{1/2}$ ($r = 0.998$) (Figure 3(b)). The ratio of the anodic peak current to cathodic peak current is almost equal to unity ($i_{pa} : i_{pc} = 1$). These results demonstrate the electrochemistry of the CD-GNs modified GCE corresponding to a diffusion-controlled process which is reversible.

3.3. Optimization of the Experimental Conditions. The influence of different conditions such as pH, the amount of CD-GNs, and accumulation time on the electroactivity of CD-GNs towards o-NP was investigated. As shown in Figures 4(a) and 4(b), the redox peak currents increased by varying pH from 4.0 to 7.0 and then decreased rapidly when the pH exceeded 7.0. This phenomenon may be ascribed to the



(a)



(b)

FIGURE 3: (a) Cyclic voltammograms of 50 μM o-NP in 0.1M phosphate buffer at the CD-GNs/GCE with different scan rates (50, 70, 100, 150, 200, 250, and 300 mV/s). (b) The peak currents of o-NP versus the square root of scan rate.

following two reasons: one is that the proton is critical in redox behavior of o-NP, and the decrease of o-NP response at high pH is possibly due to the decreases of proton concentration. The other is that the change of microenvironment weakened the inclusive ability of β -CD with o-NP and thereby decreased the o-NP concentration on the electrode and reduced the peak current. Therefore, phosphate buffer with pH 7.0 was selected for the subsequent experiments.

The effect of the amount of CD-GNs is shown in Figure 4(c). When the amount of CD-GNs suspension increased from 2 to 5 μL , the peak currents of o-NP increased dramatically. However, when it exceeded 5 μL , the peak currents decreased. This may be attributed to the thicker film of CD-GNs, which blocked the electrical conductivity. So, the amount of CD-GNs on the GCE was optimized at 5 μL .

Figure 4(d) illustrates the effects of accumulation time on the peak currents of o-NP. The peak current increased

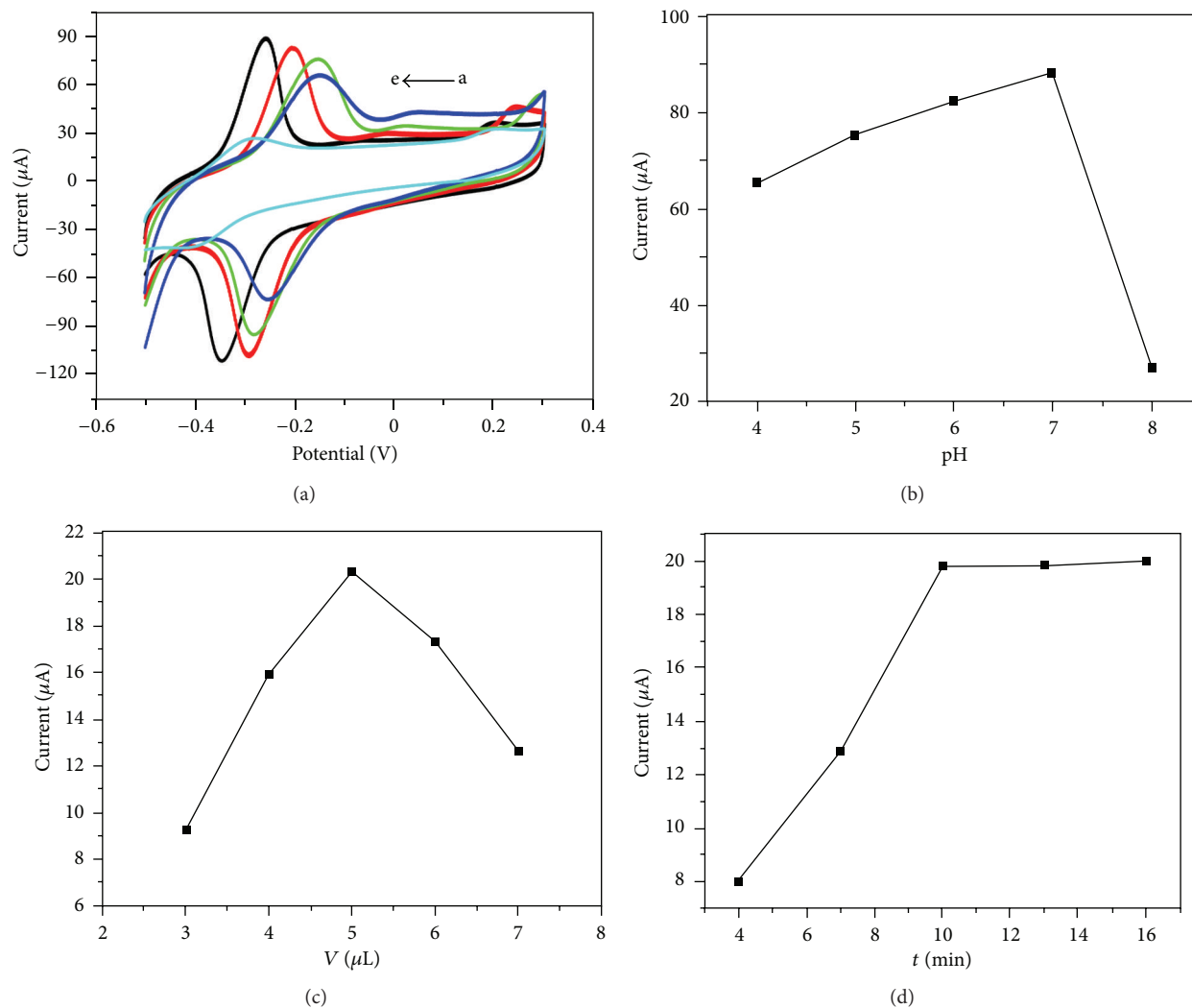


FIGURE 4: (a) Cyclic voltammograms of 50 μM o-NP at CD-GNs/GCE in a series of phosphate buffer solutions with different pH (a–e): 4, 5, 6, 7, and 8; (b) the corresponding pH-current plot. (c) The influence of the amount of CD-GNs on the peak currents. (d) The influence of the accumulation time on the peak currents.

with the accumulation time within 10 min, owing to the increased amount of o-NP on the CD-GNs/GCE. Further increment of the accumulation time did not increase the peak current obviously, which indicated the surface adsorption saturation. For practical purposes, 10 min was sufficient for the determination of o-NP.

3.4. Electrochemical Detection of o-NP. Differential pulse voltammetric (DPV) was used for the determination of o-NP under the optimum conditions. The enhanced peak current was linear with the concentration of o-NP in the range of 5.0–400 μM (Figure 5). The linear equation is $i_p (\mu\text{A}) = 0.1670 + 0.4316c (\mu\text{M})$ ($R = 0.9997$). Based on the signal-to-noise ratio of 3, the experimental detection limit was obtained as 0.3 μM . The results are superior or comparable to the method reported previously [9, 23]. As a novel sensor material for the determination of o-NP, the interference of the other two nitrophenol isomers m-nitrophenol (m-NP) and p-nitrophenol (p-NP) was investigated. In pH 7.0 phosphate

buffer solution, cyclic voltammogram of the mixtures containing 0.5 mM o-NP, m-NP, and p-NP, respectively, is shown in Figure 6. It is clearly to see that peak potentials for the reversible redox waves of o-NP are not affected by m, p-NP isomers. Therefore, the CD-GNs present good selectivity in the detection of o-NP.

3.5. Real Sample Analysis. In order to evaluate the practical application of the CD-GNs modified GCE, it was used to detect o-NP in several lake water samples. No signals for o-NP were observed in these lake water samples. Thus, the proposed method was applied to the lake water samples spiked with o-NP by adding known amount of o-NP solution. In pH 7.0 phosphate buffer solution, the samples were measured under the same condition for four times. The average recovery and relative standard deviation (RSD) were determined and shown in Table 1. The recovery values ranged from 97.4 to 102.3%, which indicates that this sensor could be used in the detection of o-NP in real water samples.

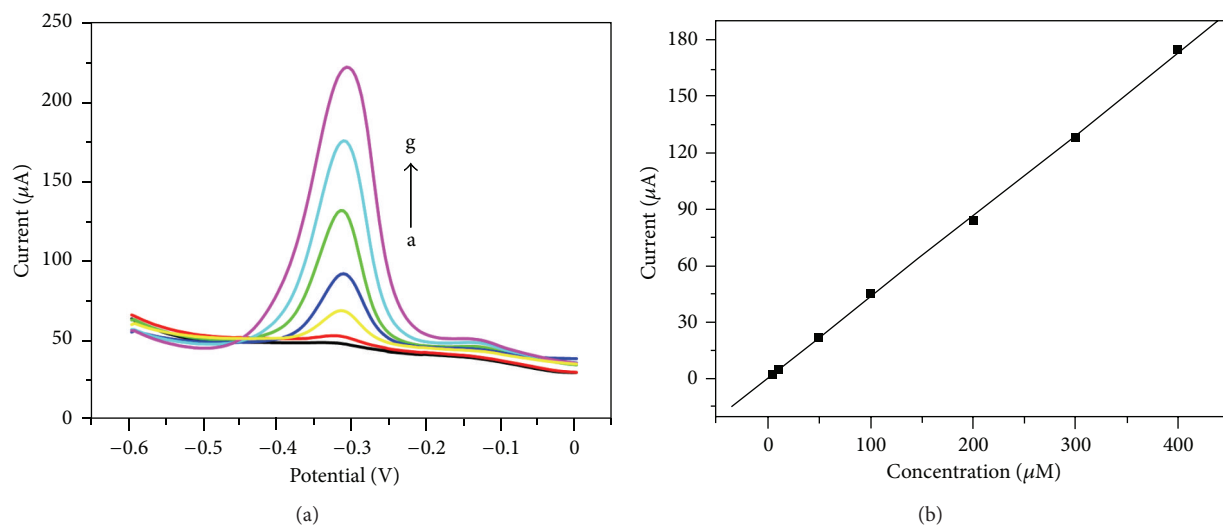


FIGURE 5: (a) The DPV response for the different concentrations of o-NP (a–g: 5, 10, 50, 100, 200, 300, and 400 μM). (b) The calibration plot of o-NP.

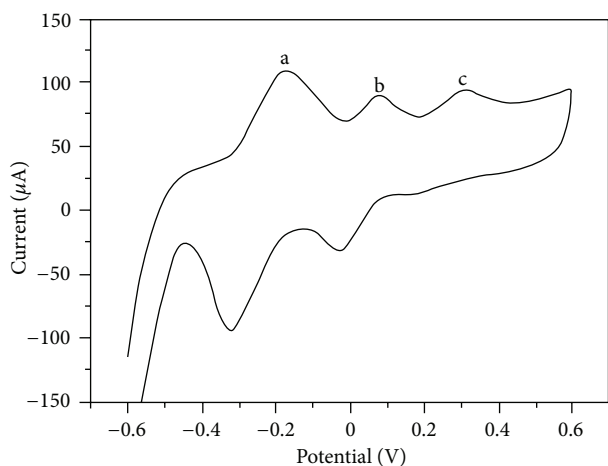


FIGURE 6: The cyclic voltammogram of three nitrophenol isomers. (a) o-NP; (b) m-NP; and (c) p-NP.

3.6. Repeatability and Stability. To estimate the repeatability of the proposed method, the current response of 50 μM o-NP was detected with the same bare GCE modified six times in the same procedure. The relative standard deviation was calculated to be 4.4%. The results revealed that the electrode possessed satisfying reproducibility. Moreover, the CD-GNs-based o-NP electrochemical sensor also exhibits a good long-term stability. The peak current can maintain over 94% of its initial value after the modified electrode stored at room temperature for 10 days.

4. Conclusion

In this work, CD-GNs were used as enhanced material for the electrochemical determination of o-NP. The simply fabricated CD-GNs-based electrochemical sensor showed superior electrochemical performance for the determination of o-NP relative to those of GNs and bare GCE. Moreover, the

TABLE 1: The recoveries of o-NP from water sample.

Sample	Added (μM)	Found (μM)	Recovery (%)	RSD (%)
1	10	10.12	101.2	2.6
2	20	19.48	97.4	3.2
3	50	49.93	99.9	4.4
4	80	81.84	102.3	2.5
5	100	98.61	98.6	3.5

electrochemical sensor exhibited good selectivity, repeatability, and stability. Thereby, the present CD-GNs-based o-NP sensors will probably be promising for a wide range of applications related to the detection of trace amounts of phenol compounds.

Acknowledgments

This research work was supported by the National Natural Science Foundation of China (no. 21275093) the Natural Science Foundation of Shanxi Province (no. 2012011007-3), the International Scientific and Technological Cooperation of China (2011DFA90830), and the National Hi-Tech Research and Development Program of China (863 Program, 2011AA06A103).

References

- [1] D. R. Hartter, "The use and importance of nitroaromatic chemicals in the chemical industry," in *Toxicity of Nitroaromatic Compounds*, D. E. Rickert, Ed., pp. 1–14, Chemical Industry Institute of Toxicology, Washington, DC, USA, 1985.
- [2] M. J. Thompson, L. N. Ballinger, S. E. Cross, and M. S. Roberts, "High-performance liquid chromatographic determination of phenol, 4-nitrophenol, β -naphthol and a number of their glucuronide and sulphate conjugates in organ perfusate," *Journal of Chromatography B*, vol. 677, no. 1, pp. 117–122, 1996.

- [3] T. Galeano-Diaz, A. Guiberteau-Cabanillas, N. Mora-Diez, P. Parrilla-Vazquez, and F. Salinas-Lopez, "Rapid and sensitive determination of 4-nitrophenol, 3-methyl-4-nitrophenol, 4,6-dinitro-o-cresol, parathion-methyl, fenitrothion, and parathion-ethyl by liquid chromatography with electrochemical detection," *Journal of Agricultural and Food Chemistry*, vol. 48, no. 10, pp. 4508–4513, 2000.
- [4] A. Niazi and A. Yazdanipour, "Spectrophotometric simultaneous determination of nitrophenol isomers by orthogonal signal correction and partial least squares," *Journal of Hazardous Materials*, vol. 146, no. 1-2, pp. 421–427, 2007.
- [5] C. Nistor, A. Oubi, M. P. Marco, D. Barceló, and J. Emnéus, "Competitive flow immunoassay with fluorescence detection for determination of 4-nitrophenol," *Analytica Chimica Acta*, vol. 426, no. 2, pp. 185–195, 2001.
- [6] X. Guo, Z. Wang, and S. Zhou, "The separation and determination of nitrophenol isomers by high-performance capillary zone electrophoresis," *Talanta*, vol. 64, no. 1, pp. 135–139, 2004.
- [7] Z. Liu, J. Du, C. Qiu et al., "Electrochemical sensor for detection of p-nitrophenol based on nanoporous gold," *Electrochemistry Communications*, vol. 11, no. 7, pp. 1365–1368, 2009.
- [8] A. K. M. Kafi and A. Chen, "A novel amperometric biosensor for the detection of nitrophenol," *Talanta*, vol. 79, no. 1, pp. 97–102, 2009.
- [9] L. Q. Luo, X. L. Zou, Y. P. Ding, and Q. S. Wu, "Derivative voltammetric direct simultaneous determination of nitrophenol isomers at a carbon nanotube modified electrode," *Sensors and Actuators B*, vol. 135, no. 1, pp. 61–65, 2008.
- [10] C. Xu, J. Wang, L. Wan, J. Lin, and X. Wang, "Microwave-assisted covalent modification of graphene nanosheets with hydroxypropyl- β -cyclodextrin and its electrochemical detection of phenolic organic pollutants," *Journal of Materials Chemistry*, vol. 21, no. 28, pp. 10463–10471, 2011.
- [11] K. S. Novoselov, A. K. Geim, S. V. Morozov et al., "Electric field in atomically thin carbon films," *Science*, vol. 306, no. 5696, pp. 666–669, 2004.
- [12] A. K. Geim and K. S. Novoselov, "The rise of graphene," *Nature Materials*, vol. 6, no. 3, pp. 183–191, 2007.
- [13] H. A. Becerril, J. Mao, Z. Liu, R. M. Stoltenberg, Z. Bao, and Y. Chen, "Evaluation of solution-processed reduced graphene oxide films as transparent conductors," *ACS Nano*, vol. 2, no. 3, pp. 463–470, 2008.
- [14] M. J. Allen, V. C. Tung, L. Gomez et al., "Soft transfer printing of chemically converted graphene," *Advanced Materials*, vol. 21, no. 20, pp. 2098–2102, 2009.
- [15] D. Li, M. B. Muller, S. Gilje, R. B. Kaner, and G. G. Wallace, "Processable aqueous dispersions of graphene nanosheets," *Nature Nanotechnology*, vol. 3, no. 2, pp. 101–105, 2008.
- [16] L. H. Tang, Y. Wang, Y. M. Li, H. B. Feng, J. Lu, and J. H. Li, "Preparation, structure, and electrochemical properties of reduced graphene sheet films," *Advanced Functional Materials*, vol. 19, no. 17, pp. 2782–2789, 2009.
- [17] X. Kang, J. Wang, H. Wu, I. A. Aksay, J. Liu, and Y. Lin, "Glucose oxidase-graphene-chitosan modified electrode for direct electrochemistry and glucose sensing," *Biosensors and Bioelectronics*, vol. 25, no. 4, pp. 901–905, 2009.
- [18] M. Zhou, Y. M. Zhai, and S. J. Dong, "Electrochemical sensing and biosensing platform based on chemically reduced graphene oxide," *Analytical Chemistry*, vol. 81, no. 14, pp. 5603–5613, 2009.
- [19] M. V. Rekharsky and Y. Inoue, "Complexation thermodynamics of cyclodextrins," *Chemical Reviews*, vol. 98, no. 5, pp. 1875–1917, 1998.
- [20] Y. Guo, S. Guo, J. Ren, Y. Zhai, S. Dong, and E. Wang, "Cyclodextrin functionalized graphene nanosheets with high supramolecular recognition capability: synthesis and host-guest inclusion for enhanced electrochemical performance," *ACS Nano*, vol. 4, no. 7, pp. 4001–4010, 2010.
- [21] W. S. Hummers and R. E. Offeman, "Preparation of graphitic oxide," *Journal of the American Chemical Society*, vol. 80, no. 6, article 1339, 1958.
- [22] C. N. R. Rao, A. K. Sood, K. S. Subrahmanyam, and A. Govindaraj, "Graphene: the new two-dimensional nanomaterial," *Angewandte Chemie—International Edition*, vol. 48, no. 42, pp. 7752–7777, 2009.
- [23] I. N. Rodriguez, M. B. Zamora, J. M. B. Salvador, J. A. M. Leyva, M. P. Hernandez-Artiga, and J. L. H. H. de Cisneros, "Voltammetric determination of 2-nitrophenol at a bentonite-modified carbon paste electrode," *Mikrochimica Acta*, vol. 126, no. 1-2, pp. 87–92, 1997.

Research Article

Influence of the Process Parameters on the Formation of $\text{CaSO}_4 \cdot 0.5\text{H}_2\text{O}$ Whiskers

Kangbi Luo, Huping Li, Chunmei Li, and Ping Ning

College of Environmental Engineering, Kunming University of Science & Technology, Kunming 650500, China

Correspondence should be addressed to Kangbi Luo; luokangbi@126.com

Received 26 January 2013; Accepted 7 May 2013

Academic Editor: Yunpeng Yin

Copyright © 2013 Kangbi Luo et al. This is an open access article distributed under the Creative Commons Attribution License, which permits unrestricted use, distribution, and reproduction in any medium, provided the original work is properly cited.

This paper discussed the influence of the process parameters such as the temperature, the mixing ways, and the molar ratios of the reactants on the morphology of the $\text{CaSO}_4 \cdot 2\text{H}_2\text{O}$ precursors and the $\text{CaSO}_4 \cdot 0.5\text{H}_2\text{O}$ whiskers. The experimental results indicated that $\text{CaSO}_4 \cdot 0.5\text{H}_2\text{O}$ whiskers with a length of 80–310 μm and a width of 0.8–8.0 μm were produced at hydrothermal condition, using $\text{CaSO}_4 \cdot 2\text{H}_2\text{O}$ fine particles as the precursors which were formed by adding Na_2SO_4 solution into CaCl_2 solution at 25°C at the molar ratio of Na_2SO_4 to CaCl_2 being 0.5 : 1. A lower supersaturation and a higher $[\text{Ca}^{2+}]/[\text{SO}_4^{2-}]$ molar ratio favored the formation of $\text{CaSO}_4 \cdot 2\text{H}_2\text{O}$ particles with small sizes and the hydrothermal synthesis of $\text{CaSO}_4 \cdot 0.5\text{H}_2\text{O}$ whiskers with high aspect ratios.

1. Introduction

As a kind of environmental friendly material, the calcium sulfate whisker is widely used as the reinforcing material in many fields such as plastics, ceramics, papers, and cements, owing to its high tensile strength, good electronic isolation, and perfect stability at high temperature or in acidic/alkaline media [1–3]. Many methods have been developed to synthesize calcium sulfate whiskers, including the hydrothermal route, the normal acidic synthesis route, the microemulsion route, and the microwave route, [4–9]. The hydrothermal method was getting more and more attention owing to the regular morphology of the product, the moderate condition, and the adjustable process parameters [10, 11].

This paper investigated the possibility of the synthesizing of $\text{CaSO}_4 \cdot 0.5\text{H}_2\text{O}$ whiskers via coprecipitation at room temperature followed by hydrothermal treatment, using Na_2SO_4 and CaCl_2 as the raw materials. The influences of the process parameters for the formation of $\text{CaSO}_4 \cdot 2\text{H}_2\text{O}$ precursors such as the temperature, the molar ratio, and the mixing ways of the raw materials on the morphology of the hydrothermal products were investigated, and the optimized synthesizing condition was suggested.

2. Experimental

2.1. Experimental Procedure. 0.2–1.2 $\text{mol} \cdot \text{L}^{-1}$ Na_2SO_4 were mixed with 0.2–1.2 $\text{mol} \cdot \text{L}^{-1}$ CaCl_2 at room temperature and stirring (350 min^{-1}) conditions via three different routes: adding CaCl_2 to Na_2SO_4 or vice versa or adding CaCl_2 and Na_2SO_4 simultaneously into a blank container. The molar ratio of CaCl_2 to Na_2SO_4 was kept as 0.1–10 : 1, and the dripping speed was 3 $\text{mL} \cdot \text{min}^{-1}$. The suspension was stirred for 1 h after the mixing of the raw materials, then transferred to a small stainless steel autoclave with an inner volume of 80 mL, heated (3°C· min^{-1}) to 120–200°C, and kept in isothermal condition for 1.0–8.0 h. After hydrothermal treatment, the product was cooled to room temperature naturally, filtrated, washed with distilled water and dried at 105°C for 2 h.

2.2. Analysis Method. The morphology of the products was observed by using the field emission scanning electron microscope (FSEM, JSM 7401F, JEOL, Japan). The composition of the products was characterized by X-ray powder diffractometer (XRD, D/Max2500, Rigaku, Japan), using $\text{CuK}\alpha$ ($\lambda = 1.54148 \text{ \AA}$). The concentrations of Ca^{2+} and SO_4^{2-} were analyzed by EDTA titration and barium chromate

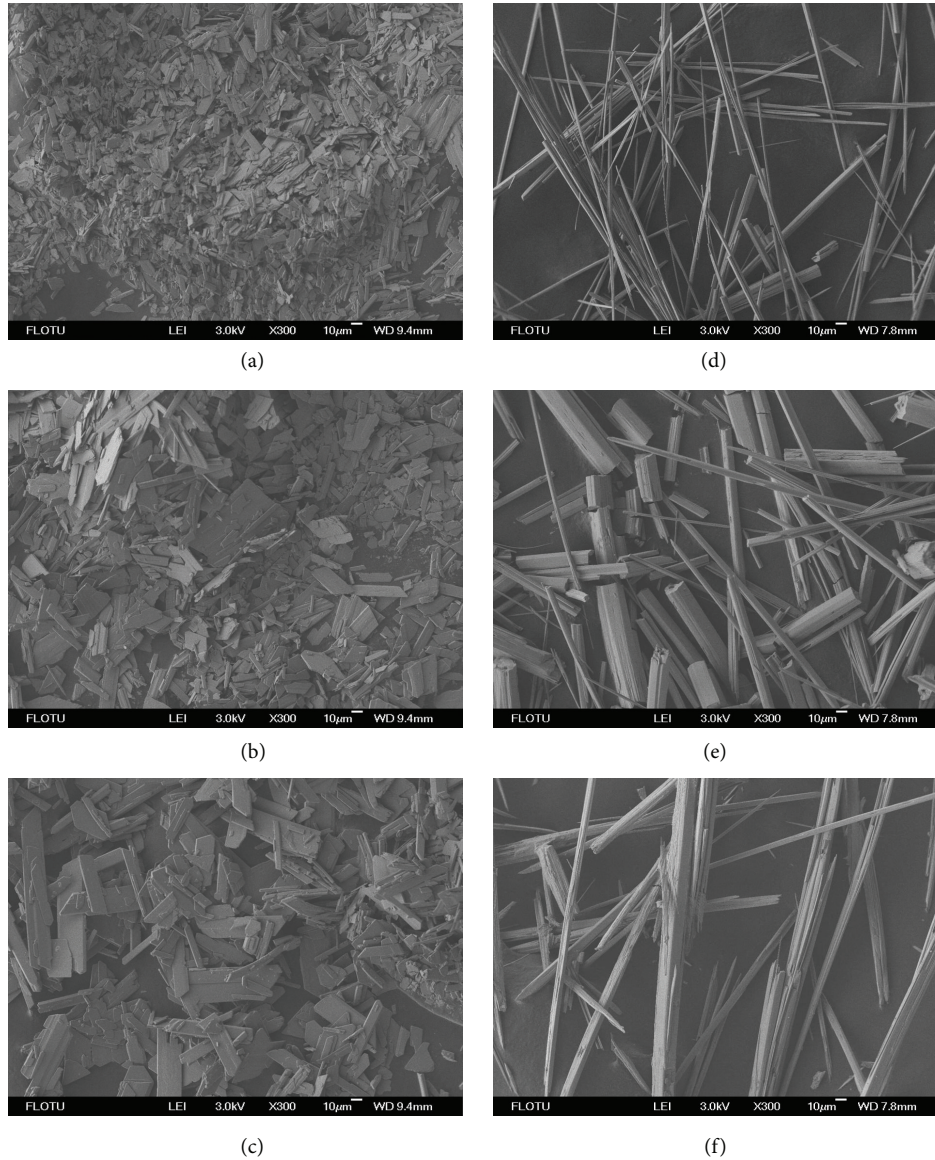


FIGURE 1: Influence of temperature on the morphology of the precursors ((a)–(c)) and the hydrothermal products ((d)–(f)). Temperature ($^{\circ}\text{C}$): (a), (d): 25, (b), (e): 60, (c), (f): 90.

spectrophotometry (Model 722, Xiaoguang, China), respectively.

3. Results and Discussion

3.1. Influence of Temperature. Figure 1 shows the morphology of the precursors and the hydrothermal products obtained by adding Na_2SO_4 solution into CaCl_2 solution at different temperatures (25 $^{\circ}\text{C}$, 60 $^{\circ}\text{C}$, and 90 $^{\circ}\text{C}$). Figure 2 shows the XRD patterns of the precursor and the hydrothermal product obtained by mixing the reactants at 25 $^{\circ}\text{C}$.

The data in Figure 1 indicated that the precursors were plate-like particles. The plates formed at 25 $^{\circ}\text{C}$, 60 $^{\circ}\text{C}$, and 90 $^{\circ}\text{C}$ were with a length of 3–45 μm , 8–80 μm , and 12–150 μm and a width of 0.8–15 μm , 1.5–28 μm , and 1.5–45 μm , respectively. The increase of temperature led to the

increase of the precursor sizes. The data in Figure 1 also showed that the morphology of the hydrothermal products was connected closely with the formation temperature of the precursors. The hydrothermal products were uniform whiskers with lengths of 80–310 μm and diameters of 0.8–8 μm if the precursor was prepared at 25 $^{\circ}\text{C}$. Being composed of the mixtures of the whiskers and the rod-like particles, the hydrothermal products with a length of 30–240 μm , 30–310 μm and a diameter of 1.5–28 μm , 4.5–22 μm were formed using the precursors formed at 60 $^{\circ}\text{C}$ and 90 $^{\circ}\text{C}$, respectively. The hydrothermal products became more ununiform and thicker as increases the precursor temperature, from 25 $^{\circ}\text{C}$ to 90 $^{\circ}\text{C}$.

The data in Figure 2 indicated that precursor was composed of $\text{CaSO}_4 \cdot 2\text{H}_2\text{O}$ and the hydrothermal product was composed of $\text{CaSO}_4 \cdot 0.5\text{H}_2\text{O}$.

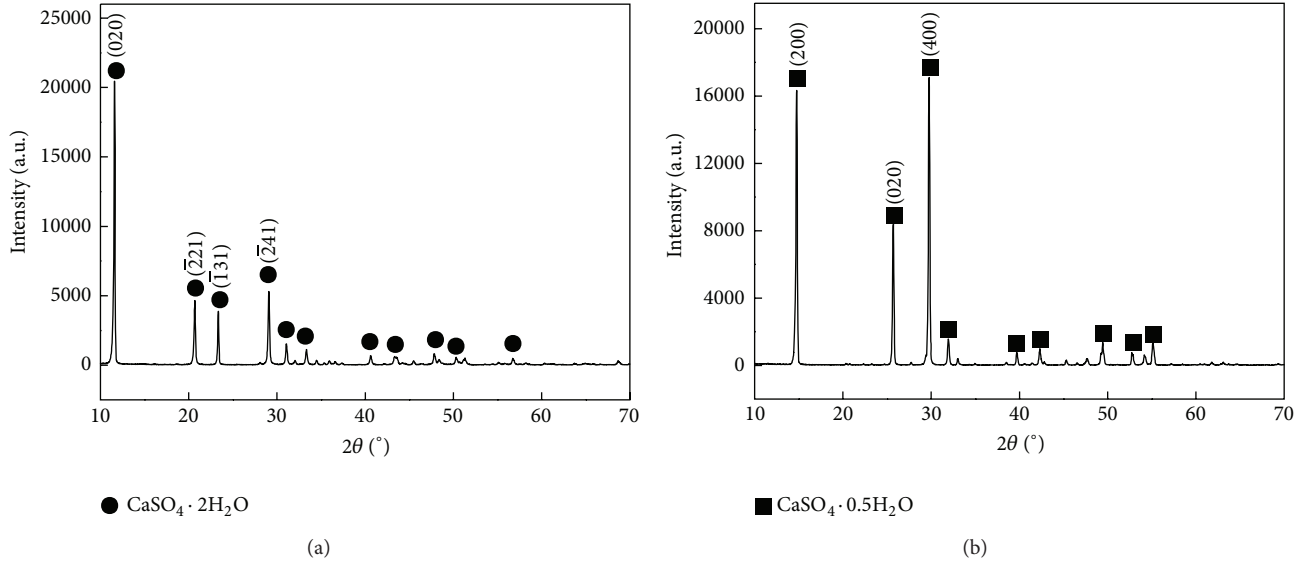


FIGURE 2: XRD patterns of the precursor (a) and the hydrothermal product (b).

TABLE 1: Influence of temperature on the supersaturation of $\text{CaSO}_4 \cdot 2\text{H}_2\text{O}$.

Temperature, $^\circ\text{C}$	K_{sp}	$[\text{Ca}^{2+}][\text{SO}_4^{2-}]$	S
25	3.178×10^{-5}	6.5043×10^{-3}	204.7
60	2.375×10^{-5}	6.5043×10^{-3}	273.9
90	1.456×10^{-5}	6.5043×10^{-3}	446.7

The change of the morphology of precursor with temperature may be connected with the varying super-saturations at different temperatures. Super-saturation (S) is defined as follows:

$$S = \frac{[\text{Ca}^{2+}][\text{SO}_4^{2-}]}{K_{\text{sp}}}, \quad (1)$$

where S is the super-saturation, $[\text{Ca}^{2+}]$ and $[\text{SO}_4^{2-}]$ are the practical concentrations of the soluble Ca^{2+} and SO_4^{2-} , respectively, and K_{sp} is the equilibrium constant for the dissolution of $\text{CaSO}_4 \cdot 2\text{H}_2\text{O}$, which can be calculated out from the HSC software [12].

The influence of temperature on the super-saturation is listed in Table 1 at the mixing time of 1 minute. It was supposed that no $\text{CaSO}_4 \cdot 2\text{H}_2\text{O}$ precipitate was formed within 1 minute of mixing time.

The data in Table 1 showed that the increase of temperature led to the decrease of the K_{sp} of $\text{CaSO}_4 \cdot 2\text{H}_2\text{O}$. Therefore, the super-saturation at high temperature is bigger than the super-saturation at low temperature. According to the crystallinity theory, the super-saturation is connected closely with the growth rate of the crystals. The bigger the super-saturation, the faster the nucleation rate and the growth rate. It is known from Figure 1 that smaller precursors were formed at lower temperature, indicating that the formation of the $\text{CaSO}_4 \cdot 2\text{H}_2\text{O}$ precursor may be connected mainly with the growth of the crystals: a lower temperature led

to a smaller super-saturation and a slower growth rate of crystals, which favored the formation of $\text{CaSO}_4 \cdot 2\text{H}_2\text{O}$ precursors with smaller particles as well as the formation of uniform $\text{CaSO}_4 \cdot 0.5\text{H}_2\text{O}$ whiskers at hydrothermal condition. Therefore, compared with 60°C and 90°C , 25°C was more favorable for the formation of $\text{CaSO}_4 \cdot 2\text{H}_2\text{O}$ precursors with small sizes.

3.2. Influence of the Mixing Ways of the Reactants. The influences of the mixing ways of the reactants at 25°C on the morphology of the precursors and the hydrothermal products are shown in Figure 3.

The particle sizes of the plate-like precursors connected closely with the mixing ways of the reactants. The lengths of the plates were $15\text{--}140 \mu\text{m}$, $3\text{--}45 \mu\text{m}$, and $10\text{--}60 \mu\text{m}$ and the widths of the particles were $1.5\text{--}35 \mu\text{m}$, $0.8\text{--}15 \mu\text{m}$, and $1.5\text{--}30 \mu\text{m}$ in the cases of the following mixing ways of the reactants: adding CaCl_2 to Na_2SO_4 , adding Na_2SO_4 to CaCl_2 and adding Na_2SO_4 and CaCl_2 , simultaneously, respectively. The particle sizes of the precursors formed by adding Na_2SO_4 to CaCl_2 were much smaller than those formed by adding CaCl_2 to Na_2SO_4 . The aspect ratios of the corresponding hydrothermal products- $\text{CaSO}_4 \cdot 0.5\text{H}_2\text{O}$ whiskers changed with the precursor sizes. The smaller the particle sizes of the precursors, the higher the aspect ratios of the whiskers. $\text{CaSO}_4 \cdot 0.5\text{H}_2\text{O}$ whiskers with a length of $80\text{--}310 \mu\text{m}$ and a diameter of $0.8\text{--}8.0 \mu\text{m}$ were formed at hydrothermal condition using the precursor formed by adding Na_2SO_4 to CaCl_2 .

The data in Figures 3 and 4(a) indicated that all of the practical super-saturations of the solutions were much bigger than K_{sp} , which favored the quick nucleation and crystal growth. The super-saturations in line a were bigger than those in line b, and the particle sizes of the corresponding precursors in line a were also bigger than those in line b, indicating that a higher super-saturation system favored the formation of bigger precursors. Compared with the case of

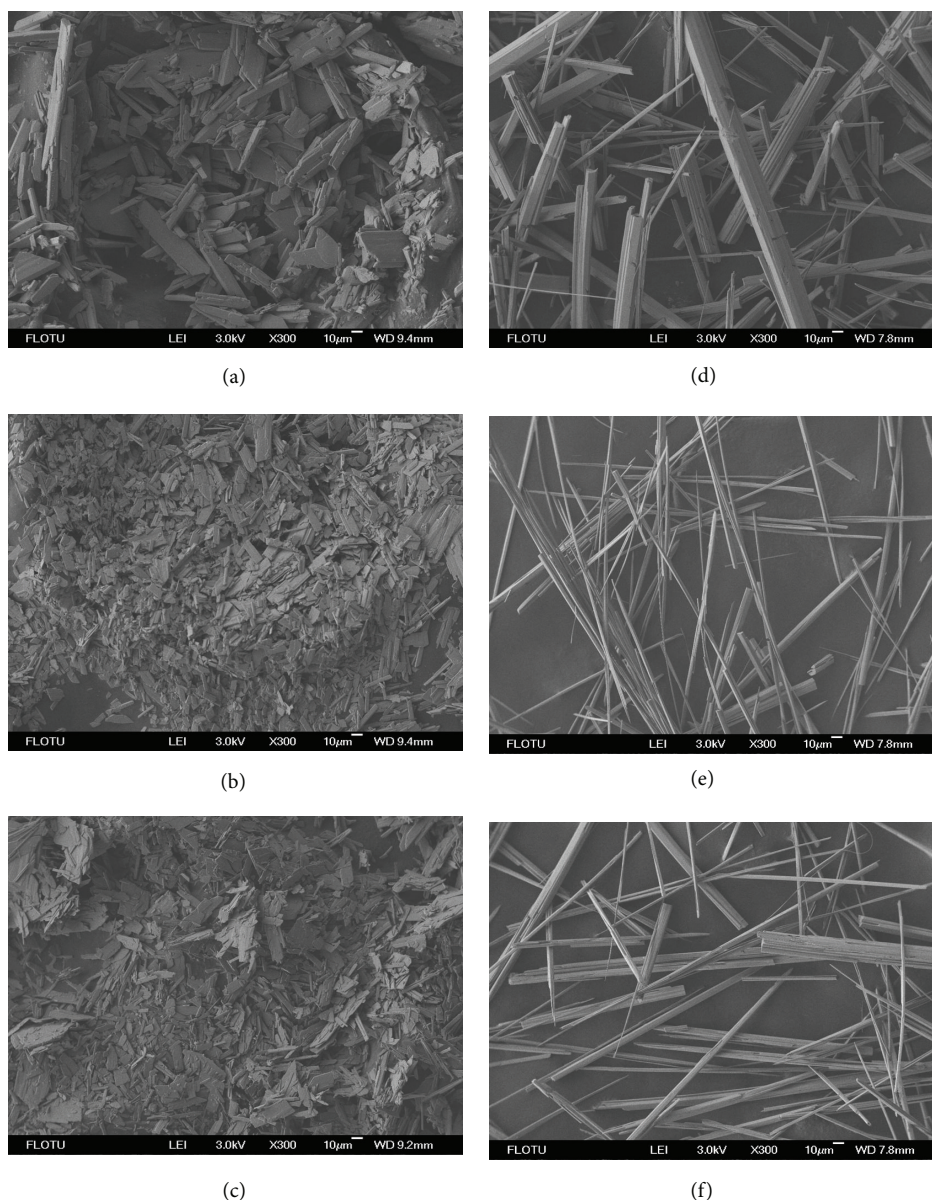


FIGURE 3: Influence of the mixing ways of the reactants on the morphology of the precursors ((a)–(c)) and the hydrothermal products ((d)–(f)). Mixing of reactants: (a), (d): adding CaCl_2 to Na_2SO_4 , (b), (e): adding Na_2SO_4 to CaCl_2 , (c), (f): adding CaCl_2 and Na_2SO_4 simultaneously to a blank container.

line a, smaller precursors were obtained despite the bigger super-saturation in the case of line c, which may be connected with the difference of the solution compositions. Figure 4(b) shows the variation of $[\text{Ca}^{2+}]/[\text{SO}_4^{2-}]$ with reaction time. The order of the values of $[\text{Ca}^{2+}]/[\text{SO}_4^{2-}]$ in lines a–c (line b > line c > line a) was in accordance with the order of the particle sizes of the precursors, indicating that a high value of $[\text{Ca}^{2+}]/[\text{SO}_4^{2-}]$ favored the formation of the $\text{CaSO}_4 \cdot 2\text{H}_2\text{O}$ with small particles. The above phenomena indicated that the particle sizes of the precursors were influenced by both the super-saturation and the value of $[\text{Ca}^{2+}]/[\text{SO}_4^{2-}]$. Adding Na_2SO_4 to CaCl_2 was considered to be a suitable mixing

way of reactants for the formation of fine precursor and the whiskers with higher aspect ratios.

3.3. Influence of the Molar Ratio of the Reactants. The influence of the molar ratios of the reactants on the morphology of the precursors and the hydrothermal products is shown in Figure 5. The precursors were prepared by adding Na_2SO_4 to CaCl_2 at 25°C .

The precursors were plate-like particles with lengths of 3–45 μm , 3–60 μm and 4.5–55 μm , and widths of 0.5–15 μm , 1.5–18 μm , and 1.5–20 μm in the cases of the molar ratios of Na_2SO_4 to CaCl_2 being 0.5 : 1, 1 : 1 and 2 : 1, respectively. A low

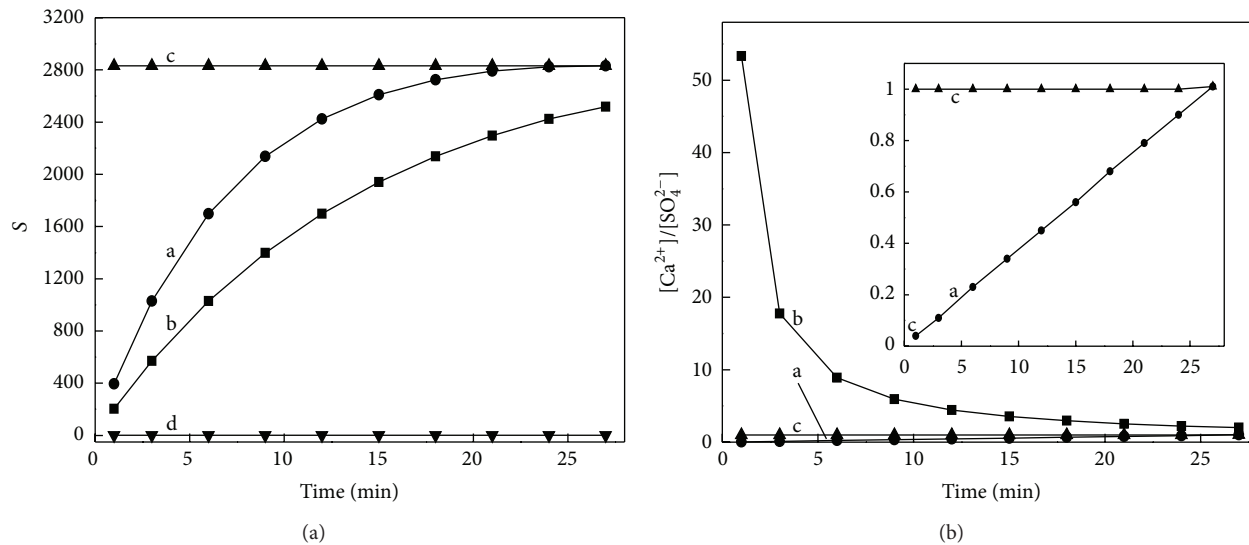


FIGURE 4: Influence of the mixing ways of reactants on the super-saturation (I) and $[Ca^{2+}]/[SO_4^{2-}]$ (II). (a): adding $CaCl_2$ to Na_2SO_4 , (b): adding Na_2SO_4 to $CaCl_2$, (c): adding $CaCl_2$ and Na_2SO_4 simultaneously to a blank container, and (d): K_{sp} of $CaSO_4 \cdot 2H_2O$.

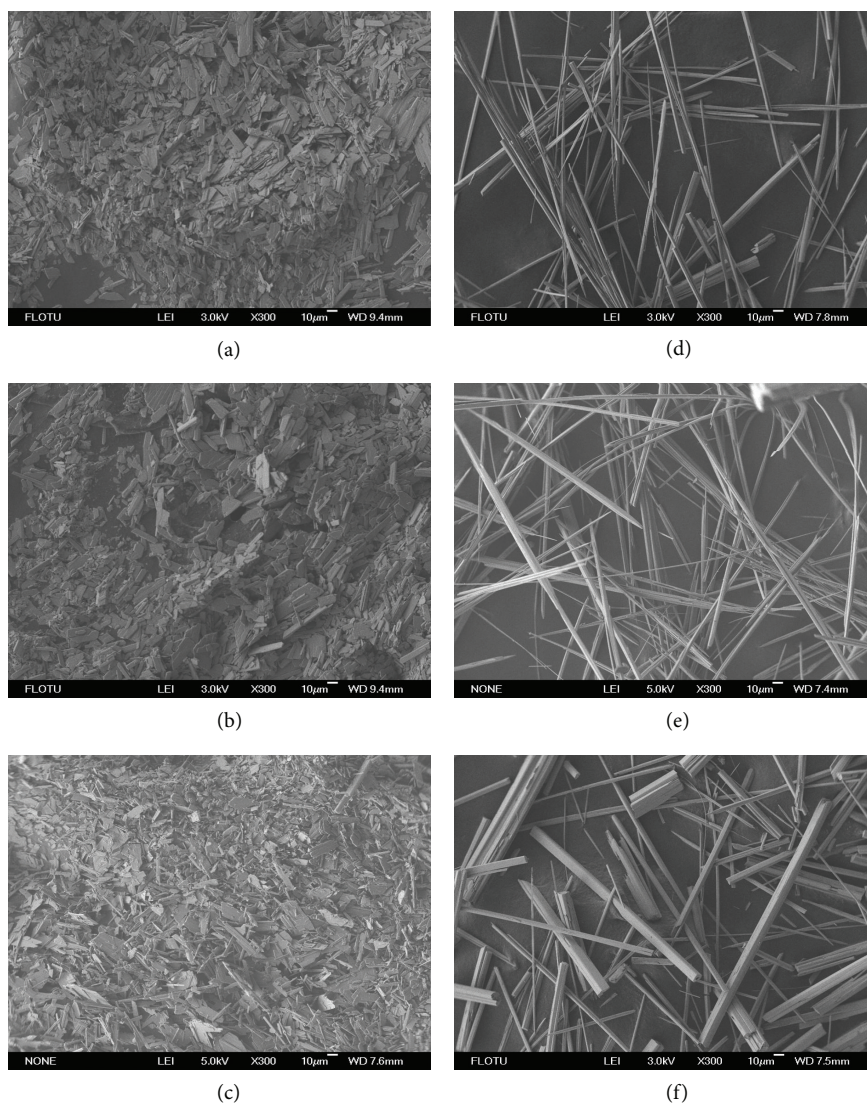


FIGURE 5: Influence of the molar ratios of Na_2SO_4 to $CaCl_2$ on the morphology of the precursors ((a)–(c)) and the hydrothermal products ((d)–(f)). Molar ratio of Na_2SO_4 to $CaCl_2$: (a), (d): 0.5 : 1, (b), (e): 1 : 1, (c), (f): 2 : 1.

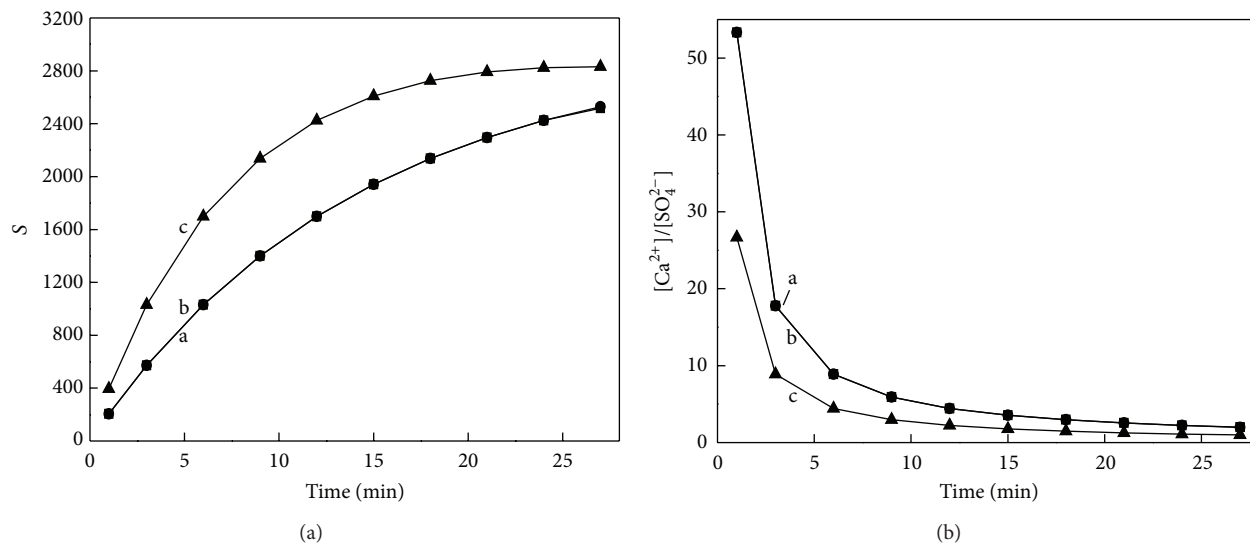


FIGURE 6: Influence of the molar ratios of Na_2SO_4 to CaCl_2 on the super-saturation and $[\text{Ca}^{2+}]/[\text{SO}_4^{2-}]$.

molar ratio of Na_2SO_4 to CaCl_2 favored the formation of the precursor with small particle size and the formation of the hydrothermal product with high aspect ratio. $\text{CaSO}_4 \cdot 0.5\text{H}_2\text{O}$ whiskers with a length of 80–310 μm and a width of 0.8–8.0 μm were formed in the case of the molar ratio of Na_2SO_4 to CaCl_2 being 0.5 : 1.

The variations of the super-saturation and $[\text{Ca}^{2+}]/[\text{SO}_4^{2-}]$ with reaction time are shown in Figure 6. Compared with the data of the molar ratios of Na_2SO_4 to CaCl_2 being 1:1 and 2:1, the super-saturations of the solutions were smaller and the values of $[\text{Ca}^{2+}]/[\text{SO}_4^{2-}]$ were bigger at the molar ratio of Na_2SO_4 to CaCl_2 being 0.5 : 1, which favored the formation of the $\text{CaSO}_4 \cdot 2\text{H}_2\text{O}$ precursors with smaller sizes.

4. Conclusion

$\text{CaSO}_4 \cdot 0.5\text{H}_2\text{O}$ whiskers were formed via co-precipitation at room temperature followed by hydrothermal treatment, using CaCl_2 and Na_2SO_4 as the raw materials. The particle sizes of the $\text{CaSO}_4 \cdot 2\text{H}_2\text{O}$ precursors formed at room temperature connected closely with the process parameters as temperature, the mixing way and the molar ratios of the reactants. The $\text{CaSO}_4 \cdot 2\text{H}_2\text{O}$ precursors with small particle sizes can be formed at the following condition: 25°C, adding Na_2SO_4 to CaCl_2 and keeping the molar ratio of Na_2SO_4 to CaCl_2 as 0.5:1 owing to the comparatively low super-saturations and the high values of $[\text{Ca}^{2+}]/[\text{SO}_4^{2-}]$, which favored the hydrothermal formation of the $\text{CaSO}_4 \cdot 0.5\text{H}_2\text{O}$ whiskers with high aspect ratios.

References

- [1] S. K. Hamdona and U. A. Al Hadad, "Crystallization of calcium sulfate dihydrate in the presence of some metal ions," *Journal of Crystal Growth*, vol. 299, no. 1, pp. 146–151, 2007.
- [2] X. Song, S. Sun, W. Fan, and H. Yu, "Preparation of different morphologies of calcium sulfate in organic media," *Journal of Materials Chemistry*, vol. 13, no. 7, pp. 1817–1821, 2003.
- [3] R. Chen, K. B. Luo, H. P. Li, and Y. X. Tan, "Application of whiskers in the materials," *Science & Technology in Chemical Industry*, vol. 15, pp. 58–61, 2007.
- [4] J. J. Eberl, E. Thelen, and H. L. Heller, "Method for the manufacture of coated calcium sulfate whisker fibers," US patent 3961105.
- [5] H. Fink and M. U. . Dipl.-Ing, "Verfahren zur herstellung von α -hydrogips und II-anhydrogips," Der offen, DE, 2613651, 1976.
- [6] G. D. Rees, R. Evans-Gowing, S. J. Hammond, and B. H. Robinson, "Formation and morphology of calcium sulfate nanoparticles and nanowires in water-in-oil microemulsions," *Langmuir*, vol. 15, no. 6, pp. 1993–2002, 1999.
- [7] D. Kuang, A. Xu, Y. Fang, H. Ou, and H. Liu, "Preparation of inorganic salts (CaCO_3 , BaCO_3 , CaSO_4) nanowires in the Triton X-100/cyclohexane/water reverse micelles," *Journal of Crystal Growth*, vol. 244, no. 3-4, pp. 379–383, 2002.
- [8] Y. Chen and Q. Wu, "Facile synthesis and properties research of single crystal calcium sulfate nanotubes through reverse micelle method," *Colloids and Surfaces A*, vol. 325, no. 1-2, pp. 33–37, 2008.
- [9] L. Li, Y. J. Zhu, and M. G. Ma, "Microwave-assisted preparation of calcium sulfate nanowires," *Materials Letters*, vol. 62, no. 30, pp. 4552–4554, 2008.
- [10] G. Xi, K. Xiong, Q. Zhao, R. Zhang, H. Zhang, and Y. Qian, "Nucleation-dissolution-recrystallization: a new growth mechanism for t-selenium nanotubes," *Crystal Growth and Design*, vol. 6, no. 2, pp. 577–582, 2006.
- [11] B. Xi, S. Xiong, H. Fan, X. Wang, and Y. Qian, "Shape-controlled synthesis of tellurium 1D nanostructures via a novel circular transformation mechanism," *Crystal Growth and Design*, vol. 7, no. 6, pp. 1185–1191, 2007.
- [12] Outokumpu Research Oy, HSC Chemistry 7.0, Finland, 2011.

Research Article

Synthesis of $\text{Al}(\text{OH})_3$ Nanostructures from $\text{Al}(\text{OH})_3$ Microagglomerates via Dissolution-Precipitation Route

Bo Yu,¹ Zhenhao Tian,¹ Jie Xiong,² and Lan Xiang¹

¹ Department of Chemical Engineering, Tsinghua University, Beijing 10084, China

² Department of Chemical Engineering, China University of Petroleum, Beijing 102249, China

Correspondence should be addressed to Lan Xiang; xianglan@mail.tsinghua.edu.cn

Received 13 January 2013; Accepted 23 April 2013

Academic Editor: Wancheng Zhu

Copyright © 2013 Bo Yu et al. This is an open access article distributed under the Creative Commons Attribution License, which permits unrestricted use, distribution, and reproduction in any medium, provided the original work is properly cited.

A facile method was developed to synthesize $\text{Al}(\text{OH})_3$ nanostructures from $\text{Al}(\text{OH})_3$ microagglomerates by dissolution in $9.0 \text{ mol}\cdot\text{L}^{-1}$ NaOH at 115°C followed by dilution and aging of the solution at room temperature. The influence of $\text{Al}(\text{OH})_3$ nanoseed and surfactants as sodium dodecyl sulfate (SDS), polyethylene glycol 6000 (PEG6000), and cetyltrimethylammonium bromide (CTAB) on the formation of the $\text{Al}(\text{OH})_3$ nano-structures was investigated. The experimental results indicated that the $\text{Al}(\text{OH})_3$ microspheres composed of nanoparticles were prepared in the blank experiment, while dispersive $\text{Al}(\text{OH})_3$ nano-particles with a diameter of 80–100 nm were produced in the presence of $\text{Al}(\text{OH})_3$ nano-seed and CTAB.

1. Introduction

The synthesis of $\text{Al}(\text{OH})_3$ nanostructures has been paid much attention in recent years owing to their unique properties and wide applications in plastics, rubbers, papers, glasses and medicines, and so forth [1–4]. $\text{Al}(\text{OH})_3$ microparticles were usually produced in the aluminum metallurgical factories via the Bayer route, which included the leaching of the bauxite ores at alkaline hydrothermal condition ($150\text{--}250^\circ\text{C}$), the removing of impurities as Si and Fe at elevated temperatures, and the precipitation of the $\text{Al}(\text{OH})_3$ microparticles in the presence of $\text{Al}(\text{OH})_3$ seed by gradually cooling of the sodium aluminate solution from $90\text{--}100^\circ\text{C}$ to $50\text{--}60^\circ\text{C}$ which usually lasted 48–72 h [5–8]. Many wet chemical methods have been developed to synthesize the $\text{Al}(\text{OH})_3$ nanostructures. For example, Li et al. [9] produced the $\text{Al}(\text{OH})_3$ nanowhiskers with a length of $8\text{--}12 \mu\text{m}$ and a diameter of 100 nm by dropping $0.05 \text{ mol}\cdot\text{L}^{-1}$ HCl to $1.6 \text{ mol}\cdot\text{L}^{-1}$ sodium aluminate at 60°C . Chen et al. [10] synthesized the $\text{Al}(\text{OH})_3$ hexagonal plates with a diameter of 100–200 nm and a thickness of 20–30 nm by carbonation of the sodium aluminate solution at room temperature. Li et al. [11] produced the $\text{Al}(\text{OH})_3$ nanoparticles with an average size of 30–40 nm from the dilute sodium aluminate solution containing $0.4 \text{ mol}\cdot\text{L}^{-1}$

NaOH in the presence of $\alpha\text{-Al}_2\text{O}_3$ nanoseed and polyethylene glycol 20000 (PEG20000). However, some problems still existed in the former methods, such as low efficiency in the dilute system, the use of the expensive organic solvents, and the discharge of waste water or byproducts. Wang et al. synthesized $\text{Al}(\text{OH})_3$ particles with an average diameters of $0.5\text{--}1.2 \mu\text{m}$ by dissolution of the agglomerated $\text{Al}(\text{OH})_3$ microagglomerates with an average diameter of $1.5 \mu\text{m}$ in $2.0 \text{ mol}\cdot\text{L}^{-1}$ NaOH solution at $90\text{--}100^\circ\text{C}$ and then cooled down to $50\text{--}70^\circ\text{C}$. Up to now, it is still a challenge to develop a moderate, efficient, and environmentally friendly method for the synthesis of $\text{Al}(\text{OH})_3$ nanostructures.

Herein, a facile dissolution precipitation method was developed in this paper to synthesize $\text{Al}(\text{OH})_3$ nanostructures from $\text{Al}(\text{OH})_3$ microagglomerates. The influences of the $\text{Al}(\text{OH})_3$ nanoseed and the surfactants including SDS, PEG6000, and CTAB on the formation of $\text{Al}(\text{OH})_3$ nanostructures were discussed.

2. Experimental

2.1. Experimental Procedure. Figure 1 shows the morphology and the thermogravimetric analysis of the raw material and the $\text{Al}(\text{OH})_3$ seed. $\text{Al}(\text{OH})_3$ raw material was Provided by

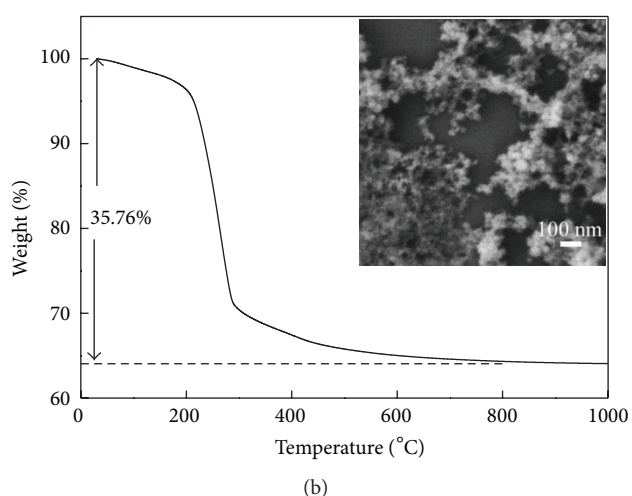
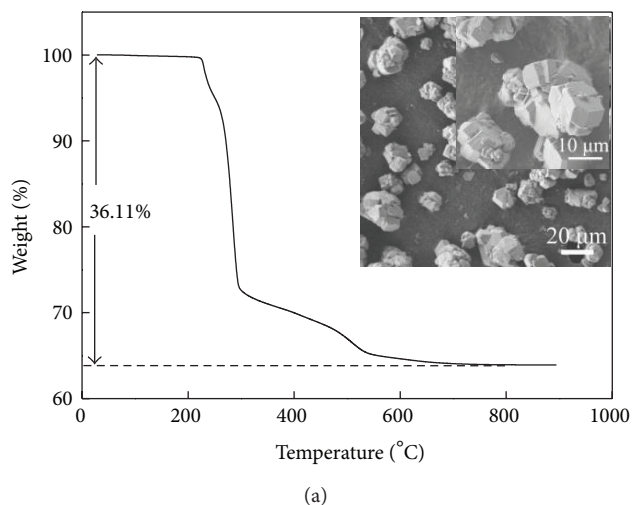


FIGURE 1: TG curve and morphology of $\text{Al}(\text{OH})_3$ raw material (a) and seed (b).

an aluminum metallurgical factory in Shandong province, China. $\text{Al}(\text{OH})_3$ seed was synthesized by coprecipitation of $0.5 \text{ mol}\cdot\text{L}^{-1}$ $\text{Al}(\text{NO}_3)_3$ and $1.0 \text{ mol}\cdot\text{L}^{-1}$ NaOH at room temperature, keeping the initial molar ratio of $\text{Al}(\text{NO}_3)_3$ to NaOH at 1: 3. As shown in Figure 1(a), $\text{Al}(\text{OH})_3$ raw material was composed mainly of the irregular agglomerates with a diameter of 5–20 μm , and the weight loss (36.11%) occurred between 30 and 800°C should be attributed to the removal of the crystal water; thus, the formula for the raw material was deduced as $\text{Al}_2\text{O}_3\cdot 3.20\text{H}_2\text{O}$. The data in Figure 1(b) showed that the particle size of the $\text{Al}(\text{OH})_3$ seed was 20–40 nm and the weight loss between 30 and 800°C was 35.04%, and then the formula for the seed was deduced as $\text{Al}_2\text{O}_3\cdot 3.15\text{H}_2\text{O}$.

Figure 2 shows the flow chart for the formation of the $\text{Al}(\text{OH})_3$ nanostructures from the $\text{Al}(\text{OH})_3$ microagglomerates.

Dissolution of $\text{Al}(\text{OH})_3$ in NaOH solution. 66.4 g of $\text{Al}(\text{OH})_3$ raw material was dissolved in 110 mL of 3.0–11.0 $\text{mol}\cdot\text{L}^{-1}$ NaOH at 115°C for 0.5 h to prepare the sodium aluminum solution with or without the existence of the un-dissolved $\text{Al}(\text{OH})_3$. The solutions or the supernatants were used to analyze the dissolution of $\text{Al}(\text{OH})_3$.

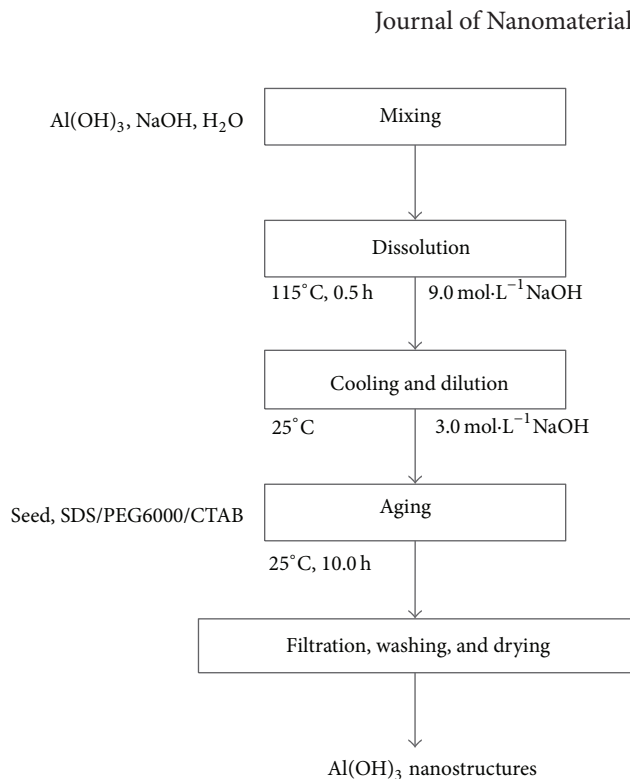


FIGURE 2: Flow chart for the formation of nano- $\text{Al}(\text{OH})_3$ from $\text{Al}(\text{OH})_3$ microagglomerates.

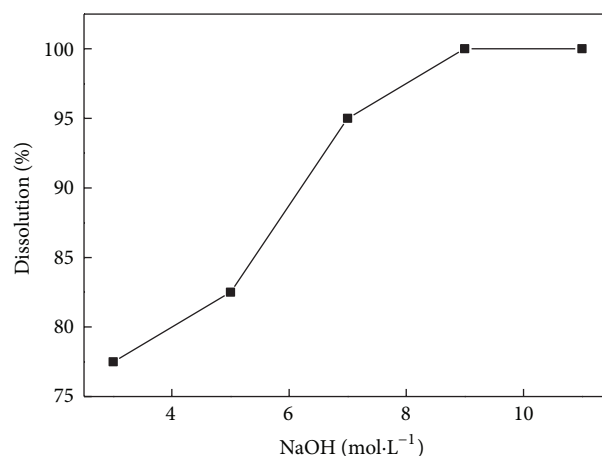


FIGURE 3: Dissolution of $\text{Al}(\text{OH})_3$ microagglomerates in NaOH solution.

Formation of $\text{Al}(\text{OH})_3$ nanostructures 66.4 g of $\text{Al}(\text{OH})_3$ raw material was dissolved in 110 mL of $9.0 \text{ mol}\cdot\text{L}^{-1}$ NaOH at 115°C for 0.5 h to get the sodium aluminum solution. The solution was then cooled down to room temperature and diluted with deionized water to get a solution containing $3.0 \text{ mol}\cdot\text{L}^{-1}$ NaOH. Then, a certain amount of the $\text{Al}(\text{OH})_3$ nanoseed and surfactant (SDS, EDTA, or PEG 6000) were added to the diluted sodium aluminum solution to produce a solution containing $0.125 \text{ mol}\cdot\text{L}^{-1}$ $\text{Al}(\text{OH})_3$ nanoseed and $13.0 \text{ g}\cdot\text{L}^{-1}$ surfactant. The sodium aluminum solution was aged for 0–10.0 h to fabricate the $\text{Al}(\text{OH})_3$ precipitate. Then, the $\text{Al}(\text{OH})_3$ precipitate was washed by deionized water and

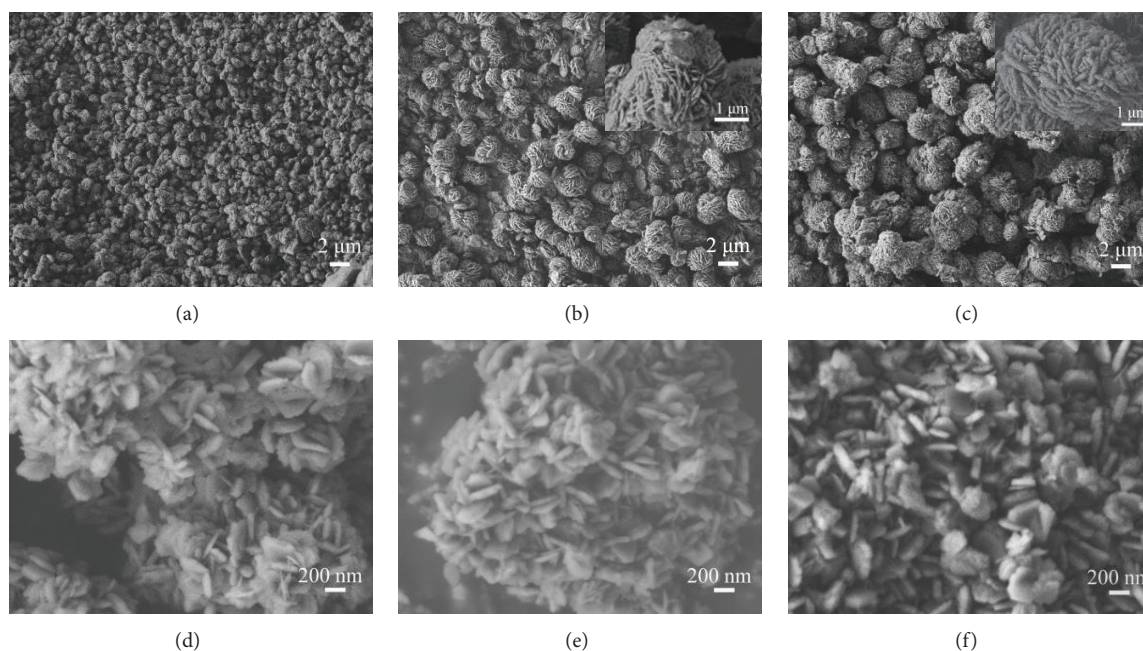


FIGURE 4: Morphology of $\text{Al}(\text{OH})_3$ formed in the absence (a–c) and presence (d–f) of seed. Aging time (h): a, c—2.0; b, d—6.0; and c, f—10.0.

ethanol and dried at 105°C for 4.0 h. All of the chemical reagents used in the experiments were analytical grade without further purification.

2.2. Analysis. The morphology of the samples was examined by the field emission scanning electron microscopy (FESEM, JSM 7401F, JEOL, Japan). The structures of the samples were identified by the X-ray powder diffraction (XRD, D8 Advance, Bruker, Germany) patterns using $\text{Cu K}\alpha$ radiation ($\lambda = 1.54178 \text{ nm}$). The composition of the samples was identified by the thermogravimetric analyzer (TG/DSC, Mettler Toledo, Switzerland). The concentration of the soluble Al ion was analyzed by the EDTA complex- Zn^{2+} titration method [12].

3. Results and Discussions

3.1. Dissolution of $\text{Al}(\text{OH})_3$ Microagglomerates in NaOH Solution. Figure 3 shows the dissolution of the $\text{Al}(\text{OH})_3$ microagglomerates in $3.0\text{--}11.0 \text{ mol}\cdot\text{L}^{-1}$ NaOH solutions. In the experimental conditions, the increase of NaOH concentration from $3.0 \text{ mol}\cdot\text{L}^{-1}$ to $11.0 \text{ mol}\cdot\text{L}^{-1}$ favored the dissolution of $\text{Al}(\text{OH})_3$. It was found that the raw material was dissolved completely if $[\text{NaOH}] \geq 9.0 \text{ mol}\cdot\text{L}^{-1}$. Therefore, $9.0 \text{ mol}\cdot\text{L}^{-1}$ NaOH was adapted to dissolve the $\text{Al}(\text{OH})_3$ raw material in the later experiments.

3.2. Precipitation of $\text{Al}(\text{OH})_3$ at Room Temperature

3.2.1. Influence of $\text{Al}(\text{OH})_3$ Nanoseed. Figure 4 shows the morphology of the $\text{Al}(\text{OH})_3$ nanostructures formed in the absence and presence of $\text{Al}(\text{OH})_3$ nanoseed. As shown in Figures 4(a)–4(c), agglomerated microspheres were prepared in the blank experiment. The microspheres were composed of the plates with a diameter of $0.6\text{--}1.0 \mu\text{m}$ and a thickness of

$0.2\text{--}0.3 \mu\text{m}$, and the plates were made up of the nanoparticles with a diameter of $80\text{--}100 \text{ nm}$. The diameters of the microspheres formed at 2.0 h, 6.0 h, and 10.0 h were $0.5\text{--}1.5 \mu\text{m}$, $1.0\text{--}3.5 \mu\text{m}$, and $1.0\text{--}4.0 \mu\text{m}$, respectively, revealing that the sizes of the microspheres increased with the increase of the aging time. Dispersive $\text{Al}(\text{OH})_3$ nanoplates with a diameter of $250\text{--}350 \text{ nm}$ and a thickness of 100 nm were produced in the presence of $0.125 \text{ mol}\cdot\text{L}^{-1}$ $\text{Al}(\text{OH})_3$ nanoseed, and the morphology of the nanoplates formed at 2.0 h, 6.0 h, and 10.0 h were quite similar to each other.

Figure 5 shows the TG curves and the XRD patterns of the $\text{Al}(\text{OH})_3$ nanoplates formed in the presence of $\text{Al}(\text{OH})_3$ nanoseed. As shown in Figure 5(a), a weight loss of 35.91% occurred in the temperature range of $30\text{--}800^\circ\text{C}$; thus, the formula of the $\text{Al}(\text{OH})_3$ nanoplates was deduced as $\text{Al}_2\text{O}_3\cdot 3.17\text{H}_2\text{O}$. The phenomenon that the number of water molecular was slightly higher than 3.0 revealed that some water was absorbed physically by the $\text{Al}(\text{OH})_3$ nanoplates. Most of the diffraction peaks in Figure 6(b) can be indexed as gibbsite (PDF no. 74-1775, $a = 8.676 \text{ \AA}$, $b = 5.070 \text{ \AA}$, and $c = 9.721 \text{ \AA}$), and the peak at $2\theta = 40.506^\circ$ revealed that a minor amount of bayerite (PDF no. 20-0011, $a = 5.062 \text{ \AA}$, $b = 8.671 \text{ \AA}$, and $c = 4.713 \text{ \AA}$) also existed in the $\text{Al}(\text{OH})_3$ nanoplates.

Figure 6 shows the influence of $\text{Al}(\text{OH})_3$ nanoseed on the precipitation of $\text{Al}(\text{OH})_3$ nanostructures. The precipitation of $\text{Al}(\text{OH})_3$ was accelerated by the addition of $\text{Al}(\text{OH})_3$ nanoseed obviously. 63.0% of the soluble Al ion in the sodium aluminate solution was converted to the $\text{Al}(\text{OH})_3$ precipitate after aging for 2.0 h, while only about 1.0% of the soluble Al ion was precipitated after aging for 2.0 h in the blank experiment.

The influence of $\text{Al}(\text{OH})_3$ nanoseed on the morphology and the precipitation of the $\text{Al}(\text{OH})_3$ nanostructures may be

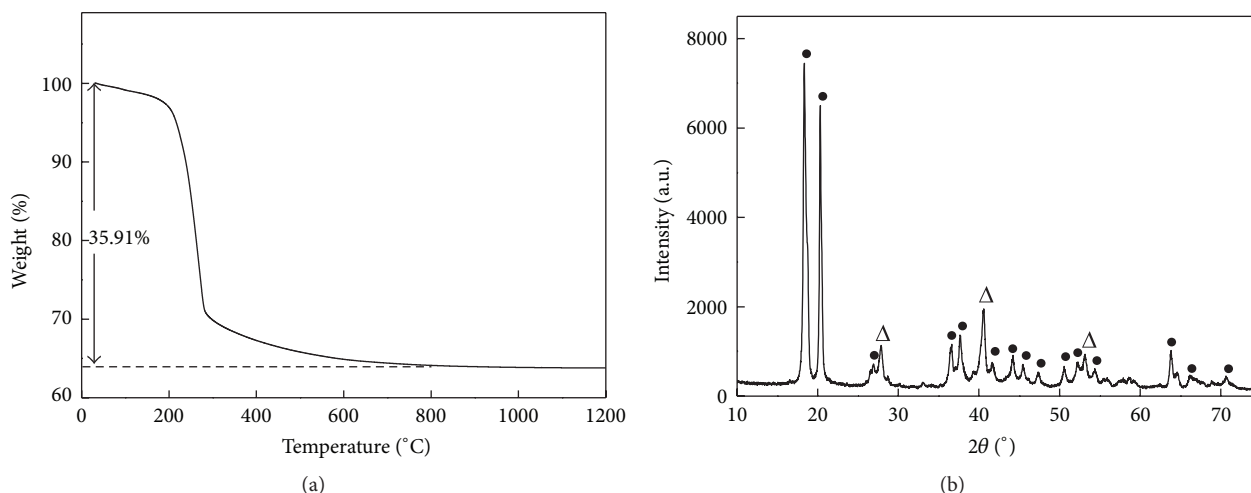


FIGURE 5: TG curve (a) and XRD spectrum (b) of $\text{Al}(\text{OH})_3$ nanoplates formed in the presence of $\text{Al}(\text{OH})_3$ nanoseed. •—Gibbsite- $\text{Al}(\text{OH})_3$, Δ —Bayerite- $\text{Al}(\text{OH})_3$.

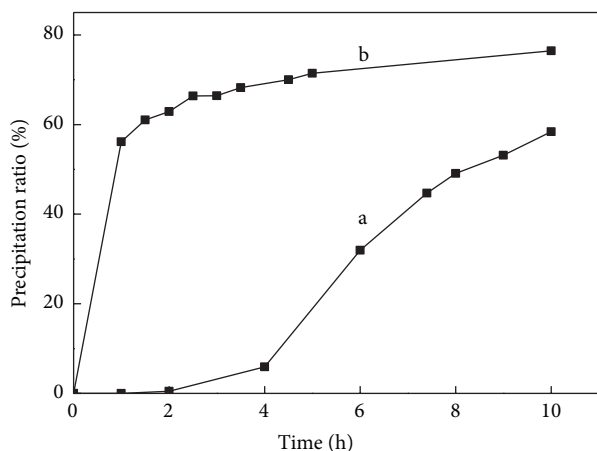


FIGURE 6: Precipitation of $\text{Al}(\text{OH})_3$ in the absence (a) and presence (b) of $\text{Al}(\text{OH})_3$ nanoseed.

explained as follows. In the absence of $\text{Al}(\text{OH})_3$ nanoseed, $\text{Al}(\text{OH})_3$ was first precipitated homogeneously and slowly from the sodium aluminate solution, and the $\text{Al}(\text{OH})_3$ fine particles formed at the early aging stage acted as the nucleus for the subsequent precipitation of $\text{Al}(\text{OH})_3$, leading to the gradual growth of the agglomerated microspheres. Meanwhile, in the presence of $\text{Al}(\text{OH})_3$ nanoseed, many $\text{Al}(\text{OH})_3$ nanoparticles were added to the initial sodium aluminate solution, and they acted as the nucleus for the later heterogeneous precipitation of $\text{Al}(\text{OH})_3$ from the sodium aluminate solution, leading to the fast conversion of most of the soluble Al ion to $\text{Al}(\text{OH})_3$ within 2.0 h of aging and producing $\text{Al}(\text{OH})_3$ nanoplates with quite similar shapes.

3.3. Influence of Surfactants. The influence of the surfactants including SDS, PEG6000, and CTAB on the morphology of the $\text{Al}(\text{OH})_3$ precipitates was shown in Figure 7. $\text{Al}(\text{OH})_3$ precipitates were prepared after aging treatment

of the sodium aluminate solutions containing $0.125 \text{ mol}\cdot\text{L}^{-1}$ $\text{Al}(\text{OH})_3$ nanoseed and $13.0 \text{ g}\cdot\text{L}^{-1}$ surfactant (SDS, PEG6000, or CTAB) for 10.0 h. Compared with those formed in the sole existence of $\text{Al}(\text{OH})_3$ nanoseed (Figure 6(f)), $\text{Al}(\text{OH})_3$ nanoparticles with smaller sizes were prepared in the presence of $\text{Al}(\text{OH})_3$ nanoseed and surfactants. $\text{Al}(\text{OH})_3$ nanoparticles with a diameter of 200–300 nm, 150–250 nm, and 80–100 nm were produced in the presence of SDS, PEG6000, and CTAB, respectively. The order of the influence of the surfactants on the formation of the $\text{Al}(\text{OH})_3$ nanoparticles was $\text{CTAB} > \text{PEG6000} > \text{SDS}$, and this phenomenon may be related to the interactions between the $\text{Al}(\text{OH})_3$ surfaces and the surfactants. The surfaces of $\text{Al}(\text{OH})_3$ formed in the concentrated NaOH solutions were negative charged owing to the adsorption of OH^- [13] which were easier to absorb the cationic surfactants as CTAB and difficult to absorb the nonionic surfactants as PEG6000 or the anionic surfactants as SDS.

Figure 8 shows the schematic diagram for the influence of $\text{Al}(\text{OH})_3$ nanoseed and the surfactants on the precipitation of $\text{Al}(\text{OH})_3$ from the sodium aluminate solution. Generally, the existence of $\text{Al}(\text{OH})_3$ nanoseed promoted the heterogeneous precipitation of $\text{Al}(\text{OH})_3$, and the adsorption of the surfactants as SDS, PEG6000 and CTAB, especially the cationic surfactant CTAB, on the surfaces of $\text{Al}(\text{OH})_3$ inhibited the growth of the $\text{Al}(\text{OH})_3$. The coinfluence of the $\text{Al}(\text{OH})_3$ nanoseed and CTAB on the precipitation of $\text{Al}(\text{OH})_3$ from the sodium aluminate solution led to the formation of the dispersive $\text{Al}(\text{OH})_3$ nanoparticles with a diameter of 80–100 nm.

4. Conclusion

$\text{Al}(\text{OH})_3$ nanostructures were synthesized from $\text{Al}(\text{OH})_3$ microagglomerates by dissolution of the $\text{Al}(\text{OH})_3$ microagglomerates in $9.0 \text{ mol}\cdot\text{L}^{-1}$ NaOH at 115°C for 0.5 h followed by dilution and aging of the solution at room temperature. The experimental results indicated that the $\text{Al}(\text{OH})_3$

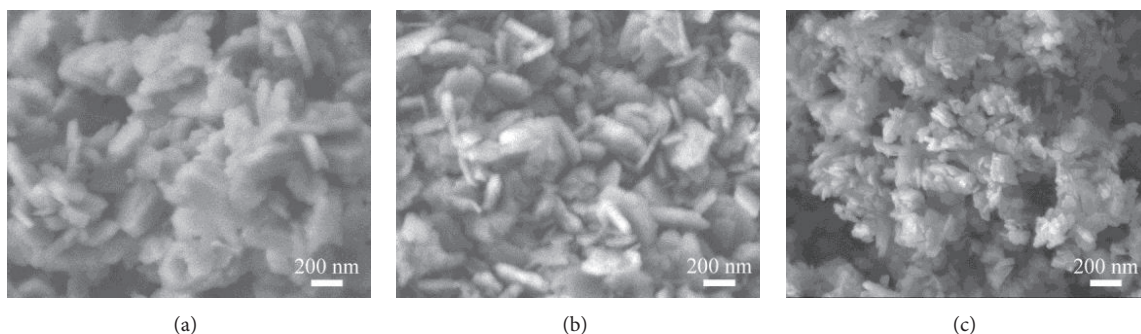


FIGURE 7: Morphology of $\text{Al}(\text{OH})_3$ nanoparticles formed in the presence of SDS (a), PEG6000 (b), and CTAB (c).

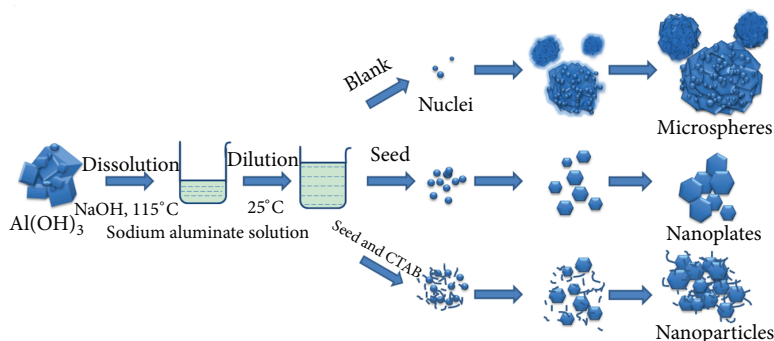


FIGURE 8: Sketch of the influence of $\text{Al}(\text{OH})_3$ nanoseed and surfactants on formation of $\text{Al}(\text{OH})_3$ nanostructures.

microspheres composed of nanoparticles were prepared in the blank experiment, while dispersive $\text{Al}(\text{OH})_3$ nanoparticles with a diameter of 80–100 nm were formed in the presence of $0.125 \text{ mol}\cdot\text{L}^{-1}$ $\text{Al}(\text{OH})_3$ nanoseed and $13.0 \text{ g}\cdot\text{L}^{-1}$ CTAB.

Acknowledgment

This work was supported by the National Natural Science Foundation (nos. 51174125 and 51234003).

References

- [1] O. Ajouyed, C. Hurel, M. Ammari, L. B. Allal, and N. Marmier, "Sorption of Cr(VI) onto natural iron and aluminum (oxy)hydroxides: effects of pH, ionic strength and initial concentration," *Journal of Hazardous Materials*, vol. 174, no. 1–3, pp. 616–622, 2010.
- [2] T. J. Reich and C. M. Koretsky, "Adsorption of Cr(VI) on gamma-alumina in the presence and absence of CO_2 : comparison of three surface complexation models," *Geochimica et Cosmochimica Acta*, vol. 75, no. 22, pp. 7006–7017, 2011.
- [3] W. Q. Cai, J. G. Yu, and M. Jaroniec, "Template-free synthesis of hierarchical spindle-like $\gamma\text{-Al}_2\text{O}_3$ materials and their adsorption affinity towards organic and inorganic pollutants in water," *Journal of Materials Chemistry*, vol. 20, no. 22, pp. 4587–4594, 2010.
- [4] N. K. Renuka, A. V. Shijina, and A. K. Praveen, "Mesoporous gamma-alumina nanoparticles: synthesis, characterization and dye removal efficiency," *Materials Letters*, vol. 82, pp. 42–44, 2012.
- [5] K. A. Blanks, "Novel synthesis of gibbsite by laser-stimulated nucleation in supersaturated sodium aluminate solutions," *Journal of Crystal Growth*, vol. 220, no. 4, pp. 572–578, 2000.
- [6] H. Li, J. Addai-Mensah, J. C. Thomas, and A. R. Gerson, "The crystallization mechanism of $\text{Al}(\text{OH})_3$ from sodium aluminate solutions," *Journal of Crystal Growth*, vol. 279, no. 3–4, pp. 508–520, 2005.
- [7] T. Radnai, P. M. May, G. T. Hefter, and P. Sipos, "Structure of aqueous sodium aluminate solutions: a solution X-ray diffraction study," *Journal of Physical Chemistry A*, vol. 102, no. 40, pp. 7841–7850, 1998.
- [8] M. J. Chen and L. Xiang, "Influence of $\text{Al}_2\text{O}_3\cdot x\text{H}_2\text{O}$ crystallinities on the morphology of AlOOH whiskers," *Nano Biomedicine and Engineering*, vol. 2, no. 2, pp. 121–125, 2010.
- [9] Y. Li, Y. F. Zhang, and C. Yang, "Fiber-like aluminum hydroxide nanoparticles prepared by neutralization of sodium aluminate solution," *The Chinese Journal of Nonferrous Metals*, vol. 18, no. 1, pp. 264–267, 2008.
- [10] J. F. Chen, L. Shao, F. Guo, and X. M. Wang, "Synthesis of nanofibers of aluminum hydroxide in novel rotating packed bed reactor," *Chemical Engineering Science*, vol. 58, no. 3–6, pp. 569–575, 2003.
- [11] H. Li, H. Lu, S. Wang, J. Jia, H. Sun, and X. Hu, "Preparation of a nano-sized $\alpha\text{-Al}_2\text{O}_3$ powder from a supersaturated sodium aluminate solution," *Ceramics International*, vol. 35, no. 2, pp. 901–904, 2009.
- [12] L. L. Lewis, M. J. Nardozi, and L. M. Melnick, "Rapid chemical determination of aluminum, calcium, and magnesium in raw

materials, sinters, and slags,” *Analytical Chemistry*, vol. 33, no. 10, pp. 1351–1355, 1961.

- [13] A. Degen and M. Kosec, “Effect of pH and impurities on the surface charge of zinc oxide in aqueous solution,” *Journal of the European Ceramic Society*, vol. 20, no. 6, pp. 667–673, 2000.

Research Article

Anti-Icing Property of Superhydrophobic Octadecyltrichlorosilane Film and Its Ice Adhesion Strength

Liang Ge, Guifu Ding, Hong Wang, Jinyuan Yao, Ping Cheng, and Yan Wang

Science and Technology on Micro/Nano Fabrication Laboratory, Research Institute of Micro/Nano Science and Technology, Shanghai Jiao Tong University, Shanghai 200240, China

Correspondence should be addressed to Yan Wang; wyyw@sjtu.edu.cn

Received 23 January 2013; Accepted 30 March 2013

Academic Editor: Huijun Wu

Copyright © 2013 Liang Ge et al. This is an open access article distributed under the Creative Commons Attribution License, which permits unrestricted use, distribution, and reproduction in any medium, provided the original work is properly cited.

An octadecyltrichlorosilane (OTS) superhydrophobic film using phase-separation method was prepared to demonstrate the anti-icing property of superhydrophobic surfaces. The superhydrophobicity of the film at -5°C was investigated. It was found that the prepared OTS film retained its superhydrophobicity at -5°C by the measurement of contact angle and roll-off angle. The icing progress of water droplets on the surface at -15°C was observed. It showed that the prepared OTS film can markedly retard the icing process of water droplets and dramatically decrease the ice adhesion strength compared with that of blank surface, which can be used as anti-icing surfaces.

1. Introduction

It is well known that icing occurs when water changes from liquid to solid phase. Ice adhesion and accumulation on critical parts of structures will cause damaging problems, severe accidents, and economic losses in the fields of aerospace, transportation and power communication. For instance, droplets of supercooled water often exist in stratiform and cumulus clouds. Aircraft flying through these clouds seed an abrupt crystallization of these droplets, which can result in the formation of ice on the aircraft's wings or blockage of its instruments, unless the aircrafts are equipped with an appropriate deicing system. Icing on plane will reduce the handling and stability performance, which may cause aviation accident.

Superhydrophobicity has drawn widespread attention for its self-cleaning character and potential application in fluid devices, water repellency textile and functional separation equipment [1–4]. Generally, a surface with a contact angle larger than 150° and a roll-off angle less than 10° is defined as superhydrophobic surface. A few kinds of superhydrophobic surfaces have been developed by self-assembling [5–8], etching [9, 10], phase-separation method [1, 11], and so forth.

Numerous researchers have reported the application of superhydrophobic surface on water repellency at room temperature [12, 13]. It has been reported that icing may be retarded on superhydrophobic surface [14]. However, few researches were concerned with the possibility of applying superhydrophobic surface in subzero environment. And the effect of surface wettability on retarding ice formation still needs experimental investigation.

In this paper, a facile method to prepare superhydrophobic surface by phase-separation technology was proposed. The hydrophobicity of the prepared OTS film was greatly enhanced compared to the conventional dip-dry method with the contact angle less than 120° [10]. To carry out the icing experiment, a small cold storage was established which could offer temperature low at -30°C . Both of the static and dynamic hydrophobicities of the prepared surface were studied in subzero environment. The icing process on the superhydrophobic surface was also observed. Based on the classical heterogeneous nucleation theory, the icing behaviors of droplets on superhydrophobic surface were discussed. Based on the bonding forces measured between the prepared surface and ice, the ice adhesion strengths were calculated and compared with those of blank surface.

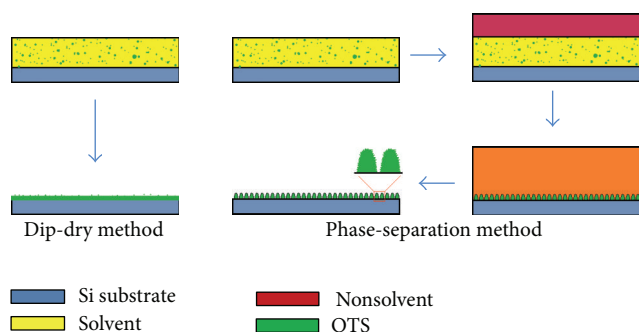


FIGURE 1: Comparison of one-step dip-dry method and phase-separation method.

2. Materials and Methods

2.1. Preparation of Samples. The substrate used in this study is silicon wafer with a radius of 3 inches and a thickness of 0.45 mm. A coating solution of 0.1 mL octadecyltrichlorosilane (OTS, Acros Organics, USA) that dissolved in 30 mL normal hexane was prepared. Dichloromethane and acetone were selected as nonsolvents. The clean silicon wafer was dipped into the coating solution for 1 minute. After evaporation for 1 minute at room temperature, the substrate coated with OTS film was immersed in the nonsolvent for 5 minutes, where a phase-separation process took place and the micro-nano rough surface structure formed. Figure 1 illustrates the procedures of one-step dip-dry method and phase-separation process.

In a phase-separation progress, it is of common occurrence that solid/liquid phases separate and liquid/liquid phases separate. Due to the interactions of these phase-separation processes, the solute will form rough microstructures after crystallization. The rough microstructures usually possess nanometer scale roughness, while the microstructures formed using the conventional dip-dry method can only show micrometer scale roughness.

2.2. Characterization and Test. The micrographs of the OTS film were characterized by a scanning electron microscope (Zeiss Ultra55). A video-based contact angle measurement system (POWREACH, JC2000D) was used to measure and record the water contact angles (WCAs) and roll-off angles of the samples. The static WCAs were measured at least 3 times using the sessile drop method by dispersing $5 \mu\text{L}$ drops of deionized water onto the sample surface. The roll-off angles were measured by tilting the substrate and the slant angles were recorded when the droplet rolled off across the surface in a downhill direction. A small cold storage was established, where the temperature could be adjusted between 0°C and -30°C by a refrigerating unit. To measure the contact and roll-off angles in subzero environment, the temperature in the cold store was set at -5°C . The relative humidity was 40%. The water and the substrate were cooled at -5°C for 3 h before the test.

The icing process was performed in the cold storage from -9°C to -15°C . The droplets were dropped onto the treated

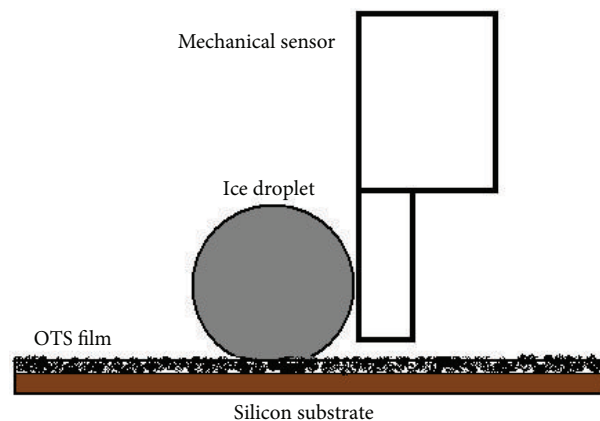


FIGURE 2: Schematic diagram of the bonding force test.

superhydrophobic surface by 1 mL syringe at 1°C . Then the temperature was reduced until icing process finished. The status of the droplets was recorded by digital camera every hour.

The bonding force between ice droplets and the film surface was tested at -15°C using a bonding force measurement system (RHESCA, PTR-1101). Figure 2 illustrated schematic diagram of the bonding force test.

As depicted in Figure 2, the water droplet froze on the OTS film surface coated on the silicon substrate which was fixed on the objective table. The probe with a mechanical sensor was set at an appropriate position by the controller. Then the probe began to move horizontally at 1 mm/s and push the ice droplet. The instantaneous value of the shear force was recorded by the mechanical sensor. The contact area between the surface and ice droplet was calculated based on the image of the ice droplet taken just before the bonding force test. The shear stress was then calculated as the ratio of the shear force and the contact area. The ice adhesion strength was the shear stress at which the ice droplet detached from the sample surface as indicated by the sudden drop of the sensed shear force to zero.

3. Results and Discussion

3.1. Surface Topography and Wettability at -5°C . Figure 3 showed the SEM images of the OTS films surface with and without treatment of nonsolvents. It can be observed from Figures 3(b) and 3(c) that there are more protrusions and voids on the treated OTS film than that on the untreated OTS film. The treatment of the nonsolvent notably changed the topography of OTS film surface. The disordered reticular structure with a submicron/nanometer size on the surface played a crucial role in the superhydrophobic property. The static contact angles and roll-off angles of the various OTS films at -5°C were listed in Table 1.

As shown in Figure 3 and Table 1, the surface of OTS film without further treatment was hydrophobic with a contact angle of 140° and a roll-off angle larger than 90° . Both the OTS films treated with dichloromethane and acetone

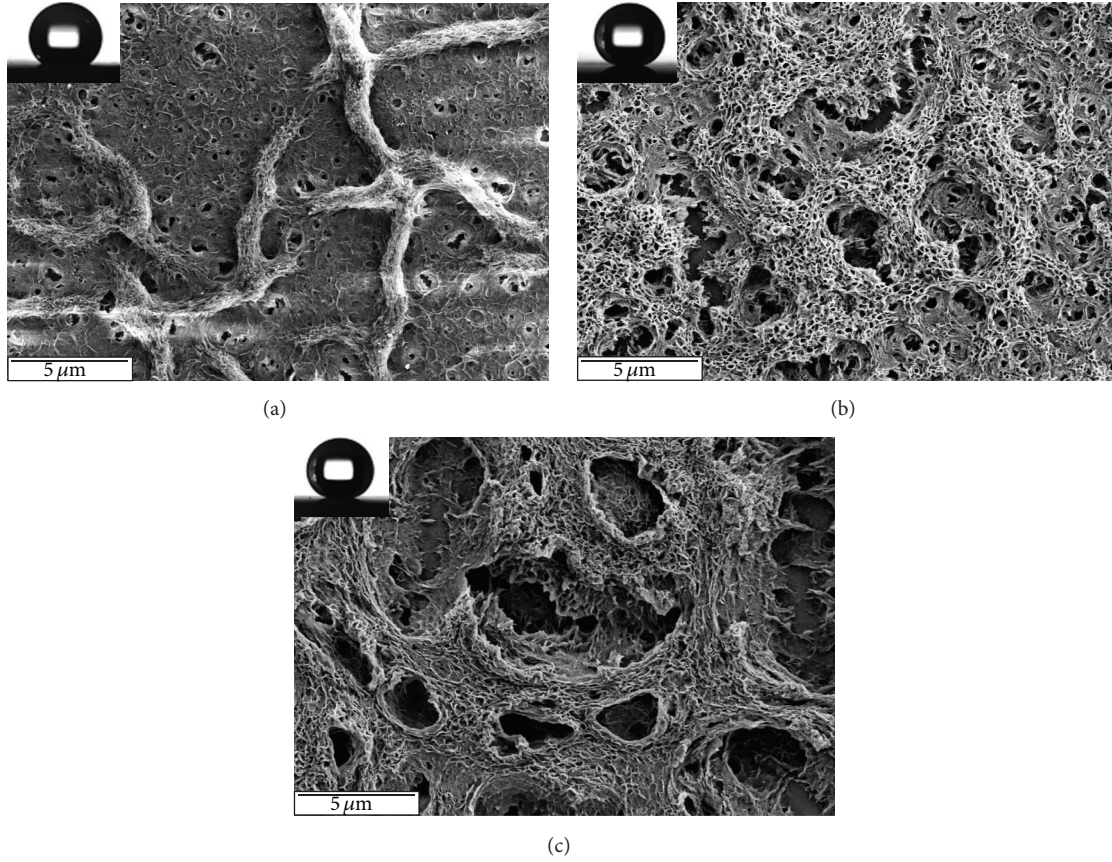


FIGURE 3: SEM images of various OTS films—(a) without treatment, (b) dichloromethane treatment, and (c) acetone treatment.

TABLE 1: Contact and roll-off angles of OTS films at -5°C without and with nonsolvent treatment.

Samples	Nonsolvent	WCA	Roll-off angle $^{\circ}$
a	Without	140°	$\geq 90^{\circ}$
b	Dichloromethane	155°	4°
c	Acetone	155°	10°

had the same contact angles of 155° and roll-off angles less than 10° . Superhydrophobicity is determined mainly by the characteristics of the solid surface. This phenomenon can be explained by the Cassie-Baxter model [15]. Cassie and Baxter proposed a gas cavity model for porous surface wettability. According to the Cassie-Baxter model, air is more likely to be trapped between the water droplets and the protrusions of the porous surface. The following equation is given for the contact angle of droplet on a real surface:

$$\cos \theta' = f(1 + \cos \theta) - 1, \quad (1)$$

where θ' is the contact angle for a real rough surface, θ is the contact angle for the corresponding ideal smooth surface, and f ($f < 1$) is the fraction of solid surface area wet by the liquid. From (1), the contact angle of a real surface is always larger than that of an ideal surface under the same conditions as $f < 1$. In this work, as shown in Figures 3 and 4,

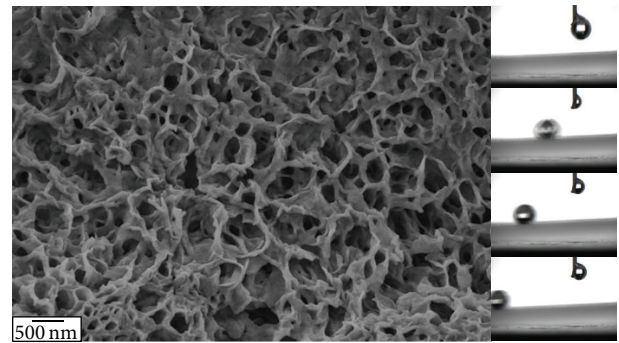


FIGURE 4: SEM image of OTS film treated with dichloromethane (left) and its dynamic hydrophobicity test (right) at -5°C .

there were many micro-nano scale protrusions on the coated silicon surface, trapping the air easily under the water droplet, so the contact fraction f decreased and the WCA was much larger than that of a smooth surface. Thus, the coating film increased the hydrophobicity of the surface and provided a superb superhydrophobic surface.

The complicated rough micro-nano binary structures modulated the three-phase contact line from continuity to discrete, which resulted in smaller adhesion force and roll-off angle [16]. So, the protrusions and voids on the surface

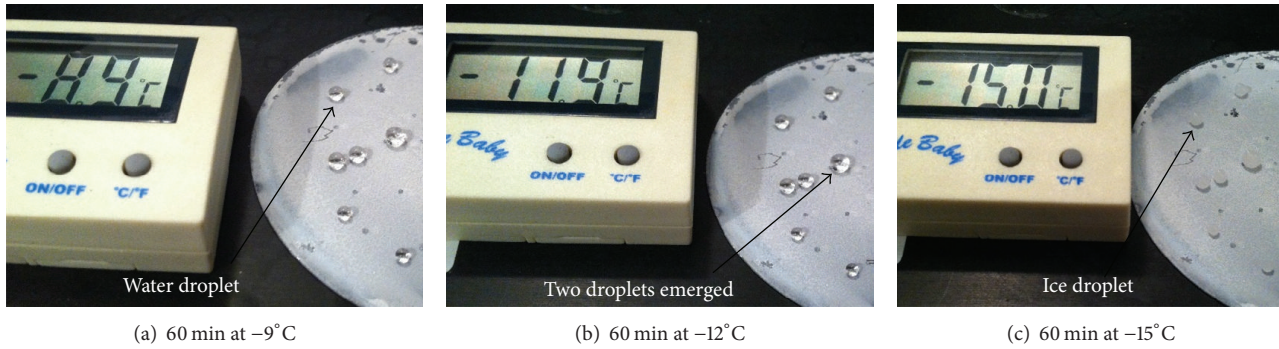


FIGURE 5: Icing process of water droplets on the OTS film treated with dichloromethane.

contributed to the greater contact angles and smaller roll-off angles for the OTS films treated with dichloromethane and acetone. As the OTS film treated with dichloromethane had a smaller roll-off angle (4°) than that by acetone (10°), it was taken for an example to study the anti-icing property as well as ice adhesion strength in the following sections. Figure 4 showed the dynamic hydrophobicity of the OTS film treated with dichloromethane. The water droplet of $5\ \mu\text{L}$ rolled off the film with a tilting angle of 4° in 0.2 s. The images of the roll-off angle were recorded by CCD camera. It could be observed that the roll-off angle was 4° and the contact angle was 155° .

3.2. Icing Behavior. Water was dropped onto OTS film treated with dichloromethane at 1°C and placed in the cold storage at 0°C for 3 h. The icing process was recorded by digital camera, as shown in Figure 5.

As shown in Figure 5, the water droplets remained in liquid state at a temperature low to -12°C on the prepared surface and did not freeze until the temperature was reduced to -15°C . The water droplets in Figures 5(a) and 5(b) could be distinguished from the ice droplets in Figure 5(c) by the reflection of light. The experimental results indicated that the icing process of water droplets on prepared superhydrophobic surface was greatly retarded, which demonstrated the superb anti-icing property of the film.

This phenomenon could be explained by the heterogeneous nucleation theory [14, 17]. It is well known that several factors, including critical nucleation radius, nucleation radius, temperature, humidity, pressure, and surface condition, contributed to the icing process of water droplet on solid surface. However, the surface condition is the dominant factor that determines the icing process under the same conditions. Compared to homogeneous nucleation theory, the free energy barrier of heterogeneous nucleation on the surface could be expressed as a function of the contact angle θ between droplets and the surface, which monotonously increased with the contact angle θ [14, 17].

Because the icing probability was dependent on the free energy barrier (the lower the free energy barrier is, the easier the droplet freezes), the phenomenon that the droplet on hydrophilic surface was more incidental to freeze than that on hydrophobic surface could be explained. In this study,

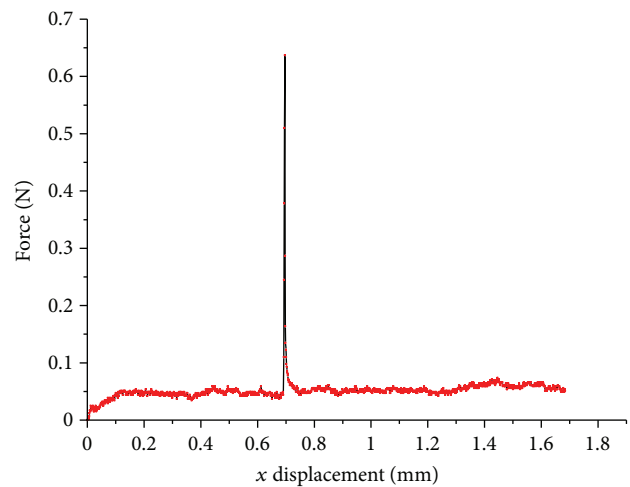


FIGURE 6: Displacement-force curve during ice adhesion test.

the water contact angle of the OTS superhydrophobic surface was 155° , while the contact angle for clean silicon surface is seldom less than 50° (see Figure 7). Thus, the potential barrier of OTS superhydrophobic surface was much larger than that of the clean silicon surface. Accordingly, the critical nucleation radius was bigger for the superhydrophobic surface. Consequently, the OTS superhydrophobic surface can retard the droplet icing on it, and the time needed to ice on OTS superhydrophobic surface is much longer than that on clean silicon surface. These results demonstrate the significant applicable probability of superhydrophobic surface in preventing the ice formation.

3.3. Ice Adhesion Strength. In order to investigate the ice adhesion strength on the superhydrophobic surface, the shear forces of ice droplets formed on the samples were measured using a bonding force measurement system. Figure 6 showed a displacement-force curve during ice bonding force test of OTS film surface. The sudden drop of shear force to zero indicates the ice detachment. Same tests were conducted at 20 different points on OTS film surface and 8 different points on clean silicon wafer.

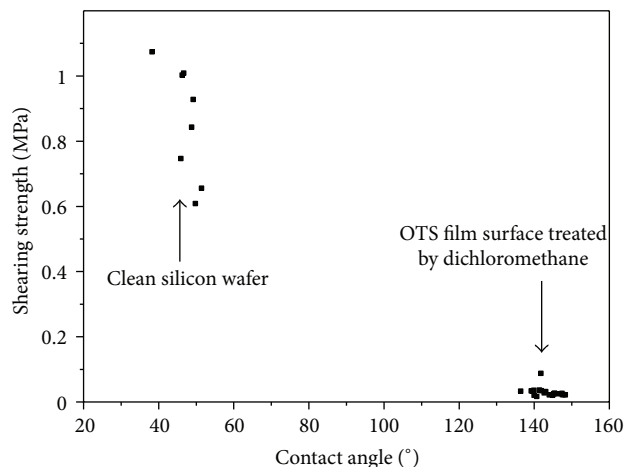


FIGURE 7: Dependence of the ice adhesion shear strength on contact angle.

Figure 7 compared the ice adhesion strength on clean silicon wafer and that on OTS film treated with dichloromethane. It showed that the ice adhesion strength on superhydrophobic surface averagely decreases 95.74% more than that on clean silicon wafer, which clearly demonstrates the outstanding performance of the superhydrophobic film on deicing. It was suggested that the disordered reticular structure plays a crucial role in the low adhesion strength between ice droplet and OTS superhydrophobic surface. In addition, during the shear forces test, the ice droplets were detached without exfoliation of the OTS film. This indicates that the adhesion strength of the OTS film on the silicon wafer is larger than that of the ice droplets on the coating film.

4. Conclusion

In this research, a superhydrophobic surface was prepared, using a simple phase-separation method. The results showed that the surface retained its excellent superhydrophobicity even in subzero environment. The superhydrophobic property was attributed to the disordered reticular structure in submicron/nanometer scale caused by the phase-separation method. The superhydrophobic surface also showed excellent anti-icing property. It was found that the OTS film surface treated with dichloromethane could markedly retard the icing progress of water droplets, as well as dramatically decrease the adhesion strength between ice droplets and the surface compared with the clean silicon surface. This indicates that the prepared OTS film surface in the study had an outstanding anti-icing performance.

Acknowledgments

The research is supported by Shanghai Science and Technology Development Foundation (no. 11DZ2290203) and the National Key Laboratory Foundation (9140C790103120-C7906).

References

- [1] H. Y. Erbil, A. L. Demirel, Y. Avci, and O. Mert, "Transformation of a simple plastic into a superhydrophobic surface," *Science*, vol. 299, no. 5611, pp. 1377–1380, 2003.
- [2] T. Sun, L. Feng, X. Gao, and L. Jiang, "Bioinspired surfaces with special wettability," *Accounts of Chemical Research*, vol. 38, no. 8, pp. 644–652, 2005.
- [3] M. Ma and R. M. Hill, "Superhydrophobic surfaces," *Current Opinion in Colloid and Interface Science*, vol. 11, no. 4, pp. 193–202, 2006.
- [4] L. Feng, Z. Yang, J. Zhai et al., "Superhydrophobicity of nanostructured carbon films in a wide range of pH values," *Angewandte Chemie International Edition*, vol. 42, no. 35, pp. 4217–4220, 2003.
- [5] M. E. McGovern, K. M. R. Kallury, and M. Thompson, "Role of solvent on the silanization of glass with octadecyltrichlorosilane," *Langmuir*, vol. 10, no. 10, pp. 3607–3614, 1994.
- [6] A. Ulman, "Formation and structure of self-assembled monolayers," *Chemical Reviews*, vol. 96, no. 4, pp. 1533–1554, 1996.
- [7] K. C. Grabar, P. C. Smith, M. D. Musick et al., "Kinetic control of interparticle spacing in Au colloid-based surfaces: rational nanometer-scale architecture," *Journal of the American Chemical Society*, vol. 118, no. 5, pp. 1148–1153, 1996.
- [8] D. I. Gittins, D. Bethell, R. J. Nichols, and D. J. Schiffrin, "Redox-connected multilayers of discrete gold particles: a novel electroactive nanomaterial," *Advanced Materials*, vol. 11, no. 9, pp. 737–740, 1999.
- [9] J. Wang, F. Liu, H. Chen, and D. Chen, "Superhydrophobic behavior achieved from hydrophilic surfaces," *Applied Physics Letters*, vol. 95, no. 8, Article ID 084104, 2009.
- [10] L. Zhu, Y. Feng, X. Ye, and Z. Zhou, "Tuning wettability and getting superhydrophobic surface by controlling surface roughness with well-designed microstructures," *Sensors and Actuators A*, vol. 130–131, pp. 595–600, 2006.
- [11] C. Y. Kuo, H. N. Lin, H. A. Tsai, D. M. Wang, and J. Y. Lai, "Fabrication of a high hydrophobic PVDF membrane via nonsolvent induced phase separation," *Desalination*, vol. 233, no. 1–3, pp. 40–47, 2008.
- [12] X. Song, J. Zhai, Y. Wang, and L. Jiang, "Fabrication of superhydrophobic surfaces by self-assembly and their water-adhesion properties," *Journal of Physical Chemistry B*, vol. 109, no. 9, pp. 4048–4052, 2005.
- [13] T. Hang, A. Hu, H. Ling, M. Li, and D. Mao, "Superhydrophobic nickel films with micro-nano hierarchical structure prepared by electrodeposition," *Applied Surface Science*, vol. 256, no. 8, pp. 2400–2404, 2010.
- [14] L. Cao, A. K. Jones, V. K. Sikka, J. Wu, and D. Gao, "Anti-icing superhydrophobic coatings," *Langmuir*, vol. 25, no. 21, pp. 12444–12448, 2009.
- [15] A. B. D. Cassie and S. Baxter, "Wettability of porous surfaces," *Transactions of the Faraday Society*, vol. 40, pp. 546–551, 1944.
- [16] Y. Lai, X. Gao, H. Zhuang, J. Huang, C. Lin, and L. Jiang, "Designing superhydrophobic porous nanostructures with tunable water adhesion," *Advanced Materials*, vol. 21, no. 37, pp. 3723–3803, 2009.
- [17] X. Y. Liu, "A new kinetic model for three-dimensional heterogeneous nucleation," *Journal of Chemical Physics*, vol. 111, no. 4, pp. 1628–1635, 1999.

Research Article

Design and Evaluation of a Three Dimensionally Ordered Macroporous Structure within a Highly Patterned Cylindrical Sn-Ni Electrode for Advanced Lithium Ion Batteries

Yongcheng Jin, Hirokazu Munakata, Naoya Okada, and Kiyoshi Kanamura

Department of Applied Chemistry, Graduate School of Urban Environmental Sciences, Tokyo Metropolitan University, 1-1 Minami-ohsawa, Hachioji, Tokyo 192-0397, Japan

Correspondence should be addressed to Kiyoshi Kanamura; kanamura@tmu.ac.jp

Received 12 January 2013; Accepted 1 April 2013

Academic Editor: Huijun Wu

Copyright © 2013 Yongcheng Jin et al. This is an open access article distributed under the Creative Commons Attribution License, which permits unrestricted use, distribution, and reproduction in any medium, provided the original work is properly cited.

A 3-dimensionally ordered macroporous (3DOM) structure within a highly patterned cylindrical Sn-Ni alloy electrode was tailored by using various monodispersed polystyrene (PS) templates via a colloidal crystal templating process coupled with an electroplating process. The pore size and the wall thickness in the “inverse opal” 3DOM structure were increased with increasing the size of the PS template beads used in this study. The electrochemical performance of prepared electrodes was examined in order to reveal the correlation between the rate capability and the 3DOM structure. Except the electrode with 1.2 μm pores, the discharge capacities gradually decreased with increasing the current density, showing a capacity conservation ratio of 87% for the electrode with 0.5 μm pores and that of 84% for the electrode with 3.0 μm pores when the current density increased from 0.05 mA cm^{-2} to 2.0 mA cm^{-2} . The reason for this difference is attributed to the fact that the wall thickness of less than 0.5 μm in the electrode with 1.2 μm pores has a short Li^+ diffusion distance in solid-state walls. In addition, it is expected that high regularity of 3DOM structure plays a great role on rate capability. Consequently, the 3DOM structure prepared from 1.2 μm PS template beads was favorable for improving the rate capability.

1. Introduction

Lithium ion batteries (LIBs) are now the predominant power sources for portable electronic devices and their performance needs to be increased to meet the energy and power density requirements for transportation systems [1, 2]. Accordingly, great efforts have been focused on developing alternative materials to component materials used in commercialized LIBs, like lithium alloying materials to carbonaceous negative electrode which has the theoretical capacity limitation of 372 mA h g^{-1} lacking for further increasing the energy density and power performance of advanced LIBs [3–5]. Among the negative electrode materials under developing, Sn-based Li alloying materials, one of the most promising candidates for carbonaceous materials, have received much attention and widely examined because of their moderate capacity ($\text{Li}_{4.4}\text{Sn}$: 994 mA h g^{-1}), low potential of about 0.4 V *versus* Li/Li^+ , and

low toxicity [6–8]. Meanwhile, the negative electrodes based on Sn materials also suffer from some fatal problems, like the mechanical instability and poor cycle stability, which were caused by the electrode volume expansion during charge-discharge cycling resulting in the loose contact between active materials and current collector [9–12]. In order to overcome these problems, great efforts have been devoted to design and fabricate Sn-based materials and electrode structures in atomic, submicron, and macro scales.

In the atomic level approaches, many attempts have been made to develop Sn-based alloying materials, including Cu-Sn [9], Ni-Sn [10, 11], and Co-Sn [12]. These materials can be abbreviated as M_xSn_y , in which M presents Li-inactive element acting as an appropriate buffering matrix for Sn. Giving an overview of them, an alleviation of fatal capacity fade of Sn-based electrodes due to the electrode volume expansion during the charge-discharge process has been achieved more

or less by controlling the composition of alloying materials [3, 6, 9–12]. In addition to absorbing stress in atomic scale, the alleviation of volume expansion of Sn-based electrodes was also attempted by using submicron scale materials, including fine sized particles with spherical shape, nanowire arrays and materials with microporous structure [13–16]. In particular, materials with microporous structure provide not only the inner space required for nearly free volume expansion but also a large electrochemical interface for Li^+ insertion and extraction. However, electrodes with such a micro-porous structure also seem to be insufficient to suppress cracking appearance on the electrode surface caused by the volume change during charge-discharge process [15, 16]. On the other hand, the cracking phenomenon observed on the electrode surface has also guided to develop a technique for preparing a highly patterned electrode in macro scale with microporous structures [17, 18].

In our previous work, we have proposed a novel electrode which can relax the volume expansion stress by integrating atomic level buffering effects, microporous structures, and macro patterned electrodes mentioned above. The electrode consists of a highly patterned Ni-Sn alloy anode with a 3 dimensionally ordered macroporous (3DOM) structure and has achieved not only high mechanical stability but also high area capacity [18]. The macrosized electrode pattern and the 3DOM structure have been successfully tailored by using photoresist substrate and monodispersed polystyrene (PS) template beads, respectively. The detailed mechanism of how the macrosized pattern and the 3DOM structure influence the mechanical stability is under exploring. On the other hand, the 3DOM structure effects on the rate performance of electrode have not been discussed concretely.

From the viewpoint of LIBs performance, the rate capability of the noble electrode mentioned above is mainly ascribed to 3DOM structure, including the pore size, interconnecting window size, and wall thickness, and subsequently using the mono-dispersed PS beads with different diameter can easily control the 3DOM structure. In the present study, we use several mono-dispersed PS beads with different diameters to design and control a 3DOM structure in a highly patterned cylindrical Ni-Sn alloy electrode, and then we examine the effect of the 3DOM structure on the rate capability of the highly patterned electrode for advanced LIBs.

2. Experimental Methods

2.1. Material Fabrication. Highly patterned Ni-Sn alloy electrodes with a 3DOM structure were prepared by using a colloidal crystal templating process coupled with an electroplating process on a flexible Cu current collector patterned with photoresist substrate. The substrate, whose pattern shape is cylinder, was supplied from Tokyo Ohka Kogyo Co., Ltd., and its SEM image can be found elsewhere [17]. The as-supplied photoresist substrate was prepared on the flexible Cu current collector, and the highly patterned cylindrical hole is with $20\ \mu\text{m}$ in diameter and $20\ \mu\text{m}$ in thickness. The estimated open hole ratio was about 54%.

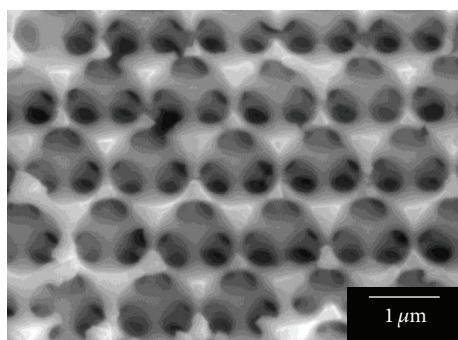
The monodispersed polystyrene (PS) latex with beads of 0.5, 1.2 and $3.0\ \mu\text{m}$ in diameter was used to fabricate colloidal crystal templates, respectively (Seradyn Inc.). The PS bead electrophoretic-deposition in holes of the photoresist substrate was conducted under an electric field of $5\ \text{V cm}^{-1}$ for 20 min. Then, heat treatment was carried out at 100°C for 8 min to interconnect the PS beads with the neighbors. Before electroplating Ni-Sn component, the wettability of the PS templates within the photoresist substrate was needed to improve by immersing into a 20 vol% ethanol aqueous solution for 20 s. Without immersion in the ethanol aqueous solution, the plating solution with the alloy component did not penetrate the PS template well. Ni-Sn alloy was electroplated into the interstices of the PS template in the plating solution containing $0.075\ \text{mol dm}^{-3}$ $\text{NiCl}_2\cdot 6\text{H}_2\text{O}$, $0.175\ \text{mol dm}^{-3}$ $\text{SnCl}_2\cdot 2\text{H}_2\text{O}$, $0.5\ \text{mol dm}^{-3}$ $\text{K}_4\text{P}_2\text{O}_7$, and $0.125\ \text{mol dm}^{-3}$ glycine. The pH of the plating solution was controlled to 8.9 using 26% NH_4OH solution. The electroplating was performed under constant current conditions of $1.75\ \text{mA cm}^{-2}$ at 50°C for 44 min using an automatic polarization system (HSV-100, Hokuto Denko Corp.). After electroplating, the electrode was immersed into acetone to remove the photoresist substrate and then put into toluene to eliminate the PS template. At last, an Ni-Si alloy electrode with an inverse-opal porous structure and a given alloying composition was obtained.

2.2. Characterizations. Composition of plated Ni-Sn alloy was determined by X-ray fluorescence (XRF, ZSX, RIGAKU). The morphology of prepared Ni-Sn alloy electrodes was observed using a scanning electron microscope (SEM, JSM-5310, JEOL). Crystallographic structures were characterized by X-ray diffraction (XRD, RINT-2000, RIGAKU) with Cu K α radiation.

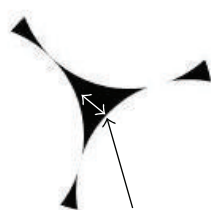
An electrochemical performance of an electrode prepared with Ni-Sn alloy was characterized by charge and discharge test using an automatic charge-discharge instrument (HJ1001SM8A, HOKUTO DENKO). The Sn-Ni alloy was set in 2032 coin cell with a mixture of ethylene carbonate and diethyl carbonate (volume ratio = 1 : 1) containing $1\ \text{mol dm}^{-3}$ LiClO_4 as an electrolyte and with Li metal as a counterelectrode. A charge process (Li^+ insertion into Ni-Sn alloy) was performed under the constant current-constant voltage (CC-CV) mode, charging at a various constant current density from $0.05\ \text{mA cm}^{-2}$ to $2.0\ \text{mA cm}^{-2}$ until 0 V versus Li/Li^+ , then charging at a constant voltage of 0 V until charge capacity reached $600\ \text{mA h g}^{-1}$. A discharge process (Li^+ extraction from Sn-Ni alloy) was carried out at a constant current with the same value in charging process. Cutoff voltages of charge and discharge processes were 0 and 2.5 V, respectively. All the electrochemical measurements were carried out at 30°C .

3. Results and Discussion

3.1. General Considerations about Electrochemical Performance and Porous Structures. Generally, for porous electrodes as shown in Figure 1(a), its electrochemical performance is mainly determined by the porous architecture, including



(a)



Li ion diffusion distance

(b)

FIGURE 1: SEM image of a 3 dimensionally ordered macroporous electrode prepared with $1.2\ \mu\text{m}$ beads (a). (b) Is a schematic illustration of porous structures including walls and interconnecting windows.

pores, interconnecting windows, and walls [19]. For example, the small pore sizes are related to the large surface area available for the electrochemical reaction, relatively big sizes of interconnecting window will favor the Li^+ diffusion through electrolyte, and the thin wall thickness will benefit the solid-state Li^+ diffusion. It should be noted that appropriate interconnecting window size and thinner walls are advantageous at high discharge rate, but not at low rates, when kinetic limitations are less important [19]. On the other hand, there is a difficulty tuning these factors mentioned above for preparing desired electrodes with high performance. In this study, we focused on the Li^+ diffusion distance through solid-state walls to design the wall thickness with different monodispersed PS template beads. A schematic illustration of a feasible correlation between the rate performance and the wall thickness is presented in Figure 2.

3.2. Properties of Prepared Ni-Sn Alloy Electrodes. The top views of Ni-Sn alloy electrodes with a 3DOM structure are presented in Figure 3. In all cases, a highly patterned cylindrical electrode was electrodeposited on the substrate with good reflection of photoresist morphology, as shown in Figures 3(a), 3(c), and 3(e). These SEM images also revealed the formation of the 3DOM structures and those pore sizes highly reflected the PS beads in different diameters used.

Besides the pore morphology in 3DOM structure, a highly ordered interconnect window and wall structure was also confirmed from Figures 3(b), 3(d), and 3(f). The sizes of pore, interconnect window, and wall thickness were increased with increasing the size of PS beads used as colloidal crystal template. Typically, by using particles with different diameter as the template, the wall thickness between macropores can be controlled to about $0.17\ \mu\text{m}$ for the electrode using $0.5\ \mu\text{m}$ PS beads, $0.45\ \mu\text{m}$ for the electrode using $1.2\ \mu\text{m}$ PS beads, and $1.0\ \mu\text{m}$ for the electrode using $3.0\ \mu\text{m}$ PS beads, respectively. It has been reported that a $0.5\ \mu\text{m}$ thick Ni-Sn thin film electrode has a large specific capacity and long cycle life [10]. With regard to the Li^+ diffusion distance and volume change, the wall thickness less than $0.5\ \mu\text{m}$ may be favorable for high rate capability of LIBs.

In all cases, a similar XRD pattern is observed for Ni-Sn alloy electrodes with different 3DOM structures. Figure 4 shows the typical XRD pattern of the photoresist substrate and the electrodeposited Ni-Sn alloy electrode. The XRD peaks were attributed to Ni_3Sn_4 , NiSn, and Cu substrate [12]. It was confirmed that Ni_3Sn_4 is the predominant phase in the microporous electrode and NiSn is small enough to be neglected. Moreover, XRF analysis was conducted to confirm the composition of the electro-deposited Ni-Sn alloy electrode and its results revealed that the atomic ratio of Ni/Sn was ca. 40/60 in all cases. Mukaibo et al. studied the effect of composition of the Ni-Sn thin film electrode on electrochemical properties. The thin film containing Sn of 62 atom% showed the highest reversible capacity [10, 11]. Ni-Sn alloy electrodes prepared in this study were close to their best composition. Therefore, one can expect that the difference in the electrochemical performance of electrodes prepared in this study is mainly attributed to 3DOM structures which were controlled by using different PS beads.

3.3. Electrochemical Performance of Prepared Ni-Sn Alloy Electrodes with Different 3DOM Structures. For electrochemical evaluation of prepared electrodes, we conducted charge-discharge measurements under given conditions. Figure 5 demonstrates the first discharge curves of highly patterned cylindrical Ni-Sn alloy electrode with 3DOM structure at different current density. In all cases, the discharge curves showed a plateau potential around $0.4\ \text{V}$ versus Li/Li^+ , indicating that the delithiation process from Sn in the Ni-Sn alloy electrode smoothly occurred. The gravimetric capacity during the first discharge cycle at the current density of $0.05\ \text{mA cm}^{-2}$ was $450\ \text{mA h g}^{-1}$ for the electrode using $0.5\ \mu\text{m}$ beads, $520\ \text{mA h g}^{-1}$ for the electrode using $1.2\ \mu\text{m}$ beads, and $595\ \text{mA h g}^{-1}$ for the electrode using $3.0\ \mu\text{m}$ beads, respectively. Besides the electrode with $1.2\ \mu\text{m}$ pores as shown in Figure 5(b), the discharge capacities gradually decreased as increasing the discharge current density (Figures 5(a) and 5(c)), showing the capacity conservation ratio of 87% for the electrode with $0.5\ \mu\text{m}$ pores and that of 84% for the electrode with $3.0\ \mu\text{m}$ pores when discharge current density increased from $0.05\ \text{mA cm}^{-2}$ to $2.0\ \text{mA cm}^{-2}$. The dependence of discharge capacity conservation ratio on the rate capability

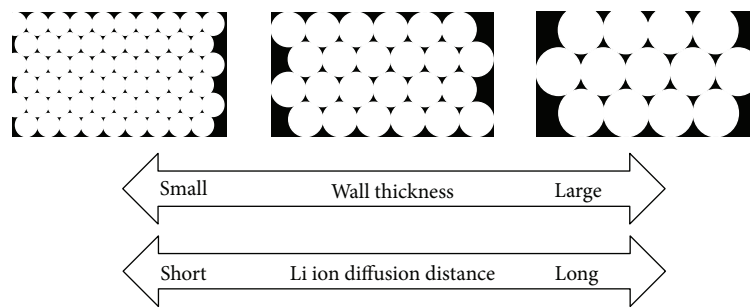


FIGURE 2: Schematic illustration of correlation between 3DOM structure and rate performance.

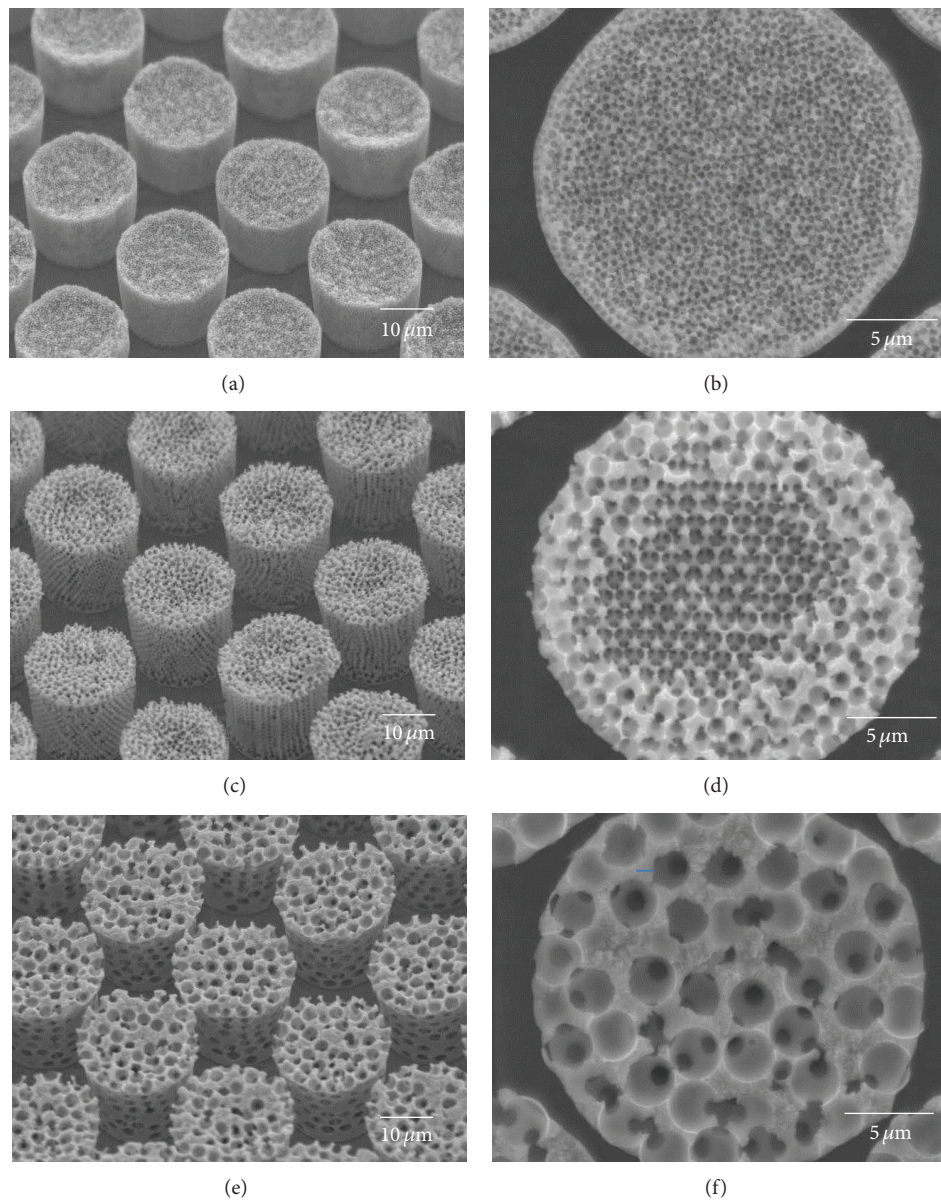


FIGURE 3: SEM images of 3DOM Ni-Sn alloy electrode with 0.5 μm pores (a) and (b), 1.2 μm pores (c) and (d), and 3.0 μm pores (e) and (f), respectively.

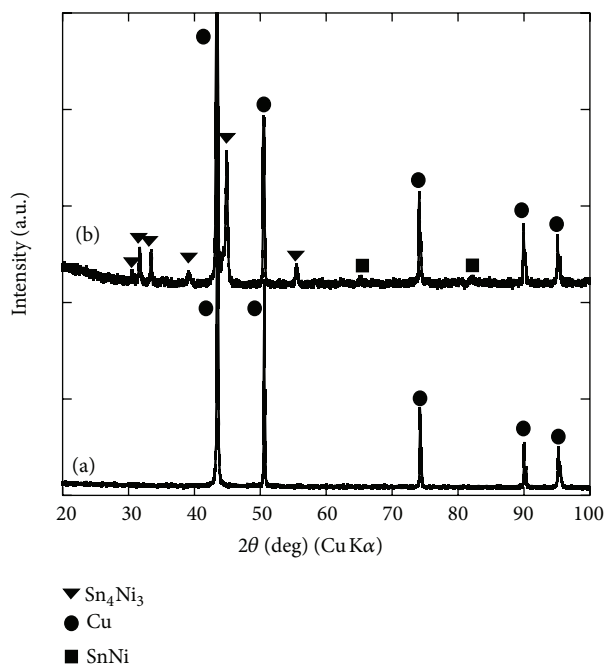


FIGURE 4: A typical XRD pattern of (a) as-prepared photoresist substrate and (b) highly patterned cylindrical Ni-Sn alloy with 3 dimensionally ordered macroporous structure.

would be attributed to different 3DOM structures. One of the reasons for this is attributed to the fact that the wall thickness is less than $0.5\ \mu\text{m}$ in the electrode. This threshold applies to the electrodes prepared with $0.5\ \mu\text{m}$ and $1.2\ \mu\text{m}$ PS beads. However, good rate capability was observed only for the electrode with $1.2\ \mu\text{m}$ pores. In detailed comparison of their 3DOM structures shown in Figures 3(b) and 3(d), it is also found that the electrode with $1.2\ \mu\text{m}$ pores has a higher regularity in pore distribution than $0.5\ \mu\text{m}$ -pored one. A higher regularity of electrode structure basically provides a more uniform current distribution that goes with better rate capability. Therefore, a good rate capability observed for $1.2\ \mu\text{m}$ -pored electrode is expected to be due to highly ordered structure as well as thin wall of 3DOM Ni-Sn.

4. Conclusion

Highly patterned cylindrical Ni-Sn alloying electrodes with 3 dimensionally ordered macroporous (3DOM) structures were successfully prepared by using colloidal crystal templating process coupled with electroplating process. The 3DOM structure was tailored with various polystyrene (PS) beads. Scanning electron microscopy observations revealed that the pores size in 3DOM structure is in good agreement with the size of PS template and the wall thickness is increased with increasing the size of PS beads used. The discharge curves of prepared electrodes with different wall thickness and pore regularity showed the 3DOM structure with $1.2\ \mu\text{m}$ pores is most favored for the rate capability of the prepared electrode.

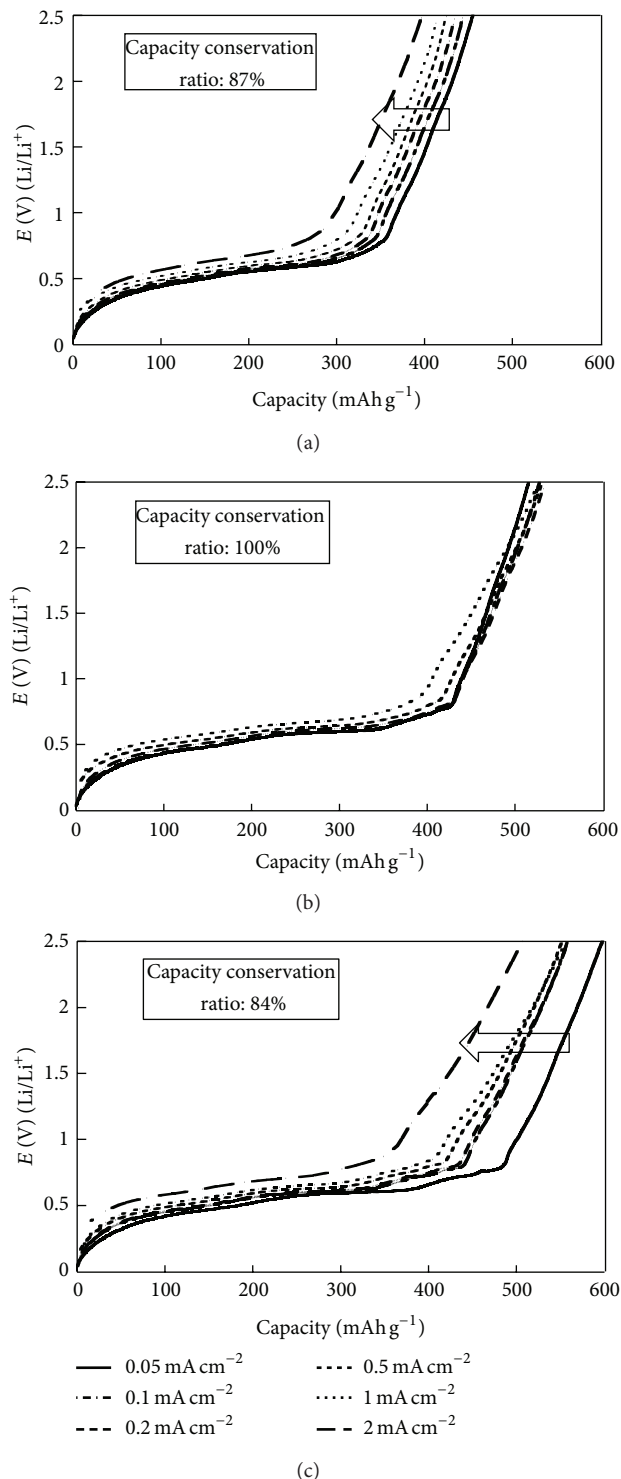


FIGURE 5: Rate performances of 3DOM Ni-Sn alloy electrode with (a) $0.5\ \mu\text{m}$ pores, (b) $1.2\ \mu\text{m}$ pores and (c) $3.0\ \mu\text{m}$ pores, respectively.

Acknowledgments

This work was partially supported by “Development of High performance Battery System for Next-generation Vehicles Project” from the New Energy and Industrial Technology Development Organization (NEDO) of Japan. The authors

especially thank Tokyo Ohka Kogyo Co., Ltd. for their help in preparing photoresist substrates.

References

- [1] B. Scrosati and J. Garche, "Lithium batteries: status, prospects and future," *Journal of Power Sources*, vol. 195, no. 9, pp. 2419–2430, 2010.
- [2] A. S. Aricò, P. Bruce, B. Scrosati, J. M. Tarascon, and W. Van Schalkwijk, "Nanostructured materials for advanced energy conversion and storage devices," *Nature Materials*, vol. 4, no. 5, pp. 366–377, 2005.
- [3] W. J. Zhang, "A review of the electrochemical performance of alloy anodes for lithium-ion batteries," *Journal of Power Sources*, vol. 196, no. 1, pp. 13–24, 2011.
- [4] A. K. Shukla and T. P. Kumar, "Materials for next-generation lithium batteries," *Current Science*, vol. 94, no. 3, pp. 314–331, 2008.
- [5] M. Winter, J. O. Besenhard, M. E. Spahr, and P. Novák, "Insertion electrode materials for rechargeable lithium batteries," *Advanced Materials*, vol. 10, no. 10, pp. 725–763, 1998.
- [6] R. A. Huggins, "Lithium alloy negative electrodes," *Journal of Power Sources*, vol. 81–82, no. 1, pp. 13–19, 1999.
- [7] M. Winter and J. O. Besenhard, "Electrochemical lithiation of tin and tin-based intermetallics and composites," *Electrochimica Acta*, vol. 45, no. 1, pp. 31–50, 1999.
- [8] D. Larcher, S. Beattie, M. Morcrette, K. Edström, J. C. Jumas, and J. M. Tarascon, "Recent findings and prospects in the field of pure metals as negative electrodes for Li-ion batteries," *Journal of Materials Chemistry*, vol. 17, no. 36, pp. 3759–3772, 2007.
- [9] M. M. Thackeray, J. T. Vaughey, A. J. Kahaian, K. D. Kepler, and R. Benedek, "Intermetallic insertion electrodes derived from NiAs-, Ni₂In-, and Li₂CuSn-type structures for lithium-ion batteries," *Electrochemistry Communications*, vol. 1, no. 1, pp. 111–115, 1999.
- [10] H. Mukaibo, T. Sumi, T. Yokoshima, T. Momma, and T. Osaka, "Electrodeposited Sn-Ni alloy film as a high capacity anode material for lithium-ion secondary batteries," *Electrochemical and Solid-State Letters*, vol. 6, no. 10, pp. A218–A220, 2003.
- [11] H. Mukaibo, T. Momma, and T. Osaka, "Changes of electrodeposited Sn-Ni alloy thin film for lithium ion battery anodes during charge discharge cycling," *Journal of Power Sources*, vol. 146, no. 1–2, pp. 457–463, 2005.
- [12] N. Tamura, M. Fujimoto, M. Kamino, and S. Fujitani, "Mechanical stability of Sn-Co alloy anodes for lithium secondary batteries," *Electrochimica Acta*, vol. 49, no. 12, pp. 1949–1956, 2004.
- [13] S. H. Ju, H. C. Jang, Y. C. Kang, and D. W. Kim, "Characteristics of Sn-Ni alloy powders directly prepared by spray pyrolysis," *Journal of Alloys and Compounds*, vol. 478, no. 1–2, pp. 177–180, 2009.
- [14] M. Tian, W. Wang, S. Lee, Y. Lee, and R. Yang, "Enhancing Ni-Sn nanowire lithium-ion anode performance by tailoring active/inactive material interfaces," *Journal of Power Sources*, vol. 196, no. 23, pp. 10207–10212, 2011.
- [15] H. R. Jung, E. J. Kim, Y. J. Park, and H. C. Shin, "Nickel-tin foam with nanostructured walls for rechargeable lithium battery," *Journal of Power Sources*, vol. 196, no. 11, pp. 5122–5127, 2011.
- [16] K. Nishikawa, K. Dokko, K. Kinoshita, S. W. Woo, and K. Kanamura, "Three-dimensionally ordered macroporous Ni-Sn anode for lithium batteries," *Journal of Power Sources*, vol. 189, no. 1, pp. 726–729, 2009.
- [17] S. W. Woo, N. Okada, M. Kotobuki et al., "Highly patterned cylindrical Ni-Sn alloys with 3-dimensionally ordered macroporous structure as anodes for lithium batteries," *Electrochimica Acta*, vol. 55, no. 27, pp. 8030–8035, 2010.
- [18] M. Kotobuki, N. Okada, and K. Kanamura, "Design of a micro-pattern structure for a three dimensionally macroporous Sn-Ni alloy anode with high areal capacity," *Chemical Communications*, vol. 47, no. 21, pp. 6144–6146, 2011.
- [19] A. Vu, Y. Qian, and A. Stein, "Porous electrode materials for lithium-ion batteries—how to prepare them and what makes them special," *Advanced Energy Materials*, vol. 2, no. 9, pp. 1056–1085, 2012.

Research Article

Effect of the Flow Channel Structure on the Nanofiltration Separation Performance

Zhi Chen, Ben Zhao, Fanglei Chen, and Jianming Li

School of Chemical Engineering, Sichuan University, Sichuan 610065, China

Correspondence should be addressed to Jianming Li; lijianming@scu.edu.cn

Received 27 January 2013; Accepted 20 March 2013

Academic Editor: Yongcheng Jin

Copyright © 2013 Zhi Chen et al. This is an open access article distributed under the Creative Commons Attribution License, which permits unrestricted use, distribution, and reproduction in any medium, provided the original work is properly cited.

Two kinds of newly designed feed channels, for example, a spiral and a serpentine feed channels, for a bench-scale nanofiltration module were developed to improve the filtration performance. The experiments were carried out with the modules using a commercial flat NF membrane to investigate the effects of Reynolds number (Re) and flow channel structures on the flux of permeate and Mg^{2+} rejection. It was shown from the experimental results that although the effects of Reynolds number on fluxes were not obvious for the two new feed channels compared with a normal flow channel structure, the Mg^{2+} rejections varied apparently with Re. The Mg^{2+} rejections were almost the same for the modules with two new feed channels and larger than that for the module with normal feed channel. The numerical simulations of fluid flow in the three kinds of feed channels were completed at Re of 4800 to explain the phenomena. The results demonstrated that there was a secondary flow in both new feed channels, which strongly influences the Mg^{2+} rejection. The rejection increased with increasing average shear stress at the membrane wall. The spiral feed channel was the best one among the flow channel structures investigated.

1. Introduction

Nanofiltration is an intermediate filtration process between reverse osmosis (RO) and ultrafiltration (UF) that rejects molecules having a size of about one nanometer [1]. It has been introduced since 1980s, mainly used for softening water and removing organics. It has found many applications in various water purification and treatment as well as product separation processes because of its two remarkable features: one is the molecular weight cut-off (MWCO) which ranges from 200 to 2000 Da; the other is the separation of electrolytes due to the membrane materials containing charged groups [2, 3]. Lots of studies on NF membrane have been carried out based on these features in the recent years, and it becomes the emphasis how to improve its separation performance.

The investigations mainly focus on two aspects: one is to develop new NF membrane materials with good separation performance; another is to improve operation conditions of NF process based on separation mechanism and modeling. Ba et al. fabricated stable NF membrane by chemical modification of P84 copolyimide asymmetric membranes using branched polyethylenimine (PEI) [4]. The membrane could

be used in severe operating environments including high temperature (100°C) and organic solvents. Jahanshahi et al. prepared two kinds of polymer composite NF membranes, that is, poly(piperazine-amide) and poly(vinyl alcohol) NF membranes, with good stability of structure and performance through a series of experiments [5]. Abu Seman et al. used the hydrophilic anionic monomer acrylic acid and the immersion method to modify a commercial polyethersulfone NF membrane by UV-initiated graft polymerization technique [6]. The membranes showed lower fouling tendency than the unmodified membrane. Ballet et al. studied experimentally the effects of feed pressure, ionic strength, concentration, and pH on the retention of phosphate anions [7]. Li et al. investigated the effects of pressure, flow rate on flux, and retention in seawater desalination process [8]. Pang carried out a research on the influences of pressure, temperature, influent flow, and pH on flux and desalination rate for the application of wastewater treatment in salt chemical plant [9]. Darvishmanesh et al. developed a new semiempirical model based on the traditional solution diffusion with imperfection model for solvent resistant nanofiltration [10]. The new model demonstrated a good prediction for the flux of solvent

through the nanofiltration. Fadaei et al. developed a mass transfer model to predict ion transport through the NF membrane account for the concentration polarization phenomenon and its influence on the ion separation [11]. They solved model equations numerically using computational fluid dynamics (CFD) techniques and successfully predicted the local concentration of ions, permeate flux, and rejection of ions in a rectangular crossflow NF membrane module. Wang et al. review the research progresses on the evaluation of pore structure and electrical property, the separation mechanism and modeling, and the electrokinetic phenomena of the NF membranes over the past two decades [12].

Furthermore, there have been investigations of flow patterns and mass transfer in NF membrane module channels using fluid dynamics for recent years [11, 13–17]. The wall shear stress could be increased by placing flow-aligned spacers [13, 17] or feed spacers [15] or utilizing vibration [14] to increase the filtration performances. However, there were few studies aiming at the influence of flow channel structures of membrane modules on the separation performance of NF membrane.

In this article, a bench-scale modules, with two kinds of new designed flow channel structures, that is, a spiral flow channel and a serpentine flow channel ones as well as a normal one, were used for experiments in order to investigate the flux and Mg^{2+} rejection of a commercial NF membrane by changing flow pattern from laminar to turbulent flow regime in the flow channel. Moreover, the numerical simulations of fluid flow in the modules with the three kinds of feed channels were completed at Reynolds number of 4800 terms of CFD techniques to observe the effects of secondary flow in curved flow duct and wall shear stress on Mg^{2+} rejection.

2. Numerical Simulation

2.1. Dean Vortex. A couple of reverse symmetric vortices which are named Dean vortex [18] generate because of secondary flow formed by centrifugal force when incompressible fluid flows in curved flow duct because the fluid in the faster core, as a result of centrifugal effects, is directed outward and, in order to satisfy continuity, the slower fluid near the boundaries is directed inward. The disturbance on membrane surface enhanced by Dean vortex will hinder concentration polarization development and membrane fouling effectively in the membrane separation process. Dean pointed out that Dean vortex generate as the result of the interaction of centrifugal force with viscous force borne by fluid in the pipe; thus, a dimensionless number which is called Dean number is defined as the ratio of centrifugal force to viscous force [19]. Fluid falls into unstable state when Dean number is above a critical value. In this paper, the numerical simulation of secondary flow was completed based on CFD technology in order to investigate the effects of Dean vortex on the flux and salt rejection.

2.2. Governing Equations. There are swirling flows when fluid flows in curved duct, such as spiral flow channel and the serpentine flow channel, in the module. Therefore, realizable

k - ε turbulence model was employed to simulate secondary flows, and empirical constants C_μ and C_1 in standard k - ε model were supposed as variables. Water was used as fluid medium in the numerical simulation. For isothermal, incompressible, Newtonian, and a steady-state flow, the governing equations, consisting of continuity equation, momentum equation, turbulent kinetic energy (k) equation, and turbulent dissipation rate (ε) equation, may be written as follows [20, 21]:

$$\begin{aligned} \frac{\partial u_i}{\partial x_i} &= 0 \\ \frac{\partial}{\partial x_j} (\rho u_j u_i) &= -\frac{\partial p}{\partial x_i} + \frac{\partial}{\partial x_j} \left[(\mu + \mu_t) \left(\frac{\partial u_j}{\partial x_i} + \frac{\partial u_i}{\partial x_j} \right) \right] + \rho g_i, \end{aligned} \quad (1)$$

where ρ is the liquid density, u is the liquid velocity, μ is the dynamic viscosity, p is the pressure, g is the acceleration of gravity, and μ_t is the turbulent dynamic viscosity expressed as follows:

$$\mu_t = C_\mu \rho \frac{k^2}{\varepsilon}, \quad (2)$$

$$C_\mu = \frac{1}{A_0 + A_s U^* k / \varepsilon},$$

$$\begin{aligned} \frac{\partial}{\partial x_j} (\rho u_j k) &= \frac{\partial}{\partial x_j} \left[\left(\mu + \frac{\mu_t}{\sigma_k} \right) \times \frac{\partial k}{\partial x_j} \right] + G_k - \rho \varepsilon, \\ \frac{\partial}{\partial x_j} (\rho \varepsilon u_j) &= \frac{\partial}{\partial x_j} \left[\left(\mu + \frac{\mu_t}{\sigma_\varepsilon} \right) \times \frac{\partial \varepsilon}{\partial x_j} \right] \\ &\quad + \rho C_1 S \varepsilon - \rho C_2 \frac{\varepsilon^2}{k + \sqrt{\nu \varepsilon}}, \end{aligned} \quad (3)$$

where the model constants are $\sigma_k = 1.0$, $\sigma_\varepsilon = 1.2$, $C_2 = 1.90$, and

$$C_1 = \max \left[0.43, \frac{\eta}{\eta + 5} \right]. \quad (4)$$

2.3. Model Geometry. The membrane module used in experiments and numerical simulations was a conventional cross-flow filtration one that had a flat circular cell with a feed chamber thickness of 14 mm and a diameter of 94 mm. Flange structure was adopted for the module to divide the cell into two sides, which was convenient for frequent dismounting and cleaning. The upside cell was used as a feed channel and the downside cell was used to place a NF membrane. There were three types of feed channels. The normal feed channel was the upside cell without any inner deflector to direct flow. The spiral feed channel and serpentine feed channel were formed by welding deflectors as shown in Figure 1.

There are three computational domains corresponding to the three types of the modules. One is the normal feed channel that consists of cylindrical cell, inlet pipe, and outlet

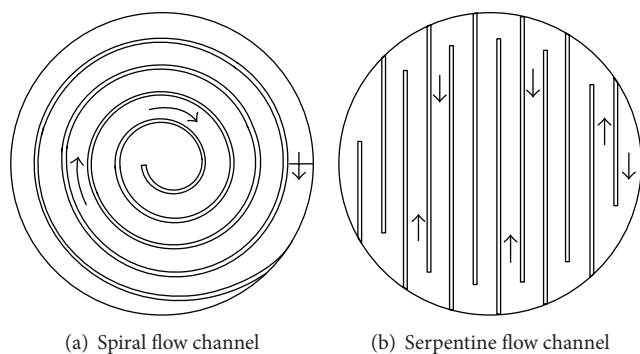


FIGURE 1: Feed channels in the upside cells of the NF membrane modules.

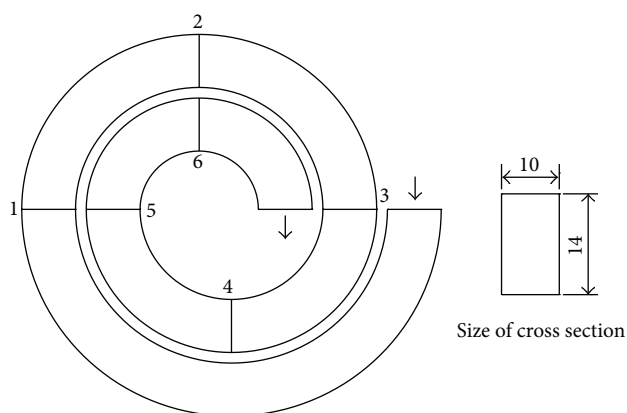


FIGURE 2: Schematic diagram of the model and section of the spiral flow channel.

pipe. The computational domain of the spiral feed channel, whose cross section size is $10\text{ mm} \times 14\text{ mm}$, is shown in Figure 2, and the computational domain of the serpentine feed channel is shown in Figure 3. The cross section size of the U-shaped duct is different from that of straight channel for the serpentine feed channel. The former is $15\text{ mm} \times 14\text{ mm}$, and the latter is $10\text{ mm} \times 14\text{ mm}$. The six cross sections are chosen to observe the velocity vector fields for both spiral and serpentine feed channels as shown in Figures 2 and 3.

2.4. Numerical Solution. The governing equations with the corresponding boundary conditions were numerically solved using FLUENT software. The software uses the finite volume method for numerical solution of model equations. The three-dimensional computational grid was generated using GAMBIT software package for each type of feed channel. The grid is an unstructured hexahedral grid with 261,203 grid points for the normal feed channel, 244,209 mesh nodes for the spiral feed channel, and 317,289 grid points for the serpentine feed channel. The consecutive simulations with the increasing number of grid points were performed until obtaining a grid-independent result. The pressure-velocity coupling SIMPLE scheme was used. The governing equations were discretized with the first-order upwind scheme. The operating temperature was of 35°C , and the channel Reynolds

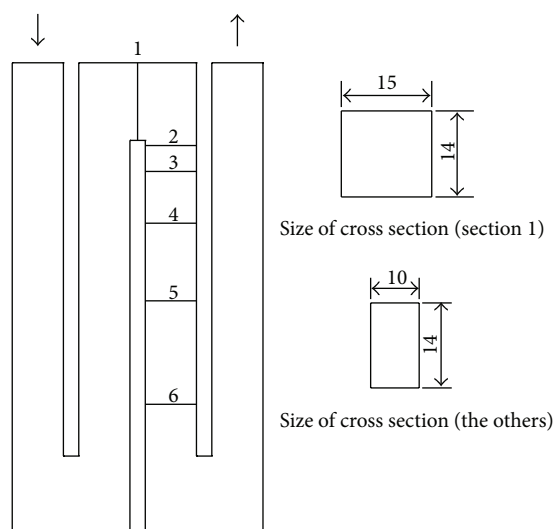


FIGURE 3: Schematic diagram of the model and sections of the serpentine flow channel.

number was 4800 in the numerical simulation. The inlet is rectangle pipe with the size of $10\text{ mm} \times 14\text{ mm}$ for each membrane module so that the inlet velocity of water could be of 0.301 m/s for the spiral feed channel or the serpentine feed channel and 0.707 m/s for the normal feed channel. Boundary conditions, such as velocity-inlet, out-flow, standard wall functions, stationary wall, and no slip conditions, were used in numerical simulation. The inlet turbulent intensity and hydraulic diameter were 2.84% and 12 mm , respectively. The numerical simulation would continue until a relative tolerance set is less than 10^{-6} .

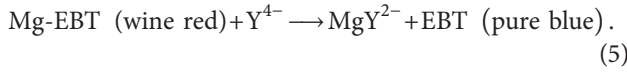
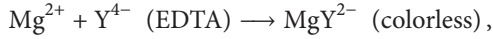
3. Experimental

3.1. Apparatus. Main apparatuses and instruments used in the experiments (as shown in Figure 4) included a vortex pump (WB25-72), two glass rotameters (LZB-15F and LZB-25F), an electronic balance (SL502N), a $1/10000$ electronic balance (FA1204B), and two pressure gauges with the grade of 1.6.

3.2. Membranes and Materials. The TFC-SR100 NF membrane was used in the experiments, and its molecular weight cut-off was about 200. Experimental reagents included ethylenediaminetetraacetic acid (EDTA), anhydrous alcohol ($0.789\text{--}0.791\text{ g/mL}$), pure ammonia, ammonium chloride (NH_4Cl), magnesium sulfate (MgSO_4), triethanolamine, and eriochrome black T. All of them are analytical grade and used as received.

3.3. Method for Measuring Mg^{2+} Concentration. The solution of magnesium sulfate, in which Mg^{2+} concentration is 150 ppm to simulate the water hardness of Yangtze River, was prepared with anhydrous magnesium sulfate and deionized water for NF experiments. EDTA complexometry [22] was used to measure Mg^{2+} concentration. The brief chemical

equations of indicator, complex, and terminal reactions are described, respectively, as



3.4. Nanofiltration Performance Tests. NF performance tests were conducted by a crossflow membrane module at different temperatures under different operating pressures, and the effective filtration area was 69.40 cm^2 . The test rig for nanofiltration is shown in Figure 4. At steady state, the weight of permeate collected in the triangular flask was measured by an electronic balance to calculate the total flux, J_v , as follows:

$$J_v = \frac{W}{A \cdot t}, \quad (6)$$

where W is the total mass permeated in the test time t and A is the effective area. The Mg^{2+} concentrations of feed and permeated samples were measured by the EDTA titration method for MgSO_4 solution to calculate the Mg^{2+} rejection, R_{obs} as follows:

$$R_{\text{obs}} = \frac{c_b - c_p}{c_b} \times 100\%, \quad (7)$$

in which c_b and c_p are the Mg^{2+} concentrations of feed and permeate, respectively.

In the experiment, feed solution in the feed tank was pumped to the membrane module by vortex pump. The permeate flowed through the membrane into the triangular flask, and the concentrate was then returned to feed tank. The operating pressure and crossflow velocity were kept constant by adjusting both the valve and the rotation speed of the pump. The temperature was regulated by controlling the flow rate of cooling water. Permeate flux was measured, and permeate sample collected at steady state that was assumed after 3 h of operation. The samples were analyzed in the method mentioned in Section 3.3. The volume of feed was of 5 L so that Mg^{2+} concentration of feed c_b might be constant because the volume of permeate was relatively small.

Firstly, membrane module with normal flow channel was selected to determine permeate fluxes of deionized water at various temperatures under pressures. The temperatures were set as 20°C , 25°C , 30°C , and 35°C , respectively. For the given temperature, the pressures were set as 0.15, 0.20, 0.25, 0.30, and 0.35 MPa, respectively. According to the collecting data, water permeability L_p of the membrane was calculated from (8) by omitting the term of osmotic pressure difference from the permeate flux equation [11] due to the deionized water used. Secondly, three types of flow channel structures including normal flow, spiral flow, and serpentine flow structures were employed in performance experiments. The permeate fluxes and Mg^{2+} rejections of the membrane were determined for laminar flow, transition flow,

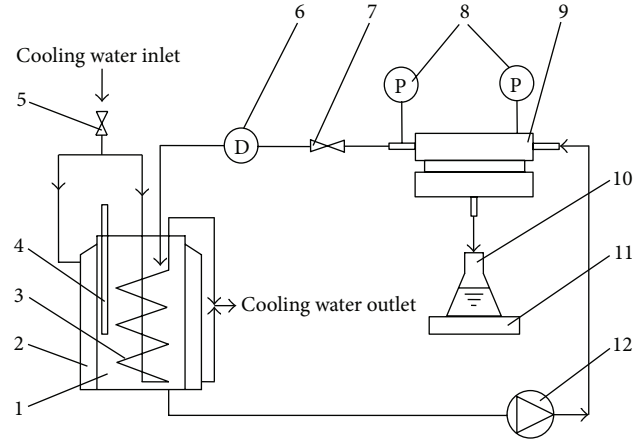


FIGURE 4: The test rig for nanofiltration performance. (1) Feed tank. (2) Coil pipe. (3) Jacket. (4) Thermometer. (5) Cooling water control valve. (6) Glass rotameter. (7) Flow control valve. (8) Pressure gauge. (9) Membrane module. (10) Triangular flask. (11) Electronic balance. (12) Vortex pump.

and turbulent flow under pressure of 0.35 MPa at temperature of 35°C . Reynolds numbers were of 1200, 1400, 1600, 1800, and 2000 for laminar flow, of 2500, 2800, 3100, 3400, and 3700 for transition flow, and were of 4000, 4200, 4400, 4600, and 4800 for turbulent flow, respectively:

$$L_p = \frac{\Delta p}{J_v}, \quad (8)$$

where Δp is the transmembrane pressure drop.

The crossflow rate q_v could be calculated from (9) for the spiral or serpentine feed channel module according to Reynolds number:

$$q_v = \frac{\text{Re} \mu A}{\rho d_h}, \quad (9)$$

where Re is Reynolds number; A the area of cross section; d_h is the hydraulic diameter. In the work, the hydraulic diameter was 11.67 mm for the spiral feed channel or the serpentine feed channel.

4. Results and Discussion

4.1. Water Permeability. Water permeability L_p was calculated based on the collecting data in order to investigate the stability of the NF membrane. Based on Hagen-Poiseuille equation, water permeability could also be given by [23]

$$L_p = \frac{r_p A_k}{8\mu\Delta x}, \quad (10)$$

where r_p is effective membrane pore radius, A_k is the membrane porosity, Δx is the effective membrane thickness, and μ is the solvent viscosity.

As shown in Figure 5, L_p would increase with increasing operating pressure at the given temperature and rise with

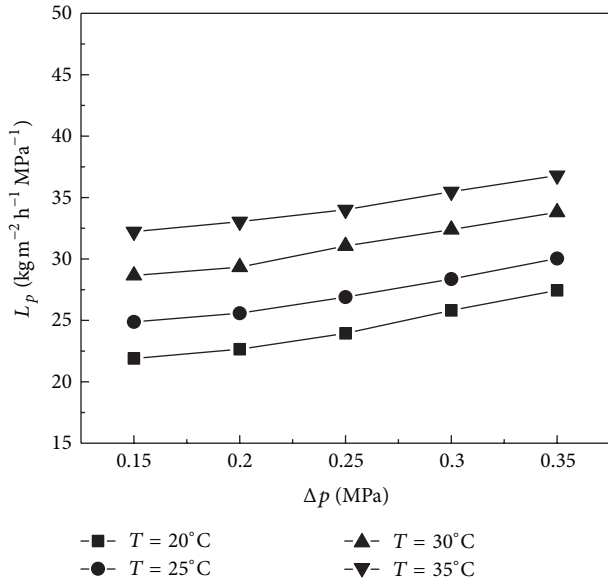


FIGURE 5: Effect of pressure on water permeability at different temperatures.

increasing operating temperature under the given operation pressure. According to Hagen-Poiseuille equation, L_p is only correlated to membrane structure parameters (r_p , A_k , and Δx) when μ keeps constant at a given temperature. On the one hand, Δx decreased if r_p and A_k kept constant when pressure increased because membrane was made up of organic polymer materials, which led to increasing L_p . On the other hand, water viscosity reduced and structure parameters of the membrane did not change when pressure kept constant and temperature rose, which resulted in increasing L_p .

In a word, water permeability of the polymer NF membrane would vary with the operating pressure and temperature. What is more, the operation temperature and pressure had obvious influences on membrane flux.

4.2. Effect of Reynolds Number. As shown in Figure 6, membrane flux varied slightly with the change of Reynolds number under the given conditions of operating pressure, temperature, and feed concentration, which was in good agreement with the idea that crossflow rate or Re had a little influence on membrane flux presented by Timmer et al. [24]. Meanwhile, Zhu and coworkers also concluded that membrane flux depended hardly on crossflow rate or Re number [25].

The flow pattern of the fluid varied from laminar flow to transition flow or even turbulence flow when Reynolds number increased due to the increase of crossflow rate. On the one hand, the curved flow channel structure hindered the concentration polarization development and the fouling of a membrane, which was helpful to improve membrane flux. On the other hand, the friction loss increased, pressure drop through the module became larger, and filtration driving force decreased with increasing crossflow rate, which went against to the above effect of increasing membrane flux. For

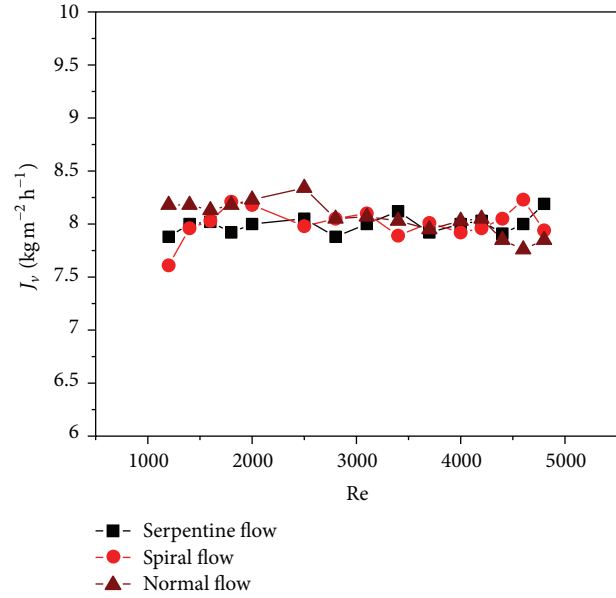


FIGURE 6: Effect of Reynolds number on flux.

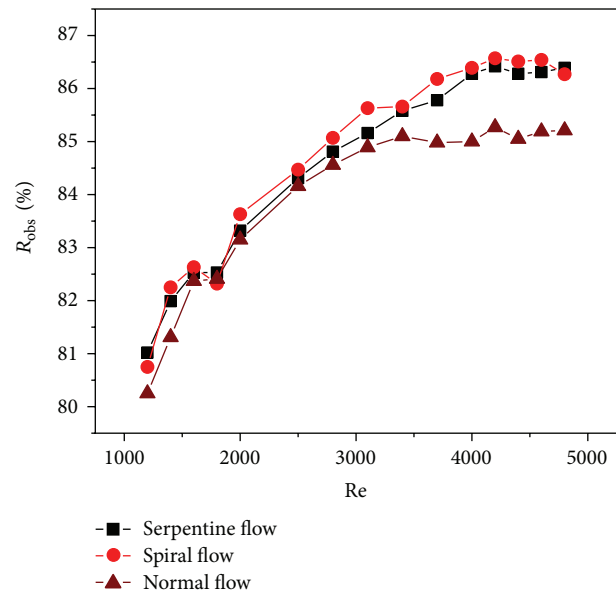


FIGURE 7: Effect of Reynolds number on Mg^{2+} rejection.

their comprehensive actions, the membrane flux kept nearly constant.

Figure 7 shows the relation of Reynolds number and Mg^{2+} rejection. As for the three types of flow channel structures, Mg^{2+} rejection had a significant increasing trend with the rising Reynolds number, which was in a good agreement with the conclusion that the increase of influent flow made ion rejection rise which is summarized by Liu [26]. It was also shown from the results that the rejection kept almost constant for all modules for turbulent flow so that the Reynolds number might hardly influence the rejection when Re was larger than 4000 under the experimental conditions.

According to the extended Nernst-Planck equation, permeation flux of solute consists of the diffusion flux, the Donnan potential flux, and the convection flux. In the experiments, the flux caused by Donnan potential almost kept constant due to the low feed Mg^{2+} concentration; so diffusion and convection played important roles on flux of Mg^{2+} . Convective mass transfer refers to that Mg^{2+} will be transferred to permeate side when feed solution flows through membrane pore. The flux of feed solution is the main influence factor. The larger the flux is, the stronger the convective mass transfer is and the more Mg^{2+} was brought through the membrane with the feed solution which results in decreasing rejection, and vice versa, Mg^{2+} rejection will increase. Diffusion mass transfer refers to that Mg^{2+} diffuses from feed side to permeate side because of the Mg^{2+} concentration difference across the membrane. Mg^{2+} concentration on the membrane surface played the key role. The higher the solute concentration on membrane surface is, the larger the diffusion transfer driving force is and the more Mg^{2+} would diffuse through membrane pores so that the rejection might decrease, and vice versa, Mg^{2+} rejection would increase. The solution turbulence would disturb the concentration boundary layer, force the solute to move back to the bulk flow, and finally lower the Mg^{2+} concentration on the membrane surface, which leads to reducing diffusion mass transfer rate and increasing rejection.

4.3. Effect of Flow Channel Structure. Effect of flow channel structure on membrane flux was also shown in Figure 6. It indicated that membrane flux remained almost unchanged for all three flow channel structures at different Re numbers. The flux of the module with normal feed channel was slightly larger for laminar flow. The flux almost kept the same for all the flow channel structures for transition flow. The flux of the module with spiral feed channel became slightly great for turbulent flow. The secondary flows generated at the spiral or serpentine feed channel with the increasing Reynolds number so that the wall shear stress might become higher, the concentration polarization might then be reduced, and the filtration driving force could be increased. Therefore, fluxes for these two feed channels were larger than that for the normal feed channel.

In the experiments, operation pressure was 0.35 MPa, and solute concentration was very low, so the osmotic pressure might be relatively low, and effects of flow channel structure on the osmotic pressure could be neglected. Therefore, the varying range of effective filtration driving force was small, and the variation of flux was not obvious. It seems that the flux was independent of the flow channel structure.

It was also shown from Figure 7 that as for laminar flow Mg^{2+} rejection for the spiral feed channel was almost the same as that for the serpentine feed channel, but both of them were slightly larger than that for the normal feed channel; as for transition flow, Mg^{2+} rejection for the spiral feed channel was larger than that for the serpentine flow channel, and for the serpentine feed channel it was greater than that for the normal feed channel; as for turbulent flow, Mg^{2+}

rejection for spiral feed channel was also the same as that for serpentine feed channel, but both of them were much larger than that for the normal feed channel. Under the experimental conditions and in varying range of selected Reynolds number, the module with the spiral feed channel had the best Mg^{2+} rejecting ability, the module with the serpentine feed channel took a second place, and the module with the normal feed channel was the most poor because the Dean vortex on membrane surface made the flow turbulent, hence, reduced Mg^{2+} concentration on the membrane wall followed by decreasing transmembrane concentration difference, which led to the decreasing driving force of diffusive mass transfer and the rising Mg^{2+} rejection due to the almost unchanged convective mass transfer rate for all the feed channels.

4.4. Results of Numerical Simulation

4.4.1. Velocity Distribution in the Channel. The turbulent flow for the each flow channel was simulated by a CFD method. It is convenient to show the secondary flow by plotting a two-dimensional (2D) velocity field in the given cross section. For spiral feed channel, velocity vector fields in the six given cross sections are shown in Figure 8. Each velocity vector field in the section could be observed along the flow direction. The top, left, or right side of the cross section represents solid wall, and the bottom side stands for membrane wall. It was apparent that secondary flow phenomenon or Dean vortex occurred and shear velocity at membrane wall was considerably large. The results showed that secondary flow generated due to the centrifugal force that worked on fluid, which enhanced the turbulence of fluid and made fluid unstable. Moreover, the large shear velocity nearby membrane wall was able to disturb boundary layer flow and improved shear stress, which hindered the concentration polarization development and the membrane fouling.

Figure 9 showed the velocity vector fields in the given cross sections of the serpentine feed channel. The section velocity vector fields could be observed along the flow direction, and bottom side also represented membrane wall. The secondary flows generated in the 6 cross sections were quite different to a great extent. The shear velocity on the membrane surface in downstream near the U-shaped duct was larger than that in the other zone. The closer to the U-shaped duct the zone was, the stronger the secondary flow was, and vice versa, it became weaker. The shear velocity nearby membrane wall was larger close to the U-shaped duct and became smaller far away from it due to the action of relatively large centrifugal force on the fluid near it. It indicated that fluid layer was strongly disturbed near the membrane wall close to the U-shaped duct, which resulted in strong turbulence.

4.4.2. Shear Stress on Membrane Wall. As the turbulence of fluid became stronger, the shear stress on membrane surface was larger, which was beneficial to destroy the concentration polarization layer and hinder the membrane fouling. Data treatment was carried out for spiral, serpentine, and normal

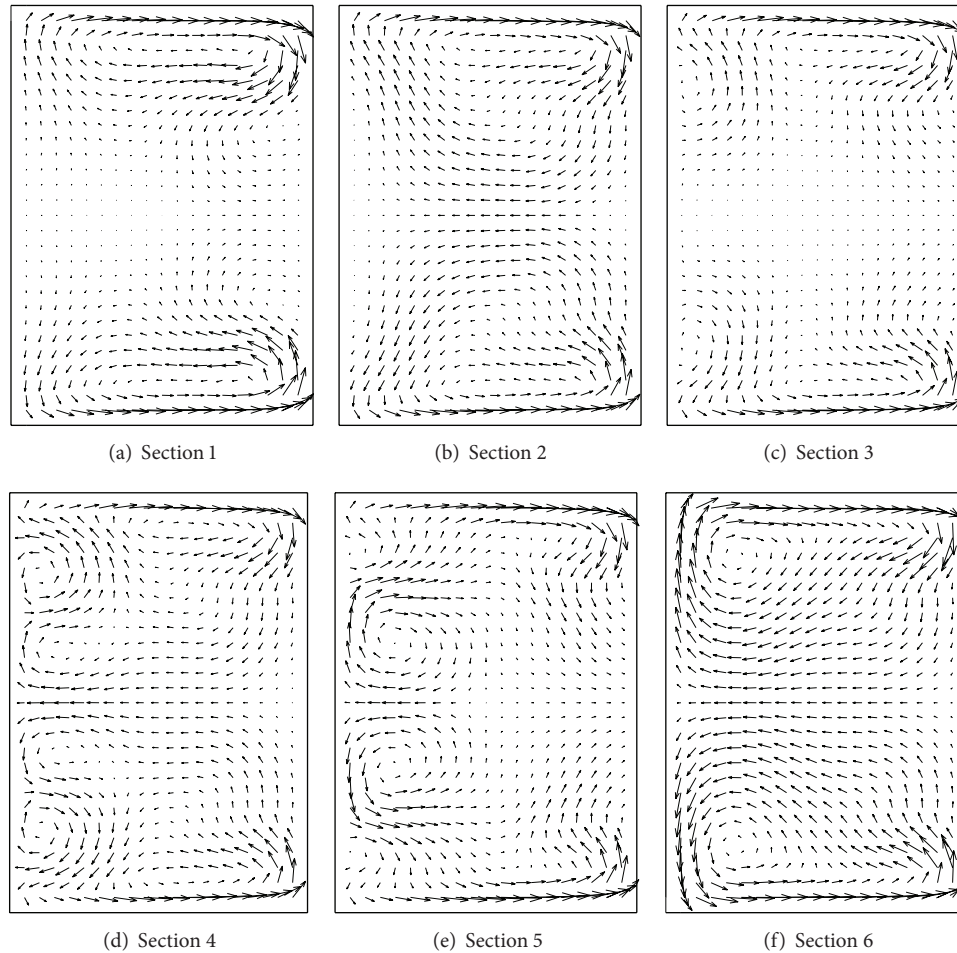


FIGURE 8: The velocity vectors in the given cross sections for the spiral feed channel.

feed channels, and the contour map of the shear stress on membrane wall was plotted for each type of flow channel structure. As mentioned in Section 2.4, the inlet velocities for the three types of feed channels were determined differently in order to keep fluid Reynolds number constant so that the effect of inlet velocity on wall shear stress near the inlet might be great. Hence, the wall shear stress field to be observed is far away from the inlet.

The local shear stress on the membrane surface for the spiral feed channel was almost the same, and the shear stress greater than 1.2 Pa was in relatively small area as shown in Figure 10. Its average wall shear stress was about 0.80 Pa that is larger than 0.633 Pa on the wall of inlet pipe due to the effect of the secondary flow. As for the serpentine feed channel, the local shear stress greater than 0.8 Pa covered a large proportion of the membrane surface, the largest or larger than 1.6 Pa stress was near the turning point due to the effect of the secondary flow, and the smallest or smaller than 0.4 Pa stress was in the area at dead corner as shown in Figure 11. The average wall shear stress is about 0.76 Pa, a little bit smaller than that for the spiral feed channel. For the normal feed channel whose inlet velocity was 0.707 m/s, the local shear stress on membrane wall was relatively large, and

flow disturbance was considerably strong in a small area near the inlet, and in a relatively large proportion of the membrane surface, the shear stress was small and even smaller than 0.4 Pa as shown in Figure 12. Its average wall shear stress was about 0.56 Pa which was very much smaller than the stress of 2.4 Pa at the entry of the cell because there was not any effect of the secondary flow in the feed channel. It was also less than the average wall shear stress of the membrane module with any other feed channel.

Generally speaking, shear velocity near the membrane surface increased due to the curved feed channel, which led to increasing wall shear stress, destroyed concentration polarization layer, and low diffusive transport of the solute across the membrane. For the module with spiral or serpentine feed channel, the crossflow rate, necessary to make Re number large, was less than that for the module with normal feed channel so that the latter might consume greater deal of energy than the former in order to get the same average wall shear stress. It indicated that when compared with the other two feed channels, using spiral feed channel would make the shear stress on membrane wall more uniform along the flow channel, destroy the concentration polarization layer, and achieve the high solute rejection. There must have been

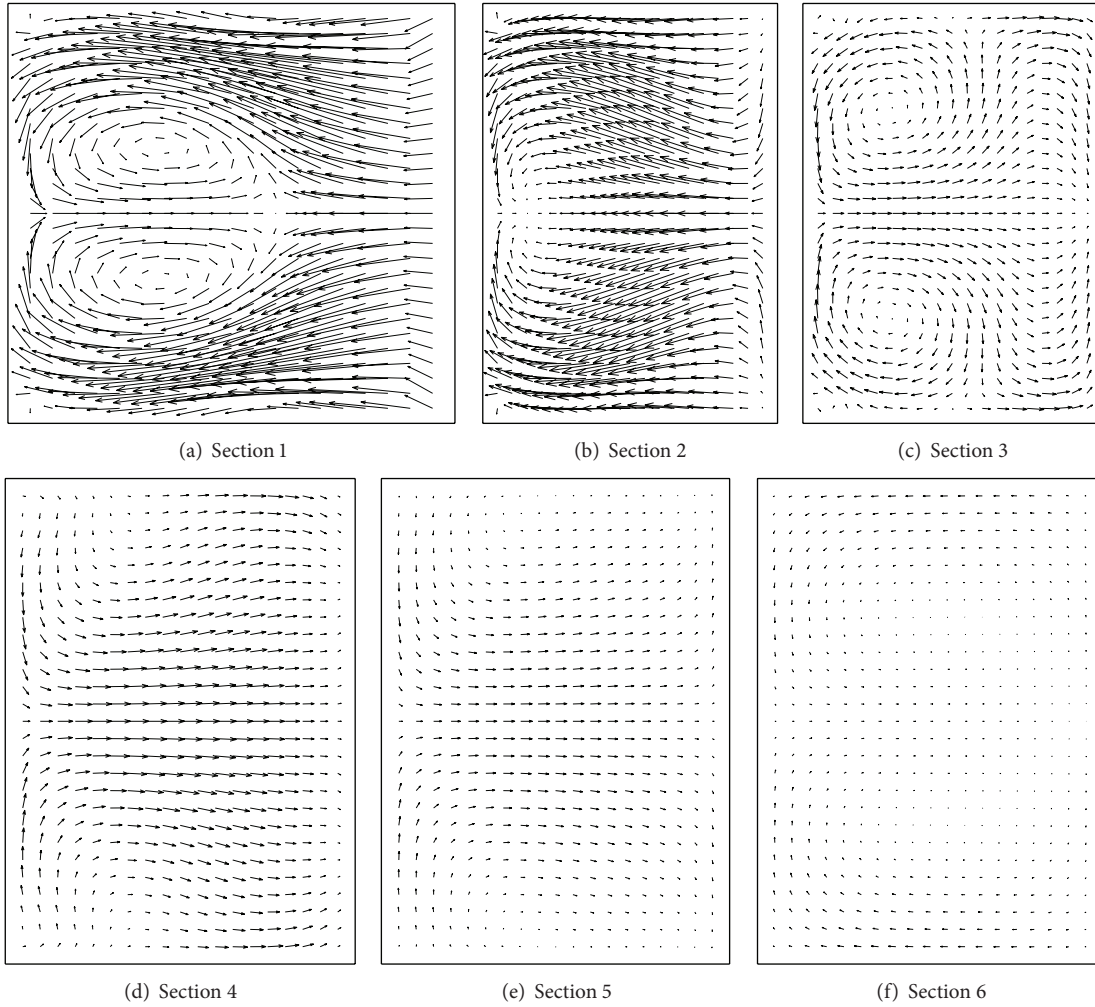


FIGURE 9: The velocity vectors in the given cross sections for the serpentine feed channel.

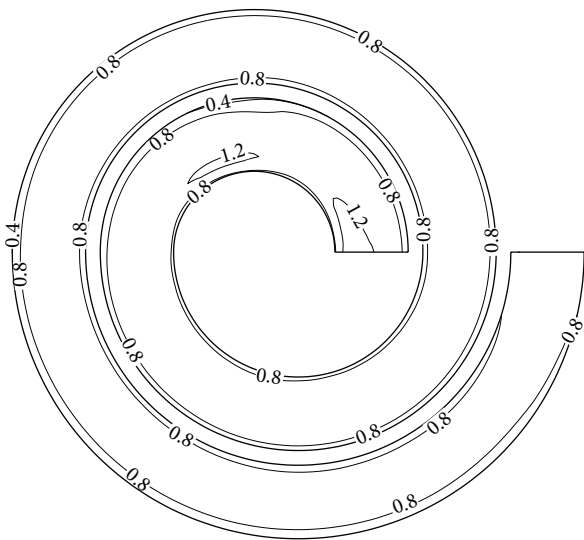


FIGURE 10: The wall shear stress on the membrane surface for the spiral feed channel, Pa.

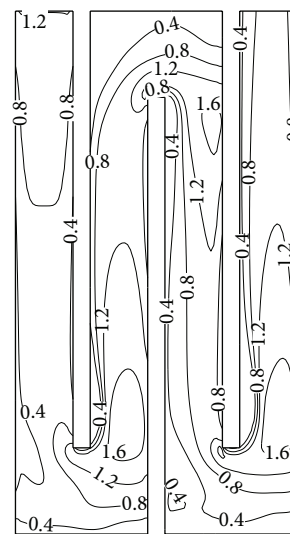


FIGURE 11: The wall shear stress on the membrane surface for the serpentine feed channel, Pa.

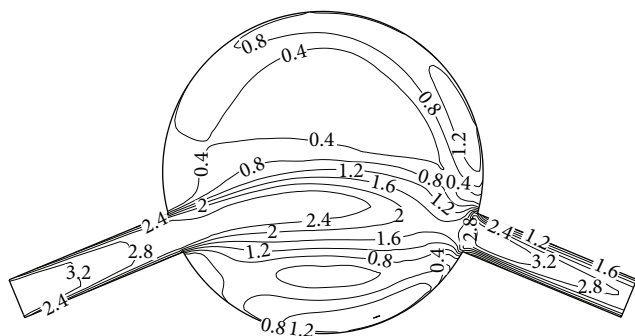


FIGURE 12: The wall shear stress on the membrane surface for the normal feed channel, Pa.

a critical wall shear stress. The concentration polarization layer would be destroyed and the solute rejection would then keep unchanged when the wall shear stress is greater than it. Thus, using a proper kind of feed channel, for example, the spiral feed channel or serpentine feed channel, could obviously increase the solute retention rate and then improve the separation performance of NF membrane.

5. Conclusions

The nanofiltration experiments were carried out using a commercial TFC-SR100 NF membrane and the modules with the normal feed channel and two newly designed feed channels, that is, the spiral and the serpentine feed channels. The experimental results showed that the effect of Reynolds number on flux was not obvious, but the Mg^{2+} rejection would increase when increasing the Reynolds number. The influence of flow channel structure on flux was not obvious. The effects of the feed channels on the rejection were not significantly at lower Re number. The rejections were almost the same for the spiral feed channel and the serpentine feed channel, but they are larger than that for the normal feed channel. Moreover, the difference between the former and the latter became greater when the Re number was larger than 4000.

The numerical simulations were also completed at Re number of 4800. The results showed that there was secondary flow in the spiral or the serpentine feed channel, which increased the shear stress on the membrane wall and destroyed the concentration polarization layer followed by increasing rejection. The wall shear stress was almost homogeneous along the flow channel for the module with the spiral feed channel. However, the wall stress was relatively low for the module with normal feed channel since there was not any secondary flow in the cell. It suggested that the spiral flow channel structure was a proper one to be used to improve the filtration performance of the NF membrane.

References

[1] P. Eriksson, "Nanofiltration extends the range of membrane filtration," *Environmental Progress*, vol. 7, no. 1, pp. 58–62, 1988.

- [2] X. L. Wang, W. J. Shang, D. X. Wang, L. Wu, and C. H. Tu, "Characterization and applications of nanofiltration membranes: state of the art," *Desalination*, vol. 236, no. 1–3, pp. 316–326, 2009.
- [3] A. I. Schafer, A. G. Fane, and T. D. Waite, *Nanofiltration: Principles and Applications*, Elsevier Science, 2004.
- [4] C. Ba, J. Langer, and J. Economy, "Chemical modification of P84 copolyimide membranes by polyethylenimine for nanofiltration," *Journal of Membrane Science*, vol. 327, no. 1–2, pp. 49–58, 2009.
- [5] M. Jahanshahi, A. Rahimpour, and M. Peyravi, "Developing thin film composite poly(piperazine-amide) and poly(vinyl-alcohol) nanofiltration membranes," *Desalination*, vol. 257, no. 1–3, pp. 129–136, 2010.
- [6] M. N. Abu Seman, M. Khayet, Z. I. Bin Ali, and N. Hilal, "Reduction of nanofiltration membrane fouling by UV-initiated graft polymerization technique," *Journal of Membrane Science*, vol. 355, no. 1–2, pp. 133–141, 2010.
- [7] G. T. Ballet, A. Hafiane, and M. Dhahbi, "Influence of operating conditions on the retention of phosphate in water by nanofiltration," *Journal of Membrane Science*, vol. 290, no. 1–2, pp. 164–172, 2007.
- [8] X. M. Li, D. Wang, T. Chai, B. W. Su, and C. J. Gao, "Study on seawater softening by nanofiltration membrane," *Journal of Chemical Engineering of Chinese Universities*, vol. 23, no. 4, pp. 582–586, 2009.
- [9] J. Z. Pang, J. Y. Li, Q. Wang, and Z. Z. Yang, "Study on treatment of salt chemical industry wastewater with nanofiltration membrane," *Journal of Tianjin Polytechnic University*, vol. 29, no. 5, pp. 6–9, 2010.
- [10] S. Darvishmanesh, A. Buekenhoudt, J. Degève, and B. van der Bruggen, "General model for prediction of solvent permeation through organic and inorganic solvent resistant nanofiltration membranes," *Journal of Membrane Science*, vol. 334, no. 1–2, pp. 43–49, 2009.
- [11] F. Fadaei, S. Shirazian, and S. N. Ashrafizadeh, "Mass transfer modeling of ion transport through nanoporous media," *Desalination*, vol. 281, pp. 325–333, 2011.
- [12] X. L. Wang, C. H. Tu, Y. Y. Fang, Y. Xiao, and B. Zhou, "The researches on the pore structure, charge property, separation mechanism and electrokinetic phenomena of nanofiltration membranes," *Membrane Science and Technology*, vol. 31, no. 3, pp. 127–134, 2011 (Chinese).
- [13] J. L. C. Santos, V. Geraldes, S. Velizarov, and J. G. Crespo, "Investigation of flow patterns and mass transfer in membrane module channels filled with flow-aligned spacers using computational fluid dynamics (CFD)," *Journal of Membrane Science*, vol. 305, no. 1–2, pp. 103–117, 2007.
- [14] M. Frappart, M. Y. Jaffrin, L. H. Ding, and V. Espina, "Effect of vibration frequency and membrane shear rate on nanofiltration of diluted milk, using a vibratory dynamic filtration system," *Separation and Purification Technology*, vol. 62, no. 1, pp. 212–221, 2008.
- [15] J. S. Vrouwenvelder, C. Picioreanu, J. C. Kruijthof, and M. C. M. van Loosdrecht, "Biofouling in spiral wound membrane systems: three-dimensional CFD model based evaluation of experimental data," *Journal of Membrane Science*, vol. 346, no. 1, pp. 71–85, 2010.
- [16] G. A. Fimbres-Weihs and D. E. Wiley, "Review of 3D CFD modeling of flow and mass transfer in narrow spacer-filled channels in membrane modules," *Chemical Engineering and Processing*, vol. 49, no. 7, pp. 759–781, 2010.

- [17] F. Cortés-Juan, B. Balannec, and T. Renouard, "CFD-assisted design improvement of a bench-scale nanofiltration cell," *Separation and Purification Technology*, vol. 82, pp. 177–184, 2011.
- [18] H. H. Zhan, H. Zhu, J. D. Chen, and G. Wang, "Numerical simulation of secondary Flow (Dean vortices) in 90° curved tube," *Boiler Technology*, vol. 41, no. 4, pp. 1–5, 2010.
- [19] W. R. Dean, "Fluid motion in a curved channel," pp. 403–419, 1928, <http://rspa.royalsocietypublishing.org/>.
- [20] T. H. Shih, W. W. Liou, A. Shabbir, Z. Yang, and J. Zhu, "A new $k - \epsilon$ eddy viscosity model for high reynolds number turbulent flows," *Computers and Fluids*, vol. 24, no. 3, pp. 227–238, 1995.
- [21] M. Lateb, C. Masson, T. Stathopoulos, and C. Bédard, "Comparison of various types of $k - \epsilon$ models for pollutant emissions around a two-building configuration," *Journal of Wind Engineering and Industrial Aerodynamics*, vol. 115, pp. 9–12, 2013.
- [22] D. M. Wang, *Fenxihuaxueshiyan*, Huazhong University of Science and Technology Press, Wuhan, China, 2007.
- [23] J. H. Ma, B. H. Sun, J. Zhou, and Q. Li, "Study of separation technology by using nanofiltration membrane in seawater," *Journal of Salt and Chemical Industry*, vol. 36, no. 5, pp. 1–5, 2007 (Chinese).
- [24] J. M. K. Timmer, H. C. van der Horst, and T. Robbertsen, "Transport of lactic acid through reverse osmosis and nanofiltration membranes," *Journal of Membrane Science*, vol. 85, no. 2, pp. 205–216, 1993.
- [25] A. N. Zhu, W. P. Zhu, and Y. C. Zhang, "Fouling problems of nanofiltration and influence factors of nanofiltration membrane performance," *Membrane Science and Technology*, vol. 23, no. 1, pp. 43–49, 2003.
- [26] D. J. Liu, *Study on seawater nanofiltration [M.S. thesis]*, Tianjin University, 2008.

Research Article

Hydrothermal Synthesis of SBA-15 Using Sodium Silicate Derived from Coal Gangue

Jing Wang, Li Fang, Fangqin Cheng, Xiaofang Duan, and Rongming Chen

State Environmental Protection Key Laboratory of Efficient Utilization Technology of Coal Waste Resources, Institute of Resource and Environment, Shanxi University, Taiyuan 030006, China

Correspondence should be addressed to Fangqin Cheng; cfangqin@sxu.edu.cn

Received 30 December 2012; Accepted 20 March 2013

Academic Editor: Yongcheng Jin

Copyright © 2013 Jing Wang et al. This is an open access article distributed under the Creative Commons Attribution License, which permits unrestricted use, distribution, and reproduction in any medium, provided the original work is properly cited.

Well-ordered SBA-15 was prepared with a hydrothermal route by sodium silicate derived from coal gangue. The as-prepared sample was analyzed by SAXRD, BET, TEM, and SEM, respectively. The results indicate that at a low hydrothermal temperature of 100°C the well-ordered mesoporous SBA-15 could be synthesized. The surface area, pore volume, and pore size of the sample are 552 m²/g, 0.54 cm³/g, and 7.0 nm, respectively. It is suggested that coal gangue could be used in obtaining an Si source to prepare mesoporous materials, such as SBA-15.

1. Introduction

The coal production of China now ranks top in the world, and so there is the biggest coal gangue yield. Despite being used as alternative material in road, pavement, embankment, foundation, or building construction, and so forth [1, 2], most of the coal gangue is still open-air stack-stored near by the coal mines and occupies vast pieces of land leading to a series of environmental problems, such as pollutions of air, water, and soil induced by the spontaneous combustion and eluviations. This became one of the highly important factors in restricting the economic sustainable development and the ecological civilization construction of the coal production area. Nevertheless, the coal-based energy structure could not change in the short term and thus the comprehensive utilization of coal gangue with high added value and minimal environmental impact turns into a big challenge.

Mesoporous silica has attracted much attention over the past decades due to not only their uniform mesostructures and excellent properties but also their amazing potential applications [3–6]. SBA-15 is one of the most extensively studied and applied example which could be prepared with highly reproducible pathways using commercial availability surfactants (such as P123), silica precursors, and facile [7, 8].

In addition, small particle size and rod-like morphology of SBA-15 received increasing interest for their fast adsorption and mass transfer [9]. Previously, most of the SBA-15 was obtained using expensive TEOS as silica precursors; thus efforts have been made to use inexpensive sodium silicate as a silica source [10–12]. In some earlier reports, the sodium silicate from fly ash has been used in the synthesis of SBA-15 [13–16], giving a good example for making good use of waste and reducing material costs.

It is well known that coal gangue mainly consists of about 20 wt.% carbon, 25 wt.% alumina, and 48 wt.% silica, and so sodium silicate could be made from the waste [17–20]. However, in the literatures, the SBA-15 synthesized using sodium silicate from coal gangue as a silica source was not reported.

Here we synthesized well-ordered SBA-15 successfully using sodium silicate derived from coal gangue under low-temperature hydrothermal condition to gain insight into the possibility of high-quality application of coal gangue.

2. Experimental

2.1. Materials. Coal gangue was donated by Lu'an Group (Shanxi, China) and used after being grinded to particles

about 200 μm in size. Hydrochloric acid (HCl, 36%), sodium carbonate (Na_2CO_3 , 98%), sodium silicate ($\text{Na}_2\text{Si}_3\text{O}_7$, with 25 wt.% SiO_2 and 14 wt.% NaOH), and acetic acid (HAc) were purchased from SCR. The triblock copolymer $\text{EO}_{20}\text{PO}_{70}\text{EO}_{20}$ (P123) was from Aldrich.

2.2. The Preparation of Sodium Silicate from Coal Gangue.

Raw coal gangue was ground to powder with a mesh size of less than 1000 μm using a mechanism grinder. The powder was calcined at 750°C for 2 h and then leached with 36% HCl at 40°C until no weight loss being observed. By this way, most aluminum oxide, ferric oxide, and other impurities were removed, which could be used to produce polyaluminum chloride employed as waste water purifier. The remained mixture was collected as silica slag. After that, soluble sodium silicate was prepared with the silica slag by a new developed low-temperature comelting method. Silica slag was mixed with Na_2CO_3 at a 3 : 2 weight ratio and grinded for 1 h using a ball mill (about 5–10 μm). The mixture was calcined at a heating rate of 5°C/min up to 850°C for 3 h in a muffle furnace. Afterwards, the liquid melt was quenched in boiled water to get small fragments and transferred into a high-pressure reactor filled with water and heated up to 150°C for 5 h. The obtained liquid mixture was filtered and then the as-prepared sodium silicate solution was obtained. The contents of the coal gangue, the silica slag, and the as-prepared sodium silicate are listed in Table 1. It can be seen that there is over 95% SiO_2 in the as-prepared sodium silicate.

2.3. Preparation of SBA-15.

The mesoporous silica was prepared using a slightly modified hydrothermal route [10]. P123 2 g was dissolved in 48 mL of 2 M HCl, in which 3.1 g HAc was added and stirred for 4 h to obtain solution A. 25 mL of the as-prepared sodium silicate solution was stirred for 10 min at room temperature as solution B. At 40°C, solution B was added into solution A dropwise under vigorous stirring. The mixture was stirred for 10 min at 40°C and then was kept motionless at room temperature for 12 h. The sediment was filtrated and washed with deionized water several times until Na^+ could not be detected in the washing liquor. Then, 20 g of deionized water was added in the washed sediment. The pH of the obtained mixture was adjusted to 1.7 with 2 M HCl before being transferred into a hydrothermal reaction kettle. After the hydrothermal reaction at 100°C or 200°C for 24 h, the collected samples were filtered, washed, dried in air, and then sintered at 650°C for 5 h to get as-prepared SBA-15 (S-slag). For comparison, pure SBA-15 samples were prepared using commercially available (pure) sodium silicate as a silica source at 100°C and 200°C, which were denoted as S-100 and S-200.

2.4. Characterization.

Small-angle X-ray diffraction (SAXRD) analysis of the as-prepared SBA-15 samples was carried out at room temperature using a Rigaku D/MAX-RB diffractometer with $\text{Cu K}\alpha$ radiation with graphite crystal monochromized. Nitrogen adsorption/desorption was performed at 77 K using in a Micromeritics ASAP2010 Sorptometer. The surface area and the pore sizes were

TABLE 1: The components of coal gangue, silica slag, and prepared sodium silicate.

Components (wt.%)	SiO_2	Al_2O_3	Fe_2O_3	K_2O	TiO_2
Coal gangue	32.35	57.79	3.37	2.77	1.15
Silica slag	80.49	8.37	0.53	1.14	2.31
Soluble sodium silicate	95.21	0.07	—	4.61	—

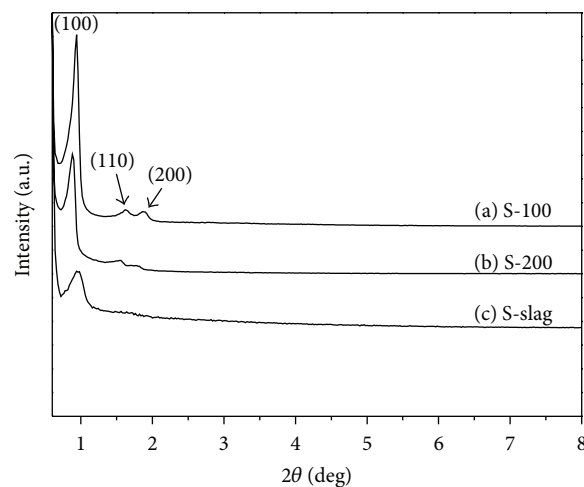


FIGURE 1: XRD patterns of the SBA-15 samples ((a) S-100, (b) S-200, and (c) S-slag (100°C)).

obtained from nitrogen adsorption isotherms by Brunauer-Emmett-Teller (BET) and Barrett-Joyner-Halenda (BJH) methods, respectively. Transmission electron microscopy (TEM) measurements were taken on a JEOL JEM-2100F field emission electron microscope with an acceleration voltage of 200 kV. Scanning electron microscopy (SEM) images were obtained on a Hitachi S-4800 electron microscope.

3. Results and Discussion

3.1. Small-Angle X-ray Diffraction.

Figure 1 shows the XRD patterns of the SBA-15 samples, S-100, S-200, and S-slag, after calcinations at 650°C for 5 h. The peaks of curve (a) of S-100 in Figure 1 show a characteristic intense (100) and two higher-order (110) and (200) reflections at 2θ values of 0.94°, 1.60°, and 1.87°, respectively, which are characteristics of SBA-15 $p6mm$ hexagonal symmetry. In comparison with the XRD patterns of SBA-15 prepared at 200°C showed as curve (b) in Figure 1, the diffractions of S-100 shift to higher 2θ degrees indicating small pore volume formed at lower hydrothermal temperature. However, significant enhancement in peak intensity can be observed when hydrothermal temperature decreased from 200°C to 100°C, indicating that the sample is highly long-range ordered with hexagonal symmetry [10]. The peak of curve (c) in Figure 1 at 0.96° gives the confirmation of typical SBA-15 structure in S-slag. The other two peaks assigned to the (110) and (200) planes do not appear in curve (c), showing a weak long-range order in the sample. This may be explained by weak long-range ordered

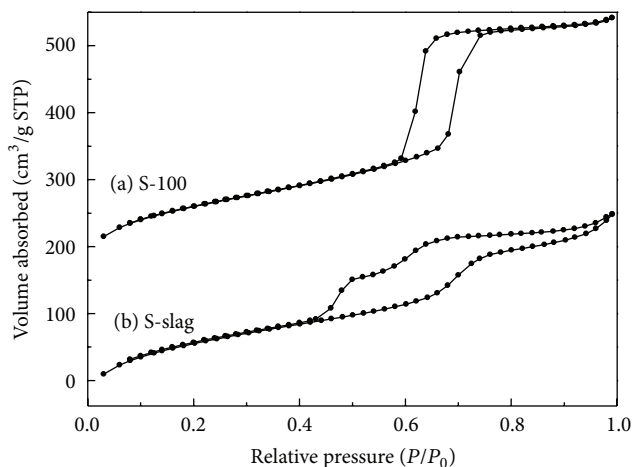


FIGURE 2: N_2 adsorption isotherms of (a) S-100 and (b) S-slag.

TABLE 2: Textural parameters of the samples.

Sample	S_{BET} (m^2/g)	V_p (cm^3/g)	d_p (nm)
S-100	567	0.68	7.2
S-slag	552	0.54	7.0

S_{BET} : specific surface area; V_p : total pore volume, and d_p : pore diameter.

crystalline formation of mesoporous silica due to lower silica content in reactant solution [13, 14]. In addition, the trace impurities introduced from S-slag, Cl^- anions, and SO_3^{2-} anions, for example, may also influence the formation of long-range ordered SBA-15. Since the existence of Cl^- and SO_3^{2-} anions may affect the micelle structures during the sol-gel process, the influence mechanism will be further investigated in detail.

3.2. Nitrogen Adsorption/Desorption. The N_2 adsorption/desorption isotherms and corresponding pore size distribution of the samples are shown in Figures 2 and 3, respectively. Curve (a) in Figure 2 (S-100) exhibits a typical-type IV isotherm [13] and a steep capillary condensation step occurred at a relative pressure (P/P_0) ranging from 0.59 to 0.76. Hysteresis appearing in the multilayer range of physisorption isotherms indicates capillary condensation in mesoporous structures. The curve exhibits H1 hysteresis loops; two branches are almost vertical and nearly parallel. According to the classification of IUPAC [21], this type is associated with porous materials consisting of agglomerates or compacts of approximately uniform rods-like particles in fairly regular array, therefore showing narrow pore size distribution (curve (a) in Figure 3). The surface area, pore volume, and pore size are $567 \text{ m}^2/\text{g}$, $0.68 \text{ cm}^3/\text{g}$, and 7.2 nm , respectively (seen in Table 2).

According to curve (b) in Figure 2, it can be seen that the isotherm of S-slag is analogous to that of S-100, but it shows a less steep capillary condensation step in a wider P/P_0 range from 0.43 to 1, indicating low pressure needed for the capillary condensation due to small pores formation and wide

distribution of pore sizes (curve (b) in Figure 3). In addition, the hysteric loop belongs to type H4, exhibiting that the stacking pores are slit-shaped tunnels which are generally induced by the irregular morphology of mesoporous silica. Clearly, the result of N_2 adsorption/desorption isotherms is consistent with the result of XRD analysis. This was also in agreement with the conclusion drawn by Wang et al., who claimed that impurities from fly ash may affect mesoporous construction [22]. By Brunauer-Emmett-Teller (BET) and Barrett-Joyner-Halenda (BJH) methods, the surface area, pore volume, and pore size of the SBA-15 samples were calculated and listed in Table 2. The surface area, pore volume, and pore size of the S-slag are $552 \text{ m}^2/\text{g}$, $0.54 \text{ cm}^3/\text{g}$, and 7.0 nm , respectively.

3.3. TEM and SEM. TEM images of S-100 and S-slag are shown in Figure 4. It can be found that both S-100 and S-slag are analogous to each other exhibiting well-ordered mesoporous materials arrayed along (100) and (110) directions as 2-dimensional hexagonal structures, in agreement with the XRD results.

The pore sizes of the particles of S-100 and S-slag were measured directly along the (110) directions in the TEM images. The results are $6.62 \mu\text{m}$ and $7.01 \mu\text{m}$ (shown in Figures 4(b) and 4(d)), respectively. The measured size of S-100 is smaller than the average pore size obtained from BET analysis, which could be explained by the difference between the methodologies.

SEM images of S-100 and S-slag are illustrated in Figure 5. It is clearly observed from Figure 5(a) that the particles of S-100 show both worm-like and rod-like morphology and aggregate together with a particle size less than $1 \mu\text{m}$, which is very similar to an earlier report [9]. On the contrary, Figure 5(b) shows that several spherical particles with diameters less than $2\text{-}3 \mu\text{m}$ together with some small irregular-shape particles are observed in the S-slag sample, indicating poor long-range ordered structures.

4. Conclusion

Sodium silicates derived from coal gangue was used as a silica source for SBA-15 synthesis via a low-temperature hydrothermal route. The characteristic of an SBA-15 $p6mm$ hexagonal symmetry structure in the as-prepared sample, S-slag, was confirmed by SAXRD, N_2 adsorption/desorption, and TEM. A weak long-range ordered crystalline formation of the mesoporous silica has been found in the sample due to lower silica content in reactant solution and the trace impurities introduced from S-slag. The results suggest that sodium silicate derived from coal gangue is a promising candidate for preparing mesoporous silica, such as SBA-15.

Acknowledgments

This work was financially supported by the International Scientific and Technological Cooperation of China (2011DFA90830), the National Hi-Tech Research and Development Program of China (863 Program,

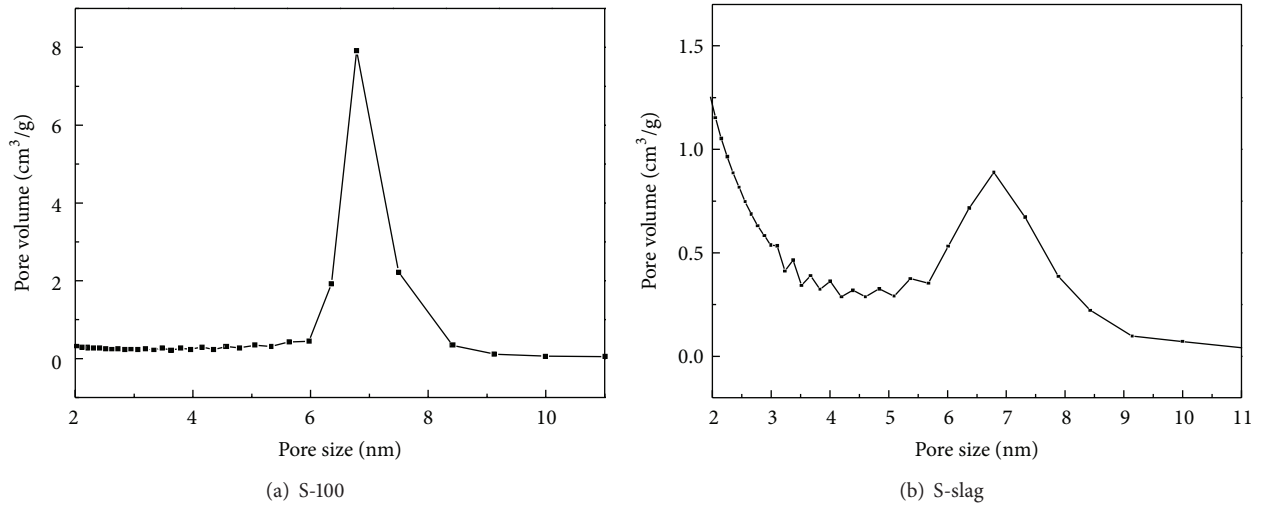


FIGURE 3: Pore size distribution of (a) S-100 and (b) S-slag.

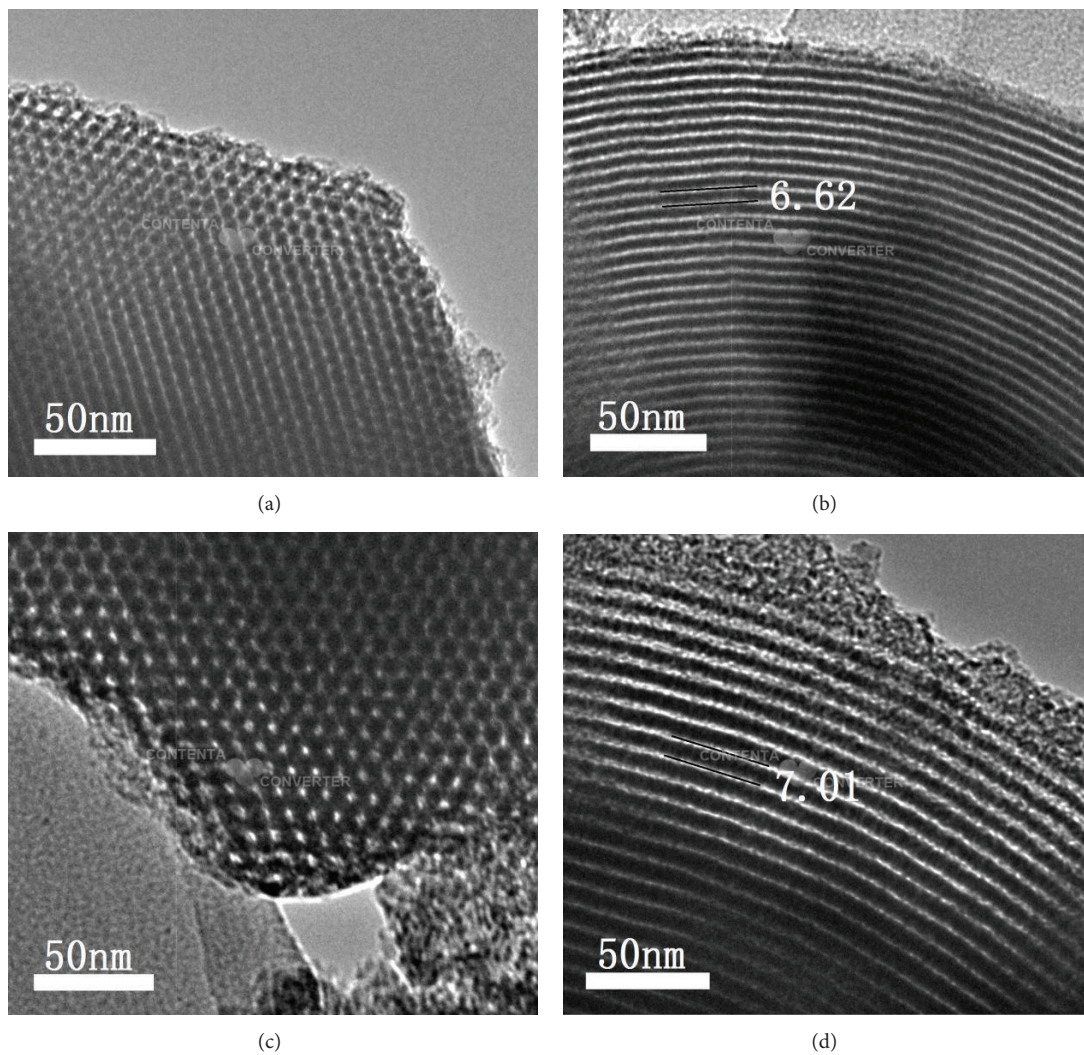


FIGURE 4: TEM images of S-100 viewed along (100) (a) and (110) (b) directions, and S-slag viewed along (100) (c) and (110) (d) directions.

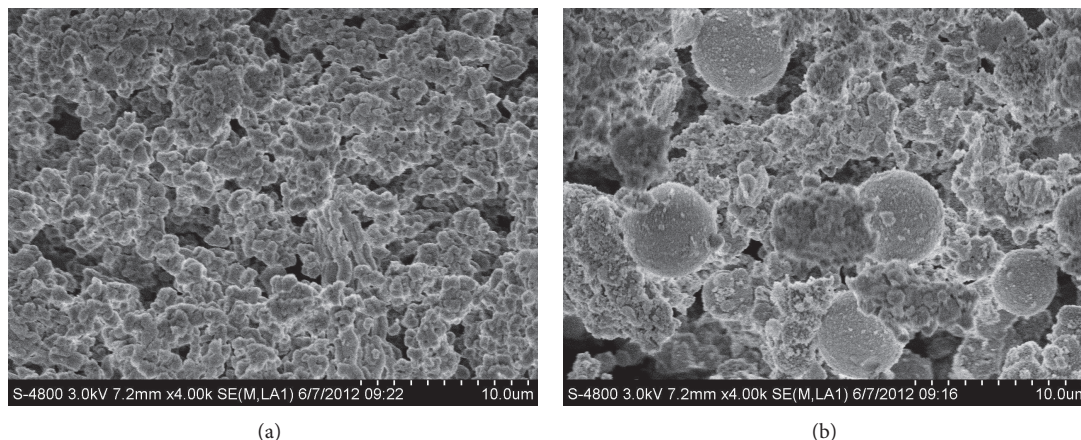


FIGURE 5: SEM images of (a) S-100 and (b) S-slag.

2011AA06A103). The authors are thankful to Xuming Wang, the professor at the Department of Metallurgical Engineering, College of Mines and Earth Sciences, University of Utah, Salt Lake City, UT, USA, for direction.

References

- [1] G.-l. Yang, R.-S. Yang, Q. Tong, and C. Huo, "Coalmine green mining with Gangue backfilling technique," *Procedia Environmental Sciences*, vol. 10, pp. 1205–1209, 2011.
- [2] N. Zhang, H. Sun, X. Liu, and J. Zhang, "Early-age characteristics of red mud-coal gangue cementitious material," *Journal of Hazardous Materials*, vol. 167, no. 1–3, pp. 927–932, 2009.
- [3] H. Yang, R. Xu, X. Xue, F. Li, and G. Li, "Hybrid surfactant-templated mesoporous silica formed in ethanol and its application for heavy metal removal," *Journal of Hazardous Materials*, vol. 152, no. 2, pp. 690–698, 2008.
- [4] L. Yang, Y. Wang, G. Luo, and Y. Dai, "Preparation and functionalization of mesoporous silica spheres as packing materials for HPLC," *Particuology*, vol. 6, no. 3, pp. 143–148, 2008.
- [5] R. Ishii, T. Itoh, T. Yokoyama et al., "On-chip encapsulation of lipase using mesoporous silica: a new route to enzyme microreactors," *Materials Letters*, vol. 63, no. 28, pp. 2445–2448, 2009.
- [6] J. Fan, J. Lei, C. Yu, B. Tu, and D. Zhao, "Hard-templating synthesis of a novel rod-like nanoporous calcium phosphate bioceramics and their capacity as antibiotic carriers," *Materials Chemistry and Physics*, vol. 103, no. 2–3, pp. 489–493, 2007.
- [7] L. Cao and M. Kruk, "Facile method to synthesize platelet SBA-15 silica with highly ordered large mesopores," *Journal of Colloid and Interface Science*, vol. 361, no. 2, pp. 472–476, 2011.
- [8] P. F. Fulvio, S. Pikus, and M. Jaroniec, "Short-time synthesis of SBA-15 using various silica sources," *Journal of Colloid and Interface Science*, vol. 287, no. 2, pp. 717–720, 2005.
- [9] X. Pang and F. Tang, "Morphological control of mesoporous materials using inexpensive silica sources," *Microporous and Mesoporous Materials*, vol. 85, no. 1–2, pp. 1–6, 2005.
- [10] D. Pan, L. Tan, K. Qian et al., "Synthesis of highly ordered and hydrothermally stable mesoporous materials using sodium silicate as a precursor," *Materials Letters*, vol. 64, no. 13, pp. 1543–1545, 2010.
- [11] Y. Ding, G. Yin, X. Liao, Z. Huang, X. Chen, and Y. Yao, "Key role of sodium silicate modulus in synthesis of mesoporous silica SBA-15 rods with controllable lengths and diameters," *Materials Letters*, vol. 75, pp. 45–47, 2012.
- [12] J. M. Kim and G. D. Stucky, "Synthesis of highly ordered mesoporous silica materials using sodium silicate and amphiphilic block copolymers," *Chemical Communications*, no. 13, pp. 1159–1160, 2000.
- [13] G. Chandrasekar, K. S. You, J. W. Ahn, and W. S. Ahn, "Synthesis of hexagonal and cubic mesoporous silica using power plant bottom ash," *Microporous and Mesoporous Materials*, vol. 111, no. 1–3, pp. 455–462, 2008.
- [14] M. Halina, S. Ramesh, M. A. Yarmo, and R. A. Kamarudin, "Non-hydrothermal synthesis of mesoporous materials using sodium silicate from coal fly ash," *Materials Chemistry and Physics*, vol. 101, no. 2–3, pp. 344–351, 2007.
- [15] R. S. Blissett and N. A. Rowson, "A review of the multi-component utilisation of coal fly ash," *Fuel*, vol. 97, pp. 1–23, 2012.
- [16] I. Majchrzak-Kuceba and W. Nowak, "Characterization of MCM-41 mesoporous materials derived from polish fly ashes," *International Journal of Mineral Processing*, vol. 101, no. 1–4, pp. 100–111, 2011.
- [17] N. Wen, G. Renyou, and L. Cuiwei, "A study of producing light refractory bricks of mullite by using coal gangues as raw materials," *Contributions to Geology and Mineral Resources Research*, vol. 12, no. 4, pp. 79–86, 1997 (Chinese).
- [18] Y. Yao and H. Sun, "A novel silica alumina-based backfill material composed of coal refuse and fly ash," *Journal of Hazardous Materials*, vol. 214, pp. 71–82, 2012.
- [19] C.-L. Park, B.-G. Kim, and Y. Yu, "The regeneration of waste foundry sand and residue stabilization using coal refuse," *Journal of Hazardous Materials*, vol. 204, pp. 176–182, 2012.
- [20] M. Yang, Z. Guo, and Y. Deng, "Preparation of CaO-Al₂O₃-SiO₂ glass ceramics from coal gangue," *International Journal of Mineral Processing*, vol. 103, pp. 112–115, 2012.
- [21] K. S. W. Sing, D. H. Everett, R. A. W. Haul et al., "Physical and biophysical chemistry division commission on colloid and surface chemistry including catalysis," *Pure and Applied Chemistry*, vol. 57, no. 4, pp. 603–619, 1985.

- [22] W. Wang, W. Shan, H. Ru, and N. Wu, "A facile and versatile partitioned cooperative self-assembly process to prepare SBA-15s with larger mesopores, high microporosity and tunable particle sizes," *Journal of Materials Chemistry*, vol. 21, no. 32, pp. 12059–12067, 2011.

Research Article

Influence of Activity of $\text{CaSO}_4 \cdot 2\text{H}_2\text{O}$ on Hydrothermal Formation of $\text{CaSO}_4 \cdot 0.5\text{H}_2\text{O}$ Whiskers

S. C. Hou and L. Xiang

Department of Chemical Engineering, Tsinghua University, Beijing 100084, China

Correspondence should be addressed to L. Xiang; xianglan@mail.tsinghua.edu.cn

Received 29 December 2012; Accepted 19 March 2013

Academic Editor: Guo Gao

Copyright © 2013 S. C. Hou and L. Xiang. This is an open access article distributed under the Creative Commons Attribution License, which permits unrestricted use, distribution, and reproduction in any medium, provided the original work is properly cited.

The influence of the activity of calcium sulfate dihydrate ($\text{CaSO}_4 \cdot 2\text{H}_2\text{O}$) on the hydrothermal formation of $\text{CaSO}_4 \cdot 0.5\text{H}_2\text{O}$ whiskers was investigated in this paper, using commercial $\text{CaSO}_4 \cdot 2\text{H}_2\text{O}$ as the raw material. The experimental results indicated that the activity of $\text{CaSO}_4 \cdot 2\text{H}_2\text{O}$ was improved after calcination of the commercial $\text{CaSO}_4 \cdot 2\text{H}_2\text{O}$ at 150°C for 6.0 h followed by hydration at room temperature for 1.0 h, corresponding to the decrease of the agglomerated particle sizes from $29.7 \mu\text{m}$ to $15.1 \mu\text{m}$, the increase of the specific surface areas (BET) from $4.75 \text{ m}^2 \cdot \text{g}^{-1}$ to $19.12 \text{ m}^2 \cdot \text{g}^{-1}$ and the grain sizes from 95 nm to 40 nm. The active $\text{CaSO}_4 \cdot 2\text{H}_2\text{O}$ produced by the calcination-hydration treatment favored the hydrothermal dissolution of $\text{CaSO}_4 \cdot 2\text{H}_2\text{O}$, promoting the formation of hemihydrate calcium sulfate ($\text{CaSO}_4 \cdot 0.5\text{H}_2\text{O}$) whiskers with high aspect ratios.

1. Introduction

The synthesis of calcium sulfate (CaSO_4) whiskers with high aspect ratios and homogeneous morphology has drawn much attention in recent years since they can be used as the reinforcing materials in many fields as plastics, ceramics and paper making, and so forth [1–6].

CaSO_4 whiskers were usually prepared by hydrothermal formation of the $\text{CaSO}_4 \cdot 0.5\text{H}_2\text{O}$ whiskers from the $\text{CaSO}_4 \cdot 2\text{H}_2\text{O}$ precursor followed by calcination of the $\text{CaSO}_4 \cdot 0.5\text{H}_2\text{O}$ whiskers at elevated temperatures. Wang et al. prepared $\text{CaSO}_4 \cdot 0.5\text{H}_2\text{O}$ whiskers with an aspect ratio of 5–20 at 115°C , using the natural gypsum as the reactant [7]. Wang et al. found that the use of the superfine $\text{CaSO}_4 \cdot 2\text{H}_2\text{O}$ precursor was essential for the formation of $\text{CaSO}_4 \cdot 0.5\text{H}_2\text{O}$ whiskers with small diameters and prepared $\text{CaSO}_4 \cdot 0.5\text{H}_2\text{O}$ whiskers with a diameter of $0.19 \mu\text{m}$ and an aspect ratio of 98 via hydrothermal conversion of the fine grinded gypsum with an agglomerated size smaller than $18.1 \mu\text{m}$ at 120°C [8]. Xu et al. prepared $\text{CaSO}_4 \cdot 0.5\text{H}_2\text{O}$ whiskers with a length of 100–750 μm and a diameter of 0.1–3 μm at 110– 150°C from the desulfurization gypsum composed mainly of $\text{CaSO}_4 \cdot 2\text{H}_2\text{O}$ (93.45 wt%) and CaCO_3 (1.76 wt%) [9], using H_2SO_4 to change the CaCO_3 impurity to active $\text{CaSO}_4 \cdot 2\text{H}_2\text{O}$.

Yang et al. prepared calcium sulfate whiskers 50–450 μm by hydrothermal treatment of the desulfurization gypsum at 130°C for 1.0 h in the presence of K_2SO_4 [10]. It was noticed that most of the former work showed that the use of the active $\text{CaSO}_4 \cdot 2\text{H}_2\text{O}$ precursor promoted the hydrothermal formation of $\text{CaSO}_4 \cdot 0.5\text{H}_2\text{O}$ whiskers with high aspect ratios.

In this paper a facile calcination-hydration hydrothermal reaction method was developed to synthesize the active $\text{CaSO}_4 \cdot 2\text{H}_2\text{O}$ precursor from the commercial $\text{CaSO}_4 \cdot 2\text{H}_2\text{O}$ and to produce the $\text{CaSO}_4 \cdot 0.5\text{H}_2\text{O}$ whiskers with high aspect ratios at hydrothermal condition. The influences of calcination and hydration on the morphology and structure of $\text{CaSO}_4 \cdot 2\text{H}_2\text{O}$ precursor as well as on the morphology of the $\text{CaSO}_4 \cdot 0.5\text{H}_2\text{O}$ whiskers were studied.

2. Experimental

2.1. Experimental Procedure. Commercial $\text{CaSO}_4 \cdot 2\text{H}_2\text{O}$ with analytical grade was used as the raw material in the experiments. The $\text{CaSO}_4 \cdot 2\text{H}_2\text{O}$ was sintered at 150°C for 3.0–6.0 h, then mixed with deionized water to keep the weight ratio of the solid to water at 1.0–5.0 wt%. After being stirred ($60 \text{ r} \cdot \text{min}^{-1}$) at room temperature for 1.0 h, the suspension

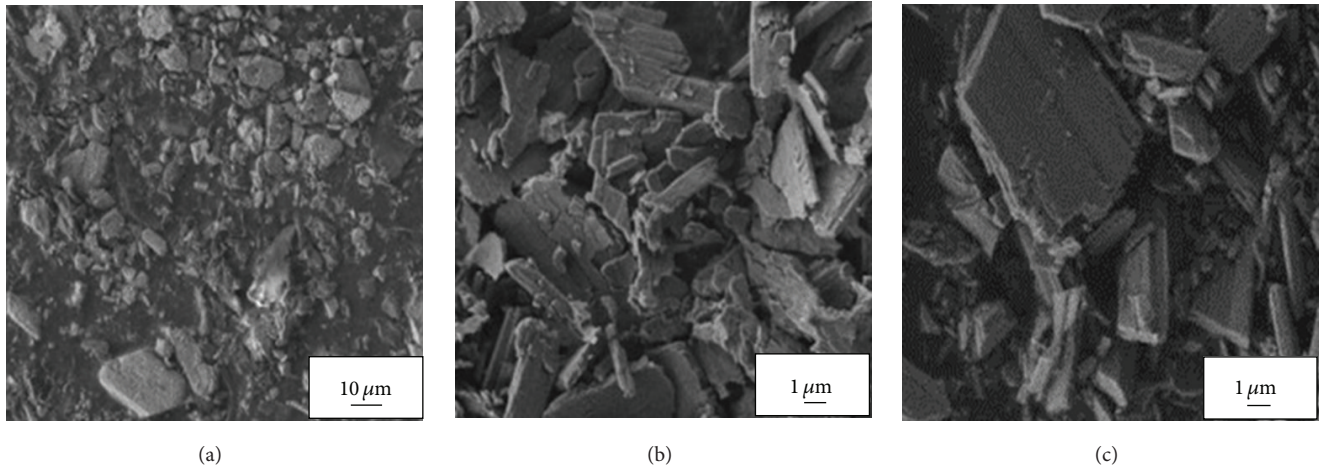


FIGURE 1: Morphology of raw material (a), calcination (b), and calcination-hydration (c) samples.

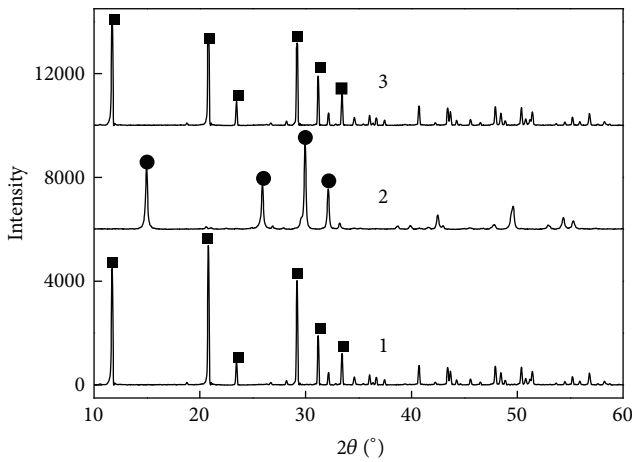


FIGURE 2: XRD patterns of raw material (1), calcination (2), and calcination-hydration (3) samples. Black square denotes $\text{CaSO}_4 \cdot 2\text{H}_2\text{O}$, black circle denotes $\text{CaSO}_4 \cdot 0.5\text{H}_2\text{O}$.

containing 1.0–5.0 wt% $\text{CaSO}_4 \cdot 2\text{H}_2\text{O}$ was then treated in an autoclave at 135°C for 4.0 h. After hydrothermal treatment, the suspension was filtrated and dried at 105°C for 6.0 h.

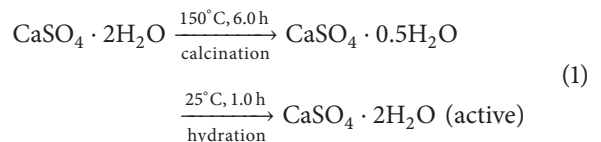
2.2. Characterization. The morphology of the samples was detected with the field emission scanning electron microscope (JSM 7401F, JEOL, Japan). The structures of the samples were identified by powder X-ray diffractometer (D8 advanced, Bruker, Germany) using $\text{Cu K}\alpha$ radiation ($\lambda = 1.54178 \text{ \AA}$). The agglomerated particle sizes of the samples were analyzed with the laser particle analyzer (Micro-plus, Germany). The soluble Ca^{2+} and SO_4^{2-} were analyzed by EDTA titration and barium chromate spectrophotometry (Model 722, Xiaoguang, China), respectively.

3. Results and Discussion

3.1. Formation of Active $\text{CaSO}_4 \cdot 2\text{H}_2\text{O}$ via Calcination-Hydration Route. The morphology and XRD patterns of the

raw material (a), the calcination sample (b), and the hydration sample (c) are shown in Figures 1 and 2, respectively. The $\text{CaSO}_4 \cdot 2\text{H}_2\text{O}$ raw material was composed of the irregular plates (a length of 1.5–20.0 μm and a width of 3.5–10.0 μm) and particles (a diameter of 0.5–5.5 μm). After the calcination treatment at 150°C for 6.0 h, the $\text{CaSO}_4 \cdot 2\text{H}_2\text{O}$ raw material was converted to the $\text{CaSO}_4 \cdot 0.5\text{H}_2\text{O}$ irregular rectangle planes with a length of 1.0–10.0 μm and a width of 0.2–3.0 μm . The hydration of the $\text{CaSO}_4 \cdot 0.5\text{H}_2\text{O}$ at room temperature led to the formation of $\text{CaSO}_4 \cdot 2\text{H}_2\text{O}$ irregular rectangle planes with a length of 1.0–5.0 μm and a width of 0.1–2.0 μm . The data in Figure 2 showed that the intensities of the XRD peaks in curve c were weaker than those in curve a, revealing that the calcination-hydration treatment promoted the formation of $\text{CaSO}_4 \cdot 2\text{H}_2\text{O}$ with poor crystallinity. The grain sizes of the raw material, the calcination sample, and the hydration sample were estimated as 94.9 nm, 37.5 nm and 39.5 nm, respectively, based on the (020) peaks located at $2\theta = 11.6^\circ$ and the Scherrer equation: $D_{hkl} = k\lambda/\beta \cos \theta$, where D_{hkl} , λ , β , and K represent the grain size, the wavelength of the $\text{Cu K}\alpha$ (1.54178 \AA), the full width at half maximum (FWHM), and the Scherrer constant ($K = 0.89$), respectively.

The BET and the agglomerated particle sizes of the raw material, the calcination sample and the hydration sample, are shown in Figure 3. The BET and the agglomerated particle sizes were $4.75 \text{ m}^2 \cdot \text{g}^{-1}$ and $29.7 \mu\text{m}$ for the raw material, $13.37 \text{ m}^2 \cdot \text{g}^{-1}$ and $15.5 \mu\text{m}$ for the calcination sample, and $19.12 \text{ m}^2 \cdot \text{g}^{-1}$ and $15.1 \mu\text{m}$ for the hydration sample, revealing the increase of BET and the decrease of the agglomerated particle sizes of the samples after calcination and calcination-hydration treatment. The above work showed that the calcination-hydration treatment favored the activation of the $\text{CaSO}_4 \cdot 2\text{H}_2\text{O}$ precursor



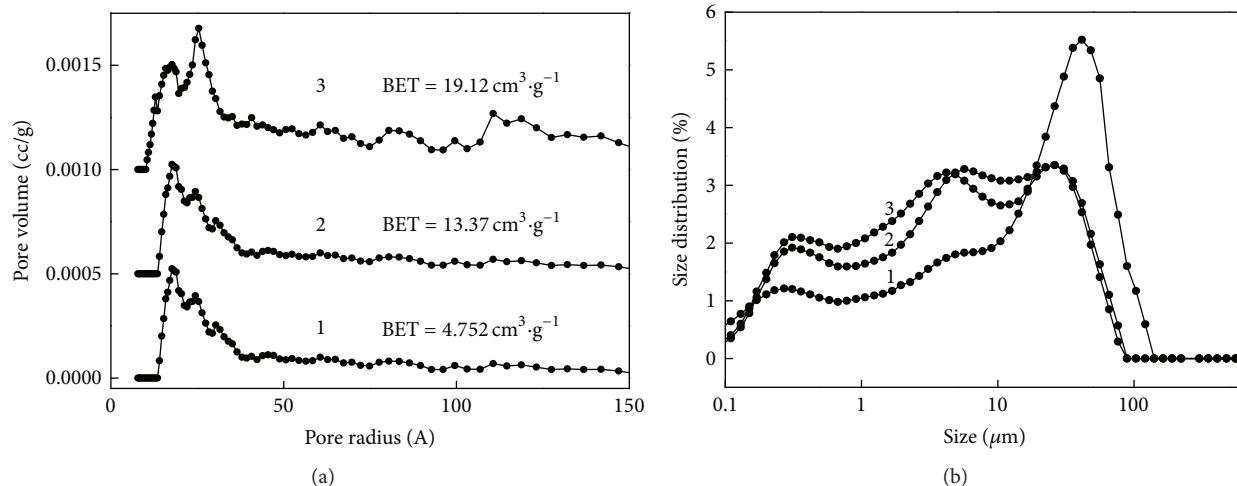


FIGURE 3: BET (a) and the agglomerated particle sizes (b) of the samples 1: commercial $\text{CaSO}_4 \cdot 2\text{H}_2\text{O}$, 2: calcination sample, and 3: calcination-hydration sample.

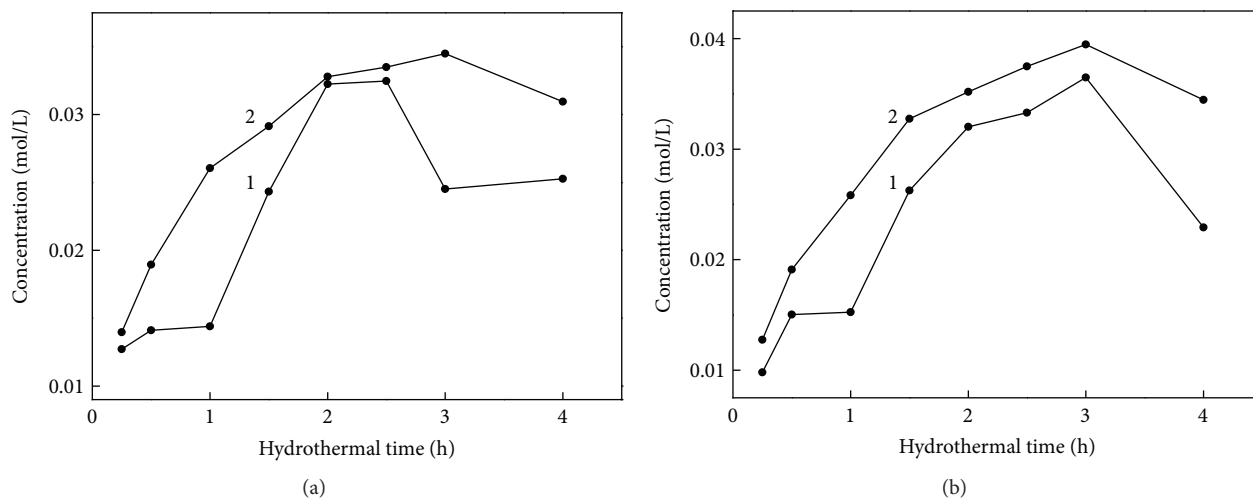


FIGURE 4: Variation of $[\text{Ca}^{2+}]$ (a) and $[\text{SO}_4^{2-}]$ (b) with hydrothermal reaction time. Precursor: 1: commercial $\text{CaSO}_4 \cdot 2\text{H}_2\text{O}$, 2: active $\text{CaSO}_4 \cdot 2\text{H}_2\text{O}$.

Hydrothermal formation of $\text{CaSO}_4 \cdot 0.5\text{H}_2\text{O}$ whiskers from active $\text{CaSO}_4 \cdot 2\text{H}_2\text{O}$ precursor.

Figure 4 shows the variation of $[\text{Ca}^{2+}]$ and $[\text{SO}_4^{2-}]$ with hydrothermal reaction time. Compared with the commercial $\text{CaSO}_4 \cdot 2\text{H}_2\text{O}$, the active $\text{CaSO}_4 \cdot 2\text{H}_2\text{O}$ produced by calcination-hydration treatment was easier to be dissolved at hydrothermal condition, so that $[\text{Ca}^{2+}]$ and $[\text{SO}_4^{2-}]$ in the active $\text{CaSO}_4 \cdot 2\text{H}_2\text{O}$ system were higher than those in the commercial $\text{CaSO}_4 \cdot 2\text{H}_2\text{O}$ system. The gradual increase of $[\text{Ca}^{2+}]$ and $[\text{SO}_4^{2-}]$ within 2.0–3.0 h indicated the faster dissolution of the $\text{CaSO}_4 \cdot 2\text{H}_2\text{O}$ than the precipitation of $\text{CaSO}_4 \cdot 0.5\text{H}_2\text{O}$, while the decrease of $[\text{Ca}^{2+}]$ and $[\text{SO}_4^{2-}]$ in the later time revealed the faster precipitation of $\text{CaSO}_4 \cdot 0.5\text{H}_2\text{O}$ than the dissolution of $\text{CaSO}_4 \cdot 2\text{H}_2\text{O}$.

Figure 5 shows the variation of the morphology of the samples with hydrothermal reaction time. The commercial $\text{CaSO}_4 \cdot 2\text{H}_2\text{O}$ was converted to $\text{CaSO}_4 \cdot 0.5\text{H}_2\text{O}$ whiskers

after 2.0 h of hydrothermal treatment, while the active $\text{CaSO}_4 \cdot 2\text{H}_2\text{O}$ produced by calcination-hydration treatment was changed to $\text{CaSO}_4 \cdot 0.5\text{H}_2\text{O}$ whiskers after 1.0 h of hydrothermal reaction owing to the acceleration of the hydrothermal dissolution-precipitation process. It was also noticed that the diameters of the $\text{CaSO}_4 \cdot 0.5\text{H}_2\text{O}$ whiskers formed from the active $\text{CaSO}_4 \cdot 2\text{H}_2\text{O}$ were much thinner than those from the commercial $\text{CaSO}_4 \cdot 2\text{H}_2\text{O}$. For example, after 4.0 h of hydrothermal reaction, the $\text{CaSO}_4 \cdot 0.5\text{H}_2\text{O}$ whiskers with a diameter of 1.0–5.0 μm , a length of 5–100 μm , and an aspect ratio of 20–80 were prepared from the commercial $\text{CaSO}_4 \cdot 2\text{H}_2\text{O}$, while $\text{CaSO}_4 \cdot 0.5\text{H}_2\text{O}$ whiskers with a diameter of 0.1–0.5 μm , a length of 30–200 μm , and an aspect ratio of 270–400 were produced from the active $\text{CaSO}_4 \cdot 2\text{H}_2\text{O}$ precursor (Figures 5(e) and 5(j)).

Figure 6 shows the schematic drawing for the conversion of the commercial/active $\text{CaSO}_4 \cdot 2\text{H}_2\text{O}$ to $\text{CaSO}_4 \cdot 0.5\text{H}_2\text{O}$

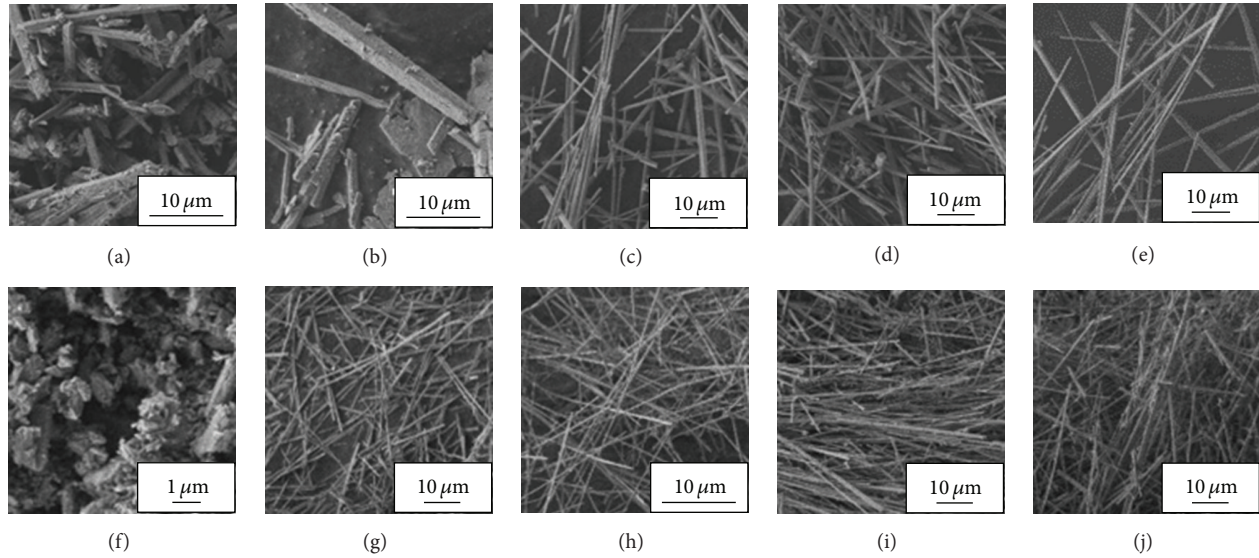


FIGURE 5: Variation of the morphology of the samples with hydrothermal reaction time Precursor: (a)–(e): commercial $\text{CaSO}_4 \cdot 2\text{H}_2\text{O}$, (f)–(j): active $\text{CaSO}_4 \cdot 2\text{H}_2\text{O}$; Time (h): (a), (f) 0.5; (b), (g) 1.0; (c), (h) 2.0; (d), (i) 3.0; (e), (j) 4.0.

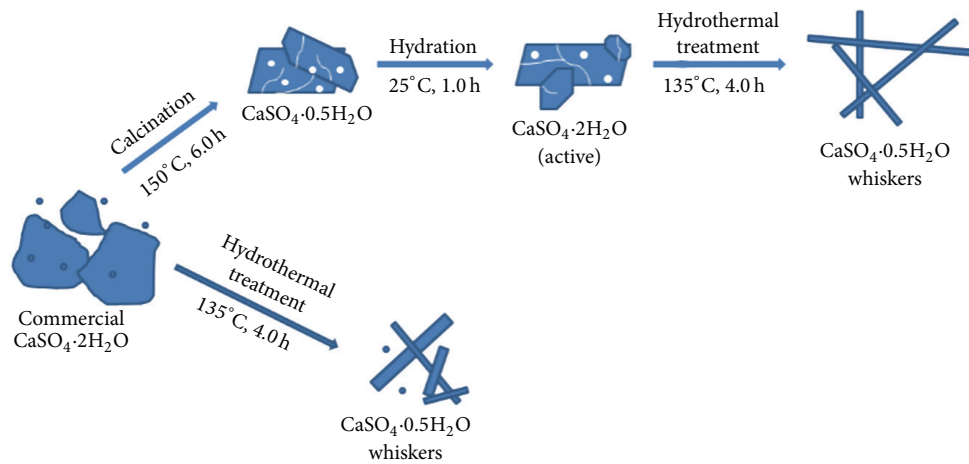


FIGURE 6: Schematic drawing for conversion of commercial/active $\text{CaSO}_4 \cdot 2\text{H}_2\text{O}$ to $\text{CaSO}_4 \cdot 0.5\text{H}_2\text{O}$ whiskers.

whiskers. The active $\text{CaSO}_4 \cdot 2\text{H}_2\text{O}$ precursor with small grain size and high BET was produced by calcination-hydration treatment, which accelerated the hydrothermal dissolution of $\text{CaSO}_4 \cdot 2\text{H}_2\text{O}$ and promoted the formation of $\text{CaSO}_4 \cdot 0.5\text{H}_2\text{O}$ whiskers with high aspect ratios.

4. Conclusion

Active $\text{CaSO}_4 \cdot 2\text{H}_2\text{O}$ precursor improved the morphology of the $\text{CaSO}_4 \cdot 0.5\text{H}_2\text{O}$ whiskers. Active $\text{CaSO}_4 \cdot 2\text{H}_2\text{O}$ was produced by calcination of the commercial $\text{CaSO}_4 \cdot 2\text{H}_2\text{O}$ at 150°C for 6.0 h followed by hydration at room temperature for 1.0 h. The use of the active $\text{CaSO}_4 \cdot 2\text{H}_2\text{O}$ favored the hydrothermal dissolution of $\text{CaSO}_4 \cdot 2\text{H}_2\text{O}$ and the formation of $\text{CaSO}_4 \cdot 0.5\text{H}_2\text{O}$ whiskers with high aspect ratios, producing $\text{CaSO}_4 \cdot 0.5\text{H}_2\text{O}$ whiskers with a length of 30–200 μm , a diameter of 0.1–0.5 μm , and an aspect ratio of 270–400.

Acknowledgments

This work was supported by the National Science Foundation of China (no. 51234003 and no. 51174125) and National Hi-Tech Research and Development Program of China (863 Program, 2012AA061602).

References

- [1] X. H. Ru, B. G. Ma, J. Huang, and Y. Huang, "Phosphogypsum transition to α -calcium sulfate hemihydrate in the presence of omongwaite in NaCl solutions under atmospheric pressure," *Journal of the American Ceramic Society*, vol. 95, no. 11, pp. 3478–3482, 2012.
- [2] T. Nissinen, M. Li, N. Brielles, and S. Mann, "Calcium sulfate hemihydrate-mediated crystallization of gypsum on Ca^{2+} -activated cellulose thin films," *CrystEngComm*, 2013.

- [3] B. Guan, X. Ma, Z. Wu, L. Yang, and Z. Shen, "Crystallization routes and metastability of α -calcium sulfate hemihydrate in potassium chloride solutions under atmospheric pressure," *Journal of Chemical and Engineering Data*, vol. 54, no. 3, pp. 719–725, 2009.
- [4] X. F. Song, L. N. Zhang, J. C. Zhao et al., "Preparation of calcium sulfate whiskers using waste calcium chloride by reactive crystallization," *Crystal Research and Technology*, vol. 46, no. 2, pp. 166–172, 2011.
- [5] L. Li, Y. J. Zhu, and M. G. Ma, "Microwave-assisted preparation of calcium sulfate nanowires," *Materials Letters*, vol. 62, pp. 4552–4554, 2008.
- [6] B. Kong, B. H. Guan, M. Z. Yates, and Z. B. Wu, "Control of α -calcium sulfate hemihydrate morphology using reverse microemulsions," *Langmuir*, vol. 28, no. 40, pp. 14137–14142, 2012.
- [7] L. Wang, J. H. Ma, Z. W. Guo, B. S. Dong, and G. M. Wang, "Study on the preparation and morphology of calcium sulfate whisker by hydrothermal synthesis method," *Material Science and Technology*, vol. 14, no. 6, pp. 626–629, 2006.
- [8] Z. T. Yuan, X. L. Wang, Y. X. Han, and W. Z. Yin, "Preparation of ultrafine calcium sulfate whiskers by hydrothermal synthesis," *Journal of Northeastern University*, vol. 29, no. 4, pp. 573–576, 2008.
- [9] A. Y. Xu, H. P. Li, K. B. Luo, and L. Xiang, "Formation of calcium sulfate whiskers from CaCO_3 -bearing desulfurization gypsum," *Research on Chemical Intermediates*, vol. 37, no. 2–5, pp. 449–455, 2011.
- [10] L. S. Yang, X. Wang, X. F. Zhu, and L. Z. Du, "Preparation of calcium sulfate whisker by hydrothermal method from flue gas desulfurization (FGD) gypsum," *Applied Mechanics and Materials*, vol. 268–270, pp. 823–826, 2013.

Research Article

Surfactant-Free Solvothermal Method for Synthesis of Mesoporous Nanocrystalline TiO₂ Microspheres with Tailored Pore Size

Yajing Zhang, Sujuan Zhang, Kangjun Wang, Fu Ding, and Jing Wu

College of Chemical Engineering, Shenyang University of Chemical Technology, Shenyang 110142, China

Correspondence should be addressed to Fu Ding; dingfuschr@hotmail.com and Jing Wu; wujing7275@163.com

Received 24 January 2013; Accepted 9 March 2013

Academic Editor: Guo Gao

Copyright © 2013 Yajing Zhang et al. This is an open access article distributed under the Creative Commons Attribution License, which permits unrestricted use, distribution, and reproduction in any medium, provided the original work is properly cited.

TiO₂ mesoporous microspheres self-assembled from nanoparticles were synthesized by a surfactant-free solvothermal route. The TiO₂ precursors were fabricated by tetrabutyl titanate, glacial acetic acid, and urea in the ethanol solution at 140°C for 20 h, and TiO₂ mesoporous microspheres were obtained by a postcalcination at temperatures of 450°C for promoting TiO₂ crystallization and the removal of residual organics. The phase structure, morphology, and pore nature were characterized by XRD, SEM, and nitrogen adsorption-desorption measurements. The as-prepared TiO₂ microspheres are in anatase phase, with 2–3 μm in diameter, and narrow pore distribution range is 3–4 nm. The adjustments of the synthetic parameters lead to the formation of the mesoporous TiO₂ microspheres with tuned pore size distributions and morphology.

1. Introduction

The existence of a close relationship between specific morphologies and unique properties in nanomaterials has ignited much attention to the synthesis of novel nanostructures for a broad domain of applications in the past decade [1]. Due to its large surface area, networked pore distribution, and unique band structure, mesoporous TiO₂ has attracted explosive attention for photocatalytic applications, such as water splitting, water and air purification, antibacterial materials and sterilization [2, 3]. A lot of chemical synthetic methods have been developed for fabricating the TiO₂ nanomaterials, including sol-gel [4], hydrolysis [5], precipitation [6], and hydrothermal methods [7, 8]. Hydrothermal method has been widely used for preparing mesoporous TiO₂ owing to the controllable morphology and porous structure as well as the high crystallization degree of the product [9]. It is found that phase selection (rutile, anatase, or brookite), particle shape and size, and crystal orientation with specific lattice plane are controllable depending on synthetic conditions [10–12]. Nevertheless, few reports focus on the effect of synthetic

conditions on the pore size distribution. Most synthesis processes use template for the growth of anisotropic nanocrystals. Templates used include hard template (porous silica, alumina, or latex spheres, etc.) and soft template (triblock copolymer or surfactants) [13–15]. However, after synthesis, the template has to be removed from the sample to make the pores accessible. This can be achieved by thermal treatment (calcination) or solvents extraction [16]. In most cases, TiO₂ mesoporous materials are calcined; the thermal treatment processes frequently lead to the partial or total collapse of the porous structure during the template removal process and thus result in the decrease of the surface area [17]. In addition, some template cannot be completely removed by either calcination or solvent extraction because it tightly bound to the materials. Therefore, developing approaches without template and surfactant to overcome these limitations are highly demanded. Moreover, during the process of use, TiO₂ nanomaterials are subjected to the difficulties in handling and additional cost for recycling process; thus micro- and submicrometer scaled materials are often preferred in the large-scale production [18].

Here, mesoporous TiO₂ microspheres self-assembled from nanoparticles have been fabricated by a surfactant-free, convenient, and low-cost solvothermal method, which can conquer the issues above-mentioned. In addition, the diameters size, pore volume, BET surface areas, and the pore size distributions can also be tuned by adjusting synthesis parameters. This synthesis method can also be extended for the fabrication of other mesoporous metal oxide materials.

2. Experimental Section

2.1. Synthesis of Mesoporous Nanocrystalline TiO₂ Microspheres. All the reagents are analytical grade and were used without further purification (from Sinopharm Chemical Reagent Ltd.). In a typical procedure, 12 mmol urea was dissolved into 60 mL of absolute ethanol; then the solution was slowly added into the other solution (mixture of 20 mL ethanol, 2 mL tetrabutyl titanate (Ti(OC₄H₉)₄), and 1 mL glacial acetic acid (CH₃COOH)) under stirring. The solution was transferred into a 100 mL Teflon-lined autoclave after stirring for 30 min. The autoclave was put into an oven and maintained at 140°C for 20 h. The precipitate was rinsed by ethanol for several times, dried at 90°C for 12 h, and then calcined at 450°C for 2 h. For comparison, different amounts of urea were added while keeping other reaction conditions constant.

2.2. Characterization of Mesoporous Nanocrystalline TiO₂ Microspheres. XRD measurements were performed on a Bruker D8 X-ray diffractometer with Cu-K α radiation ($\lambda = 1.54156 \text{ \AA}$) at a scan rate of 4° min^{-1} at 45 kV and 40 mA.

The N₂ adsorption-desorption isotherms of the TiO₂ microspheres were obtained at -196°C using a Quantachrome Autosorb I-C. Before measurements, samples were degassed under vacuum at 300°C for 4 hours. The Brunauer-Emmett-Teller (BET) approach was used to calculate specific surface area of the sample by using adsorption data over the relative pressure range of 0.05–0.30. The Barrett-Joyner-Halenda (BJH) approach was employed to determine pore size distribution and average mesopore diameter by using desorption data of the isotherms.

SEM images were obtained on a JEOL JEM 6360 scanning electron microscope with accelerating voltage of 20 kV.

3. Results and Discussion

3.1. Textural Properties. Figure 1 shows the XRD patterns of the TiO₂ samples prepared with different amounts of urea. The strong and sharp peaks observed in Figure 1 confirm the catalysts are all well crystallized. For all samples, the diffraction peaks appear at 25.17° , 38.23° , 48.09° , 55.05° , 62.83° , 69.7° and 75.3° , all the peaks can be indexed to TiO₂ phase (Anatase, JCPDS 21-1272), which corresponds to (101), (004), (200), (105), (204), (116), and (215) planes, respectively. No diffraction peaks of rutile TiO₂ phase can be detected. The XRD results indicate the as-prepared TiO₂ is of high purity. Normally, the rutile phase is more stable than the anatase phase. Here, the as-prepared TiO₂ mesoporous microspheres

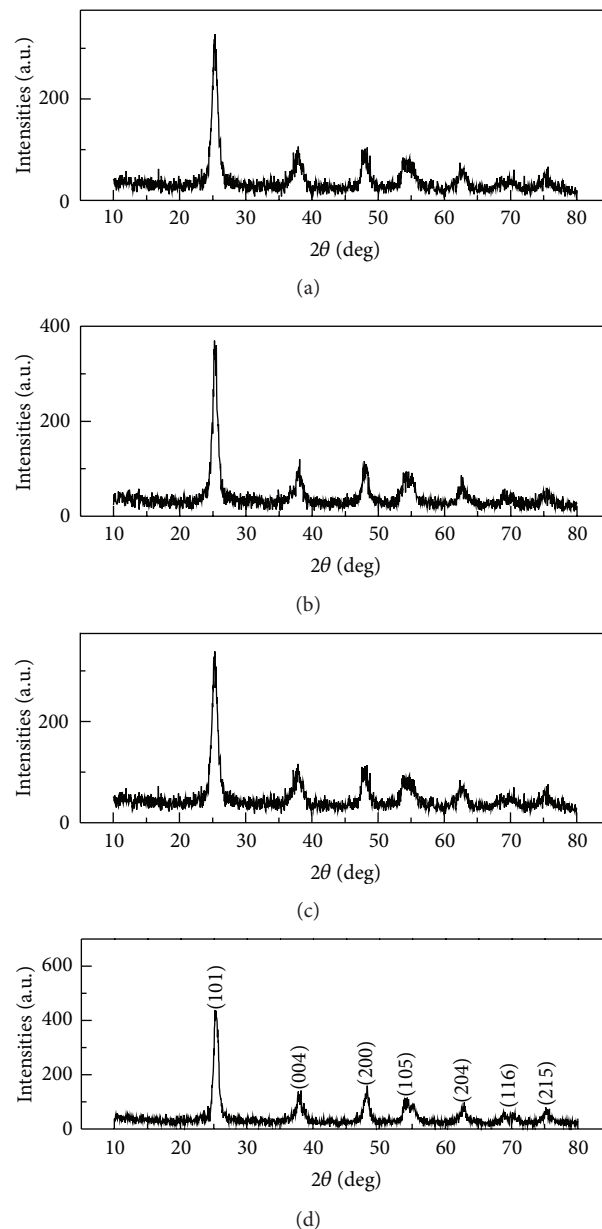


FIGURE 1: XRD patterns of mesoporous TiO₂ microspheres prepared with different amounts of urea: (a) 8 mmol; (b) 12 mmol; (c) 16 mmol; (d) 20 mmol.

are in anatase phase which could be ascribed not too high calcined temperature. The crystallite sizes of the synthesized TiO₂ samples estimated from the Debye-Scherrer equation [19], using the XRD line broadening of (101) diffraction peak, are reported in Table 1. It can be seen from Table 1 that crystallite sizes slightly decreased from 12.2 nm to 8.7 nm, with increasing the amount of urea, indicating the decrease of crystallization of the TiO₂ nanocrystals.

3.2. Morphology. The morphology and size of the TiO₂ samples were examined by SEM. Figures 2(a)–2(h) show that TiO₂ microspheres with different sizes can be achieved

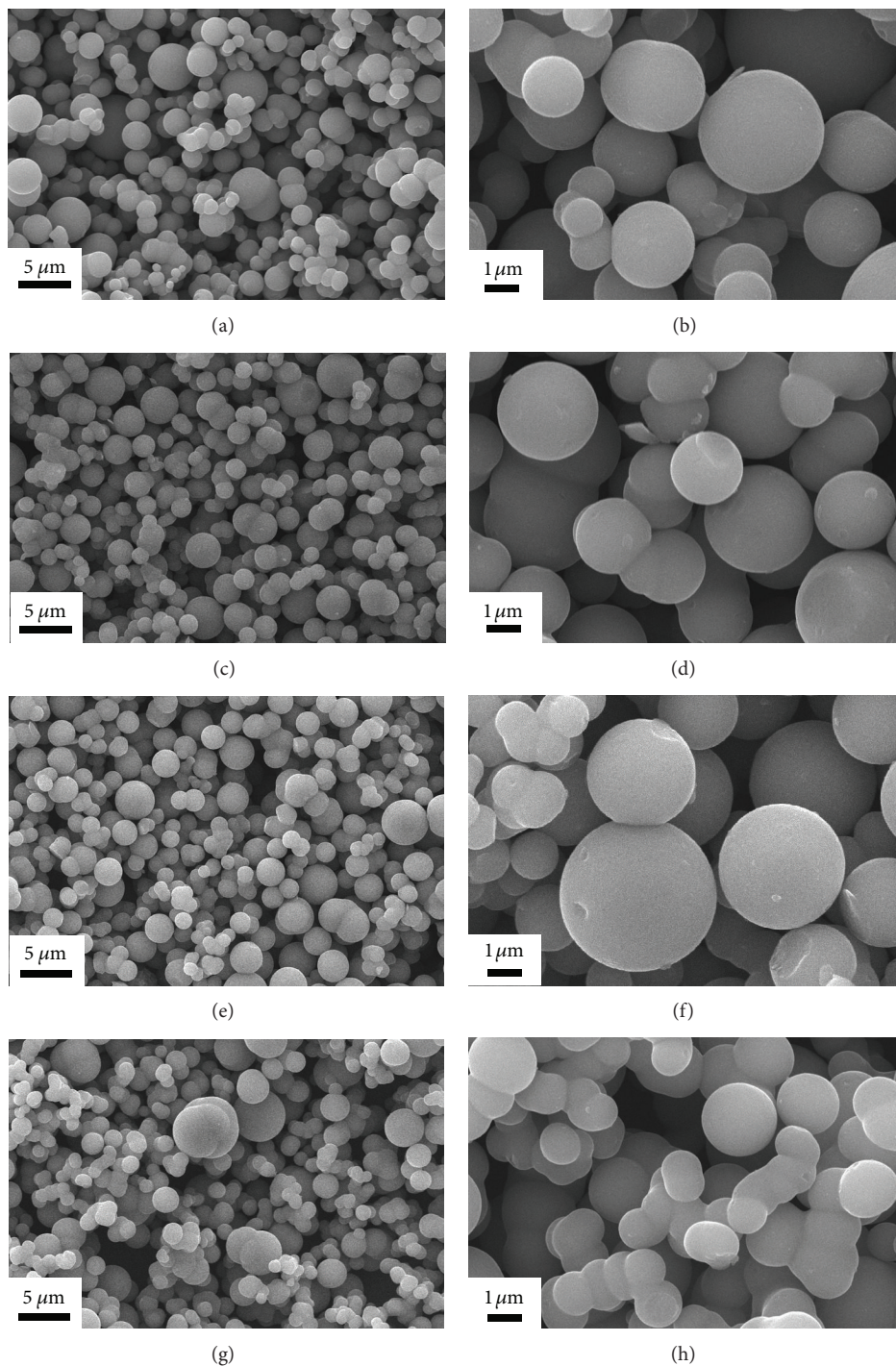


FIGURE 2: SEM images of mesoporous TiO_2 microspheres prepared with different amounts of urea: (a) 8 mmol; (b) 12 mmol; (c) 16 mmol; (d) 20 mmol.

accordingly by adjusting the amount of urea. When the amount of urea is 8 mmol, the size and surface structure of the microspheres can be observed in Figures 2(a) and 2(b). The TiO_2 microspheres are found to be 1–6 μm in diameter, the surfaces of the microspheres are very smooth, and the mean size of the diameter is about 4 μm . It is clearly seen that the microspheres disperse well, but the sizes are not

even. With the increasing amount of urea to 12 mmol (see Figures 2(c) and 2(d)), the mean diameter size of the TiO_2 microspheres decreases to about 2–3 μm , and the sizes are relatively uniform. The morphologies and sizes of the TiO_2 microspheres change little with increasing the urea amount to 16 mmol, as can be seen from Figures 2(e) and 2(f). However, if further increasing the urea amount to 20 mmol,

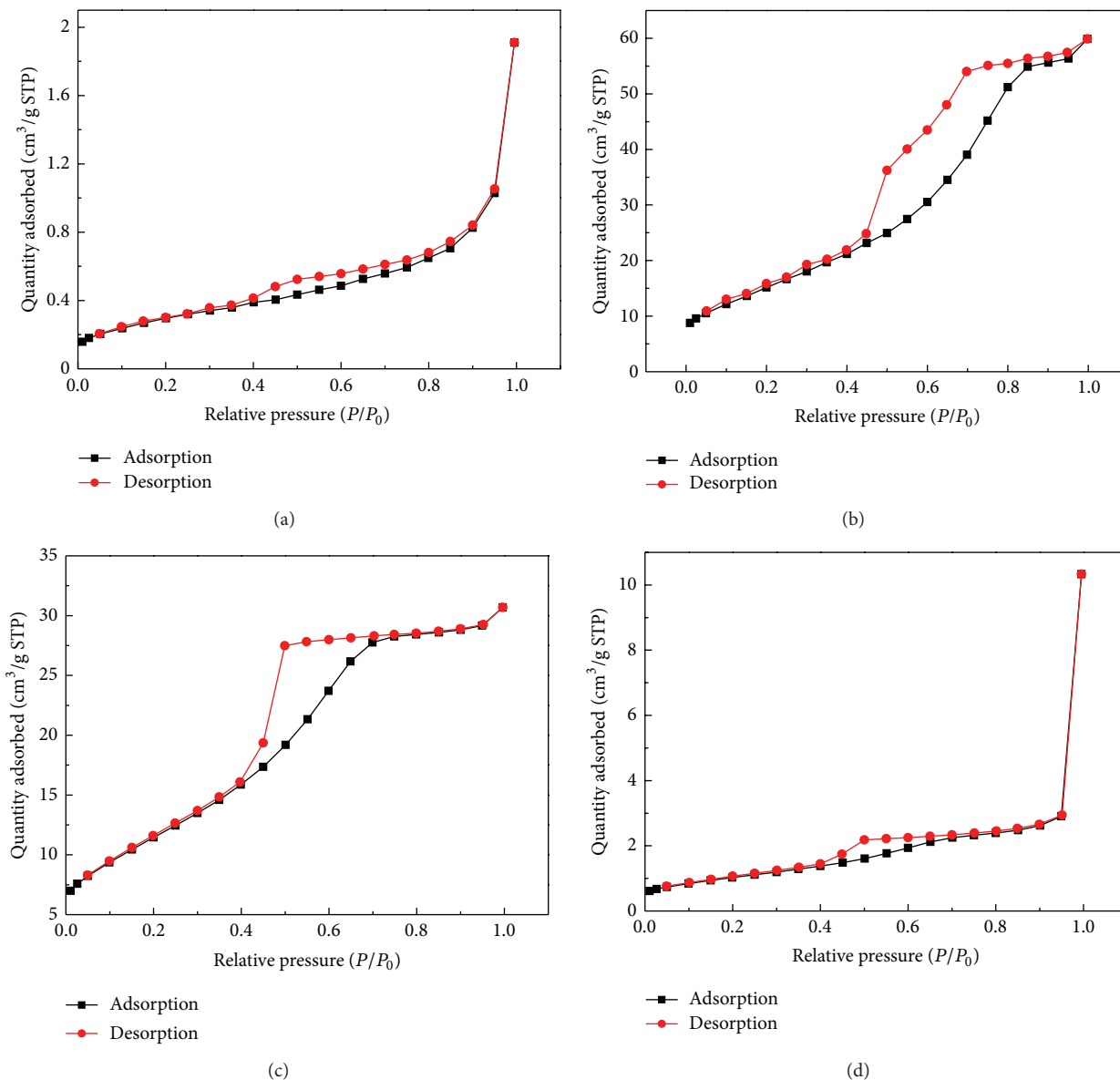


FIGURE 3: N_2 adsorption/desorption curves of mesoporous TiO_2 microspheres prepared with different amounts of urea: (a) 8 mmol; (b) 12 mmol; (c) 16 mmol; (d) 20 mmol.

it is observed from Figures 2(g) and 2(h) that “chain-like” and “peanut-like” TiO_2 microspheres are obtained, replacing the dispersed microspheres; the diameter sizes of the microspheres decrease, ranging from 1 to $3\ \mu m$ again. The result means that the amount of the urea can greatly affect the size of the products, and the size of the microspheres decreased with increasing the amount of urea. Interestingly, the microspheres structure can still maintain the morphology even after ultrasonication for 30 min, indicating the structure is stable.

3.3. Specific Surface Area and Pore Character of the TiO_2 Microspheres. The microstructural characteristics of the TiO_2 microspheres were further investigated with the N_2

adsorption/desorption analysis. The adsorption isotherms of the TiO_2 microspheres are shown in Figures 3(a)–3(d), respectively. All samples exhibit type IV adsorption isotherms with different types of hysteresis loop (lines in Figures 3(a) and 3(d) with type H_3 , while lines in Figures 3(b) and 3(c) with type H_2), typical for mesoporous materials [20]. Usually, isotherms with type H_3 hysteresis loop means the occurrence of irregular long and narrow pores, while with type H_2 hysteresis loop mean the occurrence of regular “bottle-like” pores which exhibit a smaller size of opening but a larger size of inside chamber. With small amount of urea (8 mmol), the hysteresis loop ranges $P/P_0 = 0.4 - 0.85$; when $P/P_0 = 0.9 - 1$, the adsorption increases significantly, indicating the existence of macropores with diameter of 10–100 nm [21]. This speculation can also be proved from the

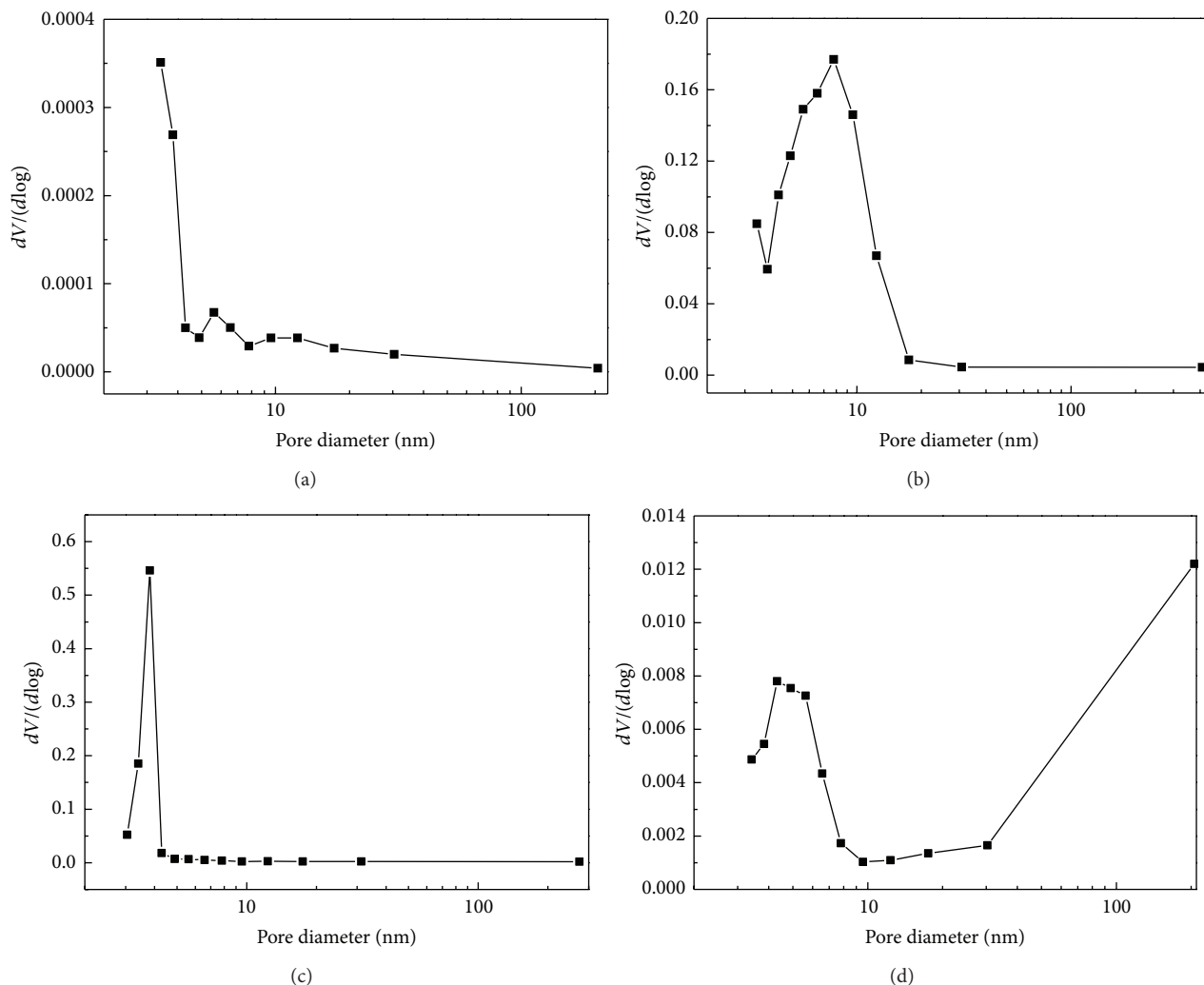


FIGURE 4: Pore size distributions of mesoporous TiO_2 microspheres prepared with different amounts of urea: (a) 8 mmol; (b) 12 mmol; (c) 16 mmol; (d) 20 mmol.

TABLE 1: Textural and structural parameters of mesoporous TiO_2 samples prepared with different amounts of urea.

Urea (mmol)	Phase	Crystallite size ^a (nm)	BET surface area ^b (m^2/g)	Pore volume ^c (cm^3/g)	Average pore diameter ^d (nm)
8	Anatase	12.2	1.09	0.002	3.5
12	Anatase	10.4	57.35	0.085	5.6
16	Anatase	9.2	42.45	0.045	3.8
20	Anatase	8.7	3.76	0.015	4.3

^aCrystallite size was calculated from the Scherrer equation based on the diffraction peak (101). ^bThe specific surface area was calculated by BET method. ^cThe total pore volume is taken from the adsorption branch of the nitrogen isotherm curve. ^dThe average pore diameter is estimated using the adsorption branch of the isotherm and BJH model.

corresponding wide pore size distribution as depicted in Figure 4(a). When the amount of urea increased to 12 mmol, the hysteresis loop also ranges $P/P_0 = 0.4 - 0.85$; at $P/P_0 = 0.9 - 1$, the adsorption increases little, implying almost all mesoporous structure of the sample. The pore size distributes 3–20 nm, as depicted in Figure 4(b). If further increasing the amount of urea; for example, 16 mmol urea were used,

and the hysteresis loop range of the sample also becomes narrow, only $P/P_0 = 0.4 - 0.75$, which demonstrates the pore size distribution is relatively concentrated, as can be seen from Figure 4(c), ranging only 3–4 nm. However, with more amount of urea (20 mmol), although the hysteresis loop still exhibits a small triangular shape and a steep desorption branch like the sample prepared with 16 mmol, the pore size

distribution becomes wide again. As indicated in Figure 4(d), there are two kinds of pore sizes, one is about 3–10 nm, and another is much larger than 30 nm (30–200 nm). It can be concluded that the amount of urea has a great influence on the pore size distribution of TiO₂ microspheres. This result can be explained from the point view of the nucleation and growth process of the TiO₂ microspheres. In our synthesis, urea can provide basic environment for the alcoholysis of Ti(OC₄H₉)₄ to Ti(OH)₄ and corresponding condensation. The overall growth mechanism of the TiO₂ precursors could be divided into two stages: the initial formation of nuclei and the subsequent growth of nuclei. When the amount of urea is too small, the alcoholysis rate is considerably slower, which can incur the greater difference of the growth times for the particle; so the diameter size uniformity of the product is poor. In contrast, if the amount of urea is too large, the alcoholysis rate is fast enough so that all nuclei are formed at the initial stage, and nearly null particles are available for the subsequent nuclei growth. Accordingly, the nuclei aggregate to become spheres driven by minimization of surface energies according to the Gibbs-Thomson law; therefore the bigger microspheres grow up at the expense of disappearance of smaller ones, and the diameter size distribution is also poor. In addition, the amount of urea influences the condensation rate of Ti(OH)₄, and the narrow pore size distribution can be obtained at suitable condensation rate. Our research results indicate nanocrystalline TiO₂ mesoporous microspheres with controlled pore size distribution which can be synthesized by controlling the amount of urea.

It is also interesting to note that BET specific surface areas, pore volumes, and average pore diameters also changed with the amount of urea used in preparation, as shown in Table 1. The BET specific surface areas and pore volumes first increase and then decrease with the increasing amount of urea. The TiO₂ samples prepared with 12 mmol urea exhibit the maximum BET surface area of 57.35 m²/g, which is a little larger than that of commercial P25 [22].

4. Conclusions

In summary, mesoporous TiO₂ microspheres self-assembled from nanoparticles are synthesized by a surfactant-free Solvothermal method combined with postcalcination route. The as-prepared TiO₂ microspheres show anatase phase, high degree of crystallinity, and large BET surface areas. By adjusting the amount of urea used in synthesis, the pore size distribution and the diameters of the mesoporous TiO₂ microspheres can be tuned. The new approach could be extended to the fabrication of other metal mesoporous materials.

Acknowledgment

The authors thank Liaoning Science and Technology Department Foundation (no. 2007223016), Liaoning Educational Department Foundation (L2011065), Shenyang Science and Technology Department Foundation (no. F11-264-1-76), and

Scientific Research Starting Foundation for Doctor, Liaoning Province (no. 20111046), for financial support.

References

- [1] Y. J. Zhang, S. W. Or, and Z. D. Zhang, "Hydrothermal self-assembly of hierarchical cobalt hyperbranches by a sodium tartrate-assisted route," *RSC Advances*, vol. 1, no. 7, pp. 1287–1293, 2011.
- [2] J. Y. Cho, W. H. Nam, Y. S. Lim, W.-S. Seo, H.-H. Park, and J. Y. Lee, "Bulky mesoporous TiO₂ structure," *RSC Advances*, vol. 2, pp. 2449–2453, 2012.
- [3] A. Wold, "Photocatalytic properties of TiO₂," *Chemistry of Materials*, vol. 5, no. 3, pp. 280–283, 1993.
- [4] D. M. Antonelli and J. Y. Ying, "Synthesis of hexagonally packed mesoporous TiO₂ by a modified sol-gel method," *Angewandte Chemie*, vol. 34, no. 18, pp. 2014–2017, 1995.
- [5] P. Kubiak, J. Geserick, N. Hüsing, and M. Wohlfahrt-Mehrens, "Electrochemical performance of mesoporous TiO₂ anatase," *Journal of Power Sources*, vol. 175, no. 1, pp. 510–516, 2008.
- [6] D. Dambournet, I. Belharouak, and K. Amine, "Tailored preparation methods of TiO₂ anatase, rutile, brookite: mechanism of formation and electrochemical properties," *Chemistry of Materials*, vol. 22, no. 3, pp. 1173–1179, 2010.
- [7] F. Liu, C.-L. Liu, B. Hu, W.-P. Kong, and C.-Z. Qi, "High-temperature hydrothermal synthesis of crystalline mesoporous TiO₂ with superior photo catalytic activities," *Applied Surface Science*, vol. 258, no. 19, pp. 7448–7454, 2012.
- [8] K. H. Lee and S. W. Song, "One-step hydrothermal synthesis of mesoporous anatase TiO₂ microsphere and interfacial control for enhanced lithium storage performance," *ACS Applied Materials & Interfaces*, vol. 3, no. 9, pp. 3697–3703, 2011.
- [9] Z. Bian, J. Zhu, F. Cao, Y. Huo, Y. Lu, and H. Li, "Solvothermal synthesis of well-defined TiO₂ mesoporous nanotubes with enhanced photocatalytic activity," *Chemical Communications*, vol. 46, no. 44, pp. 8451–8453, 2010.
- [10] Y. Zhang, L. Wu, Q. Zeng, and J. Zhi, "An approach for controllable synthesis of different-phase titanium dioxide nanocomposites with peroxotitanium complex as precursor," *Journal of Physical Chemistry C*, vol. 112, no. 42, pp. 16457–16462, 2008.
- [11] M. G. Choi, Y. G. Lee, S. W. Song, and K. M. Kim, "Lithium-ion battery anode properties of TiO₂ nanotubes prepared by the hydrothermal synthesis of mixed (anatase and rutile) particles," *Electrochimica Acta*, vol. 55, no. 20, pp. 5975–5983, 2010.
- [12] A. R. Armstrong, G. Armstrong, J. Canales, and P. G. Bruce, "TiO₂-B nanowires," *Angewandte Chemie*, vol. 43, no. 17, pp. 2286–2288, 2004.
- [13] M. Alvaro, C. Aprile, M. Benitez, E. Carbonell, and H. Garcia, "Photocatalytic activity of structured mesoporous TiO₂ materials," *Journal of Physical Chemistry B*, vol. 110, no. 13, pp. 6661–6665, 2006.
- [14] H. Shibata, T. Ogura, T. Mukai, T. Ohkubo, and H. Sakai, "Direct synthesis of mesoporous titania particles having a crystalline wall," *Journal of the American Chemical Society*, vol. 127, no. 47, pp. 16396–16397, 2005.
- [15] S. Li, Q. Shen, J. Zong, and H. Yang, "Synthesis of size-tunable mesoporous anatase titania spheres by a template-free method," *Materials Research Bulletin*, vol. 45, no. 7, pp. 882–887, 2010.
- [16] K. Yoo, H. Choi, and D. D. Dionysiou, "Ionic liquid assisted preparation of nanostructured TiO₂ particles," *Chemical Communications*, vol. 10, no. 17, pp. 2000–2001, 2004.

- [17] J. Wang, Y. Zhou, Y. Hu, R. O'hayre, and Z. Shao, "Facile synthesis of nanocrystalline TiO₂ mesoporous microspheres for lithium-ion batteries," *Journal of Physical Chemistry C*, vol. 115, no. 5, pp. 2529–2536, 2011.
- [18] S. K. Das, M. Patel, and A. J. Bhattacharyya, "Effect of nanostructuring and ex situ amorphous carbon coverage on the lithium storage and insertion kinetics in anatase titania," *ACS Applied Materials and Interfaces*, vol. 2, no. 7, pp. 2091–2099, 2010.
- [19] Y. J. Kim, S. Y. Chai, and W. I. Lee, "Control of TiO₂ structures from robust hollow microspheres to highly dispersible nanoparticles in a tetrabutylammonium hydroxide solution," *Langmuir*, vol. 23, no. 19, pp. 9567–9571, 2007.
- [20] S. Lowell, J. E. Shields, and M. A. Thomas, *Characterization of Porous Solids and Powders: Surface Area, Pore Size and Density*, Kluwer Academic Publishers, Dordrecht, The Netherlands, 2004.
- [21] G. Calleja, D. P. Serrano, R. Sanz, P. Pizarro, and A. García, "Study on the synthesis of high-surface-area mesoporous TiO₂ in the presence of nonionic surfactants," *Industrial and Engineering Chemistry Research*, vol. 43, no. 10, pp. 2485–2492, 2004.
- [22] S. Sakulkaemaruehai and T. Sreethawong, "Synthesis of mesoporous-assembled TiO₂ nanocrystals by a modified urea-aided sol-gel process and their outstanding photocatalytic H₂ production activity," *International Journal of Hydrogen Energy*, vol. 36, no. 11, pp. 6553–6559, 2011.

Research Article

Efficient Removal of Cr(VI) with Fe/Mn Mixed Metal Oxide Nanocomposites Synthesized by a Grinding Method

Wang Weilong¹ and Fu Xiaobo²

¹ Center for Energy Conservation Technology, School of Engineering, Sun Yat-sen University, Guangzhou 510006, China

² Department of Chemistry, School of Life Science and Technology, Jinan University, Guangzhou 510632, China

Correspondence should be addressed to Fu Xiaobo; txiaobofu@jnu.edu.cn

Received 5 January 2013; Accepted 13 February 2013

Academic Editor: Huijun Wu

Copyright © 2013 W. Weilong and F. Xiaobo. This is an open access article distributed under the Creative Commons Attribution License, which permits unrestricted use, distribution, and reproduction in any medium, provided the original work is properly cited.

Fe/Mn mixed metal oxides were synthesized facilely by a grinding method and were characterized by TEM, XRD, XPS, and BET. The characterization results revealed that mixed metal oxides were mainly composed of not highly crystallized Fe₂O₃ and Mn₃O₄ nanoparticles with a diameter about 3–5 nm. The specific BET surface areas of the composite were affected by the amounts of KCl diluent in the preparation process and about 268 m²/g of the composite can be achieved. Compared with metal oxide adsorbents existent, the composites showed good adsorption capacity, stability, and regeneration activity for Cr(VI) removal. The enhanced adsorption capacity was speculated to be ascribed to the synergistic effect of the mixed metal oxides. By monitoring the valence change in the adsorption process using XPS characterization, the mechanism for Cr(VI) removal on the composites was found to be a combination of electrostatic attraction and ion exchange. The above results demonstrated that the synthesized metal oxides nanocomposite is of great potential for Cr(VI) removal in the fields of remediation of environmental problems.

1. Introduction

In the past years, the removal of heavy metals from industrial waste water streams has been widely studied due to the high threat of such pollutants to public health and environment [1–4]. The contamination of hexavalent chromium species is a major problem in many industrial areas, such as electroplating and metal finishing industries [5–7]. With the development of the stringent ecological standards, it is urgent for these industries to reduce the chromium in their effluents to an acceptable level before discharging into municipal sewers. Various methods have been developed to remove the chromium from industrial waste water, such as chemical redox followed by precipitation, ion exchange, and reverse osmosis. However, these methods have many drawbacks [8]. Currently, for large-scale used chemical redox method, a major drawback related to precipitation is slurry production. Both ion exchange and reverse osmosis methods are not economically attractive as a result of their high operating costs [8]. Recently, adsorption has been recognized as one of

the most promising techniques for removal of chromium and its effectiveness has been demonstrated [5–7, 9].

In the whole adsorption process, the adsorbents play an important role. How to choose a suitable adsorbent is still a challenge. Several efforts have been devoted to the synthesis of a series of adsorbents. In general, a good adsorbent should not only process high adsorption efficiency but also be regenerated. Activated carbon, possessing high BET surface areas, was adopted as an adsorbent to remove the heavy metals and better adsorption efficiency was achieved [10]. However, activated carbon which was commonly used by commercial regenerators was regenerated at a rather high temperature. Ho et al. [11] found that *Sphagnum* peat moss is an effective adsorbent for hexavalent chromium and 50% of chromium recovery was obtained. Srivastava [12] discovered that sawdust is effective for removal of hexavalent chromium and other heavy metals. These adsorbents also have a disadvantage which is that they could not be regenerated. Therefore, the search of new adsorbents for the removal of hexavalent chromium has directed attention

to synthesize new materials with high adsorption efficiency and good regeneration ability. Meanwhile, the development of nanoscience and nanotechnology is expected to provide a solution for the remediation of environmental problems. Thus, the design and application of novel nanomaterials for environmental protection have been receiving more and more attention in recent years.

Now, several researchers have focused on metal oxide nanoparticles and their composites for their high BET surface areas and fast adsorption kinetics when subjected to the treatment of chromium from waste water. Zhong et al. [13, 14] use 3d flowerlike Fe_2O_3 nanostructures as adsorbents for the removal of Cr(VI). Compared with the commercial Fe_2O_3 particles, 3d flowerlike Fe_2O_3 nanostructures exhibit higher adsorption capacity. Chen et al. [15, 16] and his group found that magnetite and $\gamma\text{-Fe}_2\text{O}_3$ nanoparticles showed high adsorption capacity for Cr(VI) removal (about 19.4 mg/g). Meanwhile, the adsorption capacity of the $\gamma\text{-Fe}_2\text{O}_3$ particles can be enhanced by modifying the surface properties of the particles with MnO_2 [17]. After that, they coated the $\gamma\text{-Fe}_2\text{O}_3$ nanoparticles with a layer of FeOOH and the adsorption capacity for Cr(VI) was improved (about 25.6 mg/g) [18]. These results demonstrate that mixed metal oxide nanocomposites possess high adsorption capacity for removal of Cr(VI). The development of metal oxide nanocomposites, which can be used as adsorbent for Cr(VI), is of both economic and environmental significance. A growing number of methods, such as coprecipitation, sol-gel, hydrothermal methods, were involved to solve the problem. As some of mechanochemical syntheses show great potential with regards to not only energy saving and reducing cost but also improved safety, this technology should prove to be highly attractive when substituting methods of preparing conventional adsorbent [19].

In this paper, we use a grinding method to synthesize the Fe/Mn mixed oxides nanocomposites with high BET surface areas. The synthesized composites were applied in the removal of Cr(VI) and the high adsorption capacity, stability, and regeneration ability of the product were achieved. It is expected that the insight provided by this study will contribute to the Cr(VI) removal from the waste water.

2. Experimental

All chemical stock solutions were prepared from reagent-grade chemicals using Millipore ultrapure water. NaNO_3 , NaOH , HNO_3 , $\text{Fe}(\text{NO}_3)_3 \cdot 6\text{H}_2\text{O}$, $\text{MnCl}_2 \cdot 4\text{H}_2\text{O}$, KOH , KCl , and K_2CrO_4 were purchased from Sigma-Aldrich and used without further purification.

2.1. Materials Preparation. For the synthesis of mixed metal oxide nanocomposites, 6.986 g $\text{Fe}(\text{NO}_3)_3 \cdot 6\text{H}_2\text{O}$ and 1.979 g $\text{MnCl}_2 \cdot 4\text{H}_2\text{O}$ and KCl powders (with different ratio of MnCl_2 to KCl) were mixed together and ground to a very fine powder using an automatic electrical mortar at room temperature for 10 min. The mixture obtained from the grinding was a brown paste. To the mortar was added KOH powder, followed by grinding for another 30 min at room temperature.

A significant amount of heat and some vapor was given off in the first few minutes of the KOH addition. After the reaction, the resultant composite was diluted by DI water, then filtered and washed with DI water repeatedly until no Cl^- could be detected. The precipitate was collected and dried in an oven at 70°C overnight. A comparison experiment was conducted by using $\text{Fe}(\text{NO}_3)_3 \cdot 6\text{H}_2\text{O}$ or $\text{MnCl}_2 \cdot 4\text{H}_2\text{O}$ as only the starting material.

2.2. Materials Characterization. The resultant composites were characterized by powder X-ray diffraction (XRD), BET, X-ray photoelectron spectroscopy (XPS), and high resolution transmission electron microscopy (HRTEM). XRD measurements were conducted on a PANalytical X'Pert Pro X-ray Diffractometer equipped with $\text{Cu-K}\alpha$ radiation ($\lambda = 1.54178 \text{ \AA}$), applying 40 kV voltage and 40 mA current. The BET specific surface area was determined by N_2 adsorption at 77 K using a Micromeritics ASAP 2000 system after the sample was degassed in vacuum at 130°C overnight. XPS spectrum was obtained in a Physical Electronics Corporation PHI 5600 machine with $\text{Al K}\alpha$ radiation (350 W) under 10^{-7} Pa and calibrated internally by carbon deposit C_{1s} (285.0 eV). TEM observation was carried out on a JEOL JEM-2010F electron microscope equipped with a Bruker Energy Dispersive Spectrometer (EDS). The amount of iron and manganese leaching from the composites was measured using ICP-AES (Perkin Elmer Optima-3000XL). The concentration of the Cr(VI) was measured using an UV-Vis spectrometer (Shimadzu UV-Vis 5000) according to the diphenyl carbazide method [20].

2.3. Adsorption Capacity Test. The experimental procedures were according to the processes reported by Hu et al. [16–18]. The adsorption studies were performed by mixing 0.2 g nanocomposites with 40 mL K_2CrO_4 solution of varying concentration in a 100 mL stopper conical flask. The pH of the suspensions was adjusted using 0.1 M HNO_3 and 0.1 M NaOH solutions. All of the Cr(VI) solutions have a matrix of 0.1 M NaNO_3 to keep the ion strength relatively constant. All the adsorption experiments were carried out at 25°C , pH 2, and shaking rate of 200 rpm unless stated otherwise. Adsorption equilibrium studies were conducted by shaking 20 mL of Cr(VI) solution at initial concentrations varying from 10 to 200 mg/L and 0.1 g of adsorbent nanoparticles. To study the stability of the adsorbent, 0.01 M NaOH solution was used as eluant and five cycles of adsorption-desorption processes were carried out. For each cycle, 40 mL of 100 mg/L Cr(VI) solution was adsorbed on 0.2 g nanocomposites for 30 min and then desorbed with 20 mL of 0.01 M NaOH solution for 1 h. After each cycle of adsorption-desorption, the nanocomposites were washed thoroughly with ultrapure water to neutrality and reconditioned for adsorption in the succeeding five cycles.

3. Results and Discussion

3.1. Characterization of Materials. Shown in Figure 1 are the TEM micrographs of the obtained Fe/Mn mixed metal

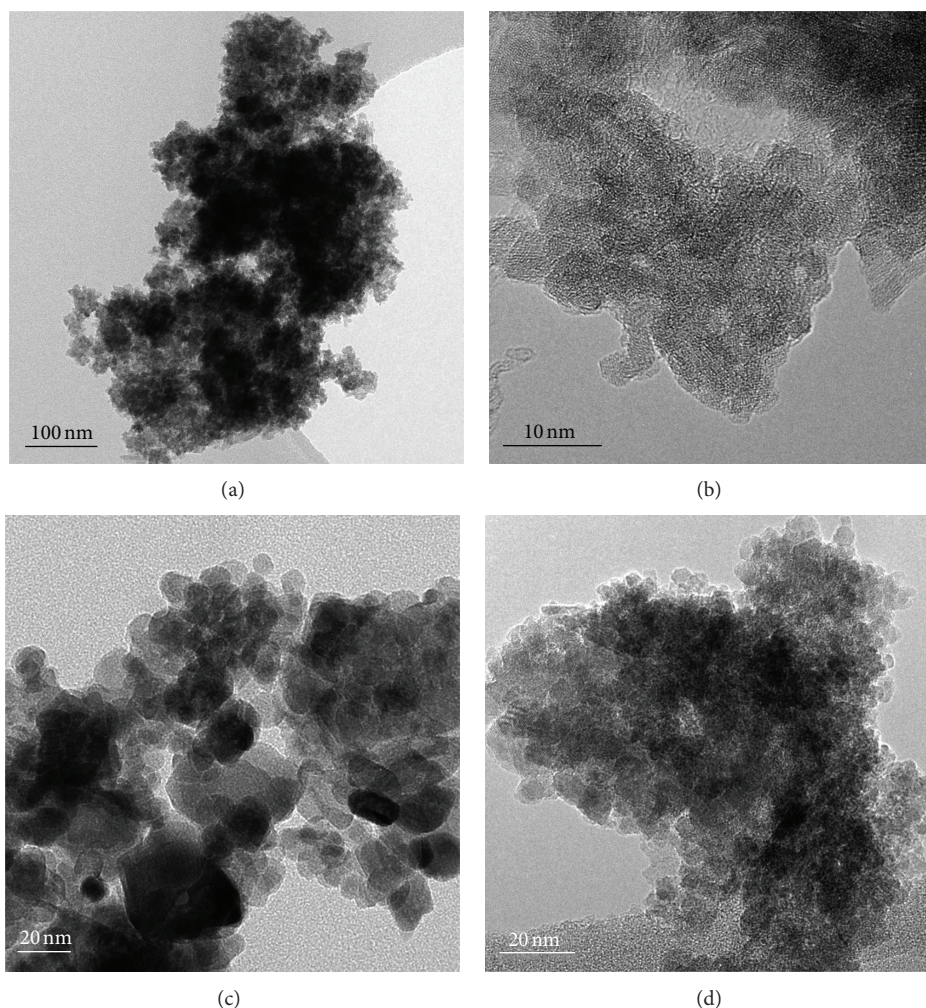


FIGURE 1: TEM pictures of Fe/Mn mixed metal oxide ((a), (b)), Mn_3O_4 (c), and Fe_2O_3 (d) nanoparticles.

oxide nanocomposites, Mn_3O_4 nanoparticles, and Fe_2O_3 nanoparticles. From Figure 1(a), it can be seen that the resultant composites were comprised of nanoparticles and these nanoparticles were aggregated together. Figure 1(b) is the HRTEM picture of the obtained nanocomposites. We can see that the diameter of these nanoparticles is about 3–5 nm and not well-crystallized. These nanoparticles were difficult to be distinguished. Figures 1(c) and 1(d) show the TEM pictures of the controlled experiments prepared by adding $\text{Fe}(\text{NO}_3)_3 \cdot 6\text{H}_2\text{O}$ or $\text{MnCl}_2 \cdot 4\text{H}_2\text{O}$ only. Figure 1(c) showed the obtained Mn_3O_4 nanoparticles. The picture presented that the Mn_3O_4 nanoparticles were highly crystalline and the diameter of the particles is about 10–50 nm, which is larger than that of mixed Fe/Mn metal oxides. Meanwhile, when using $\text{Fe}(\text{NO}_3)_3 \cdot 6\text{H}_2\text{O}$ as the only starting material, the Fe_2O_3 nanoparticles with a diameter of about 3–7 nm were obtained and these nanoparticles were also aggregated, as shown in Figure 1(d). By comparison of these four pictures, it was shown that the morphology of the mixed metal oxides was similar to that of Fe_2O_3 nanoparticles. Furthermore, we did not see any particles with size of more than 10 nm. This

observation implied that the size of Mn_3O_4 nanoparticles was reduced and the crystallinity was affected when using both $\text{Fe}(\text{NO}_3)_3 \cdot 6\text{H}_2\text{O}$ and $\text{MnCl}_2 \cdot 4\text{H}_2\text{O}$ as the starting material.

XRD characterization was performed to determine the crystalline structure of these composites and the results were shown in Figure 2. For the sample prepared using $\text{MnCl}_2 \cdot 4\text{H}_2\text{O}$ as the starting material, the diffraction pattern in Figure 2(a) agreed well with those for standard Mn_3O_4 (JCPDS 18-0803). For the sample prepared using $\text{Fe}(\text{NO}_3)_3 \cdot 6\text{H}_2\text{O}$ as the starting material, the diffraction peaks of as-synthesized products match well with those of Fe_2O_3 (JCPDS 25-1402), although the nanoparticles are not well-crystallized. However, when using both $\text{Fe}(\text{NO}_3)_3 \cdot 6\text{H}_2\text{O}$ and $\text{MnCl}_2 \cdot 4\text{H}_2\text{O}$ as the starting material, only a weak diffraction peak was detected for the prepared composites, as shown in Figure 2(c). This observation indicated that Fe/Mn mixed metal oxide nanocomposite was not well-crystallized, which was consistent with the TEM observations. Moreover, we found that adding of $\text{Fe}(\text{NO}_3)_3 \cdot 6\text{H}_2\text{O}$ led to the amorphous structure of the composites. Thus, owing to the not well-crystallized structure and small size of the sample, it was

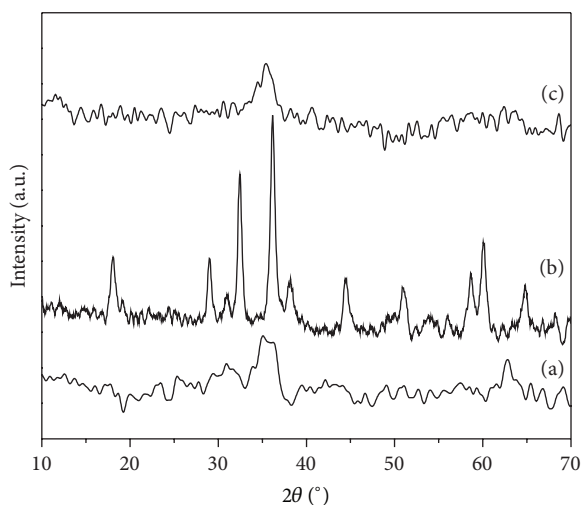


FIGURE 2: XRD patterns of Mn_3O_4 (a), Fe_2O_3 (b), and Fe/Mn mixed metal oxide (c) nanoparticles.

difficult to determine the exact structure of the obtained composite. In such a process, there were two possible products. One is to form MnFe_2O_4 nanoparticles. The other is mixed metal oxide composites. Due to the thermodynamic behavior of the MnFe_2O_4 nanoparticles [21] and the synthetic condition in our experiment, the obtained composites can only be made of mixed metal oxides. From the TEM and XRD analysis above, we speculated that the resultant composites may be made up of not well-crystallized Fe_2O_3 and Mn_3O_4 nanoparticles. However, this speculation has to be evidenced.

XPS characterization was involved to determine the structure. Figure 3 shows the XPS overall spectrum and the Mn_{2p} and Fe_{2p} spectra of the synthesized composites. The surface analysis indicated that only Fe, Mn, O, and C existed on the sample surface, implying that no other impurities existed in the product. The peak at 285.0 eV comes from the deposited carbon. From the Fe_{2p} spectra, the XPS peaks have a binding energy of 711.3 eV and a satellite feature centered at 719.9 eV, which is indicative of Fe(III) [3]. It can be concluded that only fully oxidized iron was on the sample. For the Mn species, the Mn $2p_{3/2}$ binding energy is 641.9 eV and Mn $2p_{1/2}$ binding energy is 653.6 eV, coming from Mn $2p_{3/2}$ and Mn $2p_{1/2}$ of Mn_3O_4 , which was in accordance with [21]. This result indicates that the $\text{MnCl}_2 \cdot 4\text{H}_2\text{O}$ species were fully oxidized into Mn_3O_4 . Based on the aforementioned characterizations, it could be suggested that the synthesized composites were mixed metal oxides composed of Fe_2O_3 and Mn_3O_4 . These results also demonstrated the efficiency of the grinding method for preparation of the mixed metal oxide composites.

3.2. Adsorption Kinetic Study. The as-synthesized composites were used as adsorbents for Cr(VI) removal. Figure 4 showed the effect of contact time on the adsorption of Cr(VI). It can be seen that the uptake of Cr(VI) was finished within 10 min with 93% of the Cr(VI) removed during the first minute of the reaction. The equilibrium time is independent of the initial

concentration of Cr(VI). The rapid adsorption of Cr(VI) by the composite is different from the microporous adsorption process. It is perhaps caused by external surface adsorption which is easy to access, while adsorption sites occurred in the exterior of porous adsorbents during the microporous adsorption process. At equilibrium, the adsorption capacities of Cr(VI) at initial concentrations of 50 and 150 mg/L were found to be 9.62 and 26.30 mg/g, respectively.

Compared with another oxide and their composites reported, the Fe/Mn mixed oxides nanocomposites were found to show higher adsorption capacity, as shown in Table 1. At the same time, the adsorption capacity and BET surface areas of the Fe/Mn mixed oxides nanocomposites were strongly dependent on the ratio of $\text{MnCl}_2 \cdot 4\text{H}_2\text{O}$ to KCl. For a grinding process, it is generally accepted that the necessary condition taking place in solid state reaction at room temperature is that one of the reactants should have crystalline waters or a low melting point on one hand, whilst on the other hand sufficient grinding is also required to provide the reactant molecules with more contact opportunities [22]. When the salts with crystalline water and other reactants were reacted, a layer of liquid film over particles was considered to be formed to construct a micro-aqueous-environment. Hereby, KCl and free water are expected to give a saturated solution of KCl. Then KCl was released to produce a shell surrounding the nanoparticles to prevent them from aggregating into larger particles [23]. Thus, the higher the $\text{MnCl}_2 \cdot 4\text{H}_2\text{O}$ to KCl ratio, the lower the crystal size and the higher BET surface areas. Secondly, the adsorption capacity of Fe/Mn mixed oxides composites was higher compared with separated $\gamma\text{-Fe}_2\text{O}_3$ and Mn_3O_4 . At the same time, we mixed the $\gamma\text{-Fe}_2\text{O}_3$ and Mn_3O_4 metal oxides together with Fe : Mn mole ratio equal to 2. The mixed adsorption capacity for Cr(VI) removal is lower than the prepared Fe/Mn mixed metal oxides. We speculated that the enhanced adsorption capacity may be caused by the synergistic effect of the mixed metal oxides.

3.3. Adsorption Isotherm. The adsorption isotherm experimental results for Cr(VI) on composites at pH 2, 7, and 10 and different initial Cr(VI) concentrations were shown in Figure 5. It was revealed that Cr(VI) uptake increased with the initial Cr(VI) concentrations for the composite. The equilibrium adsorption capacity decreased with an increase in pH, which indicates that the lower pH favors adsorption. The results were accordant with the results reported by Chen and his group [16, 17]. It appears that adsorption isotherms on the composites can be well described by the Langmuir equation.

3.4. Adsorbent Stability. To test the stability of the resultant composites, desorption and regeneration experiments were carried out. Figure 6 shows the reusability of the composites for Cr(VI) removal. For the desorption process, 0.01 M NaOH eluant was used and more than 95% of Cr(VI) could be removed from the adsorbent of nanocomposites within 1 h. The adsorbent was recovered by filtration and drying. Recovered nanocomposites were reused again for the adsorption

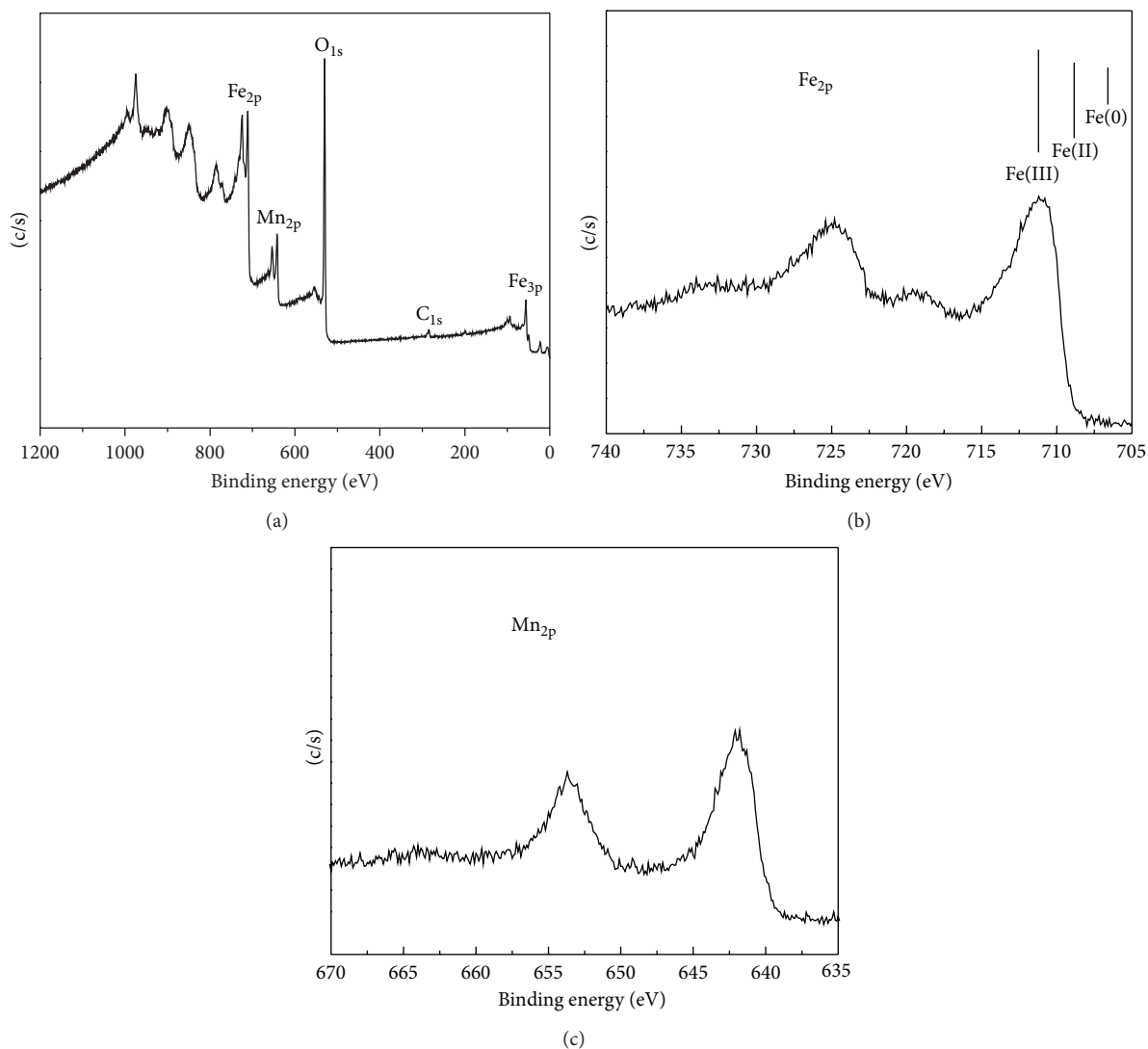


FIGURE 3: XPS spectra of Fe/Mn mixed metal oxides, (a) overall scan, (b) Fe_{2p} scan, and (c) Mn_{2p}.

of Cr(VI) and the adsorption capacity was tested. After 5 runs, the adsorption capacity tended to become steady. In the fifth cycle, the adsorption capacity was 25.3 mg/g which was 92% of the first cycle. The results indicated that the composites showed good stability and regeneration ability. In addition to chromium, iron and manganese were measured using ICP after each adsorption/desorption process, and the concentrations of these two metals were found to be nearly zero, indicating that the dissolution of the nanoparticles under the stated experimental conditions can be neglected.

3.5. Adsorbent Mechanism. For the removal of Cr(VI) from metal oxides, two commonly used mechanisms were reported by other researchers [16, 18]. One is the electrostatic attraction; the other is ion exchange. To find out any possible mechanism for Cr(VI) removal from the nanocomposites, the XPS characterization for the adsorption process was conducted. The first problem needed to be excluded is the valence change of the chromium during the adsorption

process. If the valence of the chromium changed from hexavalent to trivalent, it means that a chemical redox reaction happened and the whole process was not an adsorption process. Figure 7 showed the XPS spectra of Cr, Fe, and Mn species before adsorption and after adsorption at pH equal to 2. The peak for Cr 2p_{3/2} was centered at 579.8 eV and the peak for Cr 2p_{1/2} was centered at 587.2 eV, and both were entirely from Cr(VI) [24]. The Fe 2p_{3/2} spectrum registered at 711.5 eV, and the Fe 2p_{1/2} spectrum registered at 724.3 eV in the XPS spectra, which indicated fully oxidized iron on the surface. Mn 2p_{3/2} and Mn 2p_{1/2} peaks centered at 641.9 eV and 653.6 eV, respectively, which came from Mn₃O₄. However, the valence of the adsorbed chromium was not changed and the valence of manganese should not vary, because iron is fully oxidative. Thus, it can be suggested that there is no chemical redox reaction occurring in the adsorption process. But this does not mean that the electrostatic attraction is the only mechanism in the adsorption process. When pH is greater than pH_{ZPC} (=6.5), no Cr(VI) should be adsorbed on

TABLE 1: BET surface areas and removal capacity of different kinds of adsorbent samples.

Adsorbent samples	BET surface area ($\text{m}^2 \cdot \text{g}^{-1}$)	Adsorption capacity for Cr(VI) ($\text{mg} \cdot \text{g}^{-1}$)
$\text{Fe}_2\text{O}_3\text{-Mn}_3\text{O}_4$ (1:0)*	187	22.9
$\text{Fe}_2\text{O}_3\text{-Mn}_3\text{O}_4$ (1:2.5)*	213	21.3
$\text{Fe}_2\text{O}_3\text{-Mn}_3\text{O}_4$ (1:5)*	222	21.2
$\text{Fe}_2\text{O}_3\text{-Mn}_3\text{O}_4$ (1:10)*	264	24.6
$\text{Fe}_2\text{O}_3\text{-Mn}_3\text{O}_4$ (1:15)*	268	26.3
Mn_3O_4	61	11.6
$\gamma\text{-Fe}_2\text{O}_3$ [15]	178	19.4
Fe_3O_4	198	21.0
MnFe_2O_4 (MnO_2 and Fe_2O_3) [14]	208	31.3

*Different ratio of MnCl_2 to KCl in the preparation.

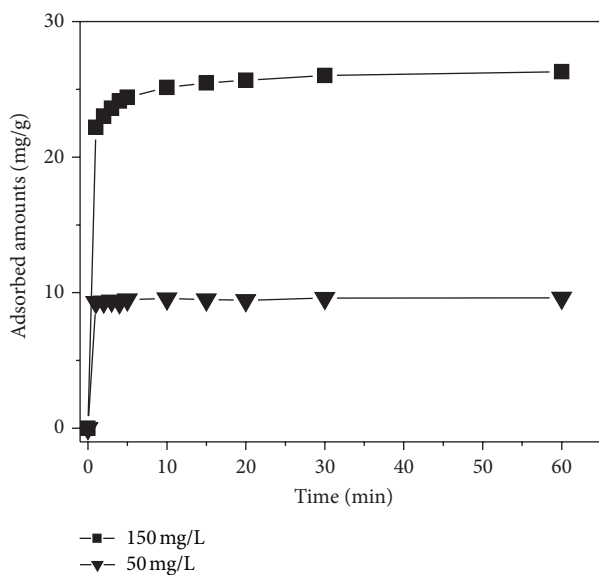


FIGURE 4: Kinetic study of Cr(VI) adsorption onto the Fe/Mn mixed metal oxides.

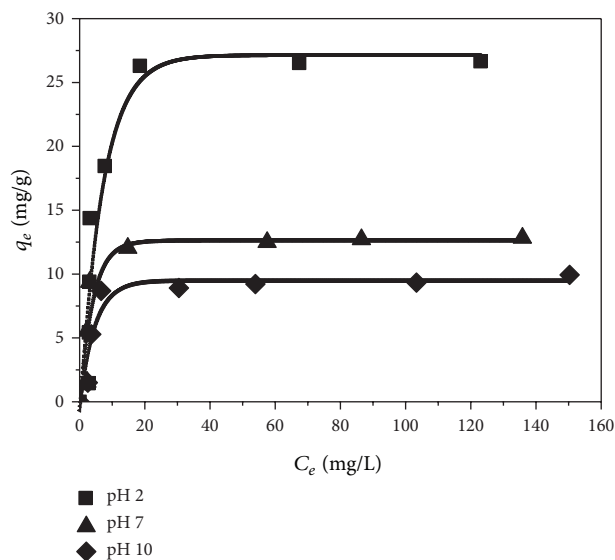


FIGURE 5: Langmuir isotherms of Cr(VI) adsorption onto the Fe/Mn mixed metal oxides at different pH.

the composites owing to the electrostatic repulsion. However, a certain amount of Cr(VI) ions was still adsorbed on the composites when the pH equal to 10. Therefore, there should be another mechanism involved in the chemical process. At pH greater than pH_{zpc} ($=6.5$), it is reported that the chromate can replace hydroxide from the surface of the hydrolyzed metal oxides as a result of the higher affinity of chromate ions with metal oxides than that of hydroxides with metal oxide [25]. Thus, it is concluded that the adsorption mechanism on the composite is the combination of electrostatic attraction and ion exchange.

4. Conclusion

In conclusion, Fe/Mn mixed metal oxide nanocomposites were successfully prepared using a grinding method at room temperature. The characterization results revealed that

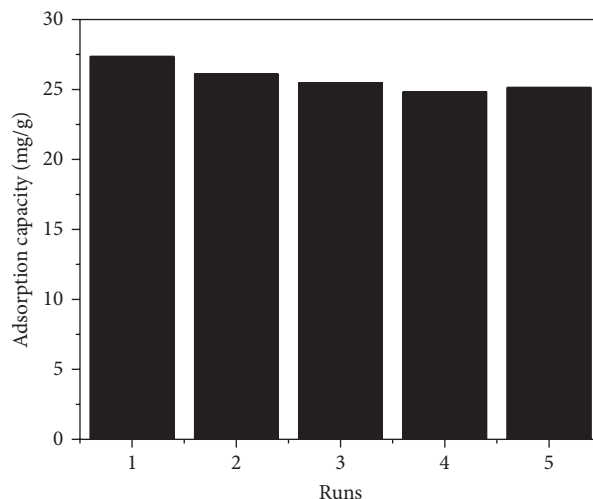


FIGURE 6: Regeneration studies of Fe/Mn mixed metal oxides after five cycles.

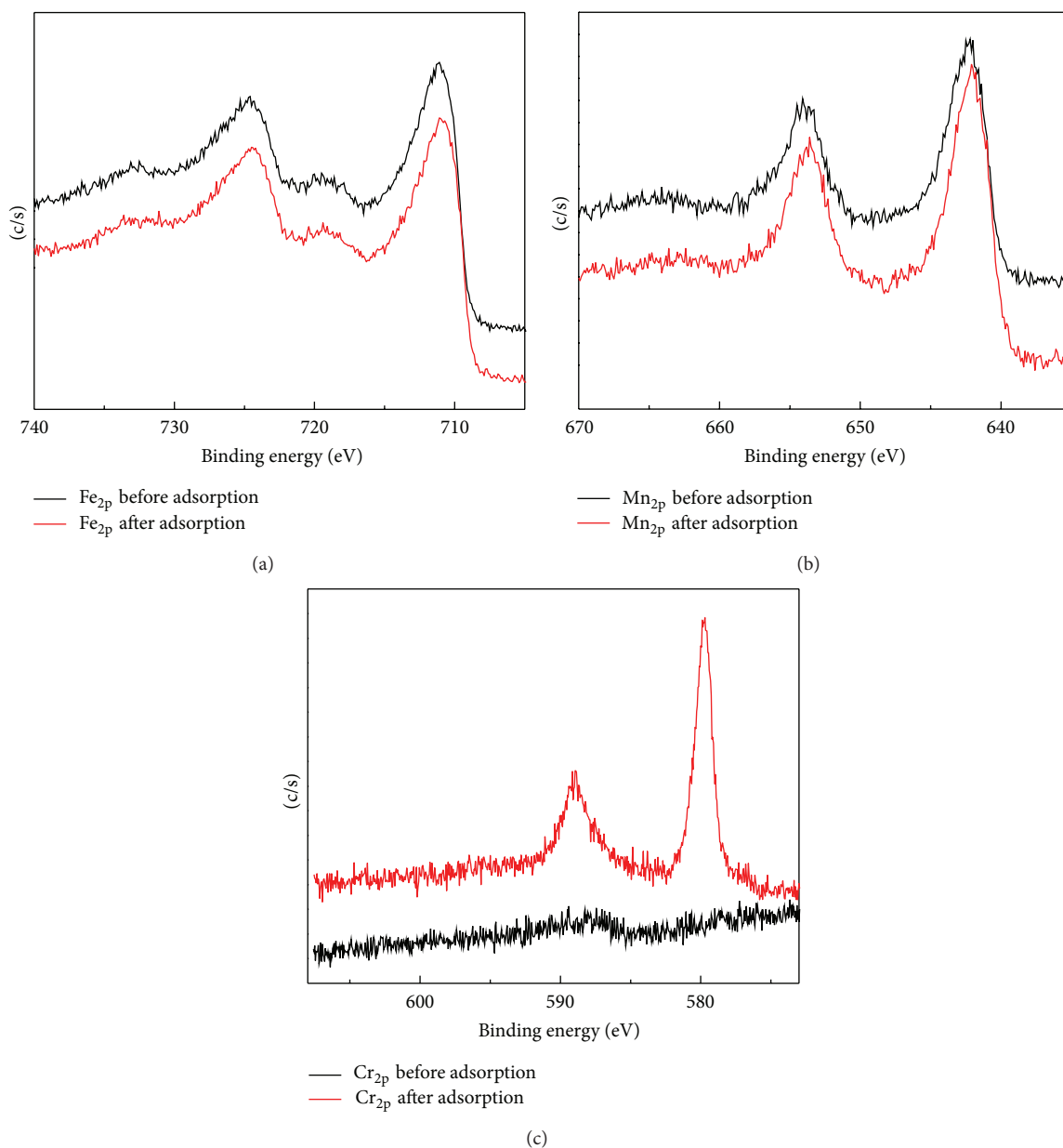


FIGURE 7: XPS spectra of Fe/Mn mixed metal oxides (a) before and (b) after adsorption of Cr(VI).

the as-synthesized composites were comprised of not well-crystallized Fe₂O₃ and Mn₃O₄ nanoparticles with a diameter about 3–5 nm. Compared with other oxides and their composites, the obtained composite was a very attractive adsorbent for the removal of the Cr(VI). The enhancement of the adsorption capacity was attributed to its higher BET surfaces and the synergistic effect coming from the mixed metal oxides. The resultant composite also showed good stability and regeneration activity. Combining the XPS results in the adsorption process, the mechanism for Cr(VI) removals on the composites was found to be a combination of electrostatic attraction and ion exchange. The new Fe/Mn mixed metal oxide composites synthesized in this work demonstrated a great potential application in the Cr(VI) removal.

Acknowledgments

The authors would like to acknowledge the funding support of Natural Science Foundation of Guangdong Province (S2012040007694), China Postdoctoral Science Foundation (20110490942), Fundamental Research Funds for the Central Universities (no. 11612328) and National Natural Science Foundation of China (51106185).

References

- [1] M. J. Zamzow, B. R. Eichbaum, K. R. Sandgren, and D. E. Shanks, "Removal of heavy metals and other cations from wastewater using zeolites," *Separation Science and Technology*, vol. 25, no. 13–15, pp. 1555–1569, 1990.

- [2] R. J. Crawford, I. H. Harding, and D. E. Mainwaring, "Adsorption and coprecipitation of multiple heavy metal ions onto the hydrated oxides of iron and chromium," *Langmuir*, vol. 9, no. 11, pp. 3057–3062, 1993.
- [3] S. R. Qiu, H. F. Lai, M. J. Roberson et al., "Removal of contaminants from aqueous solution by reaction with iron surfaces," *Langmuir*, vol. 16, no. 5, pp. 2230–2236, 2000.
- [4] R. Apak, E. Tütem, M. Hügül, and J. Hizal, "Heavy metal cation retention by unconventional sorbents (red muds and fly ashes)," *Water Research*, vol. 32, no. 2, pp. 430–440, 1998.
- [5] N. Ballav, A. Maity, and S. B. Mishra, "High efficient removal of chromium(VI) using glycine doped polypyrrole adsorbent from aqueous solution," *Chemical Engineering Journal*, vol. 198, pp. 536–546, 2012.
- [6] S. R. Singh and A. P. Singh, "Treatment of water containing chromium (VI) using rice husk carbon as a new low cost adsorbent," *International Journal of Environmental Research*, vol. 6, pp. 917–924, 2012.
- [7] J. Wang, L. Zhao, W. J. Duan, L. L. Han, and Y. F. Chen, "Adsorption of aqueous Cr(VI) by novel fibrous adsorbent with amino and quaternary ammonium groups," *Industrial & Engineering Chemistry Research*, vol. 51, pp. 13655–13662, 2012.
- [8] S. J. Ergas, B. M. Therriault, and D. A. Reckhow, "Evaluation of water reuse technologies for the textile industry," *Journal of Environmental Engineering*, vol. 132, no. 3, pp. 315–323, 2006.
- [9] S. R. Chowdhury, E. K. Yanful, and A. R. Pratt, "Chemical states in XPS and Raman analysis during removal of Cr(VI) from contaminated water by mixed maghemite-magnetite nanoparticles," *Journal of Hazardous Materials*, vol. 235, pp. 246–256, 2012.
- [10] D. C. Sharma and C. F. Forster, "Removal of hexavalent chromium from aqueous solutions by granular activated carbon," *Water SA*, vol. 22, no. 1, pp. 153–160, 1996.
- [11] Y. S. Ho, D. A. J. Wase, and C. F. Forster, "Kinetic studies of competitive heavy metal adsorption by sphagnum moss peat," *Environmental Technology*, vol. 17, no. 1, pp. 71–77, 1996.
- [12] H. C. P. Srivastava, R. P. Mathur, and I. Mehrotra, "Removal of chromium from industrial effluent by adsorption on sawdust," *Environmental Technology Letters*, vol. 7, no. 1, pp. 55–63, 1986.
- [13] L. S. Zhong, J. S. Hu, H. P. Liang, A. M. Cao, W. G. Song, and L. J. Wan, "Self-assembled 3D flowerlike iron oxide nanostructures and their application in water treatment," *Advanced Materials*, vol. 18, no. 18, pp. 2426–2848, 2006.
- [14] L. S. Zhong, J. S. Hu, A. M. Cao, Q. Liu, W. G. Song, and L. J. Wan, "3D flowerlike ceria micro/nanocomposite structure and its application for water treatment and CO removal," *Chemistry of Materials*, vol. 19, no. 7, pp. 1648–1655, 2007.
- [15] J. Hu, G. Chen, and I. M. C. Lo, "Selective removal of heavy metals from industrial wastewater using maghemite nanoparticle: performance and mechanisms," *Journal of Environmental Engineering*, vol. 132, no. 7, pp. 709–715, 2006.
- [16] J. Hu, G. Chen, and I. M. C. Lo, "Removal and recovery of Cr(VI) from wastewater by maghemite nanoparticles," *Water Research*, vol. 39, no. 18, pp. 4528–4536, 2005.
- [17] J. Hu, I. M. C. Lo, and G. Chen, "Fast removal and recovery of Cr(VI) using surface-modified jacobsite (MnFe_2O_4) nanoparticles," *Langmuir*, vol. 21, no. 24, pp. 11173–11179, 2005.
- [18] J. Hu, I. M. C. Lo, and G. Chen, "Performance and mechanism of chromate (VI) adsorption by δ -FeOOH-coated maghemite (γ - Fe_2O_3) nanoparticles," *Separation and Purification Technology*, vol. 58, no. 1, pp. 76–82, 2007.
- [19] V. V. Molchanov and R. A. Buyanov, "Mechanochemistry of catalysts," *Russian Chemical Reviews*, vol. 69, no. 5, pp. 435–450, 2000.
- [20] K. Muthukumar, N. Balasubramanian, and T. V. Ramakrishna, "Removal and recovery of chromium from plating waste using chemically activated carbon," *Metal Finishing*, vol. 93, no. 11, pp. 46–53, 1995.
- [21] G. Bonsdorf, K. Schäfer, K. Teske, H. Langbein, and H. Ullmann, "Stability region and oxygen stoichiometry of manganese ferrite," *Solid State Ionics*, vol. 110, no. 1–2, pp. 73–82, 1998.
- [22] Q. Li, G. Luo, J. Li, and X. Xia, "Preparation of ultrafine MnO_2 powders by the solid state method reaction of KMnO_4 with Mn(II) salts at room temperature," *Journal of Materials Processing Technology*, vol. 137, no. 1–3, pp. 25–29, 2003.
- [23] J. Lu, S. Yang, K. M. Ng et al., "Solid-state synthesis of monocrySTALLINE iron oxide nanoparticle based ferrofluid suitable for magnetic resonance imaging contrast application," *Nanotechnology*, vol. 17, no. 23, pp. 5812–5820, 2006.
- [24] M. Ding, B. H. W. S. De Jong, S. J. Roosendaal, and A. Vredenberg, "XPS studies on the electronic structure of bonding between solid and solutes: adsorption of arsenate, chromate, phosphate, Pb^{2+} , and Zn^{2+} ions on amorphous black ferric oxyhydroxide," *Geochimica et Cosmochimica Acta*, vol. 64, no. 7, pp. 1209–1219, 2000.
- [25] M. Dimitri, G. Vladimir, and W. Abraham, *Ion Exchange*, Marcel Dekker, New York, NY, USA, 2000.

Research Article

Influence of the Mixing Ways of Reactants on ZnO Morphology

Lining Yang and Lan Xiang

Department of Chemical Engineering, Tsinghua University, Beijing 100084, China

Correspondence should be addressed to Lan Xiang; xianglan@mail.tsinghua.edu.cn

Received 29 December 2012; Accepted 27 February 2013

Academic Editor: Guo Gao

Copyright © 2013 L. Yang and L. Xiang. This is an open access article distributed under the Creative Commons Attribution License, which permits unrestricted use, distribution, and reproduction in any medium, provided the original work is properly cited.

ZnO particles with various morphologies were synthesized by mixing ZnSO_4 and NaOH solutions at 25°C followed by aging of the suspensions at $40\text{--}80^\circ\text{C}$ for 2.0 h, keeping the initial molar ratio of Zn^{2+} to OH^- at 1:4. ZnO irregular plates were prepared by adding NaOH to ZnSO_4 while $\epsilon\text{-Zn(OH)}_2$ rhombic particles were produced using the opposite mixing way. After aging of the slurries at 80°C for 2.0 h, the ZnO plates were kept stable while the $\epsilon\text{-Zn(OH)}_2$ rhombic particles were converted to ZnO whiskers with a length of $1.0\text{--}4.0\ \mu\text{m}$ and a diameter of $0.03\text{--}0.3\ \mu\text{m}$. Thermodynamic analysis indicated that the formation of the Zn-bearing precipitates (ZnO or $\epsilon\text{-Zn(OH)}_2$) at room temperature was connected closely with the solution composition.

1. Introduction

The synthesis of ZnO with varying morphologies such as the multipods [1], the wires [2], the tubes [3], and the flowers [4] via the liquid-phase routes, including the chemical deposition [5], the microemulsion [6], the hydrothermal/solvothermal/sol-gel ways [7–9], the template-assisted method, and so forth [10], has attracted much attention in recent years owing to the moderate condition and the easy control of the properties of the ZnO products. Many former researchers have focused on the influence of surfactants on the morphology control of ZnO. For example, Sun et al. [11] synthesized ZnO nanorods from Zn via the cetyltrimethylammonium-bromide- (CTAB-) assisted route and found that the presence of CTAB promoted the erosion of Zn and the hydrothermal formation of the ZnO nanorods at 180°C . The needle- and flower-like ZnO nanocrystals were fabricated at 85°C by using ZnCl_2 and NaOH as the reactants in the presence of $0.2\ \text{mol}\cdot\text{L}^{-1}$ sodium dodecyl sulfate (SDS) [12]. Some researchers have also studied the influence of the reactants, the solvent, and the pH on the morphology of ZnO. For example, Gao et al. [13] fabricated the rotor-like ZnO at 100°C by treating the suspension containing the rod-like ZnO powders, which were produced from the $\text{NH}_3\cdot\text{H}_2\text{O}$

and ZnCl_2 and a saturated Zn(OH)_4^{2-} solution obtained by dissolving ZnO in $5\ \text{mol}\cdot\text{L}^{-1}$ NaOH. Zheng et al. [14] prepared the porous octahedron- and rod-shaped ZnO architectures from $\text{ZnC}_2\text{O}_4\cdot 2\text{H}_2\text{O}$, which was produced by the solvothermal treatment of the mixture of ZnCl_2 , $\text{H}_2\text{C}_2\text{O}_4\cdot 2\text{H}_2\text{O}$, N-dimethylformamide (DMF), and methyl orange (MO) at 180°C . Pal et al. [15] synthesized ZnO crystals with granular, flower-like and rod-like morphology by adjusting the pH of the suspension containing $\text{Zn(CH}_3\text{COO)}_2\cdot 2\text{H}_2\text{O}$ and ethylenediamine (EDA) at $80\text{--}100^\circ\text{C}$.

Herein, a facile precipitation-aging method was developed in this paper to synthesize ZnO nanoparticles and ZnO whiskers simply by changing the mixing of ZnSO_4 and NaOH solutions at room temperature followed by aging of the suspensions at $40\text{--}80^\circ\text{C}$. The influence of the solution composition on the formation of the Zn-bearing precursors and the morphology of the aging products were investigated.

2. Experimental

In a typical procedure, 20 mL of $8.0\ \text{mol}\cdot\text{L}^{-1}$ NaOH was added drop-wise ($0.67\ \text{mL}\cdot\text{min}^{-1}$) into 20 mL of $2.0\ \text{mol}\cdot\text{L}^{-1}$ ZnSO_4 at 25°C , or using the opposite mixing way. The initial molar

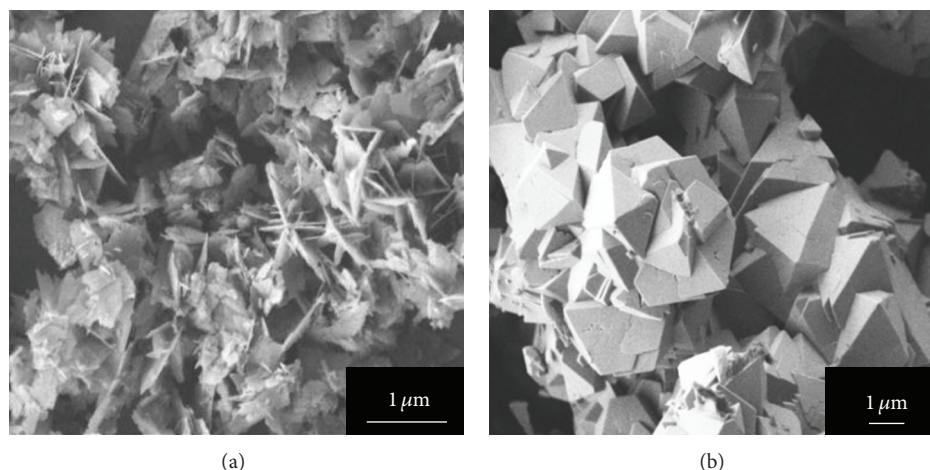


FIGURE 1: Morphology of the precipitates formed at 25°C. Mixing of reactants: (a) adding NaOH to ZnSO₄; (b) adding ZnSO₄ to NaOH.

ratio of Zn²⁺ to OH⁻ was 1:4. After being stirred (150 min⁻¹) for 1.0 h, the suspension was transferred to a Teflon-lined stainless autoclave with an inner volume of 60 mL and kept under isothermal condition at 80°C for 2.0 h. The suspension was then cooled down to room temperature naturally; the precipitate was filtered, washed with deionized water for three times, and dried at 80°C for 4.0 h.

The morphology and structure of the samples were characterized by the field-emission scanning electronic microscope (FE-SEM, JOEL 7401F, Japan) and the X-ray powder diffraction (XRD, D8 Advance, Bruker, Germany) using CuK α radiation ($\lambda = 1.5418 \text{ \AA}$), respectively. The solution pH was detected by the pH meter (FE20, METTLER-TOLEDO, Germany). The concentrations of soluble Zn²⁺ and OH⁻ were analyzed by the ethylene diaminetetraacetic acid (EDTA) titration and the acid-base neutralization methods, respectively.

3. Results and Discussion

3.1. Influence of the Mixing Way on the Formation of the Zn-Bearing Precipitates. Figures 1 and 2 show the morphology and the XRD patterns of the Zn-bearing precipitates formed at 25°C. Wurtzite ZnO (space group $P6_3mc$, $a = b = 3.250 \text{ \AA}$, $c = 5.207 \text{ \AA}$) irregular plates with a diameter of 0.3–0.6 μm were prepared if NaOH was added to ZnSO₄, while ϵ -Zn(OH)₂ (space group $P212121$, $a = 8.490 \text{ \AA}$, $b = 5.162 \text{ \AA}$, $c = 4.917 \text{ \AA}$) agglomerated octahedral particles with a diameter of 1.0–3.0 μm were produced if ZnSO₄ was added to NaOH.

Figure 3 shows the variation of the total Zn²⁺ concentration ($[\text{Zn}]_{\text{T}}$) and the solution pH with the reaction time at 25°C. In the case of adding NaOH to ZnSO₄ (Figure 3(a)), with the increase of the reaction time from 0 to 60 min, $[\text{Zn}]_{\text{T}}$ decreased from 2.0 mol·L⁻¹ to 0.08 mol·L⁻¹ and the solution pH increased from 3.8 to 12.6; in the case of adding ZnSO₄ to NaOH (Figure 3(b)), the increase of the reaction time from 0 to 60 min led to the decrease of [OH⁻] from 8.0 mol·L⁻¹ to 1.4 mol·L⁻¹, while the $[\text{Zn}]_{\text{T}}$ increased from

0 to 0.36 mol·L⁻¹ at the initial 30 min and then decreased gradually to 0.19 mol·L⁻¹ as the reaction time increased from 30 min to 60 min.

Table 1 shows the possible equilibrium reactions existed in the ZnSO₄-NaOH-H₂O system. The equilibrium constants in Table 1 were calculated from the HSC 7.1 software.

Based on the simultaneous equilibrium principle, the equilibrium concentrations of the soluble ions in varying time can be calculated from the knowing concentrations of total soluble Zn²⁺, OH⁻, Na⁺, and SO₄²⁻. To simplify the calculation process, the activity of each species was replaced by concentration due to the shortage of the basic data. Based on these equations above and the experimental data in Figure 3, the concentrations of the soluble Zn-bearing species at different reaction time were calculated and the results are shown in Figure 4.

In the case of adding NaOH to ZnSO₄ (Figure 4(a)), Zn(OH)_{2(aq)} was the predominant species and the increase of the reaction time from 10 min to 60 min led to the decrease of [Zn²⁺] and [ZnOH⁺] and the increase of [Zn(OH)₃⁻], [HZnO₂⁻], [Zn(OH)₄²⁻], and [ZnO₂²⁻]. In the case of adding ZnSO₄ to NaOH (Figure 4(b)), all of the Zn-bearing species were kept quite stable within 60 min, and the order of concentrations for these species was [Zn(OH)₄²⁻] \approx [ZnO₂²⁻] > [Zn(OH)₃⁻] \approx [HZnO₂⁻] > [Zn(OH)_{2(aq)}] > [ZnOH⁺] > [Zn²⁺]. The difference in the solution composition may be one of the major reasons for the formation of different precipitates (ZnO and ϵ -Zn(OH)₂).

3.2. Aging of the ZnO and ϵ -Zn(OH)₂ Precipitates. The morphology and the XRD patterns of the aging products formed from ZnO and ϵ -Zn(OH)₂ precursors were shown in Figures 5 and 6, respectively. Irregular ZnO plates with a similar morphology using the ZnO precursor were formed after aging treatment at 40–80°C, indicating that ZnO precursor was quite stable under the experimental conditions. In the case of the ϵ -Zn(OH)₂ precursor, the precursor was stable up to 40°C, but changed

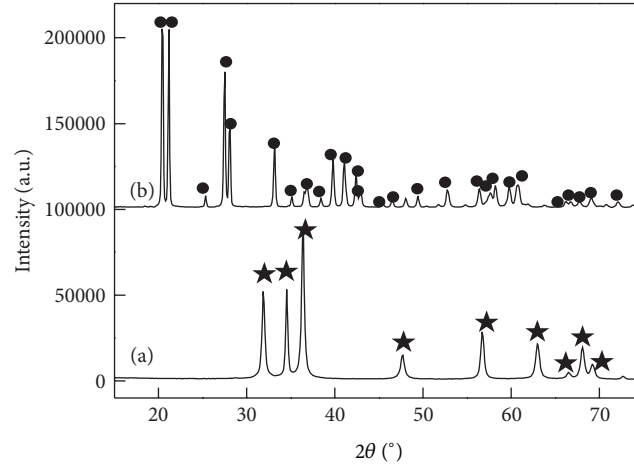


FIGURE 2: XRD patterns of the precipitates formed at 25°C. Mixing of reactants: (a) adding NaOH to ZnSO₄; (b) adding ZnSO₄ to NaOH. ★: ZnO, •: ε-Zn(OH)₂.

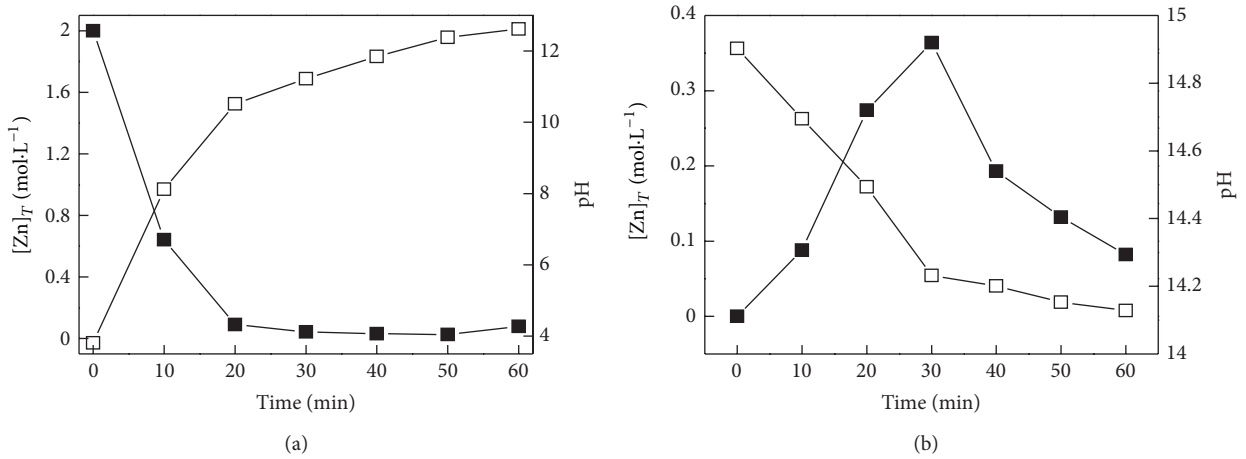


FIGURE 3: Influence of the mixing ways of the reactants on [Zn]_T and pH. Mixing of reactants: (a) adding NaOH to ZnSO₄; (b) adding ZnSO₄ to NaOH; ■: [Zn]_T, □: pH.

to ZnO rods with a length of 0.1–0.4 μm and a diameter of 40–100 nm and ZnO whiskers with a length of 1.0–14.0 μm and a diameter of 0.03–0.3 μm after aging treatment at 60°C and 80°C, respectively. The different aging behaviors of ZnO and ε-Zn(OH)₂ precursors may be connected with their different dissolution abilities in NaOH solution.

Figure 7 shows the dissolution of ZnO and ε-Zn(OH)₂ after mixing excessive amount (3.500 g) of ZnO or ε-Zn(OH)₂ with 25 mL of 8.0 mol·L⁻¹ NaOH at 25–80°C for 2.0 h. The increase of temperature from 25°C to 80°C favored the dissolution of ZnO and ε-Zn(OH)₂ in NaOH solution. Compared with ZnO, ε-Zn(OH)₂ was more soluble, which favored the formation of ZnO whiskers via the dissolution-precipitation route [16]:

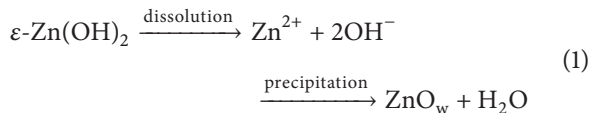


TABLE 1: Thermodynamic equilibrium reactions in ZnSO₄-NaOH-H₂O system (298 K).

Reactions	Constant	
H ₂ O = H ⁺ + OH ⁻	1.02 × 10 ⁻¹⁴	(1)
ZnSO ₄ = Zn ²⁺ + SO ₄ ²⁻	2.23 × 10 ³	(2)
HSO ₄ ⁻ = SO ₄ ²⁻ + H ⁺	1.04 × 10 ⁻²	(3)
H ₂ SO ₄ = HSO ₄ ⁻ + H ⁺	3.46 × 10 ⁹	(4)
NaOH = Na ⁺ + OH ⁻	8.45 × 10 ⁶	(5)
Na ₂ SO ₄ = 2Na ⁺ + SO ₄ ²⁻	4.73 × 10 ⁻¹	(6)
Zn ²⁺ + 2OH ⁻ = HZnO ₂ ⁻ + H ⁺	1.73	(7)
Zn ²⁺ + 2OH ⁻ = ZnO ₂ ²⁻ + 2H ⁺	2.90 × 10 ⁻¹³	(8)
Zn ²⁺ + OH ⁻ = ZnOH ⁺	1.44 × 10 ⁶	(9)
Zn ²⁺ + 2OH ⁻ = Zn(OH) _{2(aq)}	1.16 × 10 ¹³	(10)
Zn ²⁺ + 3OH ⁻ = Zn(OH) ₃ ⁻	2.50 × 10 ¹⁴	(11)
Zn ²⁺ + 4OH ⁻ = Zn(OH) ₄ ²⁻	4.61 × 10 ¹⁵	(12)

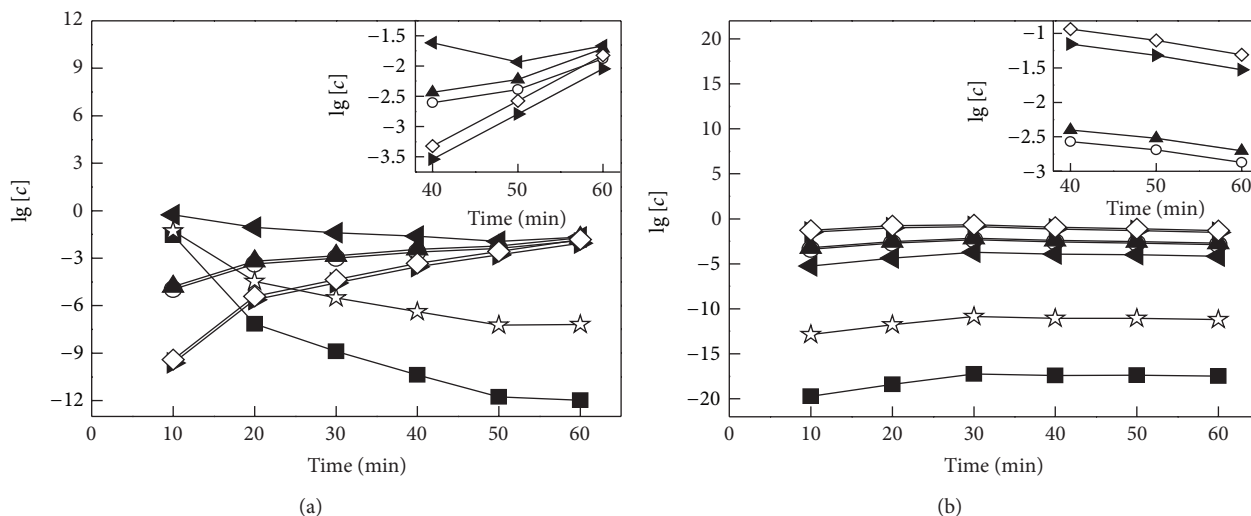


FIGURE 4: Variation of the soluble Zn-bearing species with time. Mixing of reactants: (a) adding NaOH to ZnSO_4 ; (b) adding ZnSO_4 to NaOH. ■: Zn^{2+} , ○: HZnO_2^- , ►: ZnO_2^{2-} , ☆: ZnOH^+ , ◄: $\text{Zn(OH)}_{2(\text{aq})}$, ▲: Zn(OH)_3^- , ◇: Zn(OH)_4^{2-} .

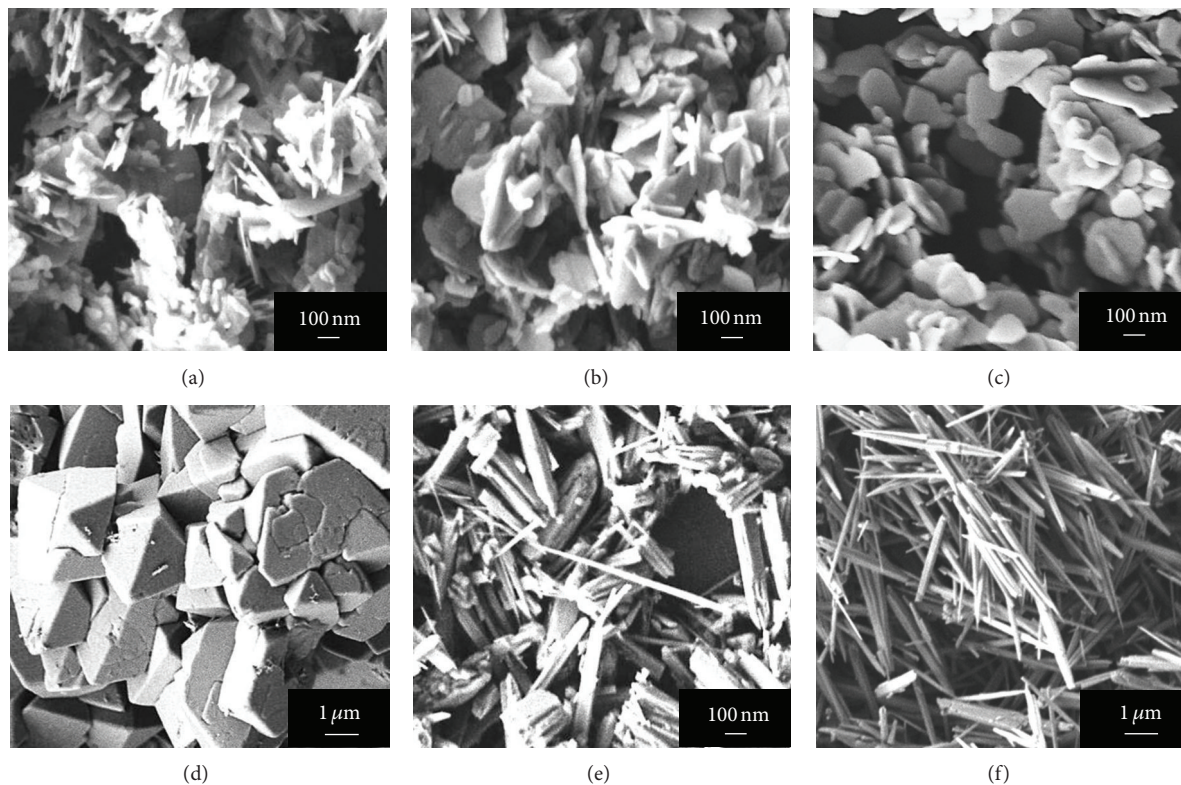


FIGURE 5: Morphology of the aging products formed from ZnO ((a)–(c)) and $\epsilon\text{-Zn(OH)}_2$ ((d)–(f)). Aging temperature ($^{\circ}\text{C}$): (a), (d): 40; (b), (e): 60; (c), (f): 80.

4. Conclusions

ZnO particles and whiskers were synthesized by changing the mixing ways of ZnSO_4 and NaOH at room temperature followed by aging of the suspensions at 40–80 $^{\circ}\text{C}$ for 2.0 h. Irregular ZnO plates were formed by adding NaOH to ZnSO_4 while $\epsilon\text{-Zn(OH)}_2$ rhombic particles were produced using the

opposite mixing way. Thermodynamic analysis indicated that the formation of ZnO and $\epsilon\text{-Zn(OH)}_2$ in different mixing ways of ZnSO_4 and NaOH should be attributed to the different solution compositions. The aging of the slurries containing $\epsilon\text{-Zn(OH)}_2$ and NaOH at 80 $^{\circ}\text{C}$ for 2.0 h led to the formation of ZnO whiskers with a length of 1.0–4.0 μm and a diameter of 0.03–0.3 μm owing to the easy dissolving of

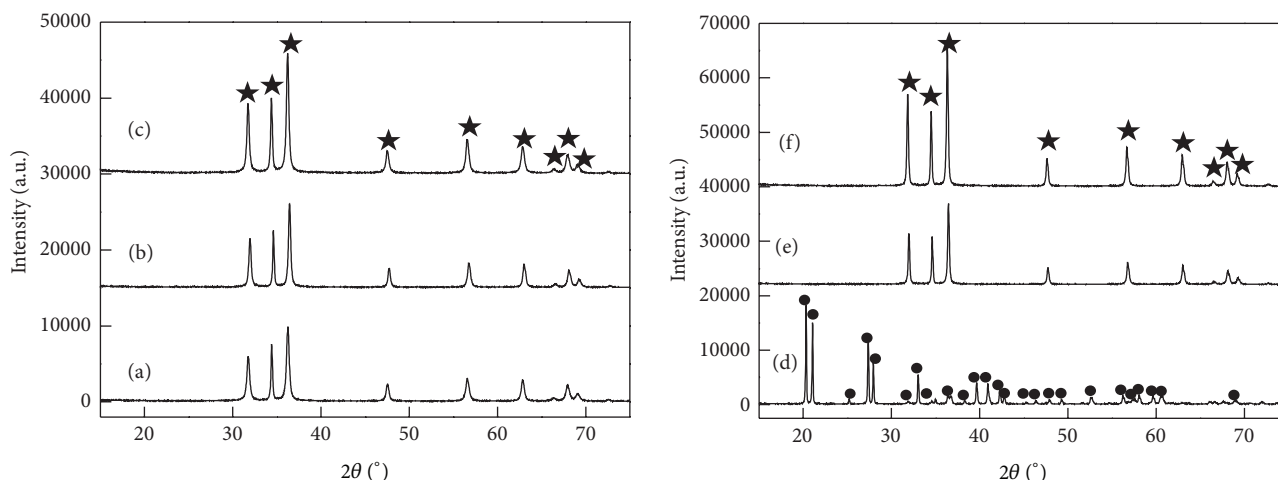


FIGURE 6: XRD patterns of the aging products formed from ZnO ((a)–(c)) and ϵ -Zn(OH)₂ ((d)–(e)). Aging temperature (°C): (a), (d): 40; (b), (e): 60; (c), (f): 80; ★: ZnO, •: ϵ -Zn(OH)₂.

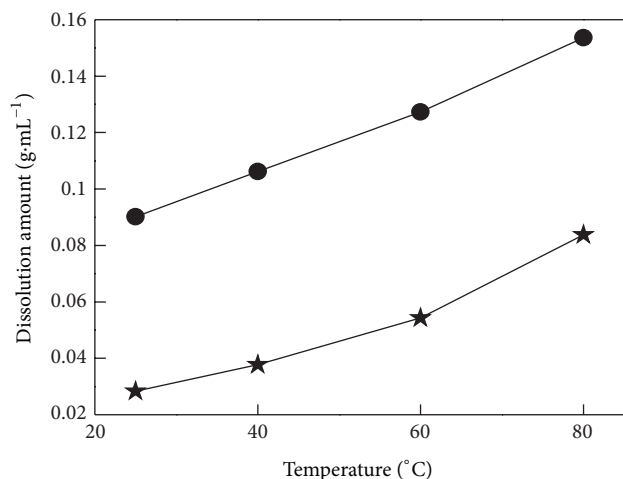


FIGURE 7: Dissolution curves of ϵ -Zn(OH)₂ and ZnO in NaOH solution; ★: ZnO, •: ϵ -Zn(OH)₂.

ϵ -Zn(OH)₂ in NaOH solution, while the ZnO plates were quite stable throughout the aging treatment.

Acknowledgments

This work was supported by the National Natural Science Foundation of China (no. 51174125 and no. 51234003) and the National Hi-tech Research and Development Program of China (863 Program, 2012AA061602).

References

- [1] J. Wang and L. Gao, "Synthesis of uniform rod-like, multi-pod-like ZnO whiskers and their photoluminescence properties," *Journal of Crystal Growth*, vol. 262, no. 1–4, pp. 290–294, 2004.
- [2] J. Zhang, L. Sun, H. Pan, C. Liaoa, and C. Yan, "ZnO nanowires fabricated by a convenient route," *New Journal of Chemistry*, vol. 26, no. 1, pp. 33–34, 2002.
- [3] B. I. Seo, U. A. Shaislamov, M. H. Ha, S. W. Kim, H. K. Kim, and B. Yang, "ZnO nanotubes by template wetting process," *Physica E*, vol. 37, no. 1–2, pp. 241–244, 2007.
- [4] R. Wahab, S. G. Ansari, Y. S. Kim et al., "Low temperature solution synthesis and characterization of ZnO nano-flowers," *Materials Research Bulletin*, vol. 42, no. 9, pp. 1640–1648, 2007.
- [5] J. Lu and K. M. Ng, "Efficient, one-step mechanochemical process for the synthesis of ZnO nanoparticles," *Industrial & Engineering Chemistry Research*, vol. 47, pp. 1095–1101, 2008.
- [6] X. Li, G. He, G. Xiao, H. Liu, and M. Wang, "Synthesis and morphology control of ZnO nanostructures in microemulsions," *Journal of Colloid and Interface Science*, vol. 333, no. 2, pp. 465–473, 2009.
- [7] B. Cheng and E. T. Samulski, "Hydrothermal synthesis of one-dimensional ZnO nanostructures with different aspect ratios," *Chemical Communications*, vol. 10, no. 8, pp. 986–987, 2004.
- [8] A. Pan, R. Yu, S. Xie, Z. Zhang, C. Jin, and B. Zou, "ZnO flowers made up of thin nanosheets and their optical properties," *Journal of Crystal Growth*, vol. 282, no. 1–2, pp. 165–172, 2005.
- [9] X. Yang, C. Shao, H. Guan, X. Li, and J. Gong, "Preparation and characterization of ZnO nanofibers by using electrospun PVA/zinc acetate composite fiber as precursor," *Inorganic Chemistry Communications*, vol. 7, no. 2, pp. 176–178, 2004.
- [10] X. Yan, Z. Li, R. Chen, and W. Gao, "Template growth of ZnO nanorods and microrods with controllable densities," *Crystal Growth and Design*, vol. 8, no. 7, pp. 2406–2410, 2008.
- [11] X. M. Sun, X. Chen, Z. X. Deng, and Y. D. Li, "A CTAB-assisted hydrothermal orientation growth of ZnO nanorods," *Materials Chemistry and Physics*, vol. 78, no. 1, pp. 99–104, 2003.
- [12] J. Xie, P. Li, Y. Li, Y. Wang, and Y. Wei, "Morphology control of ZnO particles via aqueous solution route at low temperature," *Materials Chemistry and Physics*, vol. 114, no. 2–3, pp. 943–947, 2009.
- [13] X. P. Gao, Z. F. Zheng, H. Y. Zhu et al., "Rotor-like ZnO by epitaxial growth under hydrothermal conditions," *Chemical Communications*, no. 12, pp. 1428–1429, 2004.
- [14] J. Zheng, Z. Y. Jiang, Q. Kuang, Z. X. Xie, R. B. Huang, and L. S. Zheng, "Shape-controlled fabrication of porous ZnO

architectures and their photocatalytic properties," *Journal of Solid State Chemistry*, vol. 182, no. 1, pp. 115–121, 2009.

- [15] U. Pal, J. G. Serrano, P. Santiago, G. Xiong, K. B. Ucer, and R. T. Williams, "Synthesis and optical properties of ZnO nanostructures with different morphologies," *Optical Materials*, vol. 29, no. 1, pp. 65–69, 2006.
- [16] R. A. McBride, J. M. Kelly, and D. E. McCormack, "Growth of well-defined ZnO microparticles by hydroxide ion hydrolysis of zinc salts," *Journal of Materials Chemistry*, vol. 13, no. 5, pp. 1196–1201, 2003.

Research Article

Effect of Copper Nanoparticles Dispersion on Catalytic Performance of Cu/SiO₂ Catalyst for Hydrogenation of Dimethyl Oxalate to Ethylene Glycol

Yajing Zhang, Na Zheng, Kangjun Wang, Sujuan Zhang, and Jing Wu

College of Chemical Engineering, Shenyang University of Chemical Technology, Shenyang 110142, China

Correspondence should be addressed to Jing Wu; wujing7275@163.com

Received 14 January 2013; Accepted 10 February 2013

Academic Editor: Guo Gao

Copyright © 2013 Yajing Zhang et al. This is an open access article distributed under the Creative Commons Attribution License, which permits unrestricted use, distribution, and reproduction in any medium, provided the original work is properly cited.

Cu/SiO₂ catalysts, for the synthesis of ethylene glycol (EG) from hydrogenation of dimethyl oxalate (DMO), were prepared by ammonia-evaporation and sol-gel methods, respectively. The structure, size of copper nanoparticles, copper dispersion, and the surface chemical states were investigated by X-ray diffraction (XRD), transmission electron microscopy (TEM), temperature-programmed reduction (TPR), and X-ray photoelectron spectroscopy (XPS) and N₂ adsorption. It is found the structures and catalytic performances of the catalysts were highly affected by the preparation method. The catalyst prepared by sol-gel method had smaller average size of copper nanoparticles (about 3-4 nm), better copper dispersion, higher Cu⁺/C⁰ ratio and larger BET surface area, and higher DMO conversion and EG selectivity under the optimized reaction conditions.

1. Introduction

Ethylene glycol (EG) is widely used as solvent, antifreezer, polyester fibers, and precursors in lubricant and polyester manufacture [1]. At present, a universal industrial approach to EG is the direct hydrate from ethylene oxide obtained by oxidation of ethylene with air or oxygen, while the ethylene comes from the petroleum cracking process. However, as petroleum resources shrink and the demand for EG constantly increases, the synthesis of EG from syngas attracts considerable attention because it provided an alternative non-petroleum route to produce EG [2]. Two steps are included in this route: first, the coupling of CO with methanol to oxalates; second, hydrogenation of oxalates to EG [3, 4]. Considerable efforts have been focused on the second step. The hydrogenation process can be completed by both homogeneous and heterogeneous catalysis reactions. Compared with homogeneous hydrogenation, heterogeneous process has advantages of easy to separate product and low cost. Therefore, much attention has been focused investigation on the heterogeneous catalysts [5–7]. It is known that hydrogenolysis of monoalkyl ester to alcohol has been in

successful industrial operation and the copper-based catalysts are suitable for the process [8]. However, compared with hydrogenolysis of monoalkyl ester to alcohol, hydrogenolysis of dialkyl ester is more difficult considering that this selective hydrogenation has to be sufficient to reduce the dialkyl ester and avoid overhydrogenolysis of glycol to ethanol and other by-products [9, 10].

Previous studies have shown that the copper loading, Ni species doping, preparation temperature, and support acidity have an influence on texture, structure, and catalytic performance of the catalyst [11, 12]. To achieve high catalytic activity, it is important to disperse fine metal particles on the surface of a support even at higher metal loading [13]. Although various preparation methods have been reported, including sol-gel, ammonia-evaporation, deposition-precipitation, impregnation, and coprecipitation [14–16], few reports focus on the influence of the copper nanoparticles dispersion on the Cu/SiO₂ catalysts for hydrogenation of DMO to EG.

In the present study, for comparison purpose, we adopted the sol-gel and ammonia-evaporation methods to prepare Cu/SiO₂ catalysts with same Cu loadings and evaluate their catalytic properties for the hydrogenolysis of DMO to EG,

respectively. In an attempt to understand the effect of Cu nanoparticles dispersion and preparation methods on the catalyst structure and catalytic performance, we characterized these catalysts by means of the techniques such as nitrogen physisorption, X-ray diffraction (XRD), X-ray photoelectron spectroscopy (XPS), temperature-programmed reduction (TPR), and transmission electron microscopy (TEM). This work not only can provide a research foundation for the development of industrial catalysts for the synthesis of EG via a nonpetroleum route but also can provide some deep insight for the design of high active copper-based catalysts for other reactions.

2. Experimental Section

2.1. Catalyst Preparation. All the reagents used are analytically pure. Cu/SiO₂ catalysts were prepared by ammonia-evaporation and sol-gel methods, with the same nominal copper loading of 30 wt% (CuO/(CuO + SiO₂)), respectively. The ammonia-evaporation method was carried out as follows. At room temperature, 13.6 g Cu(NO₃)₂·3H₂O (Sinopharm Chemical Reagent Ltd.) was dissolved in 150 mL of deionized water. 42 mL of 28% ammonia aqueous solution (Sinopharm Chemical Reagent Ltd.) was added and stirred for 30 min. Then 42.0 g of silica sol (JA-25, Qingdao Haiyang Chemical Ltd.) was added to the copper ammonia complex solution and the initial pH of the suspension was 11–12. The suspension was stirred for another 3 h. Then the suspension was heated to 363 K and kept at this temperature for the evaporation of ammonia. The evaporation process was not terminated until the pH decreased gradually to 6–7. Then the product was filtered, washed by deionized water for several times, and dried at 393 K for 12 h. Then the product was calcined in a muffle oven at 723 K for 4 h. After calcination, the catalyst was pelletized, crushed, and sieved to 20–40 mesh. The catalyst was referred to as Cu/SiO₂-AE.

The sol-gel method was carried out as follows. Tetraethoxysilane (TEOS, Sinopharm Chemical Reagent Ltd., China) and copper nitrate trihydrate were used as the silica and copper sources, respectively. The mixture of ethanol (C₂H₅OH) and water (H₂O) was used as solvent, the mass ratio of TEOS/C₂H₅OH/H₂O was 1/1/1. The mixture was stirred homogeneously and kept at room temperature for 20 h for gelation. Then the product was filtered, washed by deionized water for several times and dried at 393 K for 12 h. Then the product was calcined in a muffle oven at 723 K for 4 h. After calcination, the catalyst was pelletized, crushed, sieved to 20–40 mesh. The catalyst is referred to as Cu/SiO₂-SG.

2.2. Catalyst Characterization. XRD measurements were performed on a Bruker D8 X-ray diffractometer with Cu-K α radiation ($\lambda = 1.54156 \text{ \AA}$) at a scan rate of 4° min^{-1} at 45 kV and 40 mA.

BET surface areas were measured by N₂ adsorption at 77 K using a Micromeritics SSA-4000 instrument. Before measurements, samples were degassed under vacuum at 298 K for 3 h.

The XPS measurements were performed on a Perkin-Elmer PHI 5000 ESCA photoelectron spectrometer using an Al K α ($h\nu = 1,486.6 \text{ eV}$) source. The binding energies of the elements on the surfaces of the catalysts were corrected by using the carbon C1s value, 285 eV, as an internal standard.

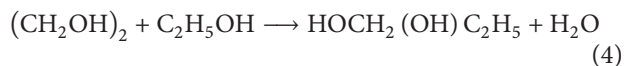
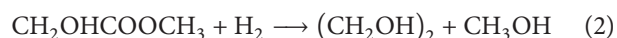
TEM images were obtained on a JEOL JEM 2010 transmission electron microscope with accelerating voltage of 200 kV.

H₂-TPR was also conducted to examine the catalyst reducibility. 50 mg of the catalyst was heated in He at 673 K for 60 min, followed by cooling to room temperature. The temperature was then raised in 50 mL/min of 10% H₂/Ar using a ramp rate of 10 K/min to 823 K. H₂ consumption was detected using TCD.

2.3. Catalyst Testing. Activity and selectivity measurements for DMO hydrogenation to EG were carried out in a continuous-flow fixed-bed reactor made of stainless steel (i.d. = 7 mm). 1.2 g catalyst was placed into the reactor. The reaction pressure was 2.0 MPa, and the reaction temperature is 453 K. Prior to the catalytic measurements, the catalyst was reduced in a stream of 10% H₂/N₂ at 553 K for 4 h under atmospheric pressure. After cooling to the reaction temperature, the catalyst bed was fed with 10% DMO in methanol and H₂, and H₂/DMO is 80 (mol/mol). The DMO in methanol was supplied by a syringe pump (SSI), vaporized, and mixed with the H₂ feed in an electrical heated stainless steel preheater at 443 K. The hydrogen feed was controlled by the mass flow controllers. The exit gases were cooled down to room temperature in a water-cooled condenser. The liquid product was collected and analyzed by gas chromatograph (Beijing Benfenruili Ltd., 3420) equipped with an FID detector.

3. Results and Discussion

3.1. Performance of Different Cu/SiO₂ Catalysts. The catalytic properties for DMO hydrogenation to EG over the Cu/SiO₂-AE and Cu/SiO₂-SG catalysts were tested. For the synthesis process of EG from hydrogenation of DMO, it can be expressed by the following reactions [17]:



During reaction process, first methyl glycolate (MG) is produced by hydrogenation of DMO, then further hydrogenation of MG to EG, while EG can dehydrate to ethanol (ET). At certain conditions, EG and ET can dehydrate to 1,2-butanol (BDO). MG is known as a partial hydrogenation product, while ET and BDO are called the excess hydrogenation products. The EG is a major product, and the other products are side products in our experiments. The conversion of DMO, the selectivity of EG and the yield of EG on Cu/SiO₂ are shown in Table 1. Compared with

TABLE 1: The catalytic activities of the Cu/SiO₂ catalysts prepared by different methods.

Catalyst	$X_{\text{DMO}}/\%$	$S_{\text{EG}}/\%$	$Y_{\text{EG}}/\%$
Cu/SiO ₂ -AE	98	96	94.1
Cu/SiO ₂ -SG	96	93	89.3

Reaction conditions: $T = 353\text{ K}$, $P = 2.0\text{ MPa}$, $\text{H}_2/\text{DMO} = 80\text{ (mol/mol)}$, $\text{LHSV} = 0.6\text{ h}^{-1}$.

Cu/SiO₂-AE catalyst, the Cu/SiO₂-SG catalyst exhibits higher activity. Conversion of DMO and selectivity of 98% and 96% are obtained on Cu/SiO₂-SG catalyst at optimal reaction conditions. It is well known that the catalytic performance of the Cu/SiO₂ catalysts is highly dependent on structure, size, and dispersion of copper species and surface chemical states of the catalysts. The different catalytic performance of the two Cu/SiO₂ catalysts could be resulted from their different structures. And further discussion will be carried out in the following parts. In addition, compared with other copper-based catalysts prepared various methods, the Cu/SiO₂-SG catalyst here also exhibits equal or higher activity [2, 10, 11].

Under the reaction temperature of 453 K, reaction pressure of 2, and Mpa and H₂/DMO molar ratio of 80, the effect of different liquid hourly space velocity (LHSV) on the performance of the Cu/SiO₂ catalysts is investigated and the results are shown in Figure 1. It can be clearly seen that conversion of DMO decreases gradually while the selectivity of EG first increases and then decreases with increasing LHSV over both Cu/SiO₂ catalysts. The EG selectivity of each catalyst reaches the maximum when the LHSV is 0.6 h⁻¹. This changing trend of the selectivity can be understood from the point of view of residence time. When the LHSV is lower, a longer residence time for reactants is obtained, resulting in overhydrogenation of EG and the production of ET and BDO, and the EG selectivity is consequently lower; While under higher LHSV, the residence time is shorter, leading to partial hydrogenation of DMO and the production of MG but not EG, and therefore the selectivity is also lower. By comparison it is found that both of the conversion of DMO and the selectivity for EG over the Cu/SiO₂-SG catalyst are greater than those of the Cu/SiO₂-AE catalysts.

3.2. The Characterization of the Cu/SiO₂ Catalysts

3.2.1. Textural Properties and Morphology. Figure 2 shows the XRD patterns of the reduced Cu/SiO₂ catalysts prepared with different methods. The strong and sharp peaks observed (see Figure 2) confirm that the catalysts are all well crystallized. For Cu/SiO₂-AE, the diffraction peaks appearing at 43.3°, 50.4°, and 74.1° can be indexed to Cu phase (JCPDS 85-1326), and the broad and diffuse diffraction peak at around 21.7° can be attributed to amorphous silica phase (JCPDS 88-1535), as shown in Figure 2. It is also found the diffraction peaks intensities of the Cu/SiO₂-SG catalyst are much weaker than those of Cu/SiO₂-AE, which implies the copper dispersion of the Cu/SiO₂-SG catalyst is higher than that of Cu/SiO₂-AE.

The physicochemical properties of the calcined catalysts are summarized in Table 2. It is clearly shown in Table 2 that

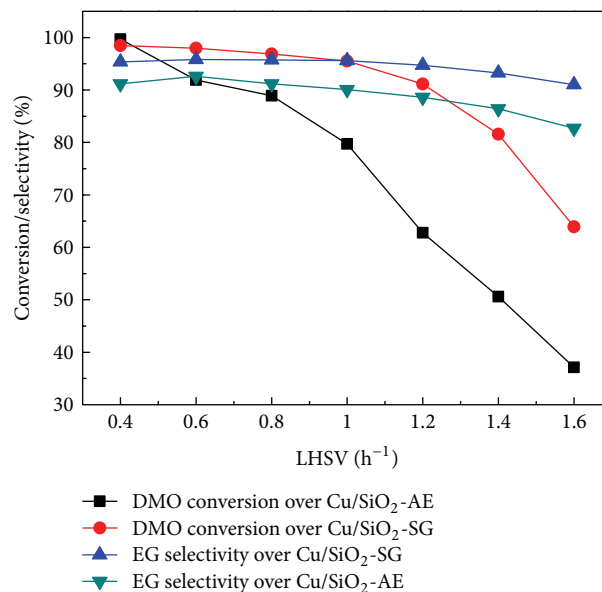


FIGURE 1: Effects of DMO LHSV on catalytic performances of Cu/SiO₂ catalysts. Reaction conditions: $P = 2.0\text{ MPa}$, $T = 453\text{ K}$, $\text{H}_2/\text{DMO} = 80\text{ (mol/mol)}$.

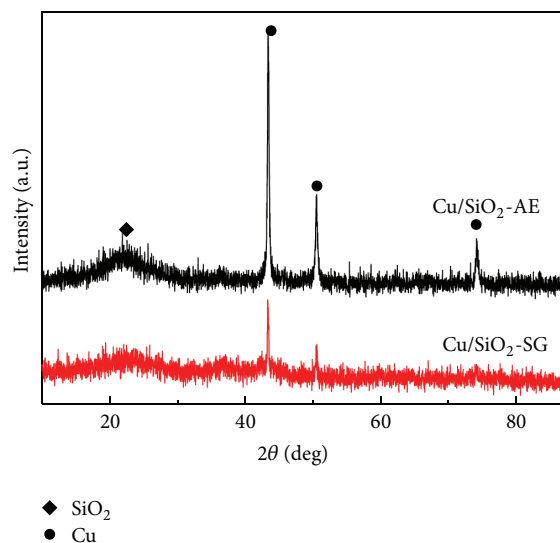


FIGURE 2: XRD patterns of the reduced Cu/SiO₂ catalysts prepared with different methods.

TABLE 2: The physicochemical properties of the Cu/SiO₂ catalysts prepared by different methods.

Catalyst	BET surface area (m ² /g)	Pore volume (cm ³ /g)	Average pore size (nm)
Cu/SiO ₂ -AE	144.0	0.51	14
Cu/SiO ₂ -SG	216.8	0.31	5.6

the BET surface area of the Cu/SiO₂-SG catalyst is much larger than that of Cu/SiO₂-AE catalyst. However, the average diameter of Cu/SiO₂-SG catalyst is much smaller than that of

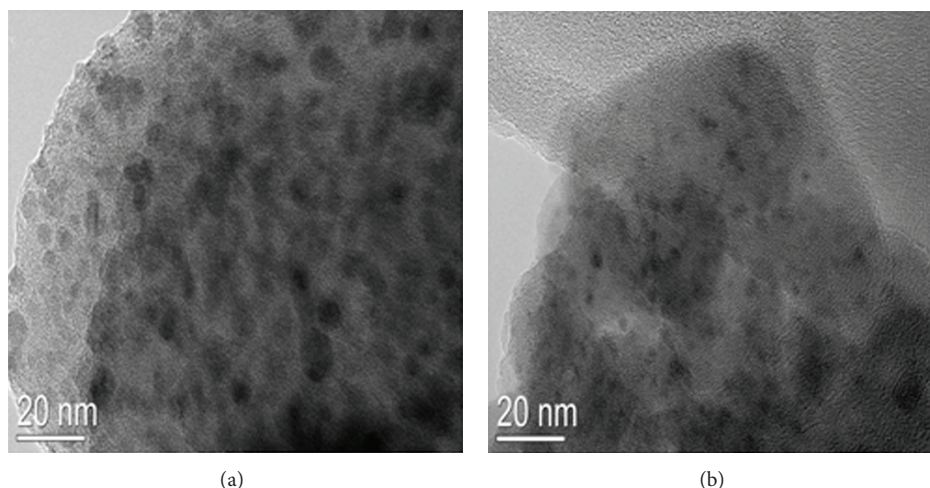


FIGURE 3: TEM images of reduced Cu/SiO₂ catalysts: (a) Cu/SiO₂-AE and (b) Cu/SiO₂-SG.

Cu/SiO₂-AE catalyst, and the average pore diameters are 14 and 5.6 nm, indicating that the two catalysts have mesoporous structures.

The copper dispersion can also be observed from the TEM images. Figure 3 shows the images of the reduced Cu/SiO₂ catalysts prepared by ammonia-evaporation method (Figure 3(a)) and sol-gel method (Figure 3(b)), respectively. It is observed that the copper species are distributed uniformly over the Cu/SiO₂-SG catalyst; the average particle size is about 3–4 nm. On the contrary, the average Cu particle size in the Cu/SiO₂-AE catalyst is about 10 nm; in addition, some Cu particles obviously aggregate together, implying poor Cu dispersion of the catalyst. The copper particles are highly distributed on the surrounding silica supports, which might increase the interaction between the copper species and the support and consequently improve the activity of the catalyst [18].

3.2.2. The Reducibility. TPR measurements were carried out to investigate the reducibility of the copper species in the Cu/SiO₂ catalysts prepared by different methods. Figure 4 presents the reduction profiles of the catalysts. As shown in Figure 4, there are two reduction peaks in the TPR profiles of the catalysts: one occurs in the range of 495–515 K and the other occurs in the range of 530–540 K, which are denoted as α peak (the low-temperature reduction peak) and β peak (the high-temperature reduction peak), respectively, implying the presence of different CuO species with slight differences in ease of reducibility. The α peak can be assigned to the reduction of well-dispersed CuO species and β peaks can be attributed to the reduction of bulk CuO. The similar assignments have also been reported for other copper based catalysts [19]. For Cu/SiO₂-AE catalyst, the area of α peak is much smaller than that of β peak, demonstrating that the quantity of larger CuO particles is much more than the smaller ones. In contrast, for Cu/SiO₂-SG catalyst, the trend changes conversely, suggesting the fractions of highly dispersed CuO species is much higher than those of bulk

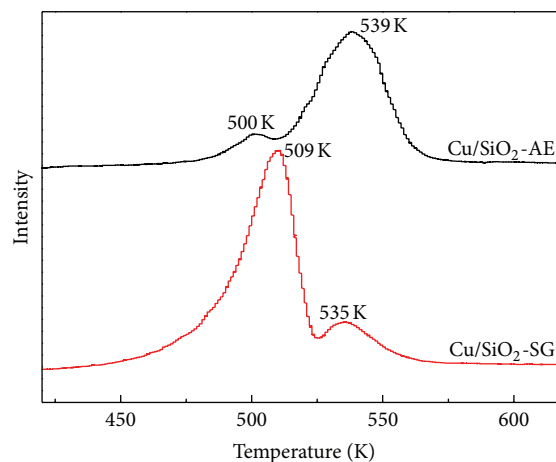


FIGURE 4: TPR profiles of different Cu/SiO₂ catalysts.

ones. The observed shift in reduction temperature may be ascribed to the different copper particle sizes, different interactions between copper oxide and silica, and different copper oxide dispersions. The TPR results further elucidate that the Cu/SiO₂ catalyst prepared by the sol-gel method can result in a better-dispersion of copper species on the SiO₂ support. In addition, the TPR results are consistent with TEM results.

3.2.3. The Surface Chemical States of the Catalysts. The XPS spectra as well as X-ray-induced Auger spectra (XAES) of the reduced catalysts are illustrated in Figures 5 and 6, respectively. As it can be seen from Figure 5, the binding energy values of Cu2p_{3/2} core levels are 932.4 and 932.7 eV of Cu/SiO₂-AE and Cu/SiO₂-SG, implying that copper has been reduced to Cu⁺ and/or Cu⁰ [20, 21]. Because the binding energy values of Cu⁺ and Cu⁰ are almost identical, the distinction between these two species present on the catalyst surface is impossible on the basis of the Cu2p level. In

TABLE 3: Surface Cu component of the reduced catalysts based on Cu LMM deconvolution.

Catalysts	KE (eV) ^a		α' (eV) ^b		Cu 2p _{3/2} BE (eV)	XCu ⁺ /Cu ^{0c} (mol/mol)
	Cu ⁺	Cu ⁰	Cu ⁺	Cu ⁰		
Cu/SiO ₂ -AE	916.3	918.3	1848.7	1850.7	932.4	1.79
Cu/SiO ₂ -SG	916.5	919.1	1849.2	1851.8	932.7	1.96

^aKinetic energy. ^bModified Auger parameter. ^cCu⁺/(Cu⁰) * 100%.

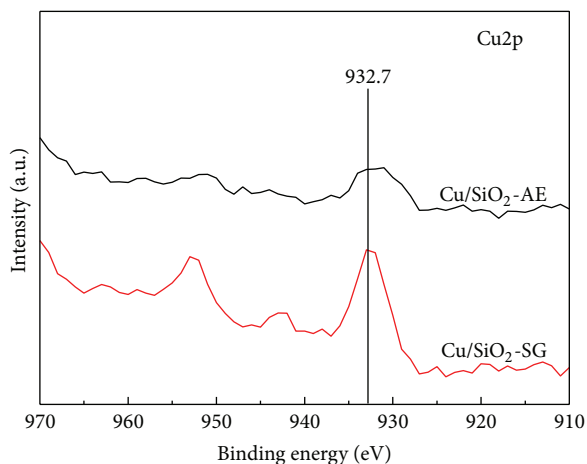


FIGURE 5: Cu2p photoelectron spectra of the reduced Cu/SiO₂ catalysts.

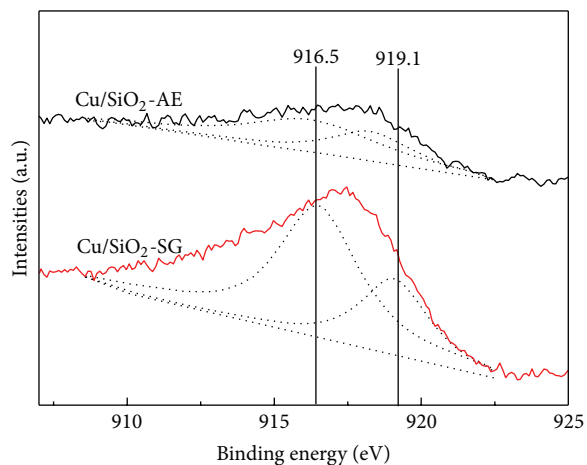


FIGURE 6: Cu LMM XAES spectra of the reduced Cu/SiO₂ catalysts.

general, Cu⁺ and Cu⁰ species can be distinguished through their kinetic energies in the XAES Cu LMM line position or the modified Auger parameters (α') [22]. It is reported that α' is ca. 1851.0 eV for Cu⁰ and 1849.0 eV for Cu⁺ [23]. As it can be seen from Figure 6, the Cu LMM spectra of catalysts show a broad and asymmetrical peak, implying the coexistence of Cu⁺ and Cu⁰ in the surface of the catalyst. Two symmetrical peaks centered at near 916 and 919 eV can be obtained by deconvolution of the original Cu LMM peaks, which are corresponding to Cu⁺ and Cu⁰ species [24]. The

deconvolution results are summarized in Table 3. As shown in Table 3, the α' value at ca. 1849 eV is ascribed to Cu⁺ and 1851 eV to Cu⁰. Compared with bulk Cu⁺, the α' values of Cu⁺ in the catalysts are 2-3 eV lower, indicating strong interaction between Cu⁺ and silica supports [25]. The Cu⁺/Cu⁰ area ratios derived from fitting the Cu LMM peaks are listed in Table 3. It is noted that the Cu⁺/Cu⁰ area ratio on the surface of reduced Cu/SiO₂-SG is 9.4% more than that of reduced Cu/SiO₂-AE, which might be one reason for the enhancement in catalytic activity for the catalyst. It is reported that higher activity can be obtained on the Cu/SiO₂ catalyst with proper ratio of Cu⁺/Cu⁰ due to their synergetic effect. The XPS and XAES results are in good agreements with TPR results. It can be concluded that the surface chemical states of the catalysts are highly effected by the preparation methods.

4. Conclusions

In summary, the Cu/SiO₂ catalysts for the synthesis of EG from hydrogenation of DMO were prepared by two methods: one was prepared by ammonia method and the other was prepared by sol-gel method. It is found that the structure, the reducibility of CuO, the particle size of Cu, and the surface chemical state are highly affected by the preparation method. By comparison, the catalyst prepared by sol-gel method exhibited higher activity and EG selectivity, and 98% DMO conversion and 96% EG selectivity can be obtained under the optimized hydrogenation conditions, due to its smaller Cu particles size, larger BET surface area, and higher dispersion in silica.

Acknowledgments

The authors thank Liaoning Science and Technology Department Foundation (Grant no. 2007223016), Liaoning Educational Department Foundation (Grant no. l2011065) and Shenyang Science and Technology Department Foundation (Grant no. F11-264-1-76) for financial support.

References

- [1] G. H. Xu, Y. C. Li, Z. H. Li, and H. J. Wang, "Kinetics of the hydrogenation of diethyl oxalate to ethylene glycol," *Industrial and Engineering Chemistry Research*, vol. 34, no. 7, pp. 2371–2378, 1995.
- [2] L. F. Chen, P. J. Guo, M. H. Qiao et al., "Cu/SiO₂ catalysts prepared by the ammonia-evaporation method: texture, structure, and catalytic performance in hydrogenation of dimethyl oxalate to ethylene glycol," *Journal of Catalysis*, vol. 257, no. 1, pp. 172–180, 2008.

- [3] G. Zhengong, L. Zhongchen, H. Fei, and X. Genhui, "Combined XPS and in situ DRIRS study of mechanism of Pd-Fe/ α -Al₂O₃ catalyzed CO coupling reaction to diethyl oxalate," *Journal of Molecular Catalysis A*, vol. 235, no. 1-2, pp. 143-149, 2005.
- [4] A. Yin, X. Guo, W. L. Dai, and K. Fan, "The nature of active copper species in Cu-hms catalyst for hydrogenation of dimethyl oxalate to ethylene glycol: New insights on the synergetic effect between Cu⁰ and Cu⁺," *Journal of Physical Chemistry C*, vol. 113, no. 25, pp. 11003-11013, 2009.
- [5] U. Matteoli, M. Bianchi, G. Menchi, P. Prediani, and F. Piacenti, "Homogeneous catalytic hydrogenation of dicarboxylic acid esters," *Journal of Molecular Catalysis*, vol. 22, no. 3, pp. 353-362, 1984.
- [6] U. Matteoli, G. Menchi, M. Bianchi, and F. Piacenti, "Selective reduction of dimethyl oxalate by ruthenium carbonyl carboxylates in homogeneous phase Part IV," *Journal of Molecular Catalysis*, vol. 64, no. 3, pp. 257-267, 1991.
- [7] A. Yin, X. Guo, W. Dai, and K. Fan, "High activity and selectivity of Ag/SiO₂ catalyst for hydrogenation of dimethyl oxalate," *Chemical Communications*, vol. 46, no. 24, pp. 4348-4350, 2010.
- [8] M. A. Karakassides, A. Bourlinos, D. Petridis, L. Coche-Guerente, and P. Labbe, "Synthesis and characterization of copper containing mesoporous silicas," *Journal of Materials Chemistry*, vol. 10, no. 2, pp. 403-408, 2000.
- [9] D. J. Thomas, J. T. Wehrli, M. S. Wainwright, D. L. Trimm, and N. W. Cant, "Hydrogenolysis of diethyl oxalate over copper-based catalysts," *Applied Catalysis A*, vol. 86, no. 2, pp. 101-114, 1992.
- [10] L. He, X. Chen, J. Ma, H. He, and W. Wang, "Characterization and catalytic performance of sol-gel derived Cu/SiO₂ catalysts for hydrogenolysis of diethyl oxalate to ethylene glycol," *Journal of Sol-Gel Science and Technology*, vol. 55, no. 3, pp. 285-292, 2010.
- [11] A. Yin, C. Wen, X. Guo, W. L. Dai, and K. Fan, "Influence of Ni species on the structural evolution of Cu/SiO₂ catalyst for the chemoselective hydrogenation of dimethyl oxalate," *Journal of Catalysis*, vol. 280, no. 1, pp. 77-88, 2011.
- [12] B. Zhang, S. G. Hui, S. H. Zhang, Y. Ji, W. Li, and D. Y. Fang, "Effect of copper loading on texture, structure and catalytic performance of Cu/SiO₂ catalyst for hydrogenation of dimethyl oxalate to ethylene glycol," *Journal of Natural Gas Chemistry*, vol. 21, pp. 563-570, 2012.
- [13] Y. Y. Zhu, S. R. Wang, L. J. Zhu, X. L. Ge, X. B. Li, and Z. Y. Luo, "The influence of copper particle dispersion in Cu/SiO₂ catalysts on the hydrogenation synthesis of ethylene glycol," *Catalysis Letters*, vol. 135, no. 3-4, pp. 275-281, 2010.
- [14] L. Lin, P. B. Pan, Z. F. Zhou et al., "Cu/SiO₂ catalysts prepared by the Sol-Gel method for hydrogenation of dimethyl oxalate to ethylene glycol," *Chinese Journal of Catalysis*, vol. 32, pp. 957-968, 2011.
- [15] M. Zheng, T. Zhao, W. Xu, F. Li, and Y. Wang, "Preparation and characterization of Cu/SiO₂ catalyst by co-gelation process," *Journal of Materials Science*, vol. 42, no. 19, pp. 8320-8325, 2007.
- [16] A. Yin, X. Guo, W. L. Dai, and K. Fan, "Effect of initial precipitation temperature on the structural evolution and catalytic behavior of Cu/SiO₂ catalyst in the hydrogenation of dimethyl oxalate," *Catalysis Communications*, vol. 12, no. 6, pp. 412-416, 2011.
- [17] C. Carlini, M. Di Girolamo, A. Macinai et al., "Selective synthesis of isobutanol by means of the Guerbet reaction part 2. Reaction of methanol/ethanol and methanol/ethanol/n-propanol mixtures over copper based/MeOna catalytic systems," *Journal of Molecular Catalysis A*, vol. 200, no. 1-2, pp. 137-146, 2003.
- [18] A. Yin, C. Wen, W. L. Dai, and K. Fan, "Surface modification of HMS material with silica sol leading to a remarkable enhanced catalytic performance of Cu/SiO₂," *Applied Surface Science*, vol. 257, no. 13, pp. 5844-5849, 2011.
- [19] X. M. Guo, D. S. Mao, S. Wang, G. S. Wu, and G. Z. Lu, "Combustion synthesis of CuO-ZnO-ZrO₂ catalysts for the hydrogenation of carbon dioxide to methanol," *Catalysis Communications*, vol. 10, pp. 1661-1664, 2009.
- [20] J. Toyir, P. Ramirez De La Piscina, J. L. G. Fierro, and N. Homs, "Highly effective conversion of CO₂ to methanol over supported and promoted copper-based catalysts: influence of support and promoter," *Applied Catalysis B*, vol. 29, no. 3, pp. 207-215, 2001.
- [21] J. Toyir, P. Ramirez de la Piscina, J. L. G. Fierro, and N. Homs, "Catalytic performance for CO₂ conversion to methanol of gallium-promoted copper-based catalysts: influence of metallic precursors," *Applied Catalysis B*, vol. 34, no. 4, pp. 255-266, 2001.
- [22] F. Márquez, A. E. Palomares, F. Rey, and A. Corma, "Characterisation of the active copper species for the NOx removal on Cu/Mg/Al mixed oxides derived from hydrotalcites: an in situ XPS/XAES study," *Journal of Materials Chemistry*, vol. 11, no. 6, pp. 1675-1680, 2001.
- [23] K. Sun, W. Lu, F. Qiu, S. Liu, and X. Xu, "Direct synthesis of DME over bifunctional catalyst: surface properties and catalytic performance," *Applied Catalysis A*, vol. 252, no. 2, pp. 243-249, 2003.
- [24] N. S. McIntyre, T. E. Rummery, M. G. Cook, and D. Owen, "X-ray photoelectron spectroscopic study of the aqueous oxidation of monel-400," *Journal of the Electrochemical Society*, vol. 123, no. 8, pp. 1164-1170, 1976.
- [25] M. A. Kohler, H. E. Curry-Hyde, A. E. Hughes, B. A. Sexton, and N. W. Cant, "The structure of Cu SiO₂ catalysts prepared by the ion-exchange technique," *Journal of Catalysis*, vol. 108, no. 2, pp. 323-333, 1987.